

**The dynamics of microtubule stability**  
**A reconstitution of regulated microtubule assembly under force**

Kok, Maurits

**DOI**

[10.4233/uuid:5cb3dd60-78ab-4272-a820-7a754c2cc6a0](https://doi.org/10.4233/uuid:5cb3dd60-78ab-4272-a820-7a754c2cc6a0)

**Publication date**

2019

**Document Version**

Final published version

**Citation (APA)**

Kok, M. (2019). *The dynamics of microtubule stability: A reconstitution of regulated microtubule assembly under force* (2019-10 ed.). [Dissertation (TU Delft), Delft University of Technology]. Casimir PhD Series. <https://doi.org/10.4233/uuid:5cb3dd60-78ab-4272-a820-7a754c2cc6a0>

**Important note**

To cite this publication, please use the final published version (if applicable).  
Please check the document version above.

**Copyright**

Other than for strictly personal use, it is not permitted to download, forward or distribute the text or part of it, without the consent of the author(s) and/or copyright holder(s), unless the work is under an open content license such as Creative Commons.

**Takedown policy**

Please contact us and provide details if you believe this document breaches copyrights.  
We will remove access to the work immediately and investigate your claim.

# **THE DYNAMICS OF MICROTUBULE STABILITY**

A RECONSTITUTION OF REGULATED MICROTUBULE  
ASSEMBLY UNDER FORCE



# **THE DYNAMICS OF MICROTUBULE STABILITY**

A RECONSTITUTION OF REGULATED MICROTUBULE  
ASSEMBLY UNDER FORCE

## **Proefschrift**

ter verkrijging van de graad van doctor  
aan de Technische Universiteit Delft,  
op gezag van de Rector Magnificus prof. dr. ir. T. H. J. J. van der Hagen,  
voorzitter van het College voor Promoties,  
in het openbaar te verdedigen op woensdag 24 april 2019 om 15:00 uur

door

**Maurits William Adriaan KOK**

Master of Science in Applied Physics,  
Technische Universiteit Delft, Nederland,  
geboren te Utrecht.

Dit proefschrift is goedgekeurd door de promotor.

Samenstelling promotiecommissie:

Rector Magnificus, voorzitter  
Prof. dr. M. Dogterom, Technische Universiteit Delft, promotor

*Onafhankelijke leden:*

Dr. M. Gardner, University of Minnesota, USA  
Dr. T. Surrey, The Francis Crick Institute, United Kingdom  
Dr. ir. L. Laan, Technische Universiteit Delft  
Prof. dr. C. L. Wyman, Technische Universiteit Delft  
Prof. dr. B. Mulder, Universiteit Wageningen  
Prof. dr. C. Dekker, Technische Universiteit Delft, reservelid

*Overige leden:*

Prof. dr. L. C. Kapitein, Universiteit Utrecht



**Keywords:** Microtubules, optogenetics, micro-fabrication, in vitro reconstitution, motor proteins, CLASP, EB3, Monte Carlo simulations

**Printed by:** Gildeprint

**Front:** *Reconstituting microtubule dynamics on a micro-fabricated chip.*  
Photograph by Maurits Kok. Nikon D7200 with Tokina 100mm: f/40, 8.0 sec, ISO 640.

Copyright © 2019 by M. W. A. Kok

Casimir PhD Series, Delft-Leiden 2019-10

ISBN 978-90-8593-392-2

An electronic version of this dissertation is available at  
<http://repository.tudelft.nl/>.

*Nothing in the world is more dangerous  
than sincere ignorance and conscientious stupidity.*

Martin Luther King Jr.



# SUMMARY

The microtubule cytoskeleton is a driving force behind cell structure, playing important roles in cell division, cell morphology, cell motility, and intracellular transport. Microtubules are self-assembling, dynamic polymers that alternate between phases of growth and shrinkage, a behaviour known as *dynamic instability*. This intrinsic property is inextricably linked to the ability of a cell to regulate the properties of its cytoskeletal network. Through the regulatory activity of microtubule associated proteins (MAPs), a cell can flexibly rearrange its shape and guide cell division. An important property of microtubules is their force generating capability, which is essential for the proper positioning of cellular components. The pushing and pulling forces generated by controlled growth and shrinkage of microtubules drive a wide range of processes, including organelle positioning, mitotic spindle assembly, and chromosome separation. Obtaining a detailed understanding on how the stability of microtubules is affected and regulated through these interactions provides valuable insight into the fundamental properties and functions of microtubules. To experimentally address this, *in vitro* reconstitution assays are an indispensable tool to dissect the dynamics of microtubules in a controlled artificial environment.

This thesis addresses two research directions. First, we investigate the stability of microtubules under force in the presence of the regulatory proteins CLASP and EB. To do so, we develop and optimize two approaches for the fabrication of sub-micron barriers that enable the *in vitro* study of microtubules interacting with rigid objects (Chapter 2). The final design comprises barriers made of SiO<sub>2</sub> with a silicon carbide (SiC) overhang that can be selectively functionalized and successfully imaged with TIRF microscopy. Secondly, we explore artificial strategies to control protein-protein interactions to include spatiotemporal regulation in *in vitro* reconstitutions.

Microtubules assemble through the association of GTP-bound tubulin in a head-to-tail fashion at the microtubule end. Hydrolysis of the microtubule lattice from GTP to GDP, leads to the formation of a transient stabilizing GTP cap. The loss of this cap triggers a catastrophe, the transition between growth and shrinkage. It is known that the interaction of growing microtubules with steric objects such as the cell cortex promotes the occurrence of catastrophes. If microtubules are unable to overcome compressive forces, they remain in a stalled state, leading to accelerated disappearance of the stabilizing cap and the subsequent onset of catastrophe. In Chapter 3 we show that the regulating protein CLASP suppresses catastrophes, including those induced by physical barriers. CLASPs suppress catastrophes by stabilizing growing microtubule ends, including incomplete ones, preventing their depolymerization and promoting their recovery. To further investigate the dynamics of the cap, we use the plus-end binding protein EB3 as a marker for the nucleotide state of the tip (Chapter 4). We show that the resulting lifetimes of stalled microtubules, as well as the corresponding life time distributions of freely growing microtubules, can be fully described with a

simple phenomenological 1D model based on noisy microtubule growth and a single EB3-dependent hydrolysis rate. This same model is furthermore capable of explaining both the previously reported catastrophe statistics during tubulin washout and the mild catastrophe dependence on microtubule growth rates.

Next, we sought to reconstitute a system to regulate the temporal activation and spatial localization of biochemical components, as this is an essential feature in cellular dynamics. Implementing such control would enable the study of simple cellular processes out of equilibrium by reversibly perturbing the system *in situ*. In Chapter 5, we use light-inducible protein-protein interactions to recruit molecular motors to a surface to control microtubule gliding activity *in vitro*. Force generation by molecular motors drives biological processes such as asymmetric cell division and cell migration. We show that the motor proteins *dynein* and *Ncd* can be recruited to the surface in well-defined patterns. We further demonstrate that light-controlled recruitment of these motor proteins result in activation of microtubule gliding along the surface, enabling control over local microtubule motility. In Chapter 6, we characterize the activation kinetics of light-inducible protein dimerization *in vitro*. We demonstrate that activation and deactivation can be regulated through the activation energy, the activation duration, and through biochemical effectors.

In summary, we showed that the microtubule assembly under force can be regulated by MAPs and understood with a simple 1D phenomenological model. Furthermore, we developed the use of light-inducible protein-protein interactions *in vitro* as a means to exert spatiotemporal control over the microtubule cytoskeleton.

# SAMENVATTING

Het skelet van de cel (cytoskelet) is bepalend voor de structuur van een levende cel en speelt een belangrijke rol in celdeling, morfogenese, cel migratie, en intracellulair transport. Het cytoskelet is een dynamisch netwerk van (onder andere) zelf-assemblerende buisjes, zogenaamde microtubuli, die voortdurend wisselen tussen fases van groei en krimp. Dit specifieke gedrag staat bekend als *dynamische instabiliteit*. Deze fundamentele eigenschap is onlosmakelijk verbonden met het vermogen van een cel om het cytoskelet flexibel te vervormen, mede door de aanwezigheid van regulerende eiwitten. Microtubuli zijn bovendien in staat om krachten te genereren door te groeien en te krimpen, cruciaal voor de positionering van cellulaire onderdelen en het sturen van celdeling. Als we kunnen begrijpen hoe de stabiliteit van microtubuli wordt beïnvloed door de interacties met andere onderdelen in de cel, kunnen we beter begrijpen hoe deze processen worden aangestuurd. De manier om dit te experimenteel te bevragen is door de processen buiten de cel in een gecontroleerde artificiële omgeving te bestuderen (*in vitro*).

Dit proefschrift bespreekt twee verschillende onderzoeksrichtingen. Allereerst onderzoeken we hoe de stabiliteit van duwende microtubuli wordt gereguleerd door de eiwitten CLASP en EB. Dit doen we door muurtjes van ongeveer één micrometer hoog te maken die dienen als obstakels waar de microtubuli tegenaan kunnen groeien (Hoofdstuk 2). The uiteindelijke ontwerp bestaat uit muurtjes gemaakt van SiO<sub>2</sub> met een overhang van siliciumcarbide (SiC). Dit resulteert in muurtjes die van een eiwit-coating kunnen worden voorzien en met TIRF microscopie gevisualiseerd kunnen worden. Ten tweede onderzoeken we de implementatie van eiwit-eiwit verbindingen die met licht worden aangestuurd om daarmee lokaal eiwitten te rekruteren.

Microtubuli zijn polymeren die spontaan assembleren door de kop-staart verbinding van GTP-gebonden tubuline eiwitten. Hydrolyse van de geïncorporeerde tubuline van GTP naar GDP leidt tot de formatie van een tijdelijk stabiliserende GTP-kap aan het uiteinde van de microtubulus. Deze kap beschermt de groeiende microtubulus tegen krimp. Verlies van de beschermende kap brengt een zogenaamde catastrofe teweeg, de transitie van groei naar krimp. Het is bekend dat de interactie van microtubuli met onbeweeglijke objecten, zoals de cel cortex, de kans op een catastrofe laat toenemen. Als de duwende microtubuli de voortvloeiende samendrukkende kracht niet te boven kunnen komen, verliest deze in versneld tempo de stabiliserende kap en ondergaat een catastrofe. In Hoofdstuk 3 laten we zien dat het eiwit CLASP de aanvang van een catastrofe kan voorkomen, waaronder die veroorzaakt door de interactie met een muurtje. Om de dynamiek van de stabiliserende kap beter te begrijpen, gebruiken we het eiwit EB3 als een marker voor de stabiliteit van het uiteinde van de microtubulus (Hoofdstuk 4). We zien dat de levensduur van zowel groeiende microtubuli als microtubuli in stilstand beschreven kan worden met een fenomenologisch eendimensionaal model dat gebaseerd is op stochastische groei en

een enkele EB3-afhankelijke hydrolyse stap.

Vervolgens zochten we naar een manier om meer controle te krijgen over de locatie en activatie van biochemische componenten in onze experimenten, aangezien dit een essentieel kenmerk is van cellulaire dynamiek. Het kunnen uitoefenen van deze controle zou de studie van simpele cellulaire processen uit evenwicht mogelijk maken. In Hoofdstuk 5 gebruiken we door licht-aangestuurde eiwit-eiwit interacties om moleculaire motoren naar een oppervlak te brengen waarop microtubuli kunnen "glijden". Moleculaire motoren oefenen krachten uit op verscheidene biologische processen, zoals asymmetrische celdeling en cell migratie. We tonen aan dat de motor eitwitten *dynein* en *Ncd* naar een oppervlak gerekruteerd kunnen worden in gecontroleerd patroon. We demonstreren dat rekrutering van de motoren naar het oppervlak middels licht, gecontroleerde glijbewegingen van microtubuli mogelijk maakt. In Hoofdstuk 6 karakteriseren we de activatie kinetiek van de eiwit-eiwit interacties *in vitro*. We tonen aan dat (de)activatie gereguleerd kan worden door de activatie energie, de activatie duur, en door biochemische effectoren.

Samenvattend laten we zien dat de assemblage van duwende microtubules gereguleerd kan worden door CLASP en EB en kan worden begrepen door middel van een eendimensionaal fenomenologisch model. Daarnaast hebben we door licht geactiveerde eiwit-eiwit verbindingen *in vitro* als een methode om controle over het cytoskelet uit te oefenen.

# CONTENTS

<b>Summary</b>	<b>vii</b>
<b>Samenvatting</b>	<b>ix</b>
<b>1 General introduction</b>	<b>1</b>
1.1 The cytoskeleton . . . . .	2
1.2 Introduction to microtubule dynamics . . . . .	2
1.3 Modulating microtubule dynamics . . . . .	7
1.4 Growing microtubules generate pushing forces . . . . .	11
1.5 Reconstitution of microtubule pushing forces . . . . .	13
1.6 Pulling forces generated by microtubule depolymerization . . . . .	14
1.7 Reconstituting microtubule pulling forces . . . . .	16
1.8 Modelling microtubule dynamics . . . . .	18
1.9 Reconstituting complex force-generating microtubule systems . . . . .	19
1.10 Thesis motivation and outline . . . . .	21
<b>2 Micro-fabrication of rigid barriers</b>	<b>25</b>
2.1 Introduction . . . . .	26
2.2 Design . . . . .	27
2.3 Fabrication . . . . .	28
2.4 SiC as a substrate for microtubule dynamics . . . . .	31
2.4.1 <i>In vitro</i> microtubule reconstitution assay . . . . .	31
2.4.2 Microtubules electrostatically interact with SiC . . . . .	32
2.4.3 Laser-induced cavitation bubbles on an SiC substrate . . . . .	32
2.5 Selective barrier functionalization . . . . .	34
2.6 Discussion . . . . .	36
<b>3 CLASP suppresses microtubule catastrophes through a single TOG domain</b>	<b>39</b>
3.1 Introduction . . . . .	40
3.2 Results . . . . .	41
3.2.1 A complex of CLASP2 $\alpha$ and EB3 suppresses catastrophes and promotes templated MT nucleation . . . . .	41
3.2.2 A single MT-tip targeted TOG-like domain of CLASP2 $\alpha$ is sufficient to suppress catastrophes . . . . .	46
3.2.3 Autoregulatory interactions within CLASP2 $\alpha$ . . . . .	48
3.2.4 CLASP2 $\alpha$ suppresses catastrophes induced by MT-depolymerizing agents. . . . .	49
3.2.5 CLASP2 $\alpha$ suppresses force-induced catastrophes . . . . .	50
3.2.6 TOG2 shows preference for a region located behind the outmost MT end . . . . .	54

3.2.7	A few CLASP2 $\alpha$ monomers stabilize incomplete MT structures . . .	55
3.3	Discussion . . . . .	58
3.4	Experimental methods . . . . .	63
<b>4</b>	<b>EB informed dynamics of the microtubule cap during stalled growth</b>	<b>75</b>
4.1	Introduction . . . . .	76
4.2	Results . . . . .	78
4.2.1	<i>In vitro</i> reconstitution of microtubule stalling . . . . .	78
4.2.2	Complete EB3 decay does not need to trigger an immediate catastrophe . . . . .	79
4.2.3	Monte Carlo simulation of microtubule stalling . . . . .	79
4.2.4	Determining the catastrophe threshold . . . . .	82
4.2.5	Both GTP hydrolysis and tip fluctuations determine stalling duration . . . . .	84
4.2.6	Simulating tubulin washout . . . . .	84
4.3	Discussion . . . . .	87
4.4	Experimental methods . . . . .	91
<b>5</b>	<b>Guided by light: Optical control of microtubule gliding assays</b>	<b>101</b>
5.1	Introduction . . . . .	102
5.2	Results . . . . .	103
5.2.1	Light-induced surface recruitment of ePDZ . . . . .	103
5.2.2	Light-induced microtubule gliding assay . . . . .	103
5.2.3	Characterization of microtubule gliding . . . . .	106
5.3	Discussion . . . . .	106
5.4	Methods . . . . .	108
<b>6</b>	<b>Characterization of light-induced heterodimerization <i>in vitro</i></b>	<b>111</b>
6.1	Introduction . . . . .	112
6.2	Results . . . . .	113
6.2.1	Determining reaction rates . . . . .	115
6.2.2	Local activation . . . . .	117
6.2.3	Imidazole speeds up the dark state recovery . . . . .	119
6.2.4	Barrier functionalization . . . . .	120
6.2.5	Light-induced cortical recruitment in water-in-oil droplets . . . . .	121
6.3	Discussion . . . . .	122
6.4	Experimental methods . . . . .	122
<b>7</b>	<b>Discussion and outlook</b>	<b>127</b>
	<b>Bibliography</b>	<b>131</b>
	<b>Acknowledgements</b>	<b>163</b>
	<b>Curriculum Vitæ</b>	<b>165</b>
	<b>List of Publications</b>	<b>167</b>

# 1

## GENERAL INTRODUCTION

*There is nothing that living things do that cannot be understood  
from the point of view that they are made of atoms  
acting according to the laws of physics.*

Richard Feynman

*Microtubules are dynamic filaments that switch between growing and shrinking states, a feature known as dynamic instability. The biochemical parameters underlying dynamic instability are modulated by a variety of microtubule-associated proteins that enable strict control over microtubule dynamics in cells. The forces generated by controlled growth and shrinkage of microtubules drive a wide range of processes, including organelle positioning, mitotic spindle assembly, and chromosome separation. In this first introductory chapter, we review the microtubule-intrinsic process of dynamic instability, the effect of external factors on this process, and how the resulting forces act on various biological systems. We especially highlight the current in vitro reconstitution-based approaches used to understand these phenomena. Finally, we motivate our research direction, sketch the future of reconstitution-based synthetic biology, and provide an outline of the thesis.*

---

This chapter is based on the publication *Understanding force-generating microtubule systems through in vitro reconstitution*, Mathijs Vleugel, [Maurits Kok](#), and Marileen Dogterom, *Cell Adh Migr* **2016**, 10:5, 475-495. <https://doi.org/10.1080/19336918.2016.1241923>.

## 1.1. THE CYTOSKELETON

Microtubules are a major constituent of the eukaryotic cytoskeleton, which also includes actin and intermediate filaments. In contrast to what is implied by the term 'cytoskeleton' (literally: skeleton of the cell), microtubules are generally very dynamic, and support a broad range of functions within the cell. For example, microtubules are essential for cell mechanics, cell division (Fig. 1.1), intracellular transport, and cell motility. Whereas the minus-ends of microtubules are usually stabilised by other structures, the plus-ends constantly switch between growing and shrinking states. The energy released by microtubule growth as well as shrinkage is used for force generation in a wide variety of cellular processes. Over the past two decades, significant advancements have been made in our understanding of the diverse range of biological functions that are supported by microtubule-generated forces. The recent development of more sophisticated reconstitution systems allows for a more in-depth characterization of the biochemical and biophysical processes underlying microtubule dynamics and force generation.

## 1.2. INTRODUCTION TO MICROTUBULE DYNAMICS

Microtubules are hollow, cylindrical polymers and are composed of heterodimers of  $\alpha$ - and  $\beta$ -tubulin subunits that assemble in a head-to-tail fashion (Fig. 1.2A). Linear

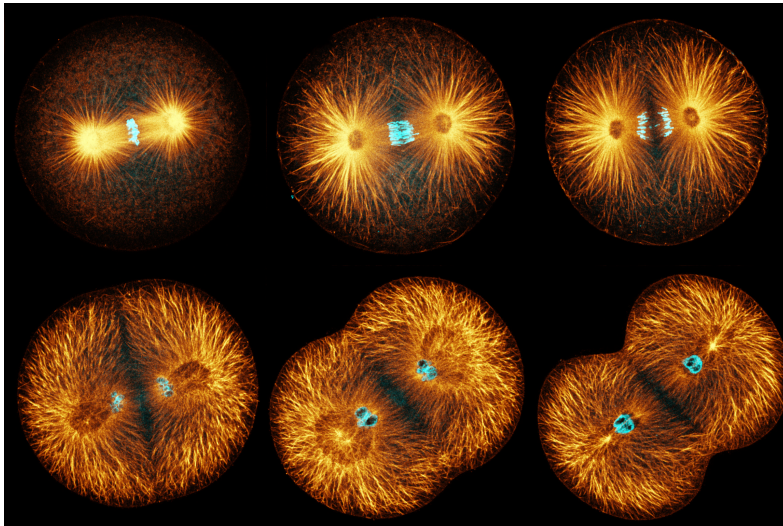


Figure 1.1: **Mitosis in a sea urchin cell.**

Confocal image sequence of a dividing sand dollar cell progressing through prometaphase, metaphase, anaphase, and telophase. The microtubule structure needs severe coordinated rearrangement during mitosis to search and capture the chromosomes, align them in the midzone and separate them faithfully into the two daughter cells. Microtubules are labelled in orange, and DNA in blue.

Credits to George von Dassow.

arrays of  $\alpha/\beta$ -tubulin dimers are termed protofilaments, 13 of which associate laterally to make up the microtubule (Fig. 1.2B) (Mandelkow et al., 1986; Tilney et al., 1973). This polarised arrangement of tubulin dimers extends into a supra-molecular polarity with an  $\alpha$ -tubulin exposed 'minus-end' and a  $\beta$ -tubulin exposed 'plus-end'.

Microtubules are constantly switching between phases of polymerisation and depolymerisation, a process known as dynamic instability (Mitchison and Kirschner, 1984). This addition and loss of tubulin subunits is a stochastic process intrinsically dependent on the nucleotide-state of the subunits (Gardner et al., 2011). This feature forms the basis for the ability of cells to swiftly remodel their microtubule network in response to intracellular or extracellular cues. In most cells, this dynamic behaviour is only observed at microtubule plus-ends, since the minus-ends are most often stably embedded into the microtubule-organizing centre (MTOC) from which microtubule nucleation is promoted. Centrosomes function as the major MTOC during mitosis, whereas during interphase significant microtubule-nucleation can be observed from other structures including the Golgi apparatus (Sanders and Kaverina, 2015). Microtubule nucleation *in vitro* takes place from short pieces of microtubule known as seeds that have been stabilized by taxol (Schiff et al., 1979) or by the incorporation of GMP-CPP (Hyman et al., 1992), a non-hydrolysable form of GTP, from purified centrosomes (Mitchison and Kirschner, 1984), or from axonemes (Kalisch et al., 2011).

## BIOCHEMISTRY OF TUBULIN

The tubulin heterodimer making up the microtubule lattice is composed of  $\alpha$ - and  $\beta$ -tubulin, each being approximately 55 kDa in size (Oakley, 2000). A third tubulin member is  $\gamma$ -tubulin, the majority of which is organised in  $\gamma$ -tubulin ring complexes ( $\gamma$ -TuRC) in the MTOC, where it stabilizes the microtubule minus ends and acts as a microtubule nucleation template (Kollman et al., 2011). The most common form of microtubules *in vivo* consists of 13 protofilaments (Tilney et al., 1973) and is ordered into a so-called B-lattice, which is characterized by homotypic lateral contacts resulting in  $\alpha$ - $\alpha$  and  $\beta$ - $\beta$  interactions (Fig. 1.2C). Due to an axial offset between the protofilaments, the lattice contains a helical twist that gives rise to a discontinuity, known as the seam. This seam runs along the length of the microtubule and contains lateral (heterotypic)  $\alpha$ - $\beta$  interactions (Nogales, 2000) (Fig. 1.2C).

The  $\alpha$ -tubulin subunit contains a non-exchangeable GTP nucleotide that is buried at the  $\alpha$ - $\beta$  interface (at the so-called 'N-site') (Fig. 1.2A). In contrast, the  $\beta$ -tubulin subunit accommodates an exchangeable GTP nucleotide (at the 'E-site'). The presence of GTP at this site favours a new dimer to bind longitudinally with a heterotypic interaction at the exposed plus-end (Nogales et al., 1999). After the incorporation of a tubulin dimer into the microtubule lattice, the GTP nucleotide at the E-site becomes hydrolysed, resulting in a lattice containing mostly GDP nucleotides at the E-site (Dimitrov et al., 2008) (Fig. 1.2D).

In cryo-electron microscopy (cryo-EM) studies, the ends of growing and shrinking microtubules adopt different structural configurations. Growing microtubule plus ends contain mostly straight protofilaments, while shrinking plus-ends peel outward after having lost the lateral interactions between its protofilaments (Mandelkow et al., 1991) (Fig. 1.2D,E). This observation introduced the early hypothesis that GTP-tubulin

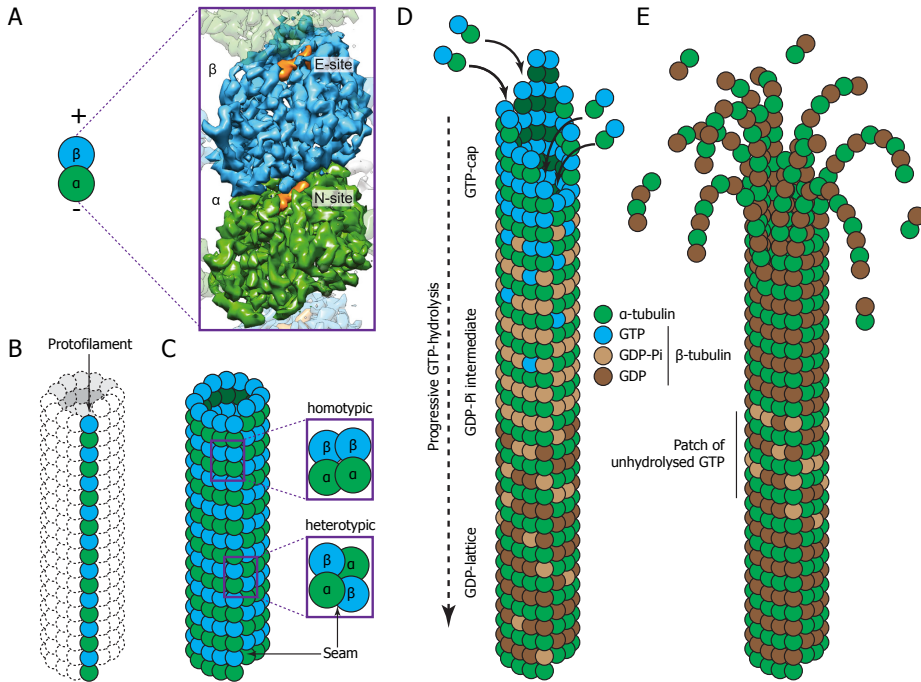


**Figure 1.2: Biochemical basis of microtubule dynamics**

(A) Schematic representation (left) and high-resolution cryo-EM structure (right) of a tubulin dimer (Alushin et al., 2014). The  $\alpha$ -tubulin (green) contains a non-exchangeable guanosine nucleotide (N-site) and  $\beta$ -tubulin (blue) contains an exchangeable guanosine nucleotide (E-site).

(B) The tubulin dimers are longitudinally arranged in a head-to-tail fashion to form protofilaments, creating a  $\beta$ -tubulin exposed “plus end” and an  $\alpha$ -tubulin exposed “minus end”.

(C) Assembly of 13 protofilaments into a cylindrical microtubule. The enlargement shows the homotypic ( $\alpha$ - $\alpha$  and  $\beta$ - $\beta$ ) lateral contact between the protofilaments and the heterotypic ( $\alpha$ - $\beta$ ) lateral contact at the discontinuity in the helical structure known as the seam.

(D) Dimer incorporation into the microtubule lattice and subsequent GTP hydrolysis. Tubulin dimers with a GTP nucleotide bound at the E-site in the  $\beta$ -tubulin bind to the plus end of the microtubule, creating a GTP-cap. Tubulin incorporation promotes progressive hydrolysis of GTP nucleotide at the E-site (blue) into GDP (brown) through the intermediary GDP-Pi state (beige).

(E) Loss of the GTP cap triggers a catastrophe after which the microtubule disassembles by the outward peeling of protofilaments. Remaining patches of unhydrolyzed GTP-bound  $\beta$ -tubulin in the microtubule lattice are hypothesized to trigger rescues.

is relatively straight whereas GDP-tubulin is more curved. However, recent work has shown that both GTP- and GDP-bound dimers have similar curvatures in solution (Ayaz et al., 2012; McIntosh et al., 2018). It is only after incorporation of GTP-bound tubulin into the microtubule lattice that a more straight conformation is adopted (Nawrotek et al., 2011). A recent comparison of GDP- and GMPCPP- (a slowly hydrolysable GTP-analogue) bound microtubules showed that GTP hydrolysis promotes

a major change in the tubulin dimer, characterized by a compaction of the E-site and strain introduction into the microtubule lattice (Alushin et al., 2014).

### THE GTP CAP

The time-delay between incorporation of a tubulin dimer into the microtubule lattice and its subsequent GTP hydrolysis generates a so-called 'GTP cap' at the growing plus-end of a microtubule (Carlier and Pantaloni, 1981) (Fig. 1.2D). GTP hydrolysis is fundamentally coupled to microtubule (in)stability (Carlier et al., 1987), but is not essential for microtubule polymerisation, as microtubule growth occurs normally in the presence of non-hydrolysable GMPCPP (Hyman et al., 1992). The terminal GTP cap is capable of preventing the GDP-rich lattice from releasing the strain build-up (Carlier et al., 1987). Upon losing the stabilizing cap, the labile GDP-rich lattice follows the conformational trajectory toward a curved structure (Fig. 1.2E), resulting in the loss of lateral contacts between the individual protofilaments and full microtubule depolymerisation. The exact size and state of this protective GTP cap is however still a matter of debate. Early studies showed that both the plus- and minus-ends of microtubules are stabilised by a short region of about 200 GTP-bound tubulin dimers (Walker et al., 1991). Although subsequent experiments with GMPCPP-stabilised microtubules suggested that a single monolayer of tubulin dimer is sufficient to stabilize microtubules (Caplow and Shanks, 1996), recent evidence suggests that the GTP cap does not exist as a monolayer (Schek et al., 2007) and can even extend to about 750 tubulin subunits *in vivo* (Seetapun et al., 2012). Fluctuations in the rate of  $\alpha/\beta$ -tubulin incorporation at the microtubule plus-end, together with the stochastic nature of GTP hydrolysis, results in a dynamic GTP cap (Howard and Hyman, 2009). As a consequence, faster growing microtubules accumulate a larger GTP cap compared to slowly growing microtubules, and are therefore less prone to undergo catastrophe (Duellberg et al., 2016).

### DYNAMIC INSTABILITY OF MICROTUBULES

Dynamic instability, the alternation between phases of microtubule growth and shrinkage, is often characterized by four parameters: 1) the rate of growth, 2) the rate of shrinkage, 3) the catastrophe frequency (the rate of switching from a growing to a shrinking state), and 4) the rescue frequency (the rate of switching from a shrinking to a growing state). Microtubule pausing, an ill-defined state during which a microtubule does not grow or shrink, is not commonly observed *in vitro* without the presence of specific Microtubule Associated Proteins (MAPs) (van Riel et al., 2017; Moriwaki and Goshima, 2016).

The microtubule growth rate is linearly dependent on the soluble tubulin concentration, whereas the shrinkage rate is not (Walker et al., 1988). Microtubules do not elongate at a constant rate and it has been proposed that the large variability in the growth rate results from fluctuations in the length of the dynamic GTP cap as it would even allow shrinkage without complete depolymerization (Howard and Hyman, 2009; Kerssemakers et al., 2006; Schek et al., 2007).

Microtubule catastrophe was originally assumed to be a single-step stochastic event that is mediated by GTP hydrolysis (Desai and Mitchison, 1997). However, it was later established that microtubule catastrophe is more likely to be a multi-step process

(Bowne-Anderson et al., 2013; Gardner et al., 2011; Maurer et al., 2012; Odde et al., 1995) and that microtubule “ageing” is responsible for the non-exponential distribution of microtubule lifetimes observed *in vitro* (Coombes et al., 2013; Gardner et al., 2011; Zakharov et al., 2015). This ageing process remains illusive and the underlying dynamics have not been elucidated. In cells, the combination of timely and spatially regulated MAPs (Gardner et al., 2013; Verde et al., 1992) and physical contact with cellular structures (Janson et al., 2003; Tischer et al., 2009) control the microtubule catastrophe frequency. This can lead to an asymmetry in cells with microtubules rapidly and persistently growing from the cell interior towards the cell margin, whereupon force-induced catastrophes increase microtubule turnover (Gregoretti et al., 2006; Komarova et al., 2002).

In contrast to the aforementioned parameters, the biochemical and biophysical principles underlying the switch from microtubule shrinkage to growth (rescue) are still poorly understood. Early studies have shown that microtubule rescue frequency shows no strong correlation with tubulin concentration (Walker et al., 1988). It has been suggested that patches of unhydrolyzed GTP in the GDP lattice (Fig. 1.2E) can disrupt microtubule depolymerisation and initiate a rescue event (Dimitrov et al., 2008). Recent studies showed that damaged microtubules can be repaired by the incorporation of GTP-bound dimers into the damaged site in the lattice, the location of which subsequently correlates with microtubule rescues (Aumeier et al., 2016; Schaedel et al., 2015). Besides these GTP-rich patches, certain MAPs such as CLASP can promote rescue events through interaction with the microtubule lattice (Al-Bassam et al., 2010) although this is mechanistically poorly understood (see Chapter 3).

## SINGLE MICROTUBULE APPROACHES FOR STUDYING MICROTUBULE DYNAMICS

Studying dynamic instability of microtubules that have a sub-diffraction-limited diameter of 25 nm can be challenging both *in vivo* and *in vitro*. Pioneering experiments using dark field microscopy to observe single microtubules (Mitchison and Kirschner, 1984) were followed up by video-enhanced differential interference microscopy (VEDIC) (Walker et al., 1988), and epi-fluorescence techniques (Verde et al., 1992). With the advent of fluorescence speckle microscopy (FSM) (Waterman-Storer et al., 1998), it also became possible to observe the dense network of microtubules in cells. Later, the use of Total Internal Reflection Fluorescence (TIRF) microscopy techniques allowed for high temporal resolution imaging with high signal-to-noise ratios due to the elimination of fluorescence background arising from free labelled tubulin in solution (Bieling et al., 2007; Brouhard et al., 2008). Fluorescence microscopy also enabled experiments using multiple fluorophores, allowing the simultaneous measurement of both microtubule dynamics and MAP localization (Gell et al., 2010). Furthermore, Fluorescence Recovery After Photobleaching (FRAP) techniques now enable the investigation of turnover times of MAPs on the microtubule lattice and tip (Dragestein et al., 2008).

Recently, the application of super-resolution fluorescence microscopy on cytoskeletal structures has enabled unprecedented levels of detail in imaging microtubules *in vivo* (Shelden et al., 2016). However, the difficulty of imaging dynamic processes with high turnover rates limits its application to mostly static structures (Letierrier et al.,

2017).

### 1.3. MODULATING MICROTUBULE DYNAMICS

The variety of different biological processes that the cytoskeleton needs to adapt to in cells requires continuous and extensive remodelling of the microtubule network. The MTOC acts as a nucleation template for microtubules and stabilizes minus-ends (Kollman et al., 2011), allowing for about 65% of the total tubulin content in cells to be polymerized (Zhai et al., 1996). The dynamic plus-ends explore the cytoplasm by constantly switching between phases of growth and shrinkage, allowing for interactions with other cellular structures at different locations in the cell. When cells enter mitosis however, the microtubule network undergoes a major transformation into a highly characteristic structure called the ‘mitotic spindle’, which is required for chromosome segregation. Extensive remodelling of the microtubule network is mostly mediated by MAPs, which can spatially and temporally alter the dynamic properties of microtubules (Akhmanova and Steinmetz, 2015; Bowne-Anderson et al., 2015).

#### TUBULIN ISOTYPES AND MODIFICATIONS

In the past decades, multiple ways for a cell to control microtubule dynamics have been uncovered. Firstly, regulation of  $\beta$ -tubulin isotype expression levels generates heterogeneous microtubules (Janke, 2014) that could be capable of exhibiting different characteristics. However, until now, only a few highly specialised microtubule types such as neuronal microtubules (Joshi and Cleveland, 1989) and ciliary axonemes (Renthal et al., 1993) have been shown to be composed of specific  $\beta$ -tubulin isotypes.

Secondly, several post-translational modifications (PTMs) have been shown to modify the stability and structure of the microtubule lattice (Hammond et al., 2008; Janke, 2014). Most PTMs affect polymerised microtubules and are not acquired on soluble tubulin (Verhey and Gaertig, 2007). For this reason, PTMs have only been observed *in vivo* on long-lived subpopulations of microtubules. These modifications may either act individually or in concert with each other by creating a combinatorial readout (Redeker et al., 2005; van Dijk et al., 2008). It has been proposed that different tubulin isotypes or PTMs, termed the ‘tubulin code’, can result in unique interactions with MAPs (Verhey and Gaertig, 2007). Detyrosination, for example, which refers to the enzymatic removal of the C-terminal tyrosine of  $\alpha$ -tubulin subunits (Hallak et al., 1977), can have extremely different outcomes in various biological systems. 1) It has been shown that the localization and activity of several proteins that affect dynamic instability are directly affected by microtubule detyrosination (Peris et al., 2006; Peris et al., 2009). 2) Recent studies revealed that detyrosination decreases the processivity of the motor protein kinesin-1, but causes the opposite effect on kinesin-2 and -7 motors (Barisic et al., 2015; Sirajuddin et al., 2014). 3) Microtubule detyrosination promotes their interaction with the sarcomere (via desmin) to regulate cardiac myocyte stiffness and contractibility (Robison et al., 2016). Whether these biological outcomes are a result of the cell specific regulation of (the expression of) downstream effectors of this PTM or whether detyrosination triggers different outcomes in combination with additional PTMs is currently unknown.

## TIP TRACKING PROTEINS

Microtubule Associated Proteins (MAPs) play a central role in adapting microtubule dynamics in order to accommodate the large variety of functions microtubules have to perform within a cell. MAPs are capable of altering various parameters of microtubule dynamics, either through direct microtubule contact or through the association with other MAPs. CLIP-170 was the first MAP observed to accumulate at growing microtubule plus ends *in vivo*. It was shown that CLIP-170 binds in stretches along microtubule ends, forming comet-like structures (Perez et al., 1999). An important subclass of MAPs comprises so-called plus-end tracking proteins (+TIPs), which are capable of accumulating specifically at the growing plus-ends of microtubules (Schuyler and Pellman, 2001). Their localization to microtubule plus-ends makes them prime candidates for establishing interactions with other intracellular structures while growing microtubules explore the cytoplasm. Since this first discovery, many +TIPs have been identified and their contribution to a large +TIP interaction network has been established (Fig. 1.3) (for reviews, see Akhmanova and Steinmetz, 2015; Galjart, 2010).

## THE END BINDING PROTEIN FAMILY

A central player in the +TIP interaction network is the conserved family of End Binding (EB) proteins. The first *in vitro* reconstitution of microtubule plus-end tracking showed that Mal3, the EB homologue in fission yeast, is able to autonomously track growing microtubule ends (Bieling et al., 2007). Three subtypes of mammalian EB proteins have been described: EB1, EB2, and EB3. EB1 and EB3 have been found to increase microtubule polymerisation rate both *in vivo* and *in vitro* (Maurer et al., 2014). In addition, EB proteins increase the microtubule catastrophe rate *in vitro* (Komarova et al., 2009) by destabilizing the GTP cap (Duellberg et al., 2016; Zhang et al., 2015). Interestingly, *in vivo* depletion of EB1 and EB3 results in a reduction of persistent microtubule growth and in an increase of catastrophe frequency, resulting in fewer microtubules being located near the cell cortex (Komarova et al., 2009). The discrepancy between these *in vitro* and *in vivo* observations is most likely the consequence of the removal of other EB dependent +TIPs that regulate microtubule dynamics (Galjart, 2010).

The interaction of EB with microtubule plus-ends is mediated by its N-terminal calponin homology (CH) domain (Slep, 2010) and does not require dimerization (Buey et al., 2011; Komarova et al., 2009). It has been demonstrated that EB can bind to the lattice of microtubules stabilised by GTP $\gamma$ S (a slowly hydrolysable GTP analogue) with similar high affinity as to the microtubule tip, but not to GMPCPP-stabilised microtubules (Maurer et al., 2011). Taking into account the intermediate curvature of GMPCPP microtubules (Muller-Reichert et al., 1998), compared to the straight lattice and the curved tubulin dimers, the view emerged that GMPCPP mimics the unhydrolysed GTP-state located at the very end of the microtubule tip, while GTP $\gamma$ S mimics an intermediate (GDP-Pi) nucleotide hydrolysis state (Brouhard and Rice, 2014). This model is further substantiated by the fact that the position of the EB comet is displaced up to ~100 nm from the tip (Duellberg et al., 2016; Maurer et al., 2014).

Recent high-resolution cryo-EM studies have now elucidated the specific interactions between EB3 proteins and the microtubule lattice and propose an explanation

for their effect on microtubule dynamics. The CH domain of EB binds at the interface of 4 tubulin dimers, except at the seam, and is therefore positioned in close proximity to the nucleotide at the E-site (Maurer et al., 2012). Once bound, EB promotes conformational changes in  $\alpha$ -tubulin leading to a compacted lattice with a unique twist. As a consequence, the catalytic residue in the  $\alpha$ -subunit of the longitudinally adjacent dimer is brought into closer proximity to the E-site, facilitating GTP hydrolysis and promoting microtubule catastrophe (Alushin et al., 2014). Since EB binds at the intersection of lateral and longitudinal contacts, it also promotes seam closure and stabilises the end structure, resulting in an increased microtubule growth rate (Zhang et al., 2015).

### THE +TIP INTERACTION NETWORK

The +TIP interaction network is built around the EB proteins, which can autonomously recognize the plus-end of a growing microtubule (Maurer et al., 2014; Zhang et al., 2015). Upon plus-end binding, EB proteins create a platform for recruiting a multitude of other MAPs through several interaction modules (Fig. 1.3) (Akhmanova and Steinmetz, 2008).

A coiled-coil region at the C-terminus of EB is required for its dimerization and mediates the interaction with other +TIPs through the EB homology (EBH) domain. Interactions with the EBH domains are mostly mediated by a microtubule tip localization signal (MtLS), which is characterized by a short Ser-x-Ile-Pro (SxIP) motif that is embedded in a region containing basic residues (Honnappa et al., 2009). Examples of +TIPs containing this SxIP motif are the microtubule-stabilizing family of CLASP proteins (Drabek et al., 2006), the microtubule-actin crosslinking factor (MACF) (Leung et al., 1999), and the microtubule-destabilizing kinesin MCAK (Desai et al., 1999). In addition to the EBH domain, the flexible C-terminal tail of EB contains an EEY/F sequence capable of binding to CAP-Gly domains present in the microtubule-rescue promoting CLIP-170 (Komarova et al., 2005) and p150<sup>glued</sup>, which is part of the dynactin complex (Schroer, 2004). The EEY/F sequence is also present on CLIP-170 itself, where it mediates an auto-inhibitory interaction with its own CAP-Gly domain (Galjart, 2005), and on  $\alpha$ -tubulin, suggesting copolymerization of tubulin and CLIP-170 onto the microtubule end (Mishima et al., 2007).

Besides EB, other +TIPs are also capable of interacting with the microtubule lattice and tip directly. The two structurally related proteins XMAP215 (homologue of human ch-TOG) and CLASP are recruited to the plus-end by conserved TOG domains. It has been shown that XMAP215 binds tubulin in a 1:1 complex and catalyses the addition of up to 25 dimers to the growing plus-end (Brouhard et al., 2008). *In vitro*, XMAP215 acts synergistically with EB to increase the growth rate to physiological levels (Zanic et al., 2013). CLASP on the other hand promotes microtubule rescue and suppresses catastrophe events, essential for proper spindle assembly (Aher et al., 2018; Al-Bassam and Chang, 2011). Acting as an 'adhesive' amongst the many +TIPs is the protein SLAIN2, which enhances +TIP interactions and promote their access to the microtubule plus-end (Akhmanova and Steinmetz, 2015; van der Vaart et al., 2011). Additionally, motor proteins are also capable of tracking the microtubule ends. The depolymerizing kinesins Kip3 and MCAK have different effects on microtubule dynamics: Kip3 slows

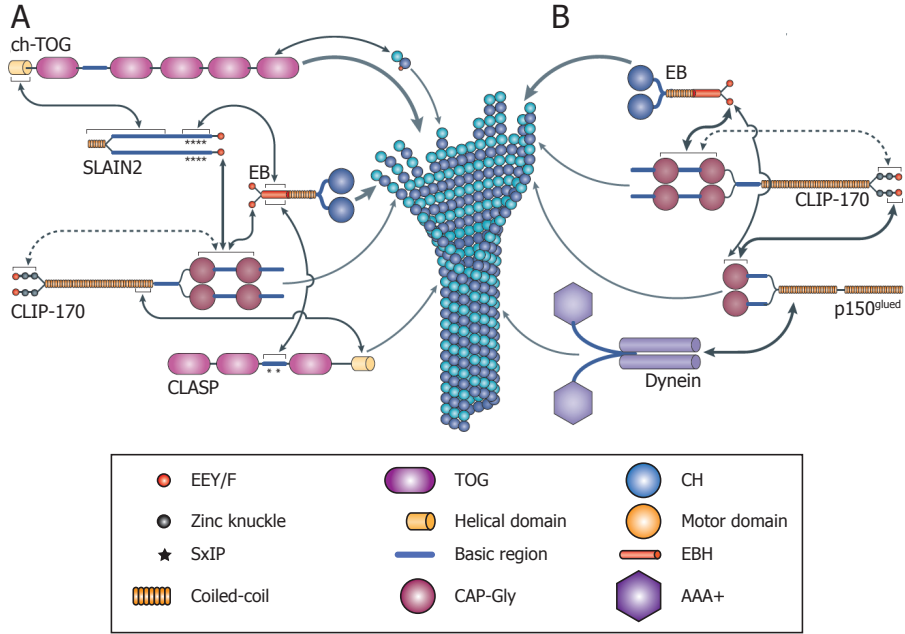


Figure 1.3: **Schematic of the +TIP interaction network**

**(A)** The combined properties of EB and SLAIN2 enable it to associate simultaneously with several different +TIPs, including ch-TOG (colonic and hepatic tumour-overexpressed gene) and cytoplasmic linker protein 170 (CLIP-170), to promote the localization of these proteins to microtubule tips. CLIP-associated proteins (CLASPs) can bind to microtubules directly and accumulate at growing microtubule plus ends by binding to EBs (via SxIP motifs) or to CLIP-170.

**(B)** Hierarchical microtubule plus-end EB-CLIP-170-p150<sup>glued</sup>-dynein network. This network is established owing to the ability of the cytoskeleton-associated protein Gly-rich (CAP-Gly) domains of CLIP-170 to bind to the EEY/F motifs of EB, and of the CAP-Gly domains of p150<sup>glued</sup> with a composite binding site formed by the zinc knuckles and EEY/F motifs of CLIP-170.

Figure is taken from (Akhmanova and Steinmetz, 2015)

down microtubule growth in a length-dependent manner and MCAK eliminates microtubule ageing altogether, transforming microtubule catastrophe into a single step process (Gardner et al., 2011). Another example of a motor protein capable of altering microtubule stability is cortical dynein, which can capture incoming microtubule plus-ends and trigger a catastrophe (Kiyomitsu and Cheeseman; 2013; Laan et al., 2012). More studies are now investigating the combinatorial effect of multiple +TIPs and motors to reconstitute and understand the dynamics observed *in vivo* (Duellberg et al., 2014; Moriwaki and Goshima, 2016).

Recently, a new perspective has been raised to view the crowded environment of the microtubule plus-end. The presence of many weakly-binding proteins at the tip could induce liquid-liquid phase separation, essentially producing a densely packed micron-sized droplet (Akhmanova and Steinmetz, 2015; Li et al., 2012). A similar effect has been observed in the nucleation of microtubules from phase-separated Tau

droplets (Hernandez-Vega et al., 2017).

## 1.4. GROWING MICROTUBULES GENERATE PUSHING FORCES

Dynamic microtubules are able to exert forces on interacting entities. Growing microtubules can generate forces by simply colliding with membranes, organelles or protein-complexes, but are also capable of promoting directed transport through the interaction of plus-end tracking complexes with their cargo partners (Fig. 1.3B). The importance of microtubule pushing forces has long been appreciated in various biological systems, most notably in mitotic spindle formation and positioning (Fig. 1.1). A wide variety of studies now starts to unveil a more diverse role for microtubule pushing forces, visible through their importance in cell polarity, directed protein transport, organelle architecture and the arrangement of other cytoskeletal networks.

### POSITIONING OF THE NUCLEUS AND MITOTIC SPINDLE

In some organisms, like yeasts, the MTOC (in this case the spindle pole body) is an integral part of the nuclear envelope throughout most of the cell cycle. This results in the concerted positioning of the nucleus and the mitotic spindle. In the fission yeast *S. pombe*, the position of the interphase nucleus is an important determinant for the position of the cleavage plane during mitosis (Chang and Nurse, 1996; Tolic-Norrelykke et al., 2005; Tran et al., 2000) (Fig. 1.4D). Microtubules are bundled in an anti-parallel fashion with their growing plus-ends oriented toward the cell poles (Hoog et al., 2007; Janson et al., 2007; Tran et al., 2001). The growing microtubule plus-ends collide with the plasma membrane at the cell tips (Hoog et al., 2007) where they exert pushing forces that result in nuclear displacement (Tolic-Norrelykke et al., 2005; Tolic-Norrelykke et al., 2004; Tran et al., 2001) (Fig. 1.4D). A balance between the pushing forces generated at opposite sides of the cell has been suggested to ensure a centralised localization of the nucleus (Oliferenko and Balasubramanian, 2002; Tolic-Norrelykke et al., 2004), even during cell elongation in interphase (Daga et al., 2006). This nuclear centring is not only achieved by balancing the number of microtubules that push on either side, but also by active regulation of microtubule dynamics by PRC1 (Ase1 in *S. pombe*) (Daga et al., 2006; Janson et al., 2007; Loiodice et al., 2005), CLIP170 (Tip1 in *S. pombe*) (Brunner and Nurse, 2000; Daga et al., 2006), and EB3 (Mal3 in *S. pombe*) (Beinhauer et al., 1997).

Recent evidence from *Drosophila* oocytes suggests that similar microtubule pushing forces are responsible for anterior-directed motion of the oocyte nucleus in order to establish the dorso-ventral axis (Zhao et al., 2012). In contrast to the microtubule bundles observed in fission yeast (Tran et al., 2001), nuclear positioning in *Drosophila* oocytes is mediated by the pushing forces generated by approximately six singular microtubules at any given time (Zhao et al., 2012).

Centrosome positioning depends on force-generating microtubules in virtually all studied organisms, but whether these microtubules are pushing or pulling is organism specific. Up to now, only limited evidence supports a clear contribution of microtubule pushing forces in MTOC positioning in non-yeast cells. Since most eukaryotic cells are significantly larger than yeast cells, they are expected to have difficulties to ef-

efficiently transmit pushing forces as a result of microtubule buckling (Dogterom et al., 2005; Dogterom and Yurke, 1997; Howard, 2006). It is therefore thought that larger cells mostly rely on microtubule pulling forces for efficient centrosome positioning (Mitchison et al., 2012).

### MICROTUBULE PUSHING FORCES IN ORGANELLE ARCHITECTURE

Microtubules play an important role in intra-cellular organization and in defining organelle shape. In addition to the formation of lateral contacts between the microtubule lattice and membrane-enclosed compartments, microtubule plus-ends and membranes can also form dynamic connections that can reshape or position a wide

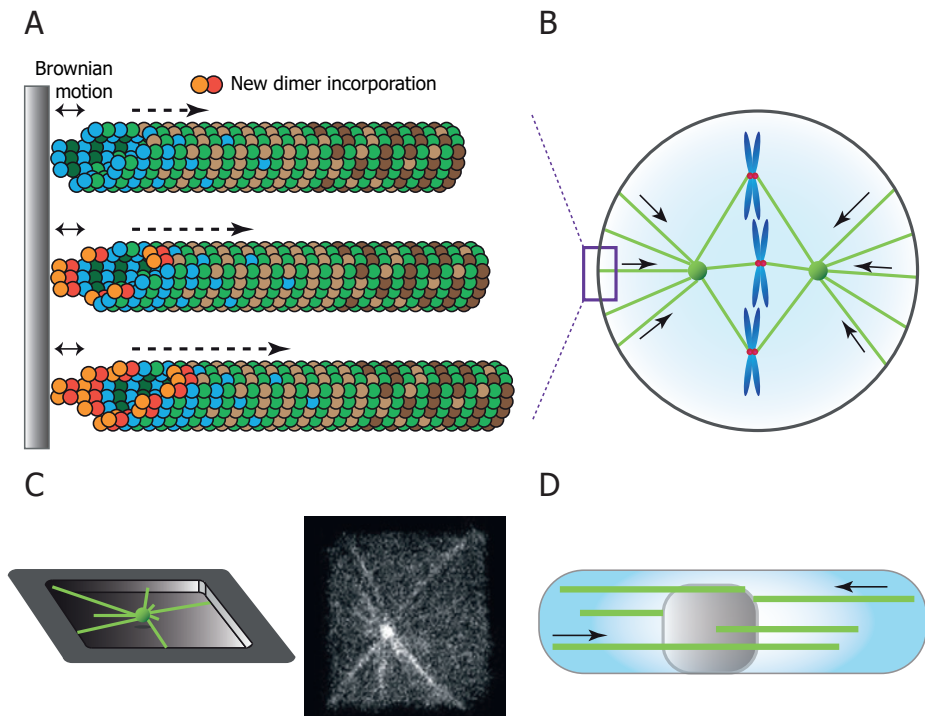


**Figure 1.4: Pushing forces generated by polymerising microtubules**

(A) Microtubule growing against a rigid object slows down microtubule growth. Brownian motion generates space between the microtubule tip and the object, slowing down the incorporation of new tubulin dimers (red/orange).

(B) Schematic representation of a eukaryotic mitotic cell, showing centrosomes (green spheres), microtubules (green lines), chromosomes (blue) and kinetochores (red) and the microtubule pushing forces (arrows) that act on the mitotic spindle.

(C) Reconstitution of microtubule aster positioning in micro-fabricated chambers, displaying a schematic representation (left) and immunofluorescent image showing fluorescent tubulin (right) (Laan et al., 2012).

(D) Nuclear positioning in fission yeast by microtubule pushing forces.

variety of intracellular structures (Gurel et al., 2014). In *Xenopus* egg extracts, growing microtubule plus-ends can interact with membranes and push out long, extended endoplasmic reticulum (ER-)tubes (Wang and Nogales, 2005; Waterman-Storer et al., 1995). The tips of ER-tubes have also been observed to track growing microtubule plus-ends in human tissue culture cells, a process that is mediated by an interaction with EB1 and the ER transmembrane protein STIM1 (Grigoriev et al., 2008; Waterman-Storer and Salmon, 1998).

In *S. pombe*, mitochondrial tubules that interact with microtubule plus-ends can shrink and extend in a coordinated motion together with microtubule (de)polymerization (Yaffe et al., 2003). This process does not depend on microtubule motor-proteins (Li et al., 2015) and is thought to promote the motility and distribution of mitochondria (Li et al., 2015; Yaffe et al., 2003). At present, the influence of microtubule pushing forces on organelle shape and positioning is relatively understudied and it is therefore unknown to what extent these processes are conserved and important for cellular fitness.

## 1.5. RECONSTITUTION OF MICROTUBULE PUSHING FORCES

The biological relevance of the pushing forces generated by growing microtubules has been appreciated for several decades. This has stimulated the extensive biophysical characterization and theoretical modelling of the force-generating capacity of growing microtubule plus-ends. In addition, significant efforts have been made to reconstitute the cellular processes that depend on microtubule pushing forces using *in vitro* bottom-up approaches. These efforts are largely focused on the reconstitution of MTOC positioning by microtubule pushing forces and will be discussed in the section below.

### BIOPHYSICAL PRINCIPLES BEHIND MICROTUBULE PUSHING FORCES

Growing microtubules are able to generate substantial pushing forces, resulting in the displacement or deformation of movable or flexible obstacles (assuming the MTOC position is fixed). On the other hand, when the obstacles are immobile and rigid, the growing microtubule can push itself away from the obstacle (assuming the MTOC position is not fixed). Microtubule pushing forces are generated by the continued incorporation of tubulin-dimers at the plus-end of a growing microtubule. According to the 'Brownian ratchet' model, thermal fluctuations in the position of the growing microtubule and the obstacle create large enough gaps to accommodate the addition of new tubulin dimers (Fig. 1.4A) (van Doorn et al., 2000). This enables the continued elongation of the microtubule plus-end (albeit at a lower speed) and the generation of a pushing force. Alternatively, the pushing force can be generated by the straightening of bent GTP-rich protofilaments at the microtubule tip into the lattice. It is suggested that thermal fluctuations of the terminal protofilaments are sufficient to promote lateral bond formation (McIntosh et al., 2018). To investigate the forces generated by growing microtubules, optical tweezers have been employed to trap a microtubule-bound dielectric bead with a focused laser (Kerssemakers et al., 2003; Schek et al., 2007). Interaction of the growing microtubule with a barrier results in a measurable

displacement of the bead, enabling the determination of the generated pushing force (Kerssemakers et al., 2006). The maximum pushing force ( $F_c$ ) that an individual microtubule can generate through continued tubulin-subunit incorporation is in the range of 3-4 pN (Dogterom and Yurke, 1997; Janson et al., 2003; Kolomeisky and Fisher, 2001). This maximum pushing force is a function of both microtubule-length ( $L$ ) and rigidity ( $\kappa$ ), and can be expressed as  $F_c = \frac{2\pi\kappa}{L^2}$  (Dogterom and Yurke, 1997; Kikumoto et al., 2006; Kurachi et al., 1995). Upon encountering a rigid barrier, growing microtubules can buckle when the exerted force is greater than the critical buckling force (the force beyond which a microtubule buckles) (Cosentino Lagomarsino et al., 2007; Dogterom and Yurke, 1997; Howard, 2006). Since the critical buckling force decreases with the square of microtubule length, long microtubules are able to generate significantly lower pushing forces compared to short microtubules (Dogterom and Yurke, 1997). However, as the cellular context wherein microtubules grow can affect their rigidity as well as PTM's (Xu et al., 2017), growing microtubules might be able to generate significantly different amounts of force *in vivo* than their length-force relationship would predict. In addition, microtubules often associate into microtubule bundles, which increases their force-generating capacity in an additive fashion (Laan et al., 2008; Valiyakath and Gopalakrishnan, 2018).

## RECONSTITUTING CENTROSOME POSITIONING

Since the amount of force that can be generated by a growing microtubule depends on its length, the shape and position of the mitotic spindle is strongly influenced by the geometrical confinement in which these spindles assemble. This idea is supported by mechanical models that describe how microtubule pushing forces mediate aster positioning in both 2D- and 3D-confinements (Holy et al., 1997; Howard, 2006; Laan et al., 2012; Maly and Maly, 2010; Pavin et al., 2012). Purified centrosomes are able to nucleate microtubules in the presence of tubulin and GTP (Mitchison and Kirschner, 1984). The forces generated by these growing microtubules are sufficient to promote self-organization of microtubule-asters in the centre of squared or round micro-fabricated chambers (Holy et al., 1997; Laan et al., 2012; Nedelec et al., 1997) (Fig. 1.4C). Once microtubules grow longer, this geometric symmetry is broken, resulting in a decentred microtubule aster position (Holy et al., 1997; Laan et al., 2012). The decentralised position of these microtubule asters is relatively stable, although a central position can be regained by increasing microtubule catastrophe rates (Faivre-Moskalenko and Dogterom, 2002). Recent developments using microfluidics now allow the first reconstitutions of mitotic spindle assembly and positioning in spherical emulsion droplets that mimic the geometrical confinement of a mammalian mitotic cell (Roth et al., 2014; Vleugel et al., 2016).

## 1.6. PULLING FORCES GENERATED BY MICROTUBULE DEPOLYMERIZATION

In order for a depolymerizing microtubule to transmit a pulling force to its potential cargo, the cargo must be capable of forming and maintaining load-bearing attachments to a rapidly shrinking microtubule. The most extensively studied examples

of microtubule polymerization-driven force-generation come from mitosis. Mitotic spindle formation and positioning are not only dependent on microtubule pushing forces, but also rely on stable links between the cell cortex and depolymerizing microtubules. In addition, mitotic chromosomes have to form stable interactions with spindle-microtubules in order to become equally distributed over the two new daughter cells. The physical separation of the replicated sister-chromatids is driven by the formation of connections between a specialized chromatin-bound protein complex, called the 'kinetochore', and depolymerizing microtubules originating from opposing centrosomes. Both cortical- and kinetochore-localized protein-complexes that interact with microtubule plus-ends are able to directly modulate the dynamic instability properties of these microtubules.

### CENTROSOME POSITIONING BY CORTICAL ANCHORS

Whereas microtubule pushing forces are the main forces underlying spindle pole body and nucleus positioning in yeast, larger eukaryotic cells usually depend on microtubule pulling forces for centrosome positioning and spindle architecture (Fig. 1.5A). Cortical microtubule anchors are capable of converting the force generated by microtubule depolymerization into a pulling force on the centrosome. Cytoplasmic dynein (hereafter referred to as 'dynein'), a minus-end directed microtubule motor, appears to play a central role in centrosome positioning both during interphase and mitosis.

During interphase, dynein localized at the cell cortex is responsible for centrosome positioning (Burakov et al., 2003) and promotes the reorientation of the MTOC toward the immunological synapse in antigen-stimulated T cells (Martin-Cofreces et al., 2008; Yi et al., 2013). During cell migration, enrichment of dynein at the leading edge of a migrating cell is required for cell polarity, MTOC positioning and cell motility (Dujardin et al., 2003; Ganguly et al., 2013; Palazzo et al., 2001).

In mitosis, cortical dynein functions as a force generating and/or force transmitting linker between microtubules and the plasma membrane in many organisms (Fig. 1.5B) (Carminati and Stearns, 1997; Laan et al., 2012; Nguyen-Ngoc et al., 2007). In budding yeast, cortical dyneins forms lateral attachments to spindle microtubules and relies on its minus-end directed motor activity to slide the microtubules along the long axis of the cell (Moore and Cooper, 2010). In metazoans, dynein is recruited to the cell cortex by the heterotrimeric Gai/LGN/NuMa complex (Kotak and Gonczy, 2013). In this case, cortical dynein pulls on centrosomes by forming load-bearing interactions with depolymerizing microtubule plus-ends (Fig. 1.5C) (Carminati and Stearns, 1997; Laan et al., 2012; Nguyen-Ngoc et al., 2007). In specialized cases, asymmetry in dynein-mediated force generation at the cell cortex is also thought to control asymmetric spindle position, like in the *C. elegans* one cell stage embryo (Grill et al., 2003; Nguyen-Ngoc et al., 2007).

In addition, early studies using a chemical inhibitor of dynein's ATPase activity have shown defects in pole-ward movement of centrosomes during late anaphase (a process known as spindle elongation) in vertebrate cells (Bouchard et al., 1981; Cande, 1982). This movement was later shown to depend on microtubule pulling forces generated by cortically anchored dynein in a wide variety of organisms (Fink et al., 2006; Kiyomitsu and Cheeseman, 2013; Nguyen-Ngoc et al., 2007; Zheng et al., 2014).

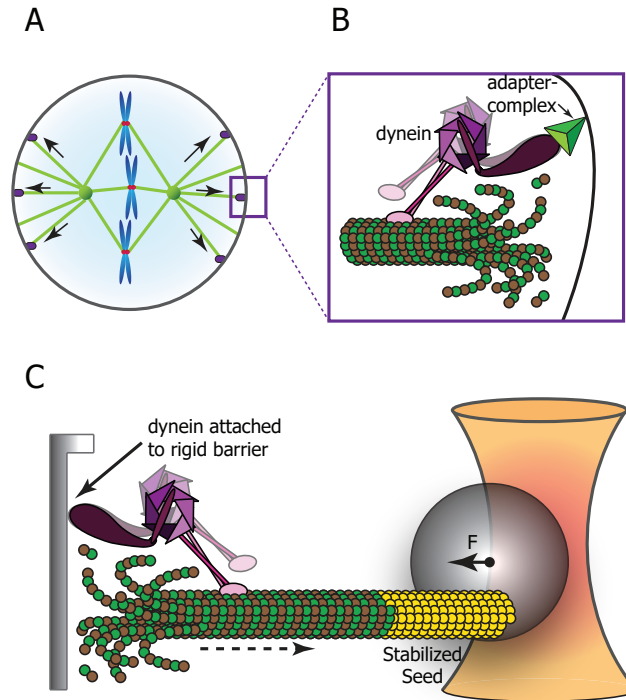


Figure 1.5: **Pulling forces generated by depolymerizing microtubules drive spindle positioning**

(A) Mitotic spindle positioning is accomplished by linking depolymerizing microtubules to the cell cortex.

(B) Dynein (purple) is anchored to the cell cortex by means of the NuMa/LGN/Göi trinary adapter complex (green) and interacts with shrinking microtubules

(C) Single molecule approach to study dynein-mediated pulling forces using an optical trap setup. Barrier (grey) attached dynein is bound to a depolymerizing microtubule that has grown from a stabilized seed (yellow) that has been linked to a dielectric bead (grey sphere). The formation of load-bearing attachments results in a pulling force ( $F$ ) that displaces the bead from the optical trap (orange).

## 1.7. RECONSTITUTING MICROTUBULE PULLING FORCES

Over the past decade, significant advancements have been made in the purification and biochemical characterization of microtubule-binding protein complexes. Since most of these proteins are unstable when separated from their biochemical context, determining their stoichiometric composition has been essential for reconstitution-based assays. This, together with the rapid development of methods to measure force-resistance of protein-protein interactions using optical tweezers setups, has provided important insights at the single-molecule level. In addition, more and more efforts are being made to reconstitute the functions of these protein complexes in cell-like geometrical confinements.

## BIOPHYSICAL PRINCIPLES BEHIND MICROTUBULE PULLING FORCES

In addition to the ability of microtubules to generate pushing forces by growing into obstacles, the energy released by microtubule depolymerization can be used to generate pulling forces. The forces associated with microtubule depolymerization are in the range of 30-65 pN (Desai and Mitchison, 1997; Grishchuk et al., 2005) and are therefore about an order of magnitude larger than the forces generated by microtubule growth (3-4 pN) (Dogterom and Yurke, 1997). Microtubule catastrophe can be actively promoted or inhibited by MAPs and physical barriers. Over long distances, microtubule-mediated pushing forces might be less efficient than pulling forces due to length-dependent microtubule buckling. In the case of mitotic spindle positioning, smaller cells (like yeasts) usually rely on microtubule pushing forces, whereas the pulling forces generated by depolymerizing microtubules drive the same process in metazoa.

## DYNEIN-MEDIATED CENTROSOME POSITIONING

In optical tweezer setups, dynein can form load-bearing attachments to the plus-ends of depolymerizing microtubules and resist up to 5 pN (Fig. 1.5C) (Hendricks et al., 2012; Kalisch et al., 2011; Laan et al., 2012). Unlike the extensive studies on kinetochore-microtubule attachments, the molecular mechanism by which dynein attaches to depolymerising microtubules remains largely elusive. For instance, it is at present unknown whether stable dynein-mediated attachments are formed by individual molecules or depend on a number of cooperating motor proteins.

Several *in vitro* studies are now building toward increasingly complex *in vivo*-like reconstitutions of the function of cortical dynein in mitotic spindle formation and positioning (Laan et al., 2012; Roth et al., 2014; Vleugel et al., 2016). In micro-fabricated 2D-chambers, the pushing forces generated by growing microtubules are sufficient to promote centrosome displacement to the periphery of the chamber. However, when the walls of these chambers are coated with dynein, centrosomes are stabilised in a more central position, even after extensive microtubule growth (Laan et al., 2012). This effect can be reconstituted in spherical (3D) water-in-oil emulsion droplets, where lipid-anchored dynein also generates a centring force on astral microtubules (Roth et al., 2014; Vleugel et al., 2016).

## MODULATING MICROTUBULE DYNAMICS THROUGH END-ON INTERACTIONS

In addition to the ability to hold on to depolymerizing microtubules, many microtubule-binding complexes at the kinetochore also actively control microtubule dynamics. Purified kinetochores from *S. cerevisiae* cannot only form load-bearing attachments to shrinking microtubules, but they also reduce the microtubule catastrophe rate when these attachments are under tension (Akiyoshi et al., 2010). Likewise, recombinant Dam1- and NDC80-complexes reduce catastrophe rates and promote rescue events *in vitro* (Franck et al., 2007; Umbreit et al., 2012). In contrast, the SKA1-complex induces the formation of and interaction with curved protofilaments (Schmidt et al., 2012). Although this is expected to promote microtubule catastrophes, there is currently no direct evidence supporting this idea.

Both in budding and fission yeast, dynein-mutant cells have significantly longer microtubules (Carminati and Stearns, 1997; Yamamoto et al., 2001) and barrier-coated

dynein has been suggested to increase microtubule catastrophe rates *in vitro* (Laan et al., 2012). Interestingly, binding of dynein to depolymerising microtubule plus-ends slows down microtubule shrinkage by straightening and thereby stabilizing protofilaments in an ATP-dependent fashion (Hendricks et al., 2012; Laan et al., 2012). Similar to dynein, a cortex-localized pool of *Drosophila* Dm-Kat60 (a functional orthologue of katanin) also interacts with microtubule plus-ends and promotes microtubule catastrophes (Zhang et al., 2011). Although cortical Dm-Kat60 and dynein seem to have a similar function in regulating cell polarization and migration (Zhang et al., 2011), it is unknown whether Dm-Kat60 also promotes this by forming load-bearing interactions with depolymerizing microtubules.

## 1.8. MODELLING MICROTUBULE DYNAMICS

Parallel to the development of microtubule reconstitution experiments, significant insights into dynamic instability came through various theoretical models coupled with stochastic simulations. Performing experiments *in silico* can compare the theoretical description with experimental observation and verify the dependence of various experimental conditions. The developed models can generally be grouped in two categories: biochemical models and mechanochemical models (Brouhard and Rice, 2018; Kim, 2018).

Biochemical models explore dynamic instability as an emergent property of the biochemical state of the microtubule tip and lattice (Chen and Hill, 1983; Gardner et al., 2011; Margolin et al., 2012; Piedra et al., 2016). Addition and removal of tubulin subunits combined with progressive hydrolysis of GTP to GDP creates a stabilizing GTP/GDP-Pi region at the microtubule end. The threshold that triggers a catastrophe depends on the dimensionality of the model. One-dimensional models, in which microtubules are treated as single filaments, initiate a catastrophe after a set number of terminal subunits have hydrolysed (Chen and Hill, 1983; Brun et al., 2009 Padinhateeri et al., 2012). Two-dimensional models use a more complex threshold based on the number of lateral interactions at the microtubule tip (Margolin et al., 2012; Martin et al., 1993; Piedra et al., 2016; VanBuren et al., 2002). Both models can describe many features of dynamic instability, but the 1D model is believed to be unable to account for microtubule ageing and the mild suppression of the catastrophe frequency with increasing tubulin concentrations (Bowne-Anderson et al., 2013). A useful property of these relatively simple models is that analytical solutions capturing the system can be formulated. This simplifies comparisons with experimental data as the effect of all parameters can be understood. As the computational cost is relatively low, these models can thus be used to understand the dynamics of a microtubule network at long time scales (Gregorette et al., 2006; Letort et al., 2016).

Mechanochemical models not only take the biochemical state of the microtubule into account, but extend the model to include Brownian dynamics of tubulin-tubulin interactions (Coombes et al., 2013; Zakharov et al., 2015; McIntosh et al., 2018). These studies simulate microtubule dynamics at high temporal resolution to capture the asymptotic evolution of the microtubule tip towards an unstable configuration. The detail obtained with these simulations can capture all aspects of dynamic instability, but also requires a large set of parameters, not all of which can be easily verified with

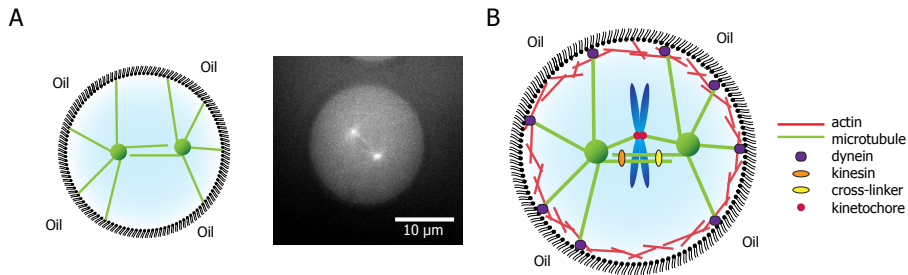


Figure 1.6: **Building toward more complex *in vitro* reconstitution systems**

(A) Reconstitution of mitotic spindle formation and positioning in spherical water-in-oil droplets, displaying a schematic representation (left) and immunofluorescent image showing fluorescent tubulin (right).

(B) Toward creating more complex reconstitution systems in which multiple cytoskeletal components are captured into geometrical confinements together with chromosomes and additional force-generators.

experiments.

## 1.9. RECONSTITUTING COMPLEX FORCE-GENERATING MICROTUBULE SYSTEMS

The studies described above have proven to be extremely valuable for our molecular and biophysical understanding of force generation by growing and shrinking microtubules. However, most of these studies have been executed in relatively simplified systems, either using force-measurements on individual microtubules or by studying the positioning of a single centrosome in simple geometrical confinements. Here we discuss recent progress on reconstituting more complex and *in vivo*-like microtubule force-generating systems, with a focus on mitotic spindle assembly and positioning.

### GEOMETRICAL CONFINEMENTS

Whereas most reconstitution studies have been performed using single-molecule assays, it will be a major challenge for the future to translate these studies into geometrical confinements mimicking the *in vivo* situation. The shape and nature of the confinement is an important determinant of the forces that can be generated by microtubules of the mitotic spindle (Minc et al., 2011). Most eukaryotic cells that lack a rigid cell wall, adopt a spherical shape when entering mitosis. Important insights will therefore come from studies on microtubule-aster positioning in spherical water-in-oil emulsion droplets generated using microfluidic technologies (Roth et al., 2014; Vleugel et al., 2016) (Fig. 1.6A). In addition, microtubule asters growing inside microfabricated chambers that resemble the asymmetric shape of the bud-neck of *S. cerevisiae*, show a highly complex positioning behaviour (Holy et al., 1997), which is at present poorly understood. In specialized cases, the mitotic spindle is positioned asymmetrically within the dividing cell, resulting in two daughter cells of different size and often with different cell fate. Reconstitution assays within the relevant geometrical

confinements will enable the quantitative assessment of the forces involved in asymmetric spindle positioning. In addition to the shape of the geometrical confinement, the nature of the confinement can also affect microtubule dynamics and force generation. Barrier flexibility directly affects the friction between microtubules and the barrier, which is predicted to directly impact on microtubule slipping behaviour (Pavin et al., 2012). To this end, it has been shown that the presence of dense actin networks is sufficient to block microtubule growth and trigger disassembly (Preciado Lopez et al., 2014; Colin et al., 2018).

### SPINDLE ASSEMBLY AND POSITIONING

During mitosis, the spindle is formed by the coordinated assembly of two microtubule asters in a bipolar orientation. It is important to note that encapsulation of two microtubule asters within the same geometrical confinement will give rise to additional effects compared to a single microtubule aster. In addition to the pushing forces that are generated by microtubules growing against the confinement boundary, microtubules originating from one centrosome can push against the second microtubule aster, resulting in centrosome repulsion (Cytrynbaum et al., 2003). This force is large enough to at least partially overcome the forces generated by astral microtubules colliding with the confinement boundary and can push centrosomes to opposite sides of the confinement (Holy et al., 1997; Vleugel et al., 2016) (Fig. 1.6B). Furthermore, the repulsion forces between two asters partially antagonises the centring forces generated by the pulling of cortical dynein (Vleugel et al., 2016).

Mitotic spindle assembly and positioning is not only achieved by the forces generated by microtubule dynamics. Many other microtubule motor proteins and crosslinkers play important roles in mitotic spindle assembly and positioning. Plus-end directed motor-proteins of the Kinesin-5 and -12 families are for instance responsible for centrosome separation and bipolar spindle formation *in vivo* (Tanenbaum and Medema, 2010). Furthermore, passive microtubule cross-linkers of the Ase1/PRC1 family are able to generate entropic forces that increase the overlap of antiparallel overlapping microtubules (Lansky et al., 2015). The complex process of bipolar spindle assembly in the presence of these and many other force-generating complexes is at present difficult to interpret. It will therefore be important to invest in the step-wise reconstitution and quantitative assessment of mitotic spindle formation and position in *in vivo*-like geometrical confinements.

### EXERCISING SPATIOTEMPORAL CONTROL

An underdeveloped part of reconstitution assays is the implementation of temporal controls over the molecular dynamics *in vitro*. Cells have various ways to control the localization, functionality, and concentration of cytoskeletal proteins in order to govern cellular dynamics (Akhmanova and Steinmetz, 2015; Etienne-Manneville, 2013; Fourest-Lieuvin et al., 2006; Watanabe et al., 2005). Within the field of microtubule reconstitution however, microtubule dynamics is often studied at steady-state in the presence of MAPs or perturbed by single external cues (Caplow et al., 1988; Duellberg et al., 2016; Marx et al., 1990). However, if microtubules are to be reconstituted in closed systems such as water-in-oil droplets, chemical cues are difficult to deliver and

would provide only a single irreversible perturbation.

In cells, a new approach developed in neurobiology known as optogenetics, uses light as the external and, most importantly, reversible cue (van Bergeijk et al., 2015). Several proteins have been found to dimerize upon the excitation with light (Losi et al., 2018; Niu et al., 2016; Pathak et al., 2013). Most often these involve either a system based on the blue light sensor LOV2 (Strickland et al., 2012; Guntas et al., 2015) or on the red light sensitive Phytochrome B (Toettcher et al., 2011). These light sensitive proteins can replace the interaction domains of other protein pairs, thus making their interaction light-inducible. Two recent examples of optogenetics involving microtubules use a light-inducible interaction between microtubules and actin (Adikes et al., 2018), and between EB and the microtubule tip (van Haren et al., 2018). Currently however, this technique is still underdeveloped *in vitro* and its application has only recently received attention (Bartelt et al., 2018; Caldwell et al., 2018).

## TOWARDS A SYNTHETIC CELL

A major future milestone will be the development of a synthetic cell capable of growing, storing information, maintaining its metabolism, and dividing (Tanenbaum and Medema, 2010). In order to successfully divide, the synthetic cell will need to define its poles and by extension the division plane, and generate forces to segregate the (artificial) chromosomes and split the cell into equal daughter cells. Incorporating a microtubule network into such a cell could provide these functionalities. Establishment of a polarized system could rely on the active transport of proteins along microtubules towards the poles of a rod-shaped cell (Taberner et al., 2015) or through local recruitment of proteins at the site of microtubule-membrane contact (Grill and Hyman, 2005; Roth et al., 2014). Eventually this cell should be able to regulate all properties autonomously, but leading up to this external cues will prove to be essential. Coupled with light-inducible dimerization, these processes can be controlled externally and reversibly with light (Pudasaini et al., 2015; Strickland et al., 2012; van Haren et al., 2018).

## 1.10. THESIS MOTIVATION AND OUTLINE

From the moment dynamic instability was first described *in vitro* (Mitchison and Kirschner, 1984), microtubule stability has been extensively studied in cells, through reconstitution assays, and with modelling approaches to understand its biochemical and mechanical origins. Now, with this wealth of information, we can start to design more complex systems to reconstitute the cellular functions of microtubules. To this end, the first steps towards building and regulating a microtubule network in cell-like compartments have been taken (Colin et al., 2018; Juniper et al., 2018; Roth et al., 2014; Taberner et al.; 2015; Vleugel et al., 2016).

In order to build and regulate an enclosed microtubule network, it is important to understand the effect of restricted microtubule growth through confinement. The stability of microtubules is affected by both the cortex as well as the presence of (cortical) microtubule associated proteins. Being able to regulate these interactions will provide control over the spatial organization of the microtubule network. This in turn could

then form the basis from which complex systems such as chromosome segregation and mitotic spindle positioning can be reconstituted.

In this thesis, we examine two aspects of microtubule reconstitution essential to successfully use and understand microtubule dynamics in confinement: 1) the stability of microtubule interactions and 2) spatiotemporal control with light-inducible protein interactions. First, we investigate the stability of pushing microtubules in a confined quasi-2D environment. We develop and improve protocols for the fabrication of micron-sized barriers that enable us to study the effect of CLASP2 $\alpha$  on the stability of pushing microtubules. To obtain a more detailed picture of microtubule stability during barrier contact, we study the contribution of nucleotide hydrolysis and microtubule tip fluctuations of stalling microtubules *in vitro*. We find that the resulting dynamics can be explained with a one-dimensional biochemical model.

Secondly, we develop and characterize the implementation of light-inducible protein interactions as a means to exert spatiotemporal control over reconstitution assays. We start with investigating the conditions required to control microtubule gliding with light. With the light-inducible hetero-dimerization protein pair LOV2-ePDZ fused to motor proteins, we show that microtubule gliding can indeed be locally controlled. To evaluate the applicability of LOV2-based regulation to *in vitro* systems in general, we characterize its activation and deactivation kinetics.

The thesis is structured as follows:

- **Chapter 2** describes the design and fabrication of novel micrometer-sized barriers with silicon carbide (SiC) overhangs to study the stability of stalling microtubules with TIRF microscopy. We characterize the use of SiC as a substrate for *in vitro* microtubule reconstitution assays.
- **Chapter 3** presents our finding that the microtubule stabilizing protein CLASP2 $\alpha$  suppresses the transition from microtubule growth to shortening. We find that the domain TOG2 fused to a tip-tracking peptide is sufficient to suppress catastrophes and stimulate rescues. In particular, we demonstrate that CLASP2 $\alpha$  prevents force-induced catastrophes during the interaction of a microtubule with a micro-fabricated barrier.
- **Chapter 4** presents our examination of the stability of stalling microtubules using the tip tracking protein EB3 as a marker of cap dynamics. Through *in vitro* reconstitutions and Monte Carlo simulations we show that both microtubule lifetimes in general and stalling dynamics in particular can be captured with a 1D biochemical model.
- **Chapter 5** describes the development of a light-inducible microtubule gliding assay as proof-of-principle to exercise control over force generating systems *in vitro*.
- **Chapter 6** details the characterization of light-inducible hetero-dimerization systems based on the LOV protein to reversibly control protein localization *in vitro*. Through a set of experiments we describe the reaction scheme and obtain the underlying kinetic rates. We show that light-inducible dimerization is a promising constituent of future *in vitro* reconstitutions.

- **Chapter 7** comprises a brief discussion and outlines possible future research directions.



# 2

## MICRO-FABRICATION OF RIGID BARRIERS

*Don't take my demons away from me  
or my angels may fly away too.*

W. H. Auden

*Polymerizing microtubules can encounter various objects in the dense cytoplasmic environment of a cell: the cell boundary, the Golgi apparatus, the Endoplasmic Reticulum and various smaller components. Obtaining an understanding of the way in which microtubules are affected through these interactions will provide insight into fundamental properties and functions of microtubules. For example, the establishment of microtubule-kinetochore connections and centrosome positioning rely on the stability of force-generating and interacting microtubules. In vitro reconstitutions have been an accurate tool to dissect the dynamics of microtubules using a controlled artificial environment. Here, we develop and optimize two approaches for the fabrication of sub-micron barriers that enable the in vitro study of microtubules interacting with rigid objects. The final design comprises barriers made of SiO<sub>2</sub> with a silicon carbide overhang that can be selectively functionalized and successfully imaged with TIRF microscopy.*

## 2.1. INTRODUCTION

The interaction of microtubules with cellular components is known to be an important regulator of the cytoskeletal network (Daga et al., 2006; di Pietro et al., 2016). *In vivo* observations have led to the view that microtubules grow persistently in the cell interior due to a low catastrophe frequency, but display highly dynamic behaviour at the cell cortex (Gregoretto et al., 2006; Komarova et al., 2002) (Fig. 2.1A). Either the membrane itself or the branched actin network at the cortex acts as a physical barrier that restricts microtubule growth and locally increases the catastrophe frequency (Colin et al., 2018). Subsequent studies revealed that microtubule associated proteins can regulate this behaviour and stabilize cortical interactions of microtubules during cell invasion (Fig. 2.1B) (Bouchet et al., 2016). Although observations in cells describe the microtubule network in its native environment, it can be difficult to address the effect of individual components in the inherently complex intracellular cytoplasm. To compose a more detailed picture of microtubule stability, *in vitro* reconstitutions have proven to be an essential experimental tool (Bieling et al., 2007). In particular, the application of micro-fabricated barriers to mimic the confinement of cellular environments have enabled the study of the organizational properties of the cytoskeleton as well as the dynamic instability of individual microtubules (Kalisch et al., 2011; Preciado Lopez et al., 2014).

In this chapter, we establish detailed protocols for fabricating sub-micron structures to investigate the interaction of microtubules with a rigid objects. Specifically, we aim to design and manufacture an *in vitro* sample that is compatible with established passivation protocols, with established functionalization and passivation protocols, and with TIRF microscopy.

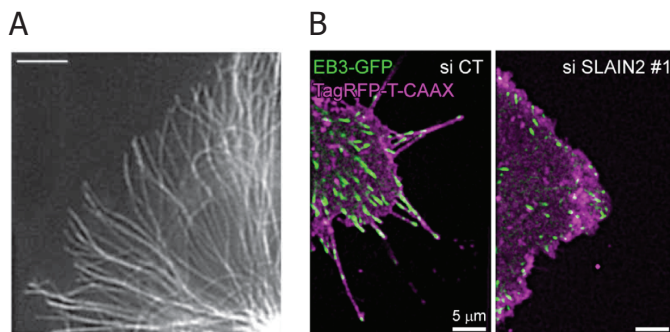


Figure 2.1: **Microtubules interact with the cortex *in vivo*.**

(A) Image of the microtubule network in a CHO cell. The catastrophe-inducing interaction of microtubules with the cell cortex leads to a cycle of persistent microtubule growth from the cell interior towards the periphery, where microtubules undergo frequent catastrophes and rescues. The scale bar denotes 5  $\mu\text{m}$ . Taken from (Komarova et al., 2002).

(B) Microtubules assist in cell invasion as they can deform the membrane in the presence of the stabilizing MAPs SLAIN and CLASP (left). In SLAIN depleted cells, only very short membrane protrusions are formed (right). Taken from (Bouchet et al., 2016).

## 2.2. DESIGN

Reconstituting the dynamics of microtubules near rigid objects requires control over the spatial structure of the *in vitro* sample. Micro-fabricated barriers have been previously used to study microtubule bending and buckling when polymerizing microtubules encounter a rigid structure (Janson et al., 2003) and to study the cortical interaction of microtubules and MAPs (Kalisch et al., 2011; Laan et al., 2012; Taberner et al., 2014). Here, we discuss the fabrication of two designs used to study the effect of +TIPs on microtubule-barrier interactions. The first design consists of SiO<sub>2</sub> barriers ~1.5 μm high (Fig. 2.2) and is used to evaluate the ability of CLASP to stabilize microtubules growing into the barriers (see Chapter 3). The barriers are spaced 15 μm apart, sufficiently restricting microtubule growth to observe interaction events.

The second design describes SiO<sub>2</sub> barriers with a silicon carbide (SiC) overhang (Fig. 2.3). The chemical inertness of SiC provides a means to selectively etch a layer of SiO<sub>2</sub> sandwiched between two layers of SiC (Fig. 2.3A). This process results in a well defined barrier structure with an SiC overhang (Fig. 2.3B,C). The overhang increases the probability of growing microtubules being trapped at the barrier, resulting in either microtubule buckling or stalling. Moreover, fluctuations of the microtubule perpendicular to the imaging surface are reduced, supporting TIRF microscopy (Fig. 2.3D). The thickness of the SiC overhang is chosen to be 250 nm and is sufficiently thick to ensure its mechanical stability, yet thin enough to remain optically transparent to visualize microtubules growing on top of it. The latter property is necessary to discriminate between microtubules growing inside the channels and on top of the barriers. This particular design is used to study the stability of stalling microtubule by visualizing the stabilizing GTP cap (see Chapter 4). Both designs share many similar fabrication steps, which will therefore be discussed only once. Any differences between the two protocols will be highlighted accordingly.

### SiC PROPERTIES

The material properties required to create stable overhangs to trap microtubules are mostly mechanical in nature, with chemical inertness and biochemical functionalization of the material as important secondary considerations. Previously, the materials of choice were silicon monoxide (Janson et al., 2003) and gold/chromium (Laan et al., 2012; Taberner et al., 2014). Problems that arose with these materials were an incompatibility with TIRF microscopy, which requires smooth surfaces with a tolerance of only a few nanometres to ensure homogeneous illumination, or a difficulty in functionalizing the surface to prevent aspecific protein adsorption. Although it would be naive to presume that any material would realize all requirements and concurrently solve all difficulties, we propose silicon carbide (SiC). Amorphous SiC is a mechanically and thermally stable semiconductor that is optically transparent in the visible spectrum (Pham, 2004) and has a refractive index of ~2.6. It is chemically inert and, due to a native oxide layer, can be functionalized in a similar manner as SiO<sub>2</sub> (Colletti et al., 2007; Dhar et al., 2009). Furthermore, deposition of the SiC layers can be achieved through Plasma-Enhanced Chemical Vapour Deposition (PE-CVD) which results in the deposition of a high quality film at rates of 30 nm/min (Iliescu et al., 2008). Currently, SiC is extensively used as an industrial material for coatings, optics, and

Process parameters	SiO <sub>2</sub>	SiC
Temperature (°C)	300	300
Pressure (mtorr)	1000	1000
N <sub>2</sub> flow rate (sccm)	162.5	0
SH <sub>4</sub> flow rate (sccm)	8.5	15
CH <sub>4</sub> flow rate (sccm)	0	75
Argon flow rate (sccm)	0	285
N <sub>2</sub> O flow rate (sccm)	710	0
Deposition rate (nm/min)	70	30

Table 2.1: PE-CVD process parameters for SiO<sub>2</sub> and SiC deposition

electronics, but only incidentally applied as a substrate in cell biology (Iliescu et al., 2008; Oliveros et al., 2013).

Although the properties listed above seem very promising, care must be taken in the knowledge that SiC is a semiconductor with a bandgap of  $\sim 2.8$  eV (Pham, 2004). As this is in the order of the commonly used 488 nm laser in fluorescence microscopy studies, possible excitation of the layer could result in optical or electrostatic effects. We will show that this does occur, but can be sufficiently mediated by optimizing the design.

## 2.3. FABRICATION

Fabrication of the SiO<sub>2</sub> barriers was achieved in a cleanroom environment by subsequent deposition, lithography, and both dry and wet etching steps (Fig. 2.2A and 2.3A). Each fabrication step will be described below.

### LAYER DEPOSITION

All samples were made with glass coverslips (Menzel Gläser, No.1 124x24 mm, 170  $\mu\text{m}$ ), which were cleaned for 10 min with base piranha, a mixture of H<sub>2</sub>O : NH<sub>4</sub>OH : H<sub>2</sub>O<sub>2</sub> in a 5:1:1 ratio heated to 70°C, after which they were rinsed with MilliQ and dried with filtered N<sub>2</sub>. The SiO<sub>2</sub> and the amorphous SiC layers were deposited with a commercial Plasma-Enhanced Chemical Vapour Deposition (PE-CVD) system (Oxford Instruments PlasmaPro 80). In general, PE-CVD is a deposition method capable of generating high deposition rates ( $\sim 50$  nm/min) at low processing temperatures (300 °C) from a specific mixture of precursor gasses (Table 2.1). Different combinations of ionized gaseous species react on the surface to form a solid layer. For this process, SiH<sub>4</sub> is the silicon donor, O<sub>2</sub> the oxygen donor, and CH<sub>4</sub> the carbon donor. Eight coverslips can be placed on a 4 inch silicon wafer, the latter of which is required as an insulating surface during deposition. It is furthermore important to pack the coverslips closely together to prevent inhomogeneous deposition due to variations in the electric field.

## PHOTOLITHOGRAPHY

First, the samples were prepared for pattern transfer by spincoating the sample with hexamethyldisilazane (HMDS) at 5000 rpm, followed by a 2 min softbake at 115°C. Then, the samples were spincoated with the photoresist S1813 (MicroChem) to form a 1.3  $\mu\text{m}$  layer, followed by softbaking for 90 seconds at 115°C. The HMDS aids in the spreading and adhesion of the photoresist. Transfer of the barrier pattern was accomplished with UV lithography (EVgroup EVG 620). The sample was exposed through a 4 inch chromium mask with a near-UV source (320-365 nm, approx. 13 mW/cm<sup>2</sup>) for 5 seconds. To reduce any backscattering of the UV light, the sample was placed on

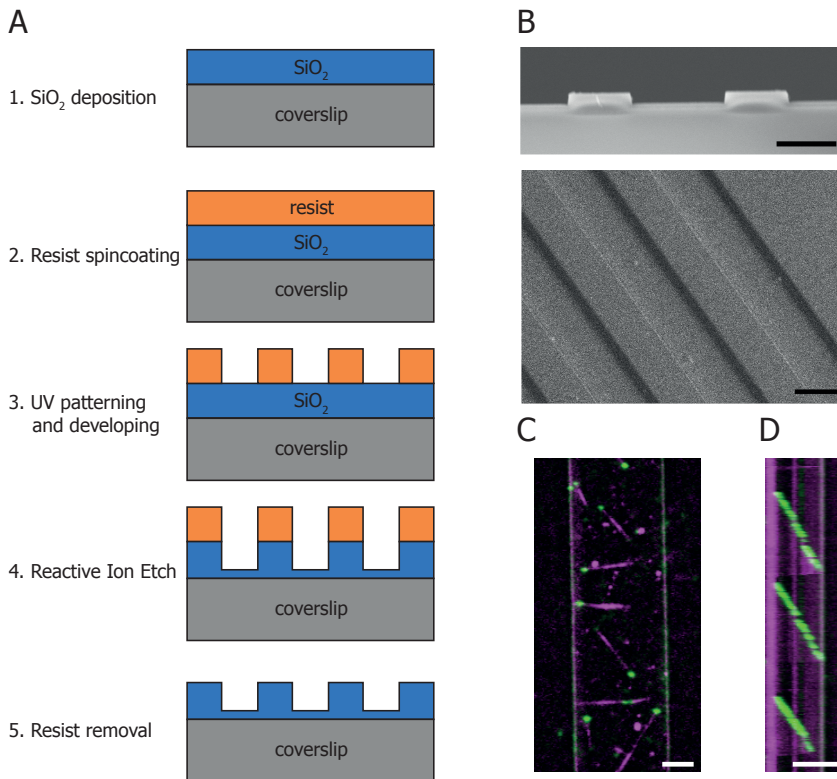


Figure 2.2: **Micro-fabrication of glass barriers.**

(A) Schematic protocol listing the steps for SiO<sub>2</sub> barrier fabrication. The design results in long (2 cm) channels with a width of 15  $\mu\text{m}$  enclosed by 10  $\mu\text{m}$  wide barriers with a height of approximately 1.5  $\mu\text{m}$ .

(B) SEM images of the barriers. The top image shows two barriers from the side and the bottom image shows a top-down view. Scale bars denote 10  $\mu\text{m}$ .

(C) TIRF image of microtubules polymerizing near barriers in the presence of 15  $\mu\text{M}$  tubulin and 20 nM GFP-EB3. Scale bar denotes 5  $\mu\text{m}$ .

(D) Kymograph of microtubule-barrier contact in the presence of 15  $\mu\text{M}$  tubulin and 20 nM GFP-EB3. Scale bar denotes 5  $\mu\text{m}$ .

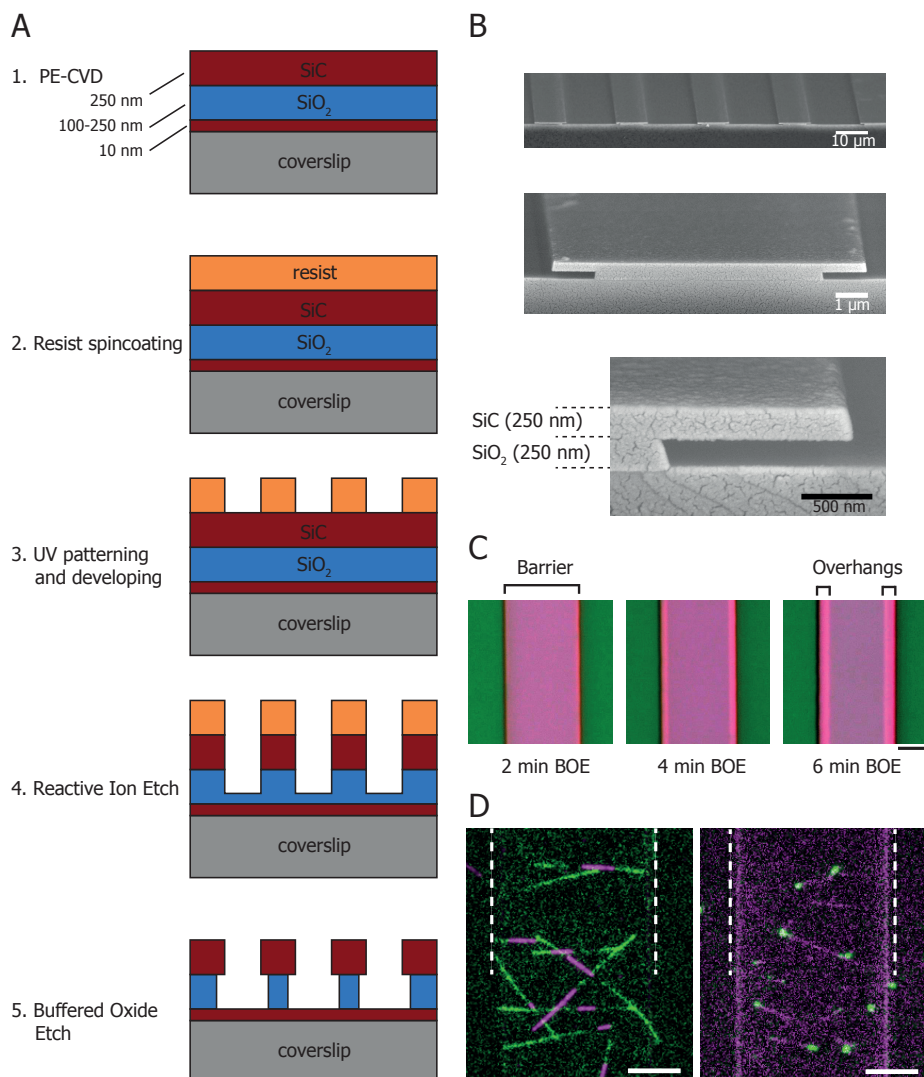


Figure 2.3: **Micro-fabrication of glass barriers with an SiC overhang.**

(A) Schematic protocol listing the required steps for the fabrication of SiO<sub>2</sub> barriers with an SiC overhang. The design produces long channels with a width of 15 μm enclosed by 10 μm wide barriers. The thickness of the SiO<sub>2</sub> layer is chosen to be between 100-250 nm and the top layer of SiC is 250 nm. The bottom layer of SiC (10 nm) is necessary to protect the glass coverslip from being etch during the Buffered Oxide Etch (5).

(B) SEM images at different zooms of a cross section of the barriers. The height of the SiC and SiO<sub>2</sub> layer is 250 nm. The sample underwent a 5 minute BOE, resulting in a 1.35 μm wide overhang and surface-barrier slope of 110°. The sample was sputter coated with a 10 nm gold layer to prevent charge build up during imaging.

(C) Brightfield microscope images of the barrier after 2, 4, and 6 minutes of 7:1 Buffered Oxide Etch. The etch rate is approximately 250 nm/min, resulting in a 1.5 μm overhang after 6 minutes. Scale bar denotes 5 μm.

(D) TIRF image of microtubules polymerizing near barriers in the presence of only tubulin (15 μM) (left) and in the presence of tubulin (15 μM) and EB3 (20 nM) (right). Scale bar denotes 5 μm.

a black rubber mat. Directly after exposure, the sample was developed in undiluted MF321 (MicroPosit) for 60 seconds, rinsed in water for 30 seconds and dried with N<sub>2</sub>.

### REACTIVE ION ETCHING

Next, Reactive Ion Etching (Leybold Hereaus) with a mixture of CHF<sub>3</sub> : O<sub>2</sub> (50 sccm : 2.5 sccm) etches through the regions unprotected by the photoresist. The system parameters for etching through SiO<sub>2</sub> and SiC are identical, although etch rates will differ slightly. The etch is performed at 50 μbar and at 50 W, resulting in a bias voltage of ~400 V and an etch rate for both materials of ~25 nm/min. Any remaining photoresist after the etch is removed by sonication of the sample in acetone for 10 minutes.

In the case of the pure SiO<sub>2</sub> barriers, care should be taken to prevent etching fully through the deposited SiO<sub>2</sub> layer as the surface of the coverslip itself is not smooth enough for TIRF microscopy after etching due to embedded impurities. For the SiC barriers, it is important to etch completely through the top SiC layer, but only partly through the SiO<sub>2</sub> layer to leave the bottom SiC layer intact.

### BUFFERED OXIDE ETCH

To create the undercuts in the barriers containing SiC, the samples are submerged in buffered hydrofluoric acid (HF : NH<sub>4</sub>F = 12.5 : 87.5%) to selectively etch the exposed SiO<sub>2</sub> with a rate of ~250 nm/min to obtain an overhang with a width of ~1.5 μm after 6 minutes of etching (Fig. 2.3B,C). Thorough rinsing of the sample followed by drying with N<sub>2</sub> results in the final barriers containing an overhang 250 nm thick and 1.5 μm long.

## 2.4. SiC AS A SUBSTRATE FOR MICROTUBULE DYNAMICS

The application of SiC as a substrate for microtubule reconstitution assays, and reconstitution assays in general, has thus far not been developed. To ensure compatibility of the bottom SiC layer with microtubule reconstitution assays imaged with TIRF microscopy, we performed such assay on a 50 nm SiC layer deposited on a glass coverslip.

### 2.4.1. *In vitro* MICROTUBULE RECONSTITUTION ASSAY

Reconstitution of microtubule dynamics was performed as previously described in (Bieling et al., 2007; Montenegro Gouveia et al., 2010). The procedure for passivating an SiC surface (with and without barriers) and a glass surface is identical. It should be noted however, that any cleaning step involving sonication of a sample containing barriers could destabilize and break down the overhangs. Sample cleaning is therefore performed with O<sub>2</sub>-plasma at 200 mtorr for 5 minutes, after which a flow channel is constructed with a cleaned glass slide and double-sided sticky tape. If barriers are present, the channel direction is perpendicular to the barriers to encourage GMPCPP-stabilized microtubule seeds to nucleate towards the barriers. Then, the surface was consecutively functionalized with 0.5 mg/ml PLL-PEG-biotin(20%) (Su-SoS AG, Switzerland), 0.2 mg/ml NeutrAvidin (Invitrogen), and 0.5 mg/ml κ-casein (Sigma). All components were kept in MRB80 buffer, comprised of 80mM piperazine-N,N'-bis(2-ethanesulfonic acid), 4 mM MgCl<sub>2</sub>, and 1 mM EGTA at a pH of 6.8. The

reaction mixture contained 14  $\mu\text{M}$  unlabelled tubulin and 1  $\mu\text{M}$  rhodamine-labelled tubulin in the presence of GFP-EB3 or Hilyte488-labelled tubulin in the absence of GFP-EB3, and was supplemented with 0.5 mg/ml  $\kappa$ -casein, 0.15% methylcellulose, 50 mM KCl, 1 mM GTP, oxygen scavenger mix (4 mM DTT, 200  $\mu\text{g}/\text{ml}$  catalase, 400  $\mu\text{g}/\text{ml}$  glucose oxidase, 50 mM glucose). GMPCPP-stabilized seeds (70% unlabelled tubulin, 18% biotinylated tubulin, 12% rhodamine-labelled tubulin) were introduced to the channel with the flow direction perpendicular to the barriers. The reaction mix is then centrifuged in an Airfuge (Beckman Coulter) at 30 psi for 8 minutes to remove any aggregated complexes before being introduced to the sample. Flow cells were sealed with vacuum grease and imaged on a TIRF microscope at between 28°C and 30°C.

Imaging of the surface can be successfully with TIRF microscopy (Fig. 2.3D, 2.4A). Any absorption of emitted light by the SiC surface does not interfere with the signal-to-noise, nor does the refractive index mismatch between the glass coverslip ( $n = 1.52$ ) and SiC ( $n \approx 2.65$ ) interfere with imaging. Also, passivation of the SiC layer performs similarly to glass as observed by the absence of non-specific adsorption of fluorescent proteins to the surface.

#### 2.4.2. MICROTUBULES ELECTROSTATICALLY INTERACT WITH SiC

During initial testing of the SiC surface as a substrate for microtubule dynamics, it became apparent that the microtubules interacted with the surface during illumination with 488 nm. Introducing additional passivation components, such as Pluronic-F127 or Tween-20, could not mitigate this interaction. The strength of the interaction turned out to be sensitive to the salt concentration (Fig. 2.4A), suggesting the interaction was based on an electrostatic attraction. The absence of additional KCl to the MRB80 buffer resulted in the growth of relatively stable and curved microtubules, whereas the addition of 100 mM KCl reduced this effect (Fig. 2.4A). Specifically, the interaction led to a clear decrease of the depolymerization speed (Fig. 2.4B), which in turn reduced the catastrophe frequency and increased the rescue frequency (Fig. 2.4C).

As this effect is most prominent when imaging with a 488 nm laser, we hypothesize that the surface might become charged as a result of the semiconducting nature of SiC. Photons of 488 nm ( $\sim 2.5$  eV) have a probability of exciting electrons in the SiC layer (bandgap  $\sim 2.8$  eV), making it conductive and/or charged. Unfortunately, the salt concentration is not a free parameter in our microtubule reconstitution assays, as it also influences the interaction of MAPs with the microtubule tip and lattice. We therefore perform the assays in the presence of 50 mM KCl, but reduce the layer thickness to 10 nm (see Chapter 4). This will minimize these interactions by reducing the photon absorption of the material, resulting in the absence of rescue events. 10 nm is the minimal layer thickness that is achievable without compromising the structural integrity of the layer as necessary for the wet etch.

#### 2.4.3. LASER-INDUCED CAVITATION BUBBLES ON AN SiC SUBSTRATE

A secondary effect of the excitation of SiC by 488 nm photons in addition to the build-up of a surface charge, is the creation of cavitation bubbles. A cavitation bubble originates from the release of heat in the form of vapour production. We found that a focussed 488 nm laser, which is optimized for FRAP experiments in our setup, is capa-

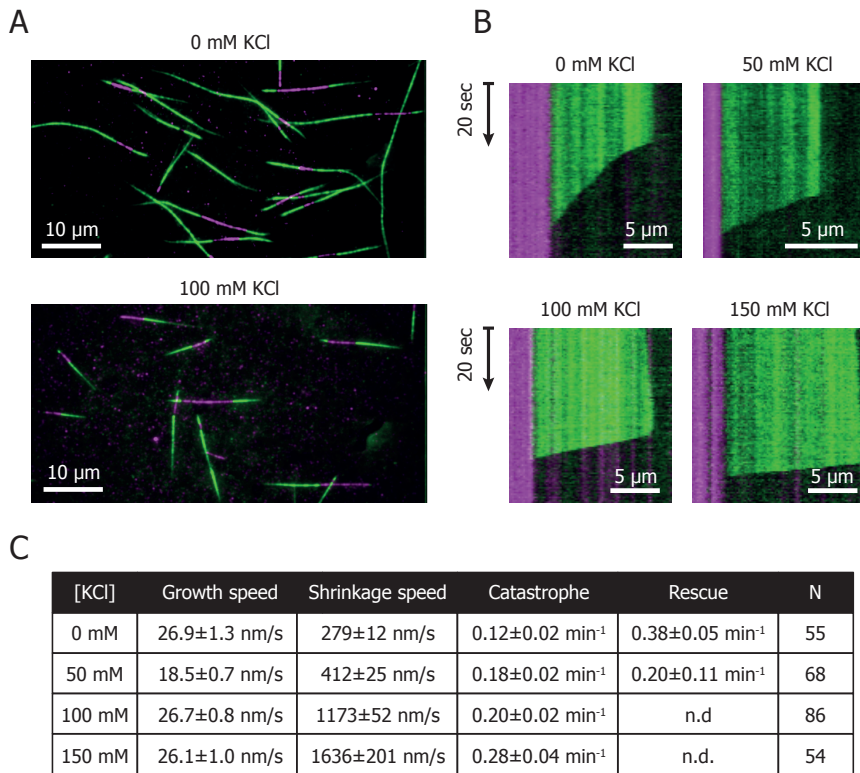


Figure 2.4: **Microtubule dynamics on a 50 nm layer of SiC**

(A) TIRF images of microtubule dynamics on a SiC layer in the presence of 0 mM KCl (**top**) and 100 mM KCl (**bottom**).

(B) Representative kymographs of microtubule depolymerization at 0, 50, 100, and 150 mM KCl. The speed of microtubule shrinkage is increased with increasing salt concentration, most likely due to electrostatic interactions between microtubules and the SiC surface.

(C) Table with measured parameters of microtubule dynamic instability at varying salt concentrations. The data indicates that microtubules are interacting electrostatically with the SiC surface as increasing concentrations of KCl shield this interaction. The shielding results in a higher microtubule shrinkage speed, higher catastrophe frequency, and lower rescue frequency.

All experiments were performed with 15 μM tubulin (7% HiLyte488-labelled) at 28 °C.

ble of producing cavitation bubbles on an SiC surface in MilliQ (Fig. 2.5A). When we set the 488 nm laser to its maximum output power of 2.4 mW and illuminated a small area on the surface for a few milliseconds, we could observe the repeatable production of a cavitation bubbles in the same location. Excitation of the surface with light of longer wavelengths (561 and 642 nm) did not produce any effect (data not shown). Interestingly, the production of cavitation bubbles was only observed for SiC layers thicker than 25 nm, suggesting that this is the minimal thickness capable of absorbing the required energy. By tuning the duration of excitation, we were able to control the size of the cavitation bubble. At a setting of 39 pulses lasting 2.00 ms, we could create a cavitation bubble with a diameter of  $\sim 5 \mu\text{m}$ , whereas below 39 repetitions, no bubble formation could be observed at the 50Hz imaging frame rate (Fig. 2.5B).

When we applied this setting our microtubule assay, we were able to sever the microtubule with a laser power normally applied to photobleach fluorophores (Fig. 2.5C). Upon severing, both ends of the microtubule depolymerized (indicated by the white arrows). Similarly, by exciting the surface at the location of a growing microtubule tip, we could sever the plus end and initiate a catastrophe event.

## 2.5. SELECTIVE BARRIER FUNCTIONALIZATION

The design of the overhangs also enables selective functionalization of the barriers, following the procedure as described in Taberner et al. 2014. In short, the SiC acts as a photomask when the sample is irradiated with UV (Fig. 2.6A). First, the sample is passivated with PLL-PEG-biotin and subsequently irradiated. The PLL-PEG-biotin will be cleaved from the surface at the exposed regions, but will remain intact underneath the SiC overhang (Azioune et al., 2009). Washing of the sample with buffer and reapplying a passivation layer of PLL-PEG without biotin will result in a fully passivated sample with specifically biotinylated barriers. To verify the efficacy of the method with the SiC overhangs, we followed the steps below to functionalize the barrier with Alexa-568 labelled streptavidin:

1. Clean the barrier sample with  $\text{O}_2$ -plasma for 5 min at 200 mtorr.
2. Incubate the sample with 0.2 mg/ml of PLL-PEG-biotin(50%) (SuSoS AG, Switzerland) for 30 min. Store the sample in plastic bag and sonicate the bag for a few seconds to disperse any air pockets trapped underneath the barriers.
3. Expose the sample to UV light with an Ozone cleaner (185 and 254 nm) for 10 min with the barriers facing upward.
4. Rinse the sample with MilliQ and blow dry with  $\text{N}_2$ .
5. Assemble a flow cell with the barrier sample and a clean glass slide with double-sided sticky tape.
6. Incubate the flow cell with 0.2 mg/ml of PLL-PEG (SuSoS AG, Switzerland) for 10 min.
7. Rinse the flow cell with MRB80 buffer.

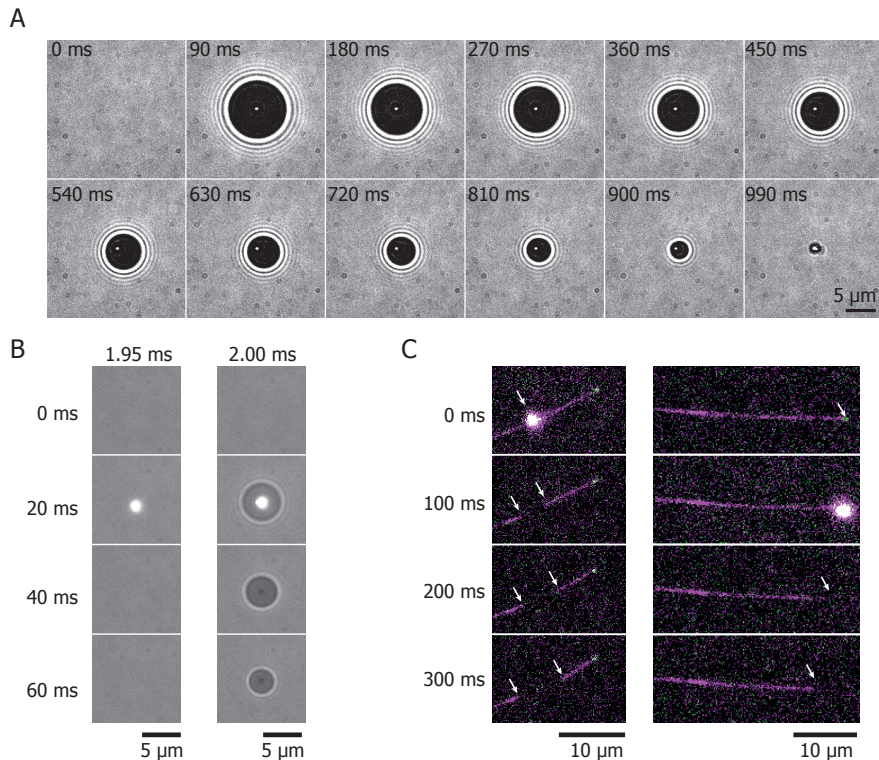


Figure 2.5: **Laser-induced cavitation bubbles**

(A) Widefield images of the production of a cavitation bubble in MilliQ through illumination of the SiC surface with a focused confocal laser (2.4 mW). A spot was illuminated with 69 pulses lasting 3.50 ms.

(B) The size of the cavitation bubble can be controlled with the excitation duration. A clear transition can be observed with our setup between 38 and 39 pulses, lasting respectively 1.95 and 2.00 ms. Below 39 repetitions the creation of a bubble cannot be observed at the imaging frame rate of 50Hz.

(C) Microtubules can be severed with an (unobservable) cavitation bubble produced with 38 sequential pulses lasting 1.95 ms. The montage on the left shows severing of the microtubule lattice and on the right of the microtubule plus-end in the presence of 15  $\mu\text{M}$  tubulin (7% rhodamine-labelled) and 20 nM GFP-EB3 at 28  $^{\circ}\text{C}$ .

8. Incubate the flow cell with 0.5mg/ml of  $\kappa$ -casein (Sigma) for 10 min.
9. Rinse the flow cell with MRB80 buffer.
10. Incubate the flow cell with a 50  $\mu\text{M}$  solution of Alexa Fluor 568 labelled streptavidin (Invitrogen) and incubate for 10 min.
11. Rinse the flow cell with MRB80 and close the channel with vacuum grease.

Inspection of the barriers show that only the area underneath the barrier is homogeneously functionalized with Alexa-568 streptavidin (Fig. 2.6B).

## 2.6. DISCUSSION

In this chapter we developed and optimized the fabrication of micron-sized barriers designed to study the interaction of microtubules with a rigid object *in vitro*. Our main ambition was to design a sample that can be fabricated relatively quickly, has a high mechanical stability, requires no specialized passivation, and is compatible with TIRF microscopy. Previous designs relied on gold to specifically functionalize the barriers through thiol-chemistry (Romet-Lemonne et al., 2005) or used a combination of gold and chromium to act as a photo-mask (Taberner et al., 2014). Although successful, the drawback of these designs include a difficulty in passivating the gold surfaces, the fragile nature of the overhangs, and the reflectivity of metals. By using SiC for the fabrication of overhangs, we are able resolve these difficulties.

We have shown that the application of amorphous SiC as a substrate for TIRF microscopy has little impact on the image quality when compared to glass. Two particular effects of SiC however require additional data treatment. First, the edge of the overhang can produce an observable scattering signal (Fig. 2.3D (bottom)). By simply increasing the width of the overhangs, the interference will not contribute to measurements at the location of SiO<sub>2</sub> barrier. The added interference can also be removed through data treatment by subtracting the minimum background signal of each pixel.

Secondly, the ability of SiC to absorb 488 nm light can result in red-shifted luminescence. Simultaneous excitation of SiC with 488 nm light and light of a longer wavelength, e.g. 561 and 642 nm, can therefore lead to an additional background signal in the emission spectrum for these wavelengths. This effect depends on the thickness of the layer and is mostly observed for the 250 nm barrier top layer and not noticeable for the 10 nm layer. Thus, to optimize the fluorescent signal is it advised to image assays

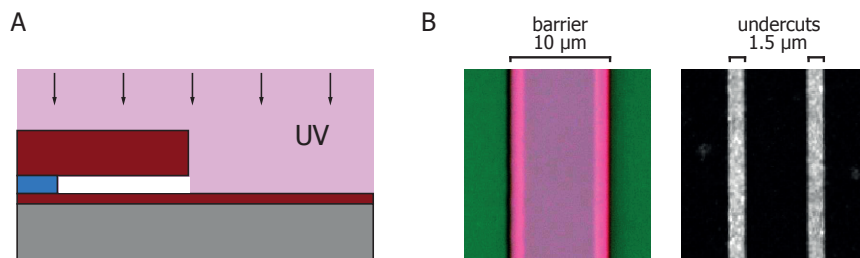


Figure 2.6: **Selective functionalization of barriers.**

(A) Schematic depiction of selective barrier functionalization through UV exposure. The sample is exposed to UV light after it has been functionalized with PLL-PEG-biotin. The PLL-PEG-biotin will be removed from the surface that is exposed to UV, but will remain intact underneath the SiC overhangs. After UV exposure, the sample is functionalized with PLL-PEG. This results in the specific biotinylation of the barriers.

(B) Verification of selective barrier functionalization. The brightfield reference image of the barriers shows the width of the overhangs (left). TIRF image of barrier functionalized with PLL-PEG-biotin and Alexa568-labelled streptavidin (right).

containing multiple fluorescent probes sequentially and not simultaneously.

Although passivation of the SiC layer is of similar quality as SiO<sub>2</sub>, it is evident that a surface charge can build up during exposure to 488 nm light. The negatively charged microtubules are attracted to the surface and stabilized, resulting in a lower catastrophe frequency, higher rescue frequency, and a slower depolymerization speed. Increasing the salt concentration of the buffer solution shields these surface charges and decreases the electrostatic interaction with the microtubules. Because the salt concentration is not a freely adjustable parameter in our microtubule reconstitution assays, we have opted to reduce the thickness of the bottom SiC layer. The minimal achievable layer thickness without compromising the structural integrity and ensure the absence of rescue events is 10 nm. This design is used in Chapter 4.

A secondary feature of SiC is the possibility to create cavitation bubbles. Without the need for a specialized laser, we can use a 488 nm laser designed for FRAP experiments to control the location and size of the bubbles and use them to sever microtubules. It is not known whether the damage to the microtubules is caused by local heating or by mechanical sheering. We make no further use of this property in this thesis, but a possible application of this effect could be in the production of cavitation bubbles to transfect individual cells (Lachaine et al., 2016; Rosenberg and Petrie, 2012; Xiong et al., 2017).

## ACKNOWLEDGEMENTS

We would like to thank Núria Taberner for her advice on the fabrication protocol and for developing the selective functionalization protocol. We thank Seungkyu Ha for his assistance in acquiring the SEM images and the technicians of the *van Leeuwenhoek Laboratory* for their technical assistance.



# 3

## CLASP SUPPRESSES MICROTUBULE CATASTROPHES THROUGH A SINGLE TOG DOMAIN

*Pipeteren kun je niet chagrijnig uitspreken.*

Paulien Cornelisse

*The dynamic instability of microtubules plays a key role in controlling their organization and function, but the cellular mechanisms regulating this process are poorly understood. Here, we show that CLASPs suppress transitions from microtubule growth to shortening, termed catastrophes, including those induced by microtubule-destabilizing agents and physical barriers. Mammalian CLASPs encompass three TOG-like domains, TOG1, TOG2 and TOG3, none of which bind to free tubulin. TOG2 is essential for catastrophe suppression, whereas TOG3 mildly enhances rescues but cannot suppress catastrophes. These functions are inhibited by the C-terminal domain of CLASP2, while the TOG1 domain can release this autoinhibition. TOG2 fused to a positively charged microtubule-binding peptide autonomously accumulates at growing but not shrinking ends, suppresses catastrophes and stimulates rescues. CLASPs suppress catastrophes by stabilizing growing microtubule ends, including incomplete ones, preventing their depolymerization and promoting their recovery into complete tubes. TOG2 domain is the key determinant of these activities.*

---

This chapter has been published as *CLASP suppresses microtubule catastrophes through a single TOG domain*, Amol Aher, [Maurits Kok](#), Ashwani Sharma, Ankit Rai, Natacha Olieric, Ruddi Rodriguez-Garcia, Eugene A. Katrukha, Tobias Weinert, Vincent Olieric, Lukas C. Kapitein, Michel O. Steinmetz, Marileen Dogterom, and Anna Akhmanova, *Dev Cell* **2018**, 46(1), 40-58.e8. <https://doi.org/10.1016/j.devcel.2018.05.032>. Maurits Kok contributed to determining the effect of CLASP on force-induced catastrophes.

### 3.1. INTRODUCTION

Microtubules (MTs) are dynamic cytoskeletal polymers composed of tubulin dimers, which attach to each other in a head-to-tail fashion to form protofilaments that interact laterally to form a hollow tube (Desai and Mitchison, 1997). MTs can alternate between phases of growth, shortening and pause, and numerous cellular factors regulate these transitions (Akhmanova and Steinmetz, 2015; Mimori-Kiyosue, 2011). Switching to MT depolymerization, termed catastrophe, can be induced by intrinsic MT properties, such as fluctuations in the size of the protective GTP cap (Brouhard, 2015; Howard and Hyman, 2009). When MTs are grown *in vitro* in a system without boundaries, the catastrophe frequency increases with MT age (Gardner et al., 2011). Recent work suggested that this behaviour could be explained by MT end tapering, which would affect tubulin binding/unbinding kinetics (Coombes et al., 2013) or the density of the protective cap close to the microtubule end (Duellberg et al., 2016). Furthermore, MT catastrophes can be induced by MT depolymerases that can cause protofilament peeling, by encounter with obstacles that block protofilament elongation or by MT-destabilizing agents that can induce structural defects at MT tips (Akhmanova and Steinmetz, 2015; Gardner et al., 2011). Interestingly, blocking just one MT protofilament at the growing MT end can disrupt growth and induce a catastrophe (Doodhi et al., 2016), but it is unclear how severe the accompanying aberrations in MT structure can be, and whether and how they can be repaired.

Cytoplasmic linker associated proteins (CLASPs) are excellent candidates to promote MT growth because they are well known to increase MT abundance and stability in mitosis and interphase. Mammalian CLASPs are essential for proper spindle MT dynamics and MT polymerization near kinetochores (Maiato et al., 2003; Maiato et al., 2005), and the depletion of CLASPs leads to severe spindle defects (Maiato et al., 2003). CLASP homologues stabilize overlapping MTs in mitotic spindles of fission yeast (Bratman and Chang, 2007) and induce MT pausing in *Drosophila* S2 cells (Sousa et al., 2007). In worms, CLASPs are required for the assembly of the central spindle in embryos (Maton et al., 2015) and suppress catastrophes in muscle cells (Lacroix et al., 2014). In plants, CLASPs inhibit catastrophes when MTs grow around sharp cell edges (Ambrose et al., 2011). In migrating mammalian cells, CLASPs stimulate MT rescues (switches from shrinkage to growth) at leading cell edges in 2D (Mimori-Kiyosue et al., 2005) and inhibit catastrophes at the tips of mesenchymal cell protrusions in a 3D matrix (Bouchet et al., 2016). Moreover, CLASPs can promote  $\gamma$ -tubulin-dependent MT nucleation at the Golgi (Efimov et al., 2007).

The ability of CLASPs to induce MT rescues, inhibit catastrophes and induce pausing has been reconstituted *in vitro* (Al-Bassam et al., 2010; Moriwaki and Goshima, 2016; Yu et al., 2016). Different CLASP homologues contain two or three TOG-like domains, protein modules known to bind to free tubulin, and it has been proposed that CLASPs act like MT polymerases by promoting the recruitment of tubulin dimers (Al-Bassam et al., 2010; Yu et al., 2016). However, unlike the TOG-domain containing MT polymerases of the XMAP215/ch-TOG family, CLASPs do not accelerate MT growth but either slow it down or do not affect it (Lawrence et al., 2018; Moriwaki and Goshima, 2016; Yu et al., 2016), and the known structures of CLASP TOG-like domains are incompatible with binding to free tubulin due to their highly convex architecture (Leano

et al., 2013; Maki et al., 2015). Alternatively, it was proposed that CLASPs might affect MTs by binding to highly curved protofilaments at MT ends (Maki et al., 2015), but this has not been directly tested. The mechanisms by which CLASPs stabilize MT growth and prevent depolymerization thus remain unresolved.

Here, by using *in vitro* MT dynamics assays, we show that CLASPs potently suppress MT catastrophes that occur spontaneously or are induced by MT-destabilizing agents and physical barriers and promote templated MT nucleation. We demonstrate that a single TOG-like domain of CLASP2, TOG2, which does not bind to free tubulin, is sufficient to induce rescues and, when targeted to MT plus ends, suppress catastrophes. Another TOG-like CLASP2 domain, TOG3, can promote rescues but does not inhibit catastrophes. The additional folded domains present in CLASPs do not bind to free tubulin or MTs but rather have autoregulatory and partner-binding functions. Furthermore, we show that CLASP2 stabilizes incomplete MT structures at the plus ends thereby enabling their restoration to promote processive MT growth. We find that TOG2 is essential and, when recruited to the MT plus end, sufficient for these functions. When tethered to MTs through a positively charged peptide, TOG2 autonomously accumulates at the growing but not depolymerizing MT ends and is enriched in a region behind the outmost tip that likely overlaps with the GTP (or GDP-Pi) cap. Taken together, our data suggest that TOG2 acts by preventing the loss of the stabilizing cap associated with MT growth.

## 3.2. RESULTS

### 3.2.1. A COMPLEX OF CLASP2 $\alpha$ AND EB3 SUPPRESSES CATASTROPHES AND PROMOTES TEMPLATED MT NUCLEATION

To investigate the impact of CLASP2 $\alpha$  on MT dynamics, we purified it from HEK293T cells (Fig. S3.1A) and analyzed its activity using an *in vitro* reconstitution assay (Bieling et al., 2007; Doodhi et al., 2016), in which MT growth from GMPCPP-stabilized seeds is observed by Total Internal Reflection Fluorescence microscopy (TIRFM). In the presence of tubulin alone, full length GFP-tagged CLASP2 $\alpha$  showed some binding to MT lattices and a very weak enrichment at MT tips (Fig. 3.1A,B). However, when mCherry-EB3 was included in the assay, CLASP2 $\alpha$  strongly accumulated at MT plus ends (Fig. 3.1A,C). MT tip recruitment of CLASP2 $\alpha$  was abrogated by mutating the Ile and Pro residues of the two tandemly arranged SxIP motifs in the middle of the protein to asparagines (IPNN mutant) or by removal of the acidic tail of EB3 (EB3 $\Delta$ Tail), as these polypeptide sequences are essential for the binding between CLASP2 and EBs (Honnappa et al., 2009) (Fig. 3.1D,E and S3.1A).

Analysis of MT dynamics showed that 30 nM CLASP2 $\alpha$  had a mild inhibitory effect on the MT growth rate both with (1.6 fold reduction) and without EB3 (1.4 fold reduction) (Fig. 3.1F). Strikingly, when recruited to MT tips by EB3, CLASP2 $\alpha$  almost completely suppressed catastrophes (Fig. 3.1C,F). CLASP1 $\alpha$ , the CLASP2 $\alpha$  paralogue that shares a very similar domain organization, displayed a very similar activity (Fig. 3.1F and Fig. S3.1A,B). Catastrophe suppression was not observed when EB3 was absent or when the binding between CLASP2 $\alpha$  and EB3 was abolished (Fig. 3.1B-F). We next attempted to compensate for the lack of interaction between CLASP2 $\alpha$  and

EB3 by increasing the concentration of CLASP2 $\alpha$  from 30 to 300 nM in the presence of EB3 $\Delta$ Tail, but found that this was insufficient to achieve the same MT tip accumulation of CLASP2 $\alpha$  as observed with 30 nM CLASP2 $\alpha$  in the presence of full length EB3 (Fig. S3.1C,D). Consistently, we observed no complete catastrophe suppression in these conditions (Fig. 3.1F). Furthermore, we observed a CLASP2 $\alpha$ -dependent increase in MT rescues, which did not strictly require CLASP2 $\alpha$  accumulation at MT tips, but which was more pronounced when EB3 was present and could interact with CLASPs (Fig. 3.1B-F). We conclude that CLASPs potently suppress catastrophes when concentrated on MT tips by EB3, and promote rescues in a manner that does not strictly depend on EB3.

To get a better insight into how CLASPs suppress catastrophes, we examined the dynamics of growing MT tips in more detail. By fitting MT fluorescence intensity profiles to the error function to determine the MT tip position with sub-pixel precision, we found that the length variability for MTs grown in the presence of EB3 and CLASP2 $\alpha$  was significantly lower than with EB3 alone (Fig. 3.1G,H and Fig. S3.1E,F). These

Figure 3.1 (following page): **CLASP2 $\alpha$  promotes processive MT polymerization and MT outgrowth from a template.**

(A) A scheme of CLASP and EB domain organization and CLASP-EB interaction.

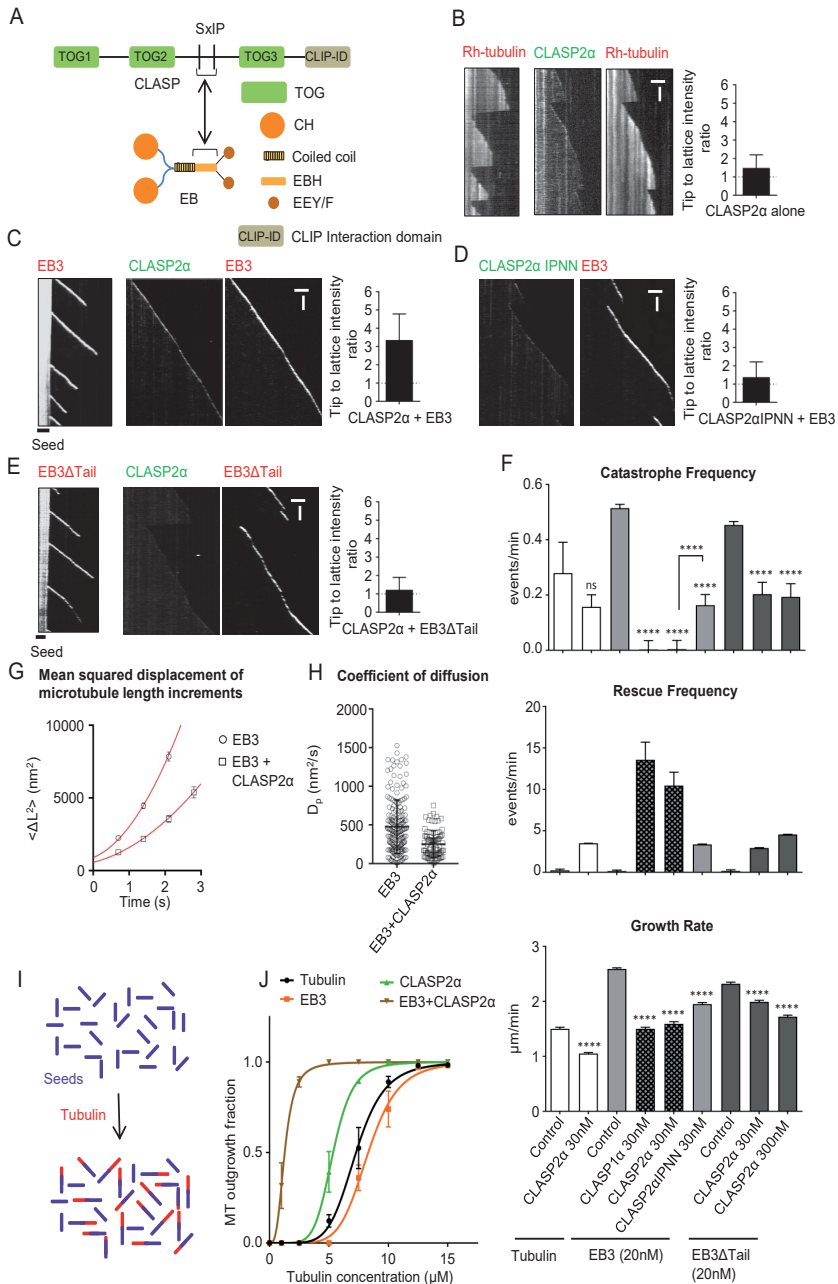
(B-E) Kymographs of MT plus end growth with rhodamine-tubulin alone or together with 30 nM GFP-CLASP2 $\alpha$  (B), 20 nM mCherry-EB3 alone or together with 30 nM GFP-CLASP2 $\alpha$  (C), 20 nM mCherry-EB3 and 30 nM GFP-CLASP2 $\alpha$ IPNN (D) and 20 nM mCherry-EB3 $\Delta$ Tail alone or together with 30 nM GFP-CLASP2 $\alpha$  (E). Plots of fluorescence intensity ratio of CLASP2 $\alpha$  at the growing MT plus end and MT lattice are shown on the right, n=27 (B), 26 (C), 25 (D) and 30 (E). Scale bars: 2  $\mu$ m (horizontal) and 60 s (vertical).

(F) Parameters of MT plus end dynamics in the presence of rhodamine-tubulin alone or together with 20 nM mCherry-EB3 or together with 20 nM mCherry-EB3 $\Delta$ Tail in combination with the indicated CLASP constructs at 30 nM or 300 nM as indicated. Number of growth events analyzed: for tubulin alone, n=135, tubulin with GFP-CLASP2 $\alpha$ , n=134, mCherry-EB3 alone, n= 207, mCherry-EB3 with GFP-CLASP1 $\alpha$ , n=110, mCherry-EB3 with GFP-CLASP2 $\alpha$ , n=110, mCherry-EB3 with GFP-CLASP2 $\alpha$ IPNN, n=182, mCherry-EB3 $\Delta$ Tail, n=182, mCherry-EB3 $\Delta$ Tail and GFP-CLASP2 $\alpha$ , n=174, mCherry-EB3 $\Delta$ Tail and 300 nM GFP-CLASP2 $\alpha$ , n=128. Error bars represent SEM.

(G,H) Average of the mean squared displacement (MSD) of MT length increments, plotted over time (G) and the values of the diffusion constant  $D_p$ , obtained from fits of the MSD curves (H). Data are shown for MTs grown either in the presence of EB3 alone or together with 30 nM of CLASP2 $\alpha$ . The average diffusion constant of  $506 \pm 41$  nm<sup>2</sup>/s for control and  $316 \pm 25$  nm<sup>2</sup>/s in presence of CLASP2 $\alpha$  were estimated from fits to the data (red line). Each dot in (H) represents the diffusion constant estimated for an individual MT growth event; control (n = 183), CLASP2 $\alpha$  (n = 88).

(I,J) Schematic of the MT outgrowth assay and plot of the fraction of the total GMPCPP seeds that show MT outgrowth in 15 minutes at increasing tubulin concentrations with tubulin alone (black) or together with GFP-EB3 (200 nM) (orange) or together with GFP-CLASP2 $\alpha$  (100 nM) (green) or together with GFP-EB3 (200 nM) and GFP-CLASP2 $\alpha$  (100 nM) (brown). For increasing tubulin concentrations in case of tubulin alone, n= 92, 96, 105, 82, 97, 87, 161, and 127 GMPCPP seeds respectively, for 200 nM GFP-EB3, n= 69, 73, 68, 77, 80, 83, 106 and 96 GMPCPP seeds respectively, for 100 nM GFP-CLASP2 $\alpha$ , n= 119, 122, 118, 119, 145, 110, 119 and 115 GMPCPP seeds respectively and for 200 nM GFP-EB3 together with 100 nM GFP-CLASP2 $\alpha$ , n= 107, 54, 85, 88, 70, 87, 85 and 70 GMPCPP seeds respectively. Data are from 2 experiments. Error bars represent SD. Solid lines indicate the sigmoidal equation fit to the data. Tubulin concentration for half-maximal MT outgrowth for tubulin alone=  $7.28 \pm 0.08$ , for 200 nM GFP-EB3=  $8.30 \pm 0.11$ , for 100 nM GFP-CLASP2 $\alpha$  =  $5.35 \pm 0.04$ , for 100 nM GFP-CLASP2 $\alpha$  and 200 nM GFP-EB3=  $1.28 \pm 0.01$ . Hill slopes for the fits with tubulin alone=  $5.99 \pm 0.34$ , for EB3=  $6.53 \pm 0.49$ , for CLASP2 $\alpha$ =  $6.46 \pm 0.31$  and for CLASP2 $\alpha$  and EB3=  $3.16 \pm 0.07$ . For all plots, \*\*\*\*p<0.0001, ns, no significant difference with control, Mann-Whitney U test.

See also Figure S3.1.



data indicate that CLASP2 $\alpha$  promotes smooth MT extension by preventing transient episodes of MT tip shortening, suggesting that in the presence of CLASP2 $\alpha$  MT plus ends are more stable.

It has been shown that factors that destabilize MT tips, like MT depolymerizing kinesin-13 MCAK, suppress MT outgrowth from templates, such as stable MT seeds or centrosomes, whereas catastrophe-suppressing factors promote MT outgrowth, an effect that becomes particularly obvious at low tubulin concentrations (Wieczorek et al., 2015). We performed similar assays in which we looked at MT outgrowth from GMPCPP seeds and found that EB3 mildly inhibited MT outgrowth, while CLASP2 $\alpha$  alone mildly increased the MT outgrowth frequency (Fig. 3.1I, J and Fig. S3.1G). When combined, CLASP2 $\alpha$  and EB3 dramatically increased MT outgrowth from GMPCPP seeds, strongly lowering its kinetic threshold: half maximal MT outgrowth was observed at a tubulin concentration that was almost 6 fold lower than in the presence of tubulin alone (Fig. 3.1J and Fig. S3.1G). These results support the notion that CLASP2 $\alpha$  in complex with EB3 potently promotes formation of stably growing MT plus ends.

Figure 3.2 (following page): **The second TOG-like domain of CLASP2 $\alpha$  is necessary and sufficient for catastrophe suppression.**

(A) A scheme of different CLASP2 constructs used. Processive MT growth is the condition in which no catastrophes were observed within 10 min in the assay with 20 nM mCherry-EB3.

(B) Representative kymographs showing MT plus end growth in the presence of 20 nM mCherry-EB3 and GFP-fusions of the indicated fusion proteins. EB3-CH domain fusion was used at 100 nM, all the other proteins at 30 nM. Scale bars: 2  $\mu$ m (horizontal) and 60 s (vertical).

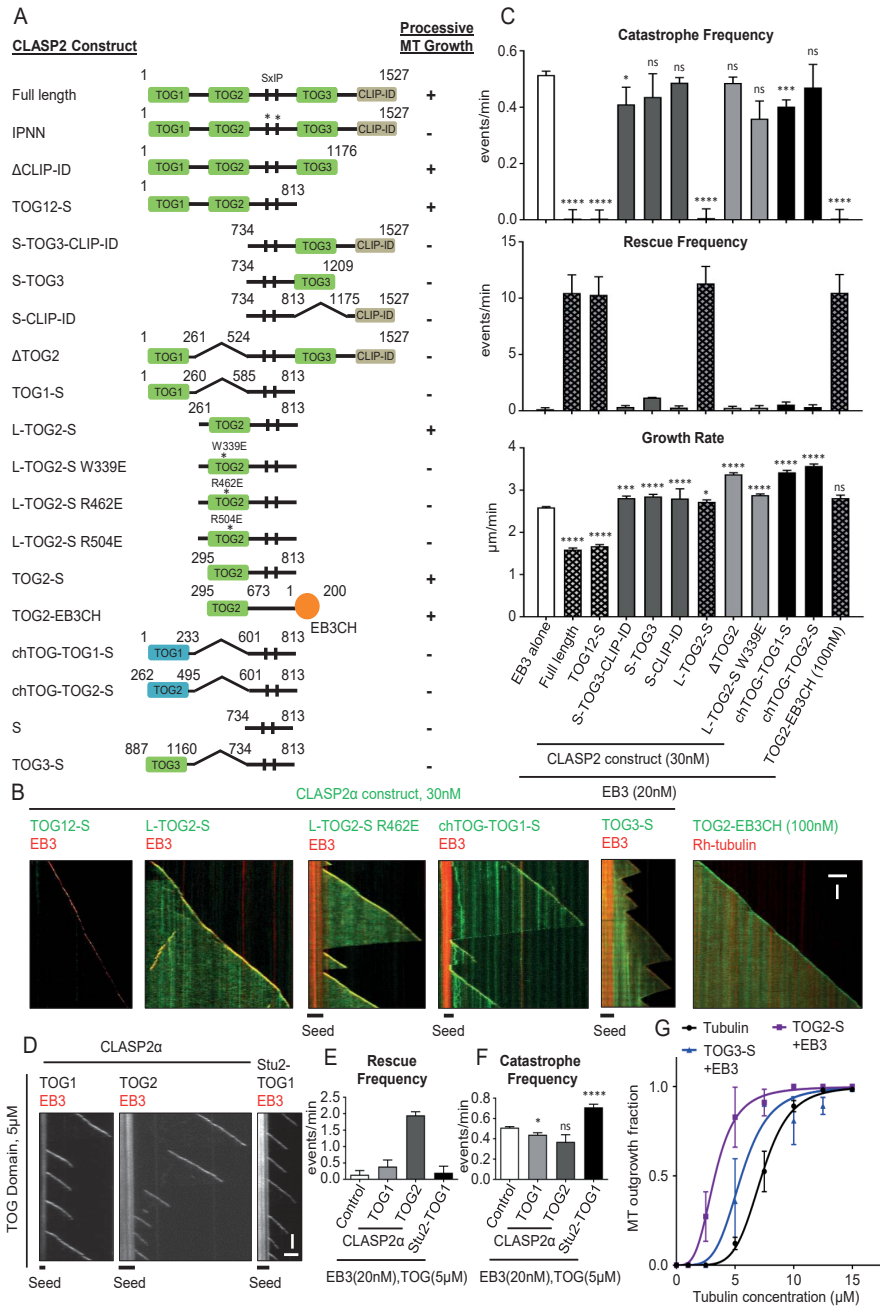
(C) Parameters of MT plus end dynamics in the presence of 20 nM mCherry-EB3 alone or together with the indicated GFP-fusion proteins. Protein concentrations were as in (B). Number of growth events analyzed: for mCherry-EB3 alone, n=207, together with GFP-CLASP2 $\alpha$ , n=110, with TOG12-S, n=110, with S-TOG3-CLIP-ID, n=117, with S-TOG3, n= 70, with S-CLIP-ID, n=136, with L-TOG2-S, n=110, with  $\Delta$ TOG2, n=154, with L-TOG2-S W339E, n=118, with chTOG-TOG1-S, n= 47, with chTOG-TOG2-S, n= 78 and for TOG2-EB3CH alone, n= 110. Error bars represent SEM. For catastrophe frequency plots, \*p<0.05, \*\*\*p<0.005, \*\*\*\*p<0.0001, for rescue frequency plots, \*p<0.05, \*\*p<0.005, \*\*\*\*p<0.0001 and for growth rate plots, \*p<0.05, \*\*\*p<0.005, \*\*\*\*p<0.0001 and ns, no significant difference with control, Mann-Whitney U test.

(D) Representative kymographs showing MT plus end dynamics in the presence of 20 nM mCherry-EB3 and 5  $\mu$ M of the indicated TOG domains from CLASP2 $\alpha$  or Stu2. Scale bars: 2  $\mu$ m (horizontal) and 60 s (vertical).

(E,F) MT plus end rescue and catastrophe frequencies in the presence of 20 nM mCherry-EB3 alone (n=207) or together with 5  $\mu$ M of CLASP2 $\alpha$  TOG1 (n=61) or TOG2 (n=100) or with Stu2-TOG1 (n=146). Error bars represent SEM. For all plots, \*p<0.05, \*\*\*\*p<0.0001 and ns, no significant difference with control, Mann-Whitney U test.

(G) Plot of the fraction of the total GMPCPP seeds that show MT outgrowth at increasing tubulin concentrations with tubulin alone (black curve) or GFP-EB3 (200nM) together with either GFP-TOG3-S (100nM) (blue) or TOG2-S (100nM) (purple). For increasing tubulin concentrations in case of tubulin alone, n= 92, 96, 105, 82, 97, 87, 161, and 127 GMPCPP seeds respectively, for GFP-TOG3-S, n=61, 52, 53, 56, 71, 59, 61 and 88 GMPCPP seeds respectively and for GFP-TOG2-S, n= 70, 64, 50, 50, 55, 66, 63 and 63 GMPCPP seeds respectively. Data are from 2 experiments. Error bars represent SD. Solid lines indicate the sigmoidal equation fit to the data. Tubulin concentration for half-maximal MT outgrowth for tubulin alone= 7.28  $\pm$  0.08, for GFP-TOG2-S with GFP-EB3= 3.29  $\pm$  0.07 and for GFP-TOG3-S with GFP-EB3 = 5.54  $\pm$  0.32. Hill slope for the fits with tubulin alone=5.99  $\pm$  0.34, for GFP-TOG2-S with GFP-EB3= 3.56  $\pm$  0.21 and for GFP-TOG3-S with GFP-EB3= 4.59  $\pm$  1.11.

See also Figure S3.2.



### 3.2.2. A SINGLE MT-TIP TARGETED TOG-LIKE DOMAIN OF CLASP2 $\alpha$ IS SUFFICIENT TO SUPPRESS CATASTROPHES

CLASP1 $\alpha$  and 2 $\alpha$  consist of three TOG-like domains (termed TOG1, 2 and 3) and a C-terminal domain responsible for interactions with CLIP-170 and other partners, CLIP-Interacting Domain (CLIP-ID) (Akhmanova et al., 2001; Al-Bassam and Chang, 2011) (Fig. 3.1A). By targeting single CLASP2 $\alpha$  domains or their different combinations to MT tips and lattices using a positively charged SxIP containing peptide of CLASP2 (termed “S” in different abbreviations, Fig. 3.2A), we found that TOG2 was necessary and sufficient to suppress catastrophes (Fig. 3.2A-C and Fig. S3.2A). Catastrophe suppression was not dependent on the linker region preceding TOG2 but was abrogated when the conserved residues in TOG2, W339, R462 and R504, corresponding to the residues which contribute to MT binding in CLASP1 and to tubulin binding in the XMAP215/ch-TOG family proteins (Leano et al., 2013), were individually mutated to glutamates (Fig. 3.2A-C and Fig. S3.2A,B). The catastrophe-suppressing properties of CLASP2 TOG2 are unique, because TOG1, TOG3 and CLIP-ID domains of CLASP2 or either of the first two TOG domains of ch-TOG had no effect on MT growth processivity when targeted to MT tips individually by an SxIP peptide (Fig. 3.2A-C and Fig. S3.2A,B). TOG3 had no effect on catastrophes irrespective of whether it was fused to the N- or the C-terminus of the SxIP peptide (S-TOG3 or TOG3-S, Fig. 3.2A-C and Fig. S3.2A,B).

A direct fusion of the CLASP2 TOG2 to the MT tip-binding calponin homology (CH) domain of EB3 (GFP-TOG2-EB3CH) was sufficient to promote processive MT growth (Fig. 3.2A-C and Fig. S3.2A,C). We note that at low (<100 nM) concentrations, this

Figure 3.3 (following page): **The C-terminal CLIP-interacting domain of CLASP2 $\alpha$  shows auto-inhibitory activity that is relieved by the first TOG-like domain or by CLIP-170.**

(A) A scheme of the CLASP-CLIP-170 interaction.

(B) A scheme of the different CLASP and CLIP-170 constructs used. Conditions showing processive MT growth in the presence of 20 nM mCherry-EB3 are indicated based on (C).

(C) Parameters of MT plus end dynamics in the presence of 20 nM mCherry-EB3 and the indicated constructs. Number of growth events: for mCherry-EB3 together with GFP-CLASP2 $\alpha$ , n=110, with TOG2-S-TOG3, n=62, with TOG2-S-CLIP-ID, n=101, with  $\Delta$ TOG1, n=141, with TOG1TOG2-S-CLIP-ID, n=116, for mCherry-EB3 and SxIPMACF-CCCLIP170 alone n=117, and together with TOG2-S-CLIP-ID, n=72, with  $\Delta$ TOG1, n=50. Error bars represent SEM.

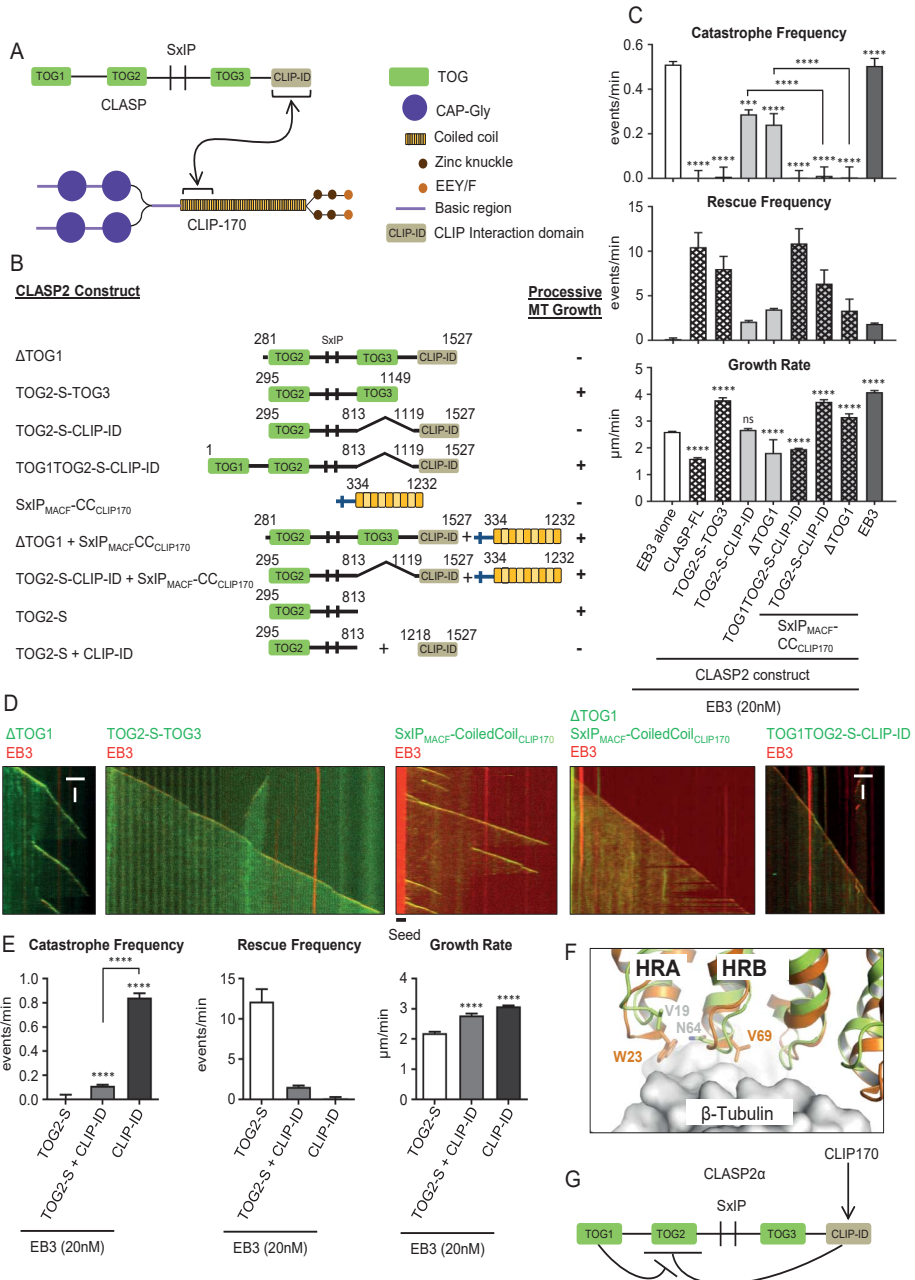
(D) Representative kymographs showing MT plus end dynamics in the presence of 20 nM mCherry-EB3 together with the indicated fusion proteins. Scale bars: 2  $\mu$ m (horizontal) and 60 s (vertical).

(E) Parameters of MT plus end dynamics in the presence of 20 nM mCherry-EB3 with 30 nM TOG2-S alone (n=62) or together with 500 nM CLIP-ID (n=96) or with CLIP-ID alone (n=115). n= number of growth events. Error bars represent SEM.

(F) Superposition of the structure of hsCLASP2-TOG1 (in green, PDB 5NR4) and scStu2-TOG1 in complex with tubulin (in orange, PDB 4FFB) at the  $\beta$ -tubulin binding interface. The scStu2-TOG1 residues located in the two first HEAT repeats (HRA and HRB) and which are involved in tubulin binding, and the equivalent hsCLASP2-TOG1 residues are indicated.

(G) Model for regulation of CLASP activity. CLIP-interacting domain inhibits the catastrophe suppressing activity of TOG2. In the context of the full-length CLASP2 $\alpha$ , this auto-inhibition is relieved by the presence of TOG1, whereas in CLASP2 isoforms like CLASP2 $\gamma$ , which lack TOG1, the auto-inhibition is relieved by engaging CLIP-ID with the CLIP-170 coiled coil domain.

For all plots, \*\*\*p<0.005, \*\*\*\*p<0.0001 and ns, no significant difference with control, Mann-Whitney U test. See also Figure S3.3.



fusion was less potent than the combination of TOG2-S and EB3 (Fig. S3.2C), likely because it is monomeric and has a lower MT tip affinity than the full length EB3, which is a dimer (Sen et al., 2013). Importantly, unlike the other proteins used in this study, which were purified from HEK293T cells, the GFP-TOG2-EB3CH protein was purified from bacteria, excluding possible contamination with MT regulators as a source of catastrophe-inhibiting activity (Fig. 3.2A-C and Fig. S3.2A,C).

MT tip-targeted TOG2 had little impact on the MT growth rate (Fig. 3.2C), while a TOG1-TOG2-S fusion reduced the MT growth rate similar to the full length CLASP2 $\alpha$  (1.6-fold), suggesting that this effect might be caused by TOG1 or the TOG1-TOG2 combination (Fig. 3.2C). The S-TOG3 fusion led to a ~8-fold increase in the rescue frequency (from  $0.14 \pm 0.13 \text{ min}^{-1}$  with EB3 alone to  $1.17 \pm 0.08 \text{ min}^{-1}$  for S-TOG3 fusion combined with EB3). This effect was suppressed when the C-terminal CLIP-ID domain was also included, leading to a 3.5 fold reduction in the rescue frequency (from  $1.17 \pm 0.08 \text{ min}^{-1}$  with S-TOG3, to  $0.34 \pm 0.13 \text{ min}^{-1}$  for S-TOG3-CLIP-ID fusion, both with EB3) (Fig. 3.2A-C, and see below). Strikingly, for all constructs containing TOG2, the depolymerization events became extremely short, leading to a dramatic increase in rescue frequency; we note, however, that the number of observed rescues was low due to extremely low catastrophe frequency.

We next investigated the activity of TOG2 without the EB3- and MT lattice-binding SxIP peptide and found that while it had little effect at nanomolar concentrations, at a concentration of  $5 \mu\text{M}$ , it increased the rescue frequency approximately 14-fold (from  $0.14 \pm 0.13 \text{ min}^{-1}$  with EB3 alone to  $1.95 \pm 0.10 \text{ min}^{-1}$  for TOG2 combined with EB3). In contrast, the TOG1 domain of CLASP2 or the tubulin-binding TOG domain of the yeast ch-TOG homologue, Stu2, did not show such an effect (Fig. 3.2D-F and Fig. S3.2A). The Stu2-TOG1 but not the TOG-like domains of CLASP2 somewhat reduced the MT growth rate, likely by sequestering tubulin dimers (Fig. 3.2D-F and Fig. S3.2D). Furthermore, both TOG2-S and TOG3-S in combination with EB3 individually lowered the kinetic threshold for MT outgrowth from GMPCPP seeds (Fig. 3.2G), but the effect was milder than with the full-length protein (Fig. 3.2J).

Previous analyses of the TOG2 and TOG3 domains of CLASP2 showed that they interact with tubulin ring-like oligomers but have only a low affinity for MT lattices (Maki et al., 2015). We confirmed that the binding of TOG2 and TOG3 to stabilized MTs was weak, while TOG1 and CLIP-ID did not bind to MTs at all, and none of these domains interacted with free tubulin (Fig. S3.2E-I). Together, these results show that TOG2 can potently regulate MT plus end dynamics when targeted to MT plus ends and has an intrinsic rescue activity, although it does not bind to free tubulin. The two latter properties make it distinct from the TOG domains of XMAP215/ch-TOG family of MT polymerases.

### 3.2.3. AUTOREGULATORY INTERACTIONS WITHIN CLASP2 $\alpha$

As mentioned above, TOG1 of CLASP2 $\alpha$  does not bind to free tubulin or MTs. Strikingly, the deletion of this domain (which converted CLASP2 $\alpha$  to the equivalent of the naturally occurring splice isoform CLASP2 $\gamma$ ), strongly diminished the ability of CLASP2 to suppress catastrophes, in agreement with a previous publication (Yu et al., 2016) (Fig. 3.3A-D). This was surprising, as the TOG2 domain sufficient for catastrophe suppres-

sion was fully retained in this mutant. Further deletion mapping showed that the presence of CLIP-ID counteracted catastrophe inhibition by TOG2, just as it suppressed MT rescue by CLASP2-TOG3 (Fig. 3.2A-C, 3.3A-D, S3.2A,B and 3.3A,B). An excess (500 nM) of purified CLIP-ID could reduce the catastrophe-suppressing activity of MT plus end-targeted TOG2, while by itself this protein had little effect on MT dynamics (Fig. 3.3E and S3.3C).

To explain these results, we hypothesized that CLIP-ID has an autoinhibitory activity that can be relieved by TOG1. If this were the case, then the binding to partners might release the CLIP-ID-induced inhibition of constructs lacking TOG1. To test this idea, we targeted the CLASP binding coiled-coil domain of CLIP-170 (Fig. 3.3A) to MT tips by fusing it to the EB-binding SxIP motif of MACF2 (Honnappa et al., 2009) (Fig. 3.3B). Addition of this construct potentially increased the anti-catastrophe activity of all TOG2-containing CLASP2 constructs that lacked TOG1 but contained CLIP-ID (Fig. 3.3A-D and S3.3B). These results suggest that CLIP-ID, when it is not bound to partners such as CLIP-170, has an inhibitory effect on TOG2, and possibly also on TOG3 (Fig. 3.2C), while TOG1 can relieve this inhibition.

In order to understand why TOG1 does not bind to free tubulin, we solved its structure by X-ray crystallography. The structure of TOG1 showed a conserved TOG-domain fold, but also demonstrated that the conserved residues required for tubulin interaction are lacking (Fig. 3.3F and S3.3E). This explains why TOG1 does not bind to either free tubulin or MTs (Fig. S3.2E,F). We also checked whether TOG1 could bind to alternative tubulin structures, such as tubulin rings induced by dolastatin or vinblastine, but found this not to be the case (Fig. S3.3D). Thus, in contrast to a previous publication suggesting that the ability of TOG1 to bind free tubulin is required for CLASP activity (Yu et al., 2016), we establish that TOG1 has an autoregulatory function (Fig. 3.3G). We note that we were unable to detect direct interactions between isolated TOG2 and TOG1 or CLIP-ID by biophysical methods (Fig. S3.3F-I), which is not surprising because autoregulatory interactions within proteins are often weak and difficult to detect using isolated protein fragments. Based on these data, we propose that the TOG1-containing CLASP1/2 $\alpha$  isoforms are constitutively active whereas the CLASP2 $\beta$ / $\gamma$  isoforms, which lack TOG1 (Akhmanova et al., 2001), require partners interacting with CLIP-ID for their optimal activity.

#### 3.2.4. CLASP2 $\alpha$ SUPPRESSES CATASTROPHES INDUCED BY MT-DEPOLYMERIZING AGENTS

The data described above revealed that CLASPs suppress spontaneous catastrophes. However, in cells catastrophes are often induced by MT-destabilizing factors (Gardner et al., 2013). To test if CLASPs can counteract the action of such factors, we first tested the effect of MT depolymerizing drugs such as colchicine and vinblastine, which perturb MT plus end structure and induce catastrophes in the presence of EBs (Mohan et al., 2013). We found that CLASP2 $\alpha$  indeed promoted longer MT polymerization events at drug concentrations that strongly inhibited MT growth (Fig. 3.4A,C and S3.4A). Similarly, CLASP2 $\alpha$  counteracted the activity of MCAK, a MT depolymerase that induces protofilament curling, even when the latter was added at a concentration that, in the absence of CLASP2 $\alpha$ , was sufficient to completely block MT outgrowth and

cause depolymerization of MT seeds (Fig. 3.4B,C and S3.4B). The minimal catastrophe-suppressing module TOG2-S could also counteract the catastrophe-inducing action of colchicine and promoted MT growth in the presence of MCAK, and was even more effective than full length CLASP2 $\alpha$  (Fig. 3.4A-C).

We next tested whether CLASPs can protect MTs from drug-induced catastrophes in cells. Simultaneous depletion of CLASP1 and CLASP2 in cells stably expressing EB3-GFP led to a mild increase in the MT catastrophe frequency in internal cell regions and resulted in more frequent catastrophes in cells treated with colchicine (Fig. 3.4D,E). Importantly, the expression of MT tip-targeted TOG1-TOG2-S and TOG2-S fusions, but not of TOG1-S or the mutated version of TOG2-S, caused a mild catastrophe inhibition in control cells and strongly suppressed catastrophes in colchicine-treated cells (Fig. 3.4F,G and S3.4C,D). These data show that the TOG2 domain potentially counteracts catastrophes induced by agents that perturb the MT end structure in different ways both *in vitro* and in cells.

### 3.2.5. CLASP2 $\alpha$ SUPPRESSES FORCE-INDUCED CATASTROPHES

Next, we investigated whether CLASP2 $\alpha$  is capable of suppressing catastrophes induced by compressive forces. It was previously shown that when a growing MT polymerizes against a solid barrier, the ensuing compressive force can advance the onset of a catastrophe (Janson et al., 2003). We used micro-fabricated barriers composed of SiO<sub>2</sub> etched on a glass coverslip (Kalisch et al., 2011). This fabrication process resulted in 1.7  $\mu$ m high barriers enclosing 15  $\mu$ m wide channels (Fig. 3.5A). MTs were allowed

Figure 3.4 (following page): CLASP2 $\alpha$  suppresses catastrophes induced by MT destabilizing agents *in vitro* and in cells.

(A) Kymographs showing MT plus end dynamics in the presence of rhodamine-tubulin alone or with 20 nM mCherry-EB3 or in the presence of 100 nM colchicine with 20 nM mCherry-EB3 alone or together with 30 nM GFP-CLASP2 $\alpha$ . Scale bars: 2  $\mu$ m (horizontal) and 60 s (vertical).

(B) Kymographs showing MT plus end depolymerization in the presence of 20 nM mCherry-EB3 and 10 nM GFP-MCAK, or plus end growth dynamics when 30 nM GFP-CLASP2 $\alpha$  or GFP-TOG2-S are added. Scale bars: 2  $\mu$ m (horizontal) and 60 s (vertical).

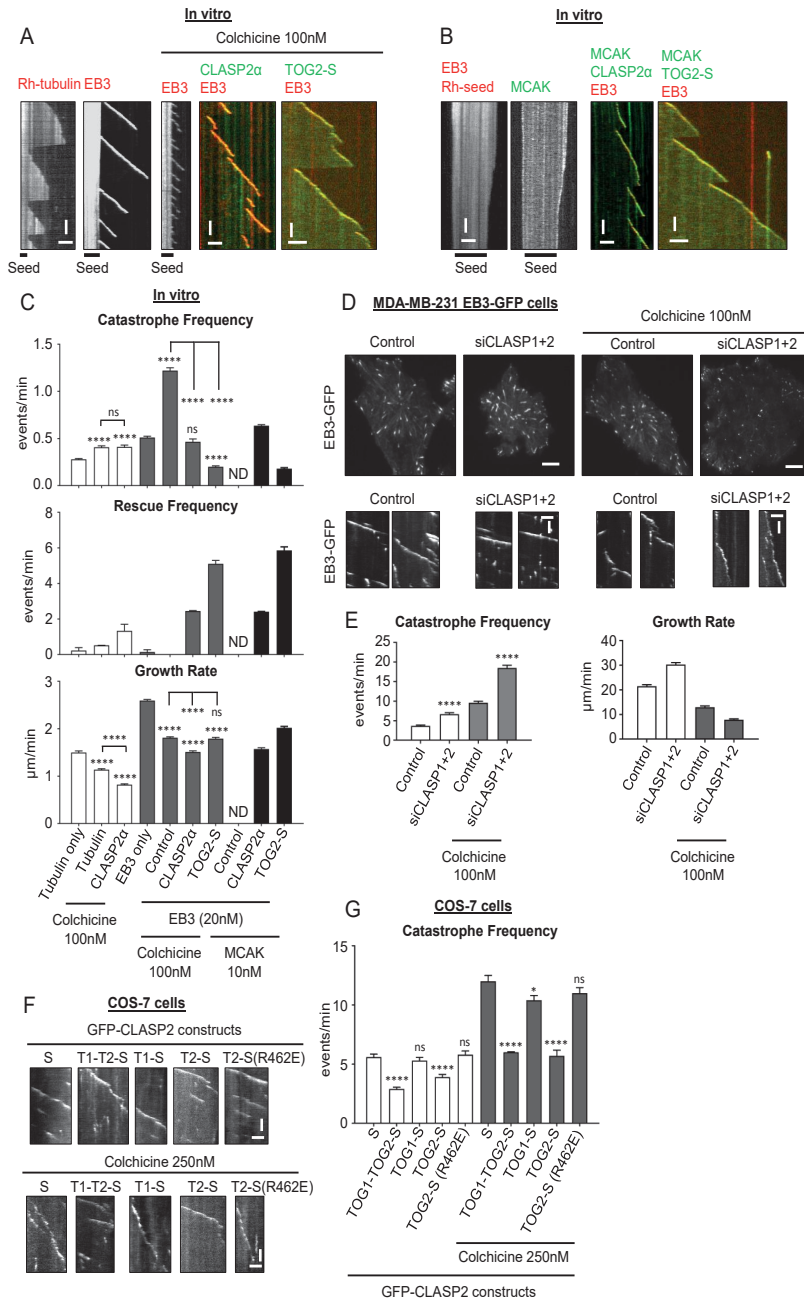
(C) Parameters of MT plus end dynamics in the presence of the indicated of proteins, with or without 100 nM colchicine. Number of growth events analyzed: for rhodamine-tubulin alone, n=135, with colchicine, n=110, with colchicine and GFP-CLASP2 $\alpha$ , n=68, for mCherry-EB3 alone, n=207, for mCherry-EB3 with colchicine, n=228, for mCherry-EB3 with Colchicine and GFP-CLASP2 $\alpha$ , n=136 and for mCherry-EB3 with colchicine and GFP-TOG2-S, n=241. For mCherry-EB3 with GFP-MCAK and GFP-CLASP2, n=144 and for mCherry-EB3 together with GFP-MCAK and GFP-TOG2-S, n=227. Error bars represent SEM.

(D) Still images of MDA-MB-231 cells stably expressing EB3-GFP and kymographs showing MT plus end growth in control or CLASP1 and CLASP2 depleted cells alone or together with 100 nM colchicine. Scale bar: 5  $\mu$ m (cell images), 2  $\mu$ m (horizontal) and 60 s (vertical) (for kymographs).

(E) MT plus end catastrophe frequency and growth rates in MDA-MB-231 cells stably expressing EB3-GFP after transfection either with control or CLASP1 and CLASP2 siRNAs, untreated or treated with 100 nM colchicine. Number of growth events from left to right, n=56, 53, 106, and 123. Error bars represent SEM.

(F) Kymographs showing MT plus end dynamics in COS-7 cells expressing the indicated GFP-fusions; cells were untreated or treated with 250 nM Colchicine. Scale bars: 2  $\mu$ m (horizontal) and 15 s (vertical).

(G) MT plus end catastrophe frequency in COS-7 cells shown in (F). Numbers of growth events from left to right n=61, 61, 65, 64 and 57 (without colchicine) and with 250 nM colchicine, n=61, 65, 92, 47 and 70 (with 250 nM colchicine). Error bars represent SEM. For all plots, \*p<0.05, \*\*\*p<0.005, \*\*\*\*p<0.0001 and ns, no significant difference with control, Mann-Whitney U test. See also Figure S3.4.



to grow from GMPCPP-stabilized seeds inside the channels and polymerize towards the barriers from varying angles and distances. The interaction of the MT plus end with the barrier gave rise to three different possible outcomes: sliding (bending and growing along the barrier), stalling, and buckling (Fig. 3.5B). Stalling indicates that a MT is unable to overcome the compressive force build-up during barrier contact and therefore cannot continue polymerizing, but instead remains in a static contact with the barrier until the onset of a catastrophe. Buckling occurs when a MT contacting the barrier keeps growing while its end remains at the same position at the barrier (indicative of a moderate compressive force).

In the absence of EB3 and CLASP2 $\alpha$ , sliding behaviour predominated for all contact angles due to the smooth surface of the barriers, while the addition of EB3 led to an increase in stalling events, particularly when the seeds were perpendicular to the barriers (Fig. 3.5B,C). The catastrophe frequency during contact in both cases was higher for stalling than for sliding, and was particularly high for MTs stalled at barriers in the presence of EB3, clearly showing that the MT plus end is less stable at high compressive forces in these conditions (Fig. 3.5E). Strikingly, the addition of EB3 and CLASP2 $\alpha$  resulted in persistent MT growth almost devoid of observable catastrophes for all event types (Fig. 3.5D). A few buckling events were observed in the presence of EB3 and CLASP2 $\alpha$  at almost perpendicular contact angles (Fig. 3.5D). During buckling, the MT growth speed decreased compared to the growth speed prior to barrier contact, but remained constant after an initial pausing phase (Fig. 3.5D). These data show that CLASP2 $\alpha$  can prevent destabilization of a growing MT tip during barrier contact even at high compressive forces during buckling.

Figure 3.5 (following page): **CLASP2 $\alpha$  inhibits force-induced catastrophes in the presence of EB3.**

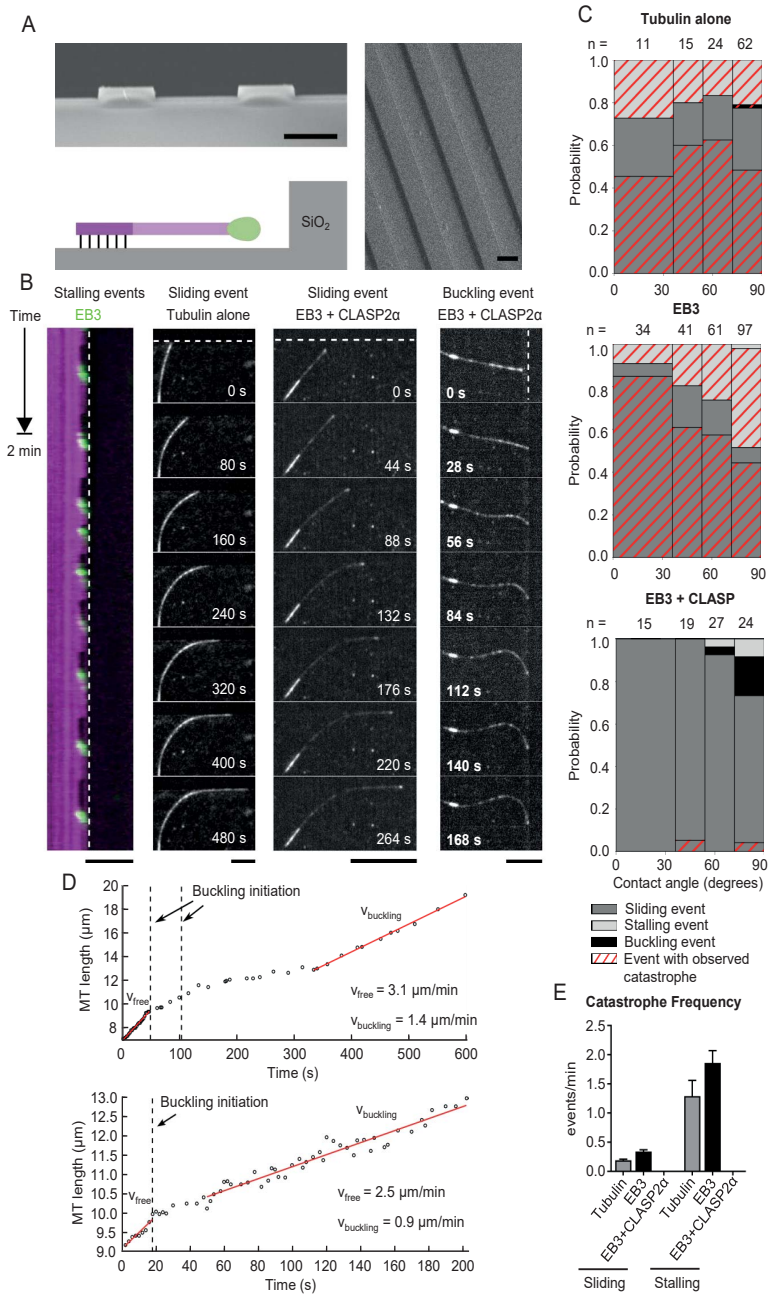
(A) Scanning Electron Microscope images with cross-sectional and top-down view of the SiO<sub>2</sub> barriers. The cartoon illustrates the MT-barrier interaction of a seed-nucleated MT in the presence of MT tip-binding proteins. Scale bars: 10  $\mu$ m.

(B) Representative kymograph and three-frame averaged montages of the three types of events during MT-barrier contact: stalling, sliding, and buckling. The location of the barrier is denoted by dashed white lines. All experiments were performed at 30°C, with the following concentrations when present: tubulin (15  $\mu$ M), EB3 (20 nM), CLASP (30 nM). Scale bars: 10  $\mu$ m.

(C) Probability of the event type during MT-barrier contact as a function of the contact angle, with 90° being perpendicular to the barrier. The red hatched events ended with a catastrophe. Number of growth events analyzed are indicated above each bin.

(D) MT growth during two buckling events. Vertical dotted lines indicate the start of a buckling event. The first graph contains two buckling initiation events, as the MT tip slipped during the first event. MT growth velocities are significantly lower during buckling compared to free growth.

(E) MT plus end catastrophe frequency during barrier contact for MTs sliding or stalling in the presence of tubulin alone or together with 20 nM mCherry-EB3 alone or with 20 nM mCherry-EB3 and 30 nM GFP-CLASP2 $\alpha$ . For sliding events, n=88, 156 and 77 and for stalling events, n=23, 77 and 3 for MTs grown in the presence of tubulin alone, together with mCherry-EB3 and with both mCherry-EB3 and GFP-CLASP2 $\alpha$ . Error bars represent SEM.



### 3.2.6. TOG2 SHOWS PREFERENCE FOR A REGION LOCATED BEHIND THE OUTMOST MT END

To get better insight into how TOG2 prevents catastrophes, we next examined the behaviour of this domain tethered to MTs by the positively charged SxIP peptide (TOG2-S) and found that at concentrations between 200-400 nM, it showed enrichment at the GMPCPP seeds and growing MT ends in the absence of EB3 (Fig. 3.6A), while the SxIP peptide alone showed no autonomous MT tip enrichment (Honnappa et al., 2009), data not shown). A similar, albeit weaker MT tip enrichment was found in the presence of EB3 $\Delta$ Tail, which does not bind to TOG2-S (Fig. S3.5A). In contrast, no TOG2-S accumulation was present at depolymerizing ends, also when MT disassembly was induced in the absence of free tubulin (Fig. 3.6B, Fig. S3.5B). At 200-400 nM, TOG2-S reduced catastrophes, stimulated rescues and induced occasional pausing events, while the MT growth rate was mildly reduced (Fig. 3.6C, Fig. S3.5C,D). TOG2-S-induced pauses or periods of very slow growth with duration of up to  $\sim$ 60 s were particularly obvious in the presence of EB3 $\Delta$ Tail, as they were never observed with EB3 or EB3 $\Delta$ Tail alone. Some weak EB3 $\Delta$ Tail accumulation at MT tips was present during such events (Fig. S3.5D), suggesting that they maintain a short stabilizing cap (Maurer et al., 2012).

We next used high-resolution simultaneous dual-colour TIRFM imaging of GFP-TOG2-S together with rhodamine-tubulin or mCherry-EB3 $\Delta$ Tail in combination with automated data analysis with subpixel precision and convolved model fitting to extract molecular density distributions of TOG2-S relative to the MT end and the EB3 $\Delta$ Tail comet, following the procedures described previously (Maurer et al., 2014). For the fitting, we modelled MT intensity as a step function, TOG2-S intensity as a combination of a step function (lattice intensity) and a delta function (point peak accumulation), and EB3 $\Delta$ Tail comet as an exponential decay function (Fig. 3.6D-F and S3.5E,F). Peak-to-lattice ratios of fluorescence intensity of TOG2-S were higher for higher growth rates (Fig. 3.6G): a clear peak of TOG2-S was visible for MTs growing faster than 1  $\mu$ m/min, but not at lower rates (Fig. 3.6H,I). Analysis of the averaged profiles indicated that the TOG2-S peak, when detectable, was positioned  $\sim$ 90 nm behind the MT end (Fig. 3.6J and S3.5). Similar analysis of averaged profiles with EB3 $\Delta$ Tail showed that the TOG2-S peak-to-lattice ratio was lower (Fig. S3.5G,H), and that TOG2-S peak was centered at  $\sim$ 60 nm behind the EB3 $\Delta$ Tail peak (Fig. 3.6J,K and S3.5J).

Previous work showed that the stabilizing (GTP or GDP-Pi) MT cap detected with EB1 as a marker starts at  $\sim$ 20-90 nm behind the MT end and decays for 200-500 nm, depending on the EB1 concentration and MT growth rate (Maurer et al., 2014). This localization broadly fits with the position of TOG2-S peak detected here with tubulin alone. However, simultaneous imaging of EB3 $\Delta$ Tail and TOG2-S showed that the peaks of the two proteins do not coincide, but that the maximal accumulation of TOG2-S was positioned at the rear of the EB3 comet (Fig. 3.6J,K) and the amplitude of this accumulation was reduced compared to the assays with tubulin alone (Fig. S3.5G,H). These findings can be explained by a combination of factors, such as the effect of EB3 $\Delta$ Tail on the MT lattice structure or GTP hydrolysis (Maurer et al., 2014), or direct competition between TOG2-S and EB3 $\Delta$ Tail. Taken together, these data indicate that in the conditions used in our study, TOG2-S shows a preference for MT end sites enriched during rapid MT growth and located  $\sim$ 10-12 tubulin layers behind the outmost

end. This region likely represents a part of the MT stabilizing cap and not the strongly curved protofilament ends that could be present at outmost MT extremities. In line with this view, TOG2-S showed no accumulation at depolymerizing MT ends, and both CLASP2 $\alpha$  and TOG2-S did not slow down, but rather mildly increased MT depolymerization rate (Fig. S3.5K,L), possibly because MT lattice polymerized in the presence of CLASPs has different properties (Grimaldi et al., 2014). Consistently, a very recent paper showed that CLASP2 $\gamma$  mildly increased MT shrinkage rate (Lawrence et al., 2018). Collectively, our data indicate that TOG2 acts to suppress MT catastrophes by binding behind the outmost MT end before rapid MT depolymerization is initiated.

### 3.2.7. A FEW CLASP2 $\alpha$ MONOMERS STABILIZE INCOMPLETE MT STRUCTURES

Next, we used single molecule analysis to investigate the number and the residence time of CLASP2 $\alpha$  molecules suppressing catastrophes. As published before (Drabek et al., 2006), we found that mammalian CLASP2 $\alpha$  is monomeric (Fig. S3.6A). The interactions of CLASP2 $\alpha$  and TOG2-S with MT tips and lattices in the presence of EB3 in our assays were very transient (Fig. S3.6B-D), with an average residence time at MT tips of  $\sim 0.2$ - $0.3$  s, similar to what was previously shown for other MT tip-tracking proteins (Bieling et al., 2007; Montenegro Gouveia et al., 2010). We note that this residence time was shorter than that recently described for CLASP2 $\gamma$  in the presence of EB1 (Lawrence et al., 2018), possibly due to differences in the proteins used or assay conditions.

By using single GFP-CLASP2 $\alpha$  molecules immobilized in a separate chamber on the same coverslip used for the MT dynamics assay, we estimated the number of CLASP2 $\alpha$  molecules necessary for catastrophe suppression and rescue induction. Due to the exponential decay of the TIRF field, the brightness of a molecule attached to a MT compared to a molecule attached to the glass surface would be lower, but the underestimate is in the range of 10% (van Riel et al., 2017). We found that one or two transiently binding molecules were sufficient to induce rescues at 3 nM CLASP2 $\alpha$  (Fig. S3.6E,F). Rescues often occurred after a short event of CLASP2 $\alpha$  tracking the depolymerizing MT end (Fig. S3.6E, white arrow). In contrast to the previous work on yeast and *Drosophila* CLASPs (Al-Bassam et al., 2010; Moriwaki and Goshima, 2016), but consistent with the work on mammalian CLASP2 $\gamma$  (Lawrence et al., 2018), rescues thus did not require the accumulation of immobile CLASP2 $\alpha$  clusters on the MT lattice. At the MT tip, 4-7 CLASP2 $\alpha$  molecules were typically present in conditions when catastrophes were fully suppressed (Fig. S3.6F). Together, these data indicate that a small number of CLASP2 $\alpha$  molecules (fewer than 10) are sufficient to suppress catastrophes, and even fewer CLASP2 $\alpha$  molecules can promote rescues.

Interestingly, the examination of kymographs of MT growth in the presence of CLASPs or the MT tip-targeted TOG2 domain often revealed the presence of two EB3 comets on the same MT – events whereby a MT tip polymerization slowed down and was subsequently restored by a “catching up” (a rear) EB3 comet that appeared behind the growing tip and was moving more rapidly than the “leading” comet (Fig. 3.7A-E). We termed such events as “tip repair” events. It has been previously shown that such events could occasionally be observed with MTs grown in the presence of EB3,

and that their frequency could be strongly increased by the protofilament-blocking agent eribulin, indicating that they occur when some protofilaments in a MT temporarily lag behind and then resume growth to “catch up” with the growing end (Doodhi et al., 2016). In the presence of full-length CLASP2 $\alpha$ , frequent and long tip repair events were observed, with the duration often exceeding 60 s and the length of up to 3-4  $\mu\text{m}$  (Fig. 3.7A,F and Fig. S3.7A,B). An increase in the frequency of tip repair events was also observed at a high concentration (400 nM) of TOG2-S together with EB3 $\Delta$ Tail (Fig. S3.7C,D). The idea that some protofilaments are missing from the MT end corresponding to the “leading” comet was supported by the reduced intensity of CLASP2 $\alpha$  or TOG2-S bound to MT lattice in these regions (Fig. 3.7B and S3.7E) and by the observation that such ends were often bent or curled, suggesting the loss of the mechanical integrity of the tube-like MT structure (Fig. 3.7G). Tip repair events that exhibited curling were also observed in cells (Fig. 3.7H), indicating that they are not an artefact of *in vitro* reconstitution.

To test if the presence of two EB3 comets on the same MT is indeed caused by stalling of a subset of the protofilaments, we collected data in the presence of TagBFP-

Figure 3.6 (following page): **TOG2 domain shows preference for a region behind the outmost MT end.**

(A) Kymographs, stills and fluorescence intensity profiles for GFP-TOG2-S at the indicated concentrations (30 nM, 200 nM and 400 nM) in the presence of rhodamine-tubulin. Scale bars for stills: 1  $\mu\text{m}$ . For kymos, scale bar: 3  $\mu\text{m}$  (horizontal) and 60 s (vertical).

(B) Stills and fluorescence intensity profiles for GFP-TOG2-S (30 nM) and rhodamine-tubulin for MTs assembled in the presence of tubulin alone after tubulin washout, with the time after tubulin washout indicated. Blue arrowheads indicate the depolymerizing MT ends. Scale bar: 2 microns

(C) Parameters of MT plus end dynamics in the presence of either rhodamine-tubulin alone (n=122) or in combination with GFP-TOG2-S at 30 nM (n=91), 200 nM (n=109) and 400 nM (n=80). Error bars denote SEM. For all plots, \*\*\*p<0.005, \*\*\*\*p<0.0001 and ns, no significant difference with control, Mann-Whitney U test.

(D) Example kymograph of GFP-TOG2-S (400 nM) (green channel) and rhodamine-tubulin (red channel) with overlaid profiles fitting results. Cyan line marks fitted position and white line marks averaged position of MT tip, derived from piecewise linear approximation. Green dots mark fitted position of TOG2-S accumulation. The opacity of dots is proportional to the amplitude of the accumulation. Scale bars are 1  $\mu\text{m}$  and 10 s.

(E) Example of an individual fitting of GFP-TOG2-S (400 nM) and rhodamine-tubulin fluorescence intensity profiles. Blue dashed line corresponds to the lattice and black dashed line to the peak accumulation components of overall TOG2-S fit function (shown with green dashed line).

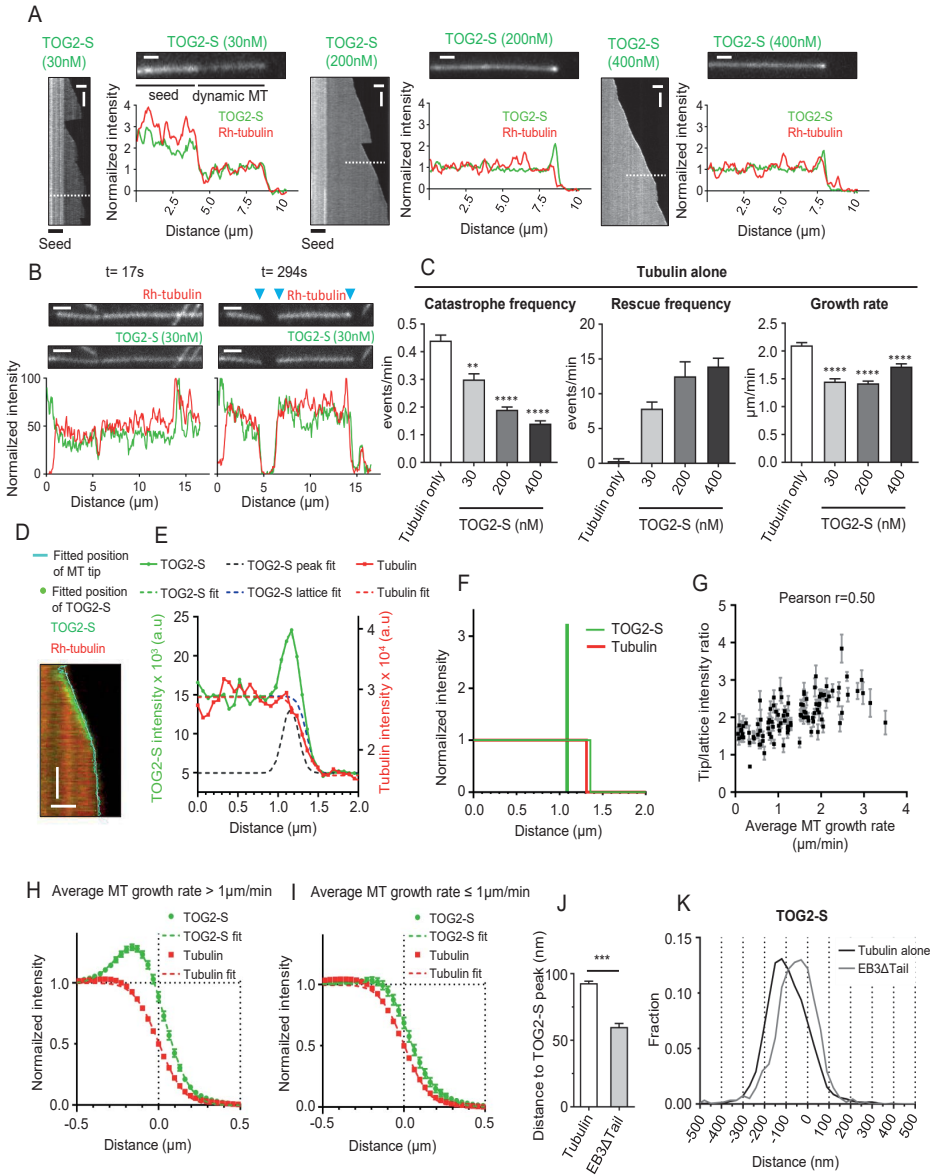
(F) Density distribution of TOG2-S (400 nM) (peak and lattice component shown separately, green lines) and MT lattice (red line) extracted from fitting shown in (E).

(G) Plot of the ratio of peak to lattice fluorescence intensity of GFP-TOG2S (400 nM) derived from fitting versus average speed of growth. Ratios are averaged for segments of constant average speed growth (128 segments, 5997 time points, 13 kymographs). Error bars represent SEM.

(H-I) Normalized, aligned, resampled and averaged fluorescent intensity profiles of GFP-TOG2-S (400 nM) and rhodamine-tubulin split based on average MT growth rate threshold value of 1  $\mu\text{m}/\text{min}$ . Profiles were first averaged per kymograph. Error bars represent SEM of second averaging among multiple kymographs (13 kymographs, 3536 left + 2461 right = 5997 total time points).

(J-K) Mean values with SEM (J) and histograms (K) of distances between TOG2-S intensity peak accumulation and the fitted position of MT tip (white bar, mean=92.9 nm, n=4586 fits) or the fitted peak of EB3 $\Delta$ Tail (grey bar, mean=59.9 nm, n=1778 fits). Only the fits where TOG2-S tip to lattice intensity ratio was above 1 were included. \*\*\*p<0.0001, two-tailed Mann-Whitney test. In the histograms, 0 corresponds to the fitted position of the MT end or EB3 $\Delta$ Tail peak.

See also Figure S3.5.



CLASP2 $\alpha$ , mCherry-EB3 and HiLyte488-labelled tubulin and analyzed MT intensity profiles in the tubulin channel during comet splitting (Fig. 3.7I). As expected, the MT intensity in the region between the leading and lagging comets was lower than the region behind the lagging comet (Fig. 3.7I, bottom panel). We considered two simple models of MT tip “erosion”: a subset of  $N$  protofilaments could be shortened by a uniform value  $d$  from the growing tip, creating a sharp drop in intensity (Model A, Fig. 3.7J), or the erosion could be gradual, and we assumed that the lengths of the missing parts of  $N$  protofilaments were distributed exponentially with a characteristic value  $d$  (Model B, Fig. 3.7J). Using these models, we performed Monte-Carlo simulations of the MT intensity, assuming that a MT has 13 protofilaments and that tubulin dimers are labelled with a probability equal to the fraction of labeled tubulin in the reaction (Fig. S3.7F-J, see Methods for details).

We analyzed two types of experimental data, the “control” situation with CLASP2 $\alpha$  and EB3, or the situation where the reaction was supplemented with 50 nM eribulin, which increases the frequency of detectable tip repair events (Fig. 3.7F). For each condition, experimental intensity profiles of tubulin were recorded at three time points: before, during and after the tip repair event (Fig. 3.7K,L). The time point during tip repair was selected at the moment when the distance between comets was approximately equal to 1  $\mu\text{m}$ . For each model, the parameters  $N$  and  $d$  were varied in search of values minimizing the residual between the experimental and theoretical profiles (Fig. 3.7M). Results for both “before” and “after” conditions were very similar and favoured Model A (sharp drop) with  $N=10$  missing protofilaments (or 3 protruding protofilaments) with a characteristic length  $d$  of 0.2-0.3  $\mu\text{m}$  (Fig. 3.7K-M). For the “catching-up” phases, the experimental profiles were better approximated by Model B (gradual) with 9-10 missing protofilaments and a much longer erosion length  $d$  of 0.9-1.2  $\mu\text{m}$  (Fig. 3.7K-M). If the assumption of gradual tip erosion from Model B is correct, this means that the rear EB3 comet intensity should gradually increase during the tip repair event, as more protofilaments are joining it, and we found that this is indeed the case (Fig. 3.7N). This increase was not due to the increasing velocity of the rear comet, which could affect EB3 intensity (Fig. S3.7K), and these data thus support the results of modelling. Taken together, our results show that a few monomeric CLASP2 $\alpha$  molecules transiently associated with MT tips prevent the onset of a catastrophe at MT ends missing a number of protofilaments and promote restoration of the MT tip structure (Fig. S3.7L).

### 3.3. DISCUSSION

CLASPs are among the most conserved regulators of MT dynamics, which are present in animals, plants and fungi, where they can suppress catastrophes and induce rescues (Bratman and Chang, 2007; Ruan and Wasteney, 2014). CLASPs contain several TOG-like domains, and we found that TOG2, targeted to MT tip, is necessary and sufficient for catastrophe suppression. Importantly, TOG2 by itself does not interact with free tubulin, and the same is true for the other folded CLASP domains. TOG2 also has only a very weak affinity for MTs; however, it normally acts as a part of CLASP, which interacts with MTs through unstructured positively charged regions and the TOG3 domain, and is targeted to the MT end-stabilizing cap by the nucleotide-sensitive CH domain

of EBs (Honnappa et al., 2009; Maurer et al., 2012). Interestingly, when tethered to MTs by a positively charged peptide, TOG2 shows some autonomous preference for the region overlapping with the stabilizing MT cap. These data suggest that the GTP-hydrolysis-dependent MT-stabilizing region, located behind the outmost MT tip is the actual site of the anti-catastrophe activity of TOG2. This view fits with our observations that CLASPs potently inhibit catastrophes irrespective of how they are initiated at the MT tip – spontaneously, mechanically or by drugs that might create defects or loss of individual protofilaments, or by a MT depolymerase that triggers protofilament peeling. This idea is also in line with the fact that TOG2 or CLASP2 $\alpha$  do not accelerate MT polymerization: TOG2 shows no preference for the outmost microtubule end and does not bind to free tubulin, and therefore does not share these two distinguishing features of the MT polymerases of the XMAP215/ch-TOG family (Brouhard et al., 2008; Maurer et al., 2014). Our data thus exclude the model that mammalian CLASPs act like MT polymerases that recruit tubulin dimers to MTs (Yu et al., 2016), although this model may still hold true for the yeast CLASP homologues (Al-Bassam et al., 2010). The difference between CLASPs and the MT polymerases of the XMAP215/ch-TOG family is further emphasized by the observation that the latter do not suppress catastrophes or induce rescues *in vitro* (Zanic et al., 2013), and our experiments showed that, in contrast to the CLASP2 TOG2, targeting of individual tubulin-binding TOG domains of ch-TOG to growing MT tips had little effect on catastrophes and rescues.

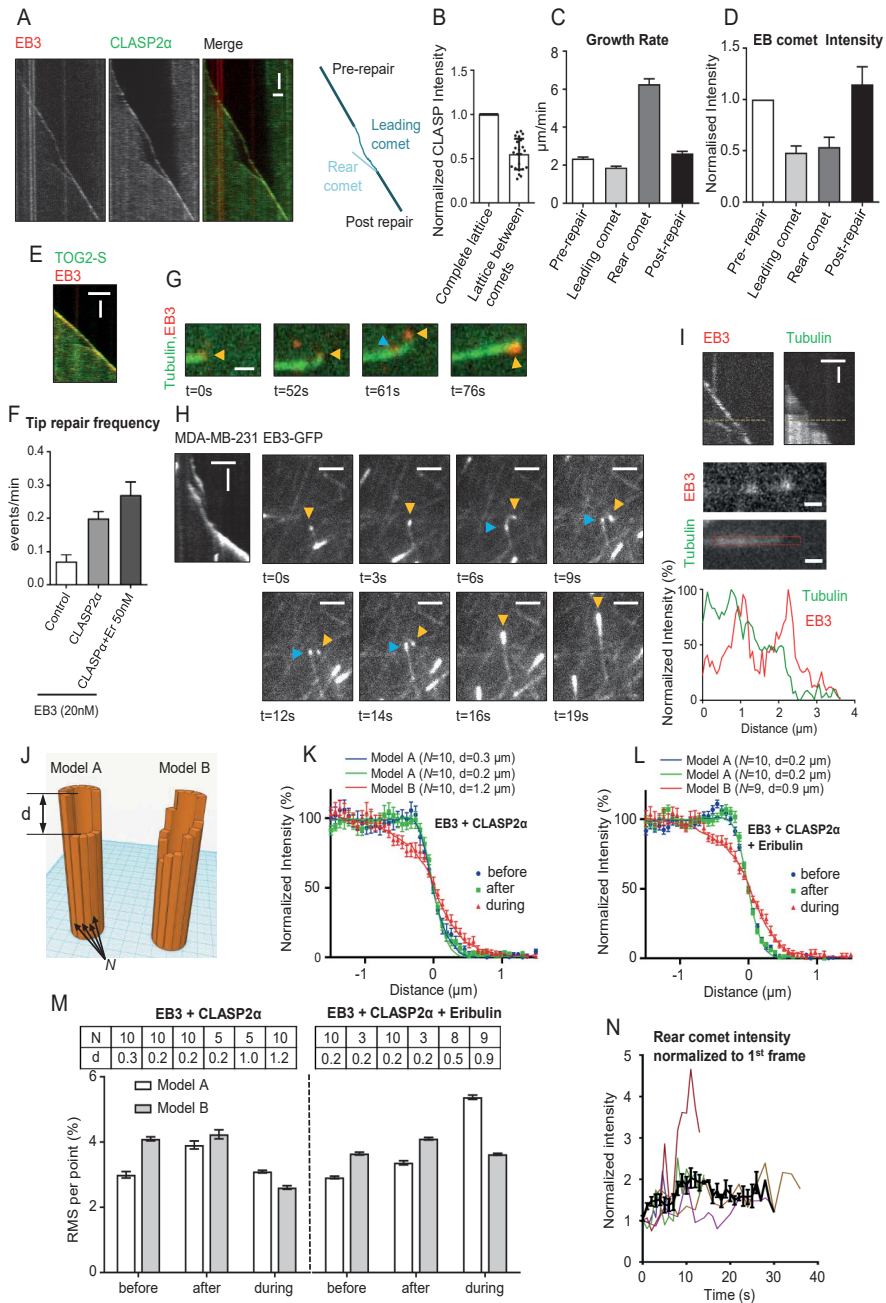
The nature of the exact binding site of TOG2 remains an important question. TOG2 has a unique convex architecture with an additional N-terminal helix that stabilizes the domain's paddle-like HEAT repeat structure (Leano et al., 2013; Maki et al., 2015), and it has been shown that it displays a higher affinity for drug-induced tubulin ring-like oligomers (Maki et al., 2015). We showed that the TOG2 residues W339, R462 and R504, corresponding to the amino acids that contribute to tubulin binding in the TOG domains of XMAP215/ch-TOG family proteins, are required for TOG2 function in our assays, in agreement with the previous analysis of MT binding by CLASP1 (Leano et al., 2013). However, this does not mean that CLASP TOG2 binds to highly bent tubulin dimers. TOG2-S does not concentrate on depolymerizing MT ends or at the outmost ends of growing microtubules, where the most strongly curved conformation of tubulin dimers is expected to be found. Since TOG2 structure is unique, its binding site might be completely different from that of other TOG domains. We find that TOG2-S shows some preference for GMPCPP MTs and to a region overlapping with the GTP or GDP-Pi cap, and is enriched at rapidly growing MT ends that are expected to have a long cap. Therefore, it is possible that, similar to EBs, TOG2 binds to a site that overlaps with interprotofilament contacts, the structure of which is known to be sensitive to GTP hydrolysis by tubulin (Maurer et al., 2012). The fact that TOG2-S accumulation at MT tips is reduced in the presence of EB3 $\Delta$ Tail, possibly due to structural changes in the cap region or through direct competition, supports this view, which would need to be tested by structural approaches. It is important to emphasize that since the enrichment of TOG2-S at the growing MT ends is only observed at high concentrations, TOG2 affinity for the stabilizing cap is low, and at lower concentrations, TOG2 requires other domains or proteins, such as EBs, to be positioned in this region.

CLASPs prevent catastrophe onset but do not slow down MT shortening ((Lawrence

et al., 2018), this paper). This finding combined with the experiments showing TOG2-S enrichment behind the outmost tip at the MT plus end suggests that CLASPs, through their TOG2 domain, promote the stability of the MT region corresponding to the GTP (or GDP-Pi) cap so long as it is present. Recent work showed that the onset of a MT catastrophe occurs with a delay, which is visible as a MT pause or a very slow depolymerization that corresponds to the gradual loss of MT-stabilizing EB1-binding sites within the cap (Duellberg et al., 2016). Since only the density of such stabilizing sites at the outmost end of the cap is critical (Duellberg et al., 2016), this would explain how a small number of CLASP molecules can be sufficient to prevent catastrophes. This idea also fits with the data that CLASP prevents short depolymerization excursions and that TOG2-S can induce MT pausing, during which some EB-binding sites are still present at MT ends. The number of such stabilizing sites at the pausing MT ends is lower than at growing ends, explaining why TOG2-S, which has a low affinity to these sites, is not

Figure 3.7 (following page): **CLASP2 $\alpha$  stabilizes incomplete MT tip structures.**

- (A) Kymographs showing a MT tip repair event with 20 nM mCherry-EB3 and 30nM GFP-CLASP2 $\alpha$ ; a schematic of the same event is shown on the right. Scale bars: 2  $\mu$ m (horizontal) and 60 s (vertical).
- (B) Averaged fluorescence intensity of GFP-CLASP2 $\alpha$  in the MT lattice region between the leading and lagging comet, normalized to the intensity of the complete MT lattice (n=23). Mean  $\pm$  SD.
- (C,D) Growth rates (C) (n=65 events) and the EB-comet intensities (D) (n=17 events) before, during and after comet splitting, EB-comet intensities are normalized to the comet intensity before splitting.
- (E) Kymograph showing a tip repair event in the presence of 20 nM mCherry-EB3 and 30 nM GFP-TOG2-S. Scale bars: 2  $\mu$ m (horizontal) and 45 s (vertical).
- (F) Frequency of tip repair for MTs grown in the presence of 20 nM mCherry-EB3 alone (n=49) or together with 30 nM TagBFP-CLASP2 $\alpha$  (n=103) or in the presence of 20 nM mCherry-EB3, 30 nM TagBFP-CLASP2 $\alpha$  and 50 nM Eribulin-A488 (n=56). The frequency was calculated by dividing the number of observed tip repair events by the total growth time, n=number of MTs analyzed in each condition. Error bars represent SEM.
- (G) Still images of a MT grown in the presence of Alexa488-tubulin, 20 nM mCherry-EB3 and 30 nM TagBFP-CLASP2 $\alpha$  showing curling in the region between the leading and the lagging comet. Arrowheads point to the EB comets, yellow points to the leading and blue to the rear comet. Scale bar: 1  $\mu$ m.
- (H) Kymograph and corresponding still images showing a MT tip repair event in MDA-MB-231 cells stably expressing EB3-GFP. The yellow arrowhead points to the leading comet and the blue one to the rear comet. Scale bars: 2  $\mu$ m (horizontal) and 5 s (vertical) (kymograph) and 2  $\mu$ m (cell image).
- (I) Kymograph showing a MT tip repair event in the presence of HiLyte-488 tubulin, 20 nM mCherry-EB3 and 30 nM TagBFP-CLASP2 $\alpha$ , still images and line-scans along the red (EB3) and green (tubulin) channel during tip repair. Scale bars: 2  $\mu$ m (horizontal) and 30 s (vertical) (kymograph) and 0.5  $\mu$ m (still images).
- (J) Illustration of two different MT end tapering models representing sharp (Model A, left) and gradual (Model B, right) loss of protofilaments.
- (K,L) Averaged tip intensity profiles of tubulin channel (green) for MTs grown in the presence of 20 nM mCherry-EB3 and 30 nM TagBFP-CLASP2 $\alpha$  (K), n=16, 17 and 17 for before, after and during tip repair, respectively, and for MTs grown in the presence of 20 nM mCherry-EB3, 30 nM TagBFP-CLASP2 $\alpha$  and 50 nM Eribulin, n=40, 44 and 27 for before, after and during tip repair, respectively. Error bars represent SEM. Lines correspond to the best fits of simulations with the optimal model type and parameter values indicated at the top of each plot.
- (M) The distribution of minimal residuals between simulated and experimental profiles depending on the model. Top table shows optimal parameter values for each case (d is in  $\mu$ m). For each case n=3. Error bars represent SD.
- (N) Changes of the mCherry-EB3 comet intensity over time for the lagging comet before the tip repair. Individual traces represent a single tip repair event. The black line is the average of several time traces (n=22). Intensity values were normalized to the value at the first time point.
- See also Figures S3.6 and S3.7.



enriched at pausing ends. For this reason, in order to induce pausing, TOG2-S concentration must be sufficiently high to decorate the whole MT. Recent work showed that CLASP2 does not affect the length of the GTP cap (Lawrence et al., 2018), which suggests that CLASPs stabilize MT ends directly rather than by regulating GTP hydrolysis by tubulin.

An important clue about the catastrophe-suppressing mechanism is provided by the finding that in the presence of CLASPs, persistently growing MTs could tolerate the loss of a significant number of protofilaments at the growing end. Recent work suggested that MT tapering and the accompanying reduction in the stabilizing cap density might be the underlying cause of MT age-induced catastrophes (Coombes et al., 2013; Duellberg et al., 2016). Interestingly, while in the presence of CLASP2 or TOG2-S catastrophes were almost completely blocked, we observed a ~3 fold increase in the frequency of tip repair events, in which a transient MT growth perturbation and protofilament loss was followed by the appearance of a rear, “catching up” comet that restored the complete MT plus end structure. Our previous work indicated that such events occur when at least one MT protofilament is transiently blocked but can later resume elongation (Doodhi et al., 2016). The frequency of tip repair events in the presence of CLASP2 (~0.2 per minute) was lower than the catastrophe frequency in control assays (~0.5 per minute), which means that these events could represent at least a fraction of the suppressed catastrophes. However, we note that the detection of tip repair events is limited by the resolution of optical microscopy, and might thus be underestimated, and the contribution of such events to MT growth persistence could in fact be significant. Furthermore, the presence of very long (up to 4  $\mu\text{m}$ ) tip repair events shows that CLASPs can prevent disassembly of stabilizing caps on partial MT structures and thus create a window of opportunity for MT tip restoration.

While TOG2 is key for catastrophe suppression, TOG3 did not suppress catastrophes but mildly promoted rescues together with EB3. The distinct activities of TOG2 and TOG3 suggest that catastrophe suppression and rescue induction might be mechanistically different, and in line with this view, more CLASP2 $\alpha$  molecules were needed to suppress catastrophes than to induce rescues.

Many cytoskeletal proteins are known to be controlled by autoinhibitory interactions that are released by partner binding. Here, we showed that CLASPs share this property, because their C-terminal domain (CLIP-ID), responsible for the interactions with the majority of known CLASP partners such as CLIP-170 (Akhmanova et al., 2001; Efimov et al., 2007; Hannak and Heald, 2006; Lansbergen et al., 2006), can inhibit the MT-directed activities of TOG2 and possibly TOG3. The N-terminal TOG domain of CLASP2 $\alpha$ , TOG1, which does not bind to either MTs or free tubulin because it lacks the conserved residues necessary for contacting tubulin, can release this autoinhibition. TOG1 is present in CLASP1/2 $\alpha$  but absent in CLASP2 $\beta$  and CLASP2 $\gamma$  isoforms (Akhmanova et al., 2001). CLASP2 can thus be expressed both as a constitutively active and regulated isoforms, which might be important for controlling CLASP activity at specific cellular sites.

Our findings provide insight into how CLASPs work in different cellular settings, for example, by helping MTs to withstand compression when they make sharp turns in plant cells (Ambrose et al., 2011) or in the protrusions of cancer cells invading a 3D

matrix (Bouchet et al., 2016). The finding that the CLASP-EB complex strongly lowered the kinetic threshold for template-based MT outgrowth explains why CLASPs can stimulate  $\gamma$ -tubulin-dependent MT nucleation from the Golgi (Efimov et al., 2007). Both TOG2 and TOG3 are likely to cooperate in this process, as they both display partial activity compared to the full length CLASP2 $\alpha$  protein. Taken together, our data reveal how a combination of distinct domains with anti-catastrophe, rescue, partner binding and autoregulatory activities make CLASPs potent MT regulators that help to maintain MTs in a growing state.

### 3.4. EXPERIMENTAL METHODS

#### EXPERIMENTAL MODEL AND SUBJECT DETAILS

*E.coli* expression strain BL21 (DE3) was used for recombinant expression of individual CLASP2 $\alpha$  TOG domains used for MT pelleting, tubulin binding, biophysical and X-ray crystallography experiments. The CLASP2-TOG-EB3CH protein was also purified from *E.coli* BL21 (DE3). The cells were cultured in standard LB medium. All the other CLASP, chTOG, MCAK full length, truncations and fusion constructs were overexpressed in HEK293T cells for purification. MDA-MB-231 cells stably expressing EB3-GFP (Bouchet et al., 2016) were cultured in DMEM supplemented with 10% FCS. COS-7 and HEK 293T cells were cultured in DMEM/F10 (1:1 ratio, Lonza, Basel, Switzerland) supplemented with 10% FCS, both grown at 37°C. HEK293T, MDA-MB-231 and COS-7 cell lines used here were not found in the database of commonly misidentified cell lines maintained by ICLAC and NCBI BioSample, were not authenticated and were negative for mycoplasma contamination.

#### DNA CONSTRUCTS, CELL LINES, AND CELL CULTURE

CLASP truncations expressed in mammalian cells were made from the full length constructs described previously (Akhmanova et al., 2001; Mimori-Kiyosue et al., 2005) in modified pEGFP-C1 or pmCherry-C1 vectors with a StrepII tag. Ch-TOG construct was a gift of S. Royle (University of Warwick, UK). For siRNA transfection, MDA-MB-231 cells stably expressing EB3-GFP were simultaneously treated with siRNAs specific for CLASP1 and CLASP2 (Mimori-Kiyosue et al., 2005) or with control (luciferase) siRNA (Bouchet et al., 2016) for 72 hours. EB3-GFP comets were imaged in live cells on a TIRF microscope and kymographs were analyzed to determine the effects of CLASP1/2 depletion on MT plus end dynamics. For overexpression of CLASP2 constructs, COS-7 cells were transiently transfected with different StrepII-GFP-CLASP2 constructs (as indicated in the figures) for 12 hours, and the GFP signals of these constructs were used to quantify MT dynamics. Live imaging of COS-7 cells overexpressing different constructs of CLASP2 in the presence of colchicine (250 nM) was performed within 40 min of colchicine treatment.

#### PROTEIN PURIFICATION FROM HEK293T CELLS FOR *in vitro* RECONSTITUTION ASSAYS

GFP-CLASP1 $\alpha$ , mCherry-CLASP2 $\alpha$ , Tag-BFP-CLASP2 $\alpha$ , GFP-CLASP2 $\alpha$ , its TOG-domain truncations, point mutants, fusion proteins with the TOG domains of chTOG and coiled

coil of CLIP-170, and GFP-MCAK used in the *in vitro* reconstitutions assays were purified from HEK293T cells using the Strep(II)-streptactin affinity purification. Cells were harvested 2 days after transfection. Cells from a 15 cm dish were lysed in 500  $\mu$ l of lysis buffer (50 mM HEPES, 300 mM NaCl and 0.5% Triton X-100, pH 7.4) supplemented with protease inhibitors (Roche) on ice for 15 minutes. The supernatant obtained from the cell lysate after centrifugation at 21,000 x g for 20 minutes was incubated with 40  $\mu$ l of StrepTactin Sepharose beads (GE) for 45 minutes. The beads were washed 3 times in the lysis buffer without the protease inhibitors. The protein was eluted with 40  $\mu$ l of elution buffer (50 mM HEPES, 150 mM NaCl, 1 mM MgCl<sub>2</sub>, 1 mM EGTA, 1 mM dithiothreitol (DTT), 2.5 mM d-Desthiobiotin and 0.05% Triton X-100, pH 7.4). Purified proteins were snap-frozen and stored at -80 °C.

### CLONING, PROTEIN EXPRESSION, AND PURIFICATION FROM *E. coli*

Individual domains of CLASP2 (Fig. S3.2A, rightmost panel) were cloned into a pET-based bacterial expression vector using the restriction free positive selection method (Olieric et al., 2010). All recombinant proteins contained either an N-terminal thioredoxin-6xHis or 6xHis cleavable tag for affinity purification. For standard expression, the proteins were transformed into the *E. coli* expression strain BL21(DE3). Transformed cells were cultivated in LB at 37°C until an OD600 between 0.4 to 0.6 was reached. The cultures were subsequently cooled down to 20°C prior to induction with 0.4 mM isopropyl 1-thio- $\beta$ -galactopyranoside (IPTG, Sigma). Expression was carried out overnight at 20°C. Cells were harvested by centrifugation at 4°C for 15-20 min and lysed by sonication (50 mM HEPES, pH 8.0, 500 mM NaCl, 10 mM Imidazole, 10% Glycerol, 2 mM  $\beta$ -mercaptoethanol, proteases inhibitors (Roche)). The crude extracts were cleared by centrifugation at 20,000 x g for 20 min and the supernatants were filtered through a 0.45 micron filter before purification.

TOG domain proteins were purified by immobilized metal-affinity chromatography (IMAC) on HisTrap HP Ni<sup>2+</sup> Sepharose columns (GE Healthcare) at 4°C according to the manufacturer's instructions. The thioredoxin-6xHis or 6xHis tags were cleaved by 3C protease during dialysis against lysis buffer (without proteases inhibitors). Cleaved samples were reapplied onto an IMAC column to separate the cleaved products from the respective tags and potentially uncleaved protein. Processed proteins were concentrated and gel filtrated on a HiLoad Superdex 75 16/60 size exclusion chromatography column (GE Healthcare) equilibrated in 20 mM Tris HCl, pH 7.5, 150 mM NaCl, 2 mM DTT. Protein fractions were analyzed by Coomassie stained SDS-PAGE. Fractions containing the target protein were pooled and concentrated by ultrafiltration. Protein concentrations were estimated by UV at 280 nm and the pure proteins were aliquoted, flash frozen in liquid nitrogen and stored at -80°C.

### MT PELLETING ASSAY

MT pelleting assays were performed as previously described (Campbell and Slep, 2011). Briefly, taxol-stabilized MTs were assembled in BRB80 buffer (80 mM PIPES-KOH, pH 6.8, 1 mM MgCl<sub>2</sub>, 1 mM EGTA) from pure bovine brain tubulin at 1 mg/mL. 50  $\mu$ l of polymerized MTs were incubated 20 min with 20  $\mu$ l of the protein of interest at 2 mg/mL (diluted to the desired protein concentration with 2 x BRB80 buffer) and 50

$\mu\text{L}$  of BRB80. The mixture was centrifuged at  $25^\circ\text{C}$  for 20 min at  $180,000 \times g$ . Mix, supernatant and pellet fractions were analyzed by Coomassie stained 12% SDS-PAGE. As controls, MTs alone and individual TOG domains were processed the same way.

### ISOTHERMAL TITRATION CALORIMETRY (ITC)

All the proteins were buffer exchanged to BRB80 buffer supplemented with 50 mM NaCl by overnight dialysis at  $4^\circ\text{C}$ . ITC experiments were performed at  $25^\circ\text{C}$  using an ITC200 system (Microcal) by step wise addition of different TOG domain proteins (syringe concentration was  $150 \mu\text{M}$  for CLASP2 TOG1, TOG2 and TOG3,  $200 \mu\text{M}$  for CLIP-ID, and  $250 \mu\text{M}$  for Stu2 TOG1) in the ITC cell containing  $15 \mu\text{M}$  bovine brain tubulin. The resulting heats were integrated and fitted in Origin (OriginLab) using the standard 'one set of sites' model implemented in the software package. Only for Stu2 TOG1 the dissociation constant of binding to tubulin could be determined ( $K_d = 18.8 \pm 3.21 \text{ nM}$ ). TOG1-TOG2 interaction was probed using  $227 \mu\text{M}$  of CLASP2 TOG1 in the syringe and  $60 \mu\text{M}$  TOG2 in the cell). TOG2-CLIP-ID interaction was probed using  $500 \mu\text{M}$  CLIP-ID in the syringe and  $50 \mu\text{M}$  TOG2 in the cell.

### SIZE EXCLUSION CHROMATOGRAPHY FOLLOWED BY MULTI-ANGLE LIGHT SCATTERING (SEC-MALS)

SEC-MALS experiments were performed in 20 mM Tris-HCl, pH 7.5, 150 mM NaCl, 2 mM DTT) using a S-200 10/300 analytical size exclusion chromatography column connected in-line to a miniDAWN TREOS light scattering and Optilab T-rEX refractive index detector (Wyatt Technology). Measurements were carried out at  $20^\circ\text{C}$  and each sample was injected at 1 mg/ml (injected volume:  $30 \mu\text{L}$ ). Data analysis was performed using the software package provided by the instrument.

### CRYSTALLIZATION, DATA COLLECTION AND STRUCTURE SOLUTION

CLASP2-TOG1 (HsCLASP2 residues 2-228) crystals were obtained by the hanging-drop vapour diffusion method at  $20^\circ\text{C}$  in the Morpheus crystallization condition B12 (Molecular Dimensions) by mixing  $2 \mu\text{L}$  of the protein at 7 mg/mL with  $2 \mu\text{L}$  of the reservoir solution. Crystals appeared over-night and were frozen directly in liquid nitrogen. A single-wavelength anomalous diffraction experiment from intrinsic sulphur atoms (S-SAD) was performed at the macromolecular crystallography super-bending magnet beamline

X06DA (PXIII) at the Swiss Light Source, Villigen, Switzerland.  $360^\circ$  native data sets were collected at  $1.0 \text{ \AA}$  wavelength on a single crystal at 100 K. Multi-orientation  $360^\circ$  data were collected on the same crystal at 100 K at a wavelength of  $2.066 \text{ \AA}$  with  $0.2^\circ$  oscillation and 0.1 sec exposure at 8 different orientations of multi-axis. The sample-to-detector distance was set to 120 mm. The data were processed using XDS (Kabsch, 2010) and scaled and merged with XSCALE (Kabsch, 2010).

Substructure determination and phasing were performed with SHELXC/D/E (Sheldrick, 2010). The successful SHELXD substructure solution that was found in a search for 20 sites had a CCall and a CCweak of 41.27 and 23.45, respectively. 154 cycles of density modification resulted in a clear separation of hands. Model building was performed using Buccaneer (Cowtan, 2006). The resulting model was improved

through iterative model rebuilding in Coot (Emsley and Cowtan, 2004) and refined in the PHENIX software package (Adams et al., 2010). The quality of the structure was assessed with MolProbity (Chen et al., 2010). See Table S1 for crystallography data collection and refinement statistics. The structure was deposited in the PDB with the accession code 5NR4.

### *In vitro* MT DYNAMICS ASSAYS

Reconstitution of MT growth dynamics *in vitro* was performed as described previously (Montenegro Gouveia et al., 2010). GMPCPP-stabilized MT seeds (70% unlabelled tubulin, 18% biotin tubulin and 12% of rhodamine-tubulin or HiLyte 488 tubulin) were prepared as described before (Mohan et al., 2013). Flow chambers, assembled from plasma-cleaned glass coverslips and microscopic slides were functionalized by sequential incubation with 0.2 mg/ml PLL-PEG-biotin (Susos AG, Switzerland) and 1 mg/ml NeutrAvidin (Invitrogen) in MRB80 buffer (80 mM piperazine-N,N[prime]-bis(2-ethanesulfonic acid), pH 6.8, supplemented with 4 mM MgCl<sub>2</sub>, and 1 mM EGTA. MT seeds were attached to the coverslip through biotin-NeutrAvidin interactions. Flow chambers were further blocked with 1 mg/ml  $\kappa$ -casein. The reaction mixture with or without CLASP proteins (MRB80 buffer supplemented with 15  $\mu$ M porcine brain tubulin, 0.5  $\mu$ M rhodamine-tubulin, 50 mM KCl, 1 mM guanosine triphosphate, 0.2 mg/ml  $\kappa$ -casein, 0.1% methylcellulose, and oxygen scavenger mix (50 mM glucose, 400  $\mu$ g/ml glucose oxidase, 200  $\mu$ g/ml catalase, and 4 mM DTT)) was added to the flow chamber after centrifugation in an Airfuge for 5 minutes at 119,000  $\times$  g. For experiments in the presence of EB3, concentration of mCherry-EB3 or GFP-EB3 was as indicated in the figures and rhodamine-tubulin was excluded from the assay. The flow chamber was sealed with vacuum grease, and dynamic MTs were imaged immediately at 30°C using TIRF microscopy. All tubulin products were from Cytoskeleton Inc.

For experiments to test binding of TOG2-S to depolymerizing MTs, MT seeds were elongated in the presence of 20  $\mu$ M porcine brain tubulin with 10% rhodamine-tubulin for 5 minutes in the buffer containing 50 mM KCl, 1 mM guanosine triphosphate, 0.2 mg/ml  $\kappa$ -casein, 0.1% methylcellulose, and oxygen scavenger mix (50 mM glucose, 400  $\mu$ g/ml glucose oxidase, 200  $\mu$ g/ml catalase, and 4 mM DTT) in MRB80. Subsequently, stable GMPCPP caps were added by exchanging the reaction mixture to the one supplemented with 0.125 mM GMPCPP and 10% HiLyte647 labelled 5  $\mu$ M porcine tubulin for 10 minutes. Finally, the GMPCPP-containing mixture was exchanged for a reaction mixture without tubulin, containing the indicated concentrations of GFP-TOG2-S (30 nM and 200 nM) and imaged for 30 minutes to observe depolymerizing MT ends.

### TIRF MICROSCOPY

*In vitro* reconstitution assays were imaged on a TIRF microscope setup as described previously (Mohan et al., 2013) or on an Ilas<sup>2</sup> TIRF setup. In brief, we used an inverted research microscope Nikon Eclipse Ti-E (Nikon) with the perfect focus system (Nikon), equipped with Nikon CFI Apo TIRF 100x 1.49 N.A. oil objective (Nikon) and controlled with MetaMorph 7.7.5 software (Molecular Devices). The microscope was equipped with TIRF-E motorized TIRF illuminator modified by Roper Scientific France/PICT-IBiSA, Institut Curie. To keep the *in vitro* samples at 30°C, a stage top

incubator model INUBG2E-ZILCS (Tokai Hit) was used. For excitation, 491 nm 100 mW Calypso (Cobolt) and 561 nm 100 mW Jive (Cobolt) lasers were used. We used ET-GFP 49002 filter set (Chroma) for imaging of proteins tagged with GFP or ET-mCherry 49008 filter set (Chroma) for imaging of proteins tagged with mCherry. Fluorescence was detected using an EMCCD Evolve 512 camera (Roper Scientific) with the intermediate lens 2.5X (Nikon C mount adapter 2.5X) or using the CoolSNAP HQ2 CCD camera (Roper Scientific) without an additional lens. In both cases the final magnification was 0.063  $\mu\text{m}/\text{pixel}$ .

Ilas<sup>2</sup> system (Roper Scientific, Evry, FRANCE) is a dual laser illuminator for azimuthal spinning TIRF (or Hilo) illumination and with a custom modification for targeted photomanipulation. This system was installed on Nikon Ti microscope (with the perfect focus system, Nikon), equipped with 150 mW 488 nm laser and 100 mW 561 nm laser, 49002 and 49008 Chroma filter sets, EMCCD Evolve mono FW DELTA 512x512 camera (Roper Scientific) with the intermediate lens 2.5X (Nikon C mount adapter 2.5X), CCD camera CoolSNAP MYO M-USB-14-AC (Roper Scientific) and controlled with MetaMorph 7.8.8 software (Molecular Device). To keep the *in vitro* samples at 30°C, a stage top incubator model INUBG2E-ZILCS (Tokai Hit) was used. The final resolution using EMCCD camera was 0.065  $\mu\text{m}/\text{pixel}$ , using CCD camera it was 0.045  $\mu\text{m}/\text{pixel}$ .

### ***In vitro* TEMPLATE-BASED MT OUTGROWTH ASSAY**

GMPCPP MT seeds labeled with HiLyte 488 tubulin were attached to the coverslips through biotin-neutravidin interaction as described above. After washing out unbound seeds, the flow chambers were blocked with 1 mg/ml  $\kappa$ -casein followed by the polymerization reaction mixture as above with different concentrations of rhodamine-labelled tubulin. The nucleation probability was estimated as the fraction of the total GMPCPP seeds that showed MT outgrowth within 15 min imaging window. The nucleation probabilities over different tubulin concentration were fitted to the sigmoidal equation using GraphPad Prism 7.

### **MICRO-FABRICATION OF SiO<sub>2</sub> BARRIERS**

Fabrication of the SiO<sub>2</sub> barriers was achieved in a cleanroom environment by subsequent deposition, lithography, and plasma etching steps, as previously described in (Kalisch et al., 2011). In short, the glass coverslips are first cleaned with a 70°C solution of base piranha (5:1:1 of H<sub>2</sub>O:NH<sub>4</sub>OH:H<sub>2</sub>O<sub>2</sub>) to remove any organic residues. To ensure a smooth surface for TIRF imaging, etching of the barriers must be done in pure SiO<sub>2</sub>. To that end, we deposit a layer of 2  $\mu\text{m}$  SiO<sub>2</sub> via Plasma-Enhanced Chemical Vapor Deposition with a deposition rate of 70 nm/min at 300°C (Oxford Instruments PlasmaPro 80). Then, a 2.2  $\mu\text{m}$  layer of the positive resist S1813 (MicroChem) is spin coated at 1500 rpm on the coverslip and baked at 115°C for 90 seconds on a hotplate. Photolithography (EVG-620) with near-UV (13 mW/cm<sup>2</sup>) through a chromium mask for 5 seconds transfers the barrier pattern into the resist. The sample is then developed in MF-321 (MicroPosit) for 60 seconds to remove the regions of UV-exposed resist. Next, Reactive Ion Etching (Leybold Hereaus) with a mixture of CHF<sub>3</sub>:O<sub>2</sub> (50sccm:2.5sccm) ensures an anisotropic etch into the exposed SiO<sub>2</sub> with an etch rate of 33 nm/min. We

made sure not to etch completely through the SiO<sub>2</sub> layer as the original surface of the glass coverslip is too rough for TIRF microscopy after etching. Finally, the remaining resist is removed and the sample cleaned in HNO<sub>3</sub> for 5 min. The final barriers were 10 μm wide and 1.7 μm high, enclosing channels with a width of 15 μm.

### MT GROWTH AGAINST SiO<sub>2</sub> BARRIERS AND ANALYSIS OF BARRIER CONTACT EVENTS

The micro-fabricated samples were passivated with PLL-PEG-biotin and κ-casein. Biotinylated GMPCPP-stabilized seeds were attached to the surface via streptavidin. The direction of flow of the seed mix was perpendicular to the barriers in order to favour perpendicular MT-barrier contact events. The height and straightness of the barriers in combination with methyl-cellulose in solution prevents MTs from growing over the barriers. The experiments without CLASP in solution were imaged on an Olympus TIRF microscope with a 60x, 1.45 NA oil immersion objective using an additional magnification of 1.6 to obtain 96x image magnification. Images were collected on two Andor iXon Ultra 897 EMCCD cameras for simultaneous dual-colour acquisition. The experiments with CLASP2α were imaged on a Ilas<sup>2</sup> TIRF setup described in the TIRF microscopy section.

All MT-barrier contact events were separated into three different event types, i.e. sliding, stalling, and buckling. The contact angle of a MT with a barrier and the barrier contact times were determined and analyzed with a custom written MATLAB script, adapted from (Ruhnnow et al., 2011). The catastrophe frequency was determined by counting the number of observed catastrophes and dividing this by the time a MT spends in contact with the barrier. The statistical error was obtained by dividing this number by the square root of the number of measured contact events. The growth of buckling MTs was determined by manually tracking the MT (Fig. 3.5D).

### QUANTIFICATION OF THE INTENSITIES OF EB COMETS

To obtain the intensity values of EB comets in Fig. 3.7D, we collected the intensity profiles of mCherry-EB3 comets along several time points for each individual growth event by averaging across 6-pixel wide lines. The intensity profile for each time point was fitted to a Gaussian function with the background intensity ( $I_{BG}$ ) to obtain the amplitude of the comet's peak  $I_A$  according to:

$$I_p(x, t) = I_{BG}(t) + I_A(t) \cdot \exp\left(-\frac{(x - x_c)^2}{2\sigma^2}\right)$$

The final values were obtained by averaging the  $I_A(t)$  for each individual growth event.

### TIP-AVERAGING OF MT INTENSITY PROFILES

To build average HyLite 488 tubulin intensity distribution at the growing tip (Fig. 3.7K,L) we generated intensity profiles of 6 pixel thick line (400 nm) of 2-3 μm length with its middle point positioned approximately at the MT tip using Fiji (Schindelin et al., 2012) (similar to (Maurer et al., 2014)). Resulting profiles  $I(x)$  were fitted with the error function shifted in x using custom written MATLAB script:

$$I_p(x, t) = I_{BG} + \frac{1}{2} I_{AMP} \left( 1 + \operatorname{erf} \left( \frac{x - x_c}{\sqrt{2}\sigma} \right) \right)$$

where fitting parameter  $I_{BG}$  corresponds to the intensity of background,  $I_{AMP}$  to the amplitude of the fluorescent signal,  $x_c$  to the position of the MT tip and  $\sigma$  to the degree of tip tapering convolved with microscope's point spread function (PSF) (see Fig. S3.7H,J). Each profile was shifted by its  $x_c$  value, background subtracted with  $I_{BG}$  and normalized by  $I_{AMP}$  (Fig. S3.7H,J).

### FITTING AND AVERAGING OF GFP-TOG2-S INTENSITY PROFILES

For simultaneous two color imaging of GFP-TOG2-S/rhodamine tubulin labeled MTs and GFP-TOG2-S/mCherry-EB3 $\Delta$ Tail we used OptoSplit III beamsplitter (Cairn Research Ltd, UK) equipped with double emission filter cube projecting two channels on the camera chip simultaneously. To account for chromatic aberrations of the objective, images of a calibration photomask with round 500 nm features positioned equidistantly with 2  $\mu$ m (Compugraphics, UK) were acquired simultaneously in GFP and mCherry channels using transmitted bright-field illumination (Maurer et al., 2014). Based on feature detections we made sub-pixel channels alignment and non-linear registration using B-spline transform implemented in our Detection of Molecules ImageJ plugin and described earlier (version 1.1.5, [https://github.com/ekatruxha/DoM\\_Utrecht](https://github.com/ekatruxha/DoM_Utrecht), (Chazeau et al., 2016)). Registered movies were used to create kymographs by drawing segmented lines of 20 pixel width (1.25  $\mu$ m) along growing MTs using KymoResliceWide plugin with maximum transverse intensity (<http://fiji.sc/KymoResliceWide>). Using kymograph images, we traced the growing MT tips with the "Segmented Line" ROI tool from ImageJ to mark the approximate position of the growing tip used for exact fitting later. The fitting of fluorescent intensity profiles was performed using a custom-written MATLAB script. Intensity profiles were extracted from kymographs at each time point corresponding with a range of  $\pm 1 \mu$ m from the approximate growing tip position marked earlier.

For the fitting of the rhodamine-labelled MT tip we used the complimentary error function:

$$I(x) = I_{BG} + \frac{1}{2} I_{AMP} \cdot \operatorname{erfc} \left( \frac{x - x_c}{\sqrt{2}\sigma} \right)$$

where the fitting parameter  $I_{BG}$  corresponds to the intensity of background,  $I_{AMP}$  to the amplitude of the fluorescent signal,  $x_c$  to the position of the MT tip and  $\sigma$  to the degree of tip tapering convolved with microscope's point spread function (PSF). For the averaging, each raw fluorescent profile was shifted by its  $x_c$  value, background subtracted with  $I_{BG}$  and normalized by  $I_{AMP}$ .

For the fitting of the mCherry-EB3 $\Delta$ Tail profile we assumed that the density distribution of EB3 in the comet decays exponentially from its maximum value close to the MT tip. To represent its convolution with microscope's PSF, we used a sum of the complimentary error function (lattice binding) and an exponentially modified Gaussian distribution:

$$I(x) = I_{BG} + \frac{1}{2} I_{lattice} \cdot \operatorname{erfc} \left( \frac{x - x_c}{\sqrt{2}\sigma} \right) + \frac{1}{2} I_{EB} \cdot \exp \left( \frac{\lambda}{2} (\sigma^2 \lambda + 2(x - x_c)) \right) \left( 1 - \operatorname{erf} \left( \frac{\sigma^2 \lambda + x - x_c}{\sqrt{2}\sigma} \right) \right)$$

where fitting parameter  $I_{BG}$  corresponds to the intensity of background,  $I_{lattice}$  to the amplitude of the fluorescent intensity fraction associated with the MT lattice binding,  $I_{EB}$  to the amplitude of convolved exponential decay,  $x_c$  to the position of the maximum number of molecules in the molecules distribution (start of exponential decay position),  $\sigma$  to the PSF standard deviation and  $\lambda$  to the exponential decay constant. For the averaging, each raw fluorescent profile was shifted by its  $x_c$  value, background subtracted with  $I_{BG}$  and normalized by the maximum  $I(x)$  value.

For the fitting of the GFP-TOG2-S profile, we used a sum of the complimentary error function (lattice binding) and a Gaussian peak with standard deviation equal to microscopes point spread function (corresponding to the peak accumulation):

$$I(x) = I_{BG} + \frac{1}{2} I_{lattice} \cdot \operatorname{erfc} \left( \frac{x - x_c}{\sqrt{2}\sigma} \right) + I_{peak} \cdot \exp \left( -\frac{1}{2} \left( \frac{x - x_c - x_{peak}}{\sigma_{PSF}} \right)^2 \right)$$

where fitting parameter  $I_{BG}$  corresponds to the intensity of background,  $I_{lattice}$  to the amplitude of the fluorescent intensity fraction associated with the lattice binding,  $I_{peak}$  to the amplitude of peak accumulation,  $x_c$  to the position of the lattice binding tip and  $\sigma$  to the degree of tip tapering,  $x_{peak}$  to the position of peak accumulation with respect to the lattice tip and fixed parameter  $\sigma_{PSF}$  is equal to the PSF standard deviation (1.5 px = 97.5 nm). For the averaging, each raw fluorescent profile was background subtracted with  $I_{BG}$ , normalized by  $I_{lattice}$  and shifted by  $x_c$  value of either rhodamine-tubulin or mCherry-EB3 $\Delta$ Tail.

After normalization and alignment, all profiles corresponding to specific condition were linearly interpolated with the same step size of half-pixel (32.5 nm) and averaged for each individual kymograph. The final profiles (Fig. 3.6H,I and S3.5G) represent averages among several average kymograph profiles.

To calculate MT tip to lattice intensity ratio for GFP-TOG2-S we took into account differences in the convolution of step function (lattice) and delta-function (point-peak accumulation) using following formula:

$$ratio = \frac{I_{peak} \sqrt{2\pi} \sigma_{PSF}}{I_{lattice}}$$

where  $I_{lattice}$  and  $I_{peak}$  are fitted values and  $\sigma_{PSF}$  is equal to the PSF standard deviation.

To find segments with continuous average speed of growth we decomposed fitted time sequences  $x_c(t)$  of rhodamine-tubulin and mCherry-EB3 $\Delta$ Tail by piecewise linear approximations. It was done using multiscale trend analysis Matlab code (<https://github.com/ekatruxha/MTA>) based on (Zaliapin et al., 2005).

### END TAPERING SIMULATIONS

Monte-Carlo simulations of MTs tips were performed using 13 element- (protofilament-) wide regular array with 8 nm longitudinal distance between dimers as a MT lattice representation (Fig. S3.7F). Absent length of  $N$  protofilaments was constant and defined by parameter  $d$  for Model A. For Model B it was randomly sampled from an exponential distribution with parameter  $d$ . Present tubulin dimers were labelled with a probability equal to the fraction of labelled tubulin in the corresponding experiment (0.09). Only labelled dimers were assumed to generate intensity profile in molecule number (Fig. S3.7F) and its version convoluted with PSF of used microscope (Fig. S3.7G). The PSF was approximated with a Gaussian function with the standard deviation of 122 nm. Convoluted intensity values were binned together according to the image pixel size (65 nm) and the Gaussian noise was added leading to the signal-to-noise ratio of 7 observed in experiment (Fig. S3.7I). Noise containing profiles were fitted and normalized using the same procedure as described in the previous section. For a single iteration of simulation, we used the same number of MTs as in the corresponding experimental condition with lengths determined from the fitting. A total of 50 iterations were run and averaged for each parameters combination of  $N$  and  $d$ . Residual between simulated and experimental profiles was calculated as a sum of squared differences using only those pixels in  $x$  which contain all individual profiles. The final fitting result was obtained by varying  $N$  and  $d$  independently in a search for a minimal residual value (Fig. 3.7M).

### ANALYSIS OF MT GROWTH VARIABILITY

Time lapse images of growing MTs labelled with HiLyte 488 tubulin were recorded at intervals of 0.7 s for 5 min and 350-400 ms of exposure time. To estimate the position of the MT plus end, we fitted MT intensity profiles as described above. Subsequently, the change in MT length over time was calculated as  $\Delta L(t) = L(t) - L(\text{first frame})$ . Next, as described previously (Gardner et al., 2011), we calculated the average mean squared displacement (MSD) of the MT length increments  $\langle \Delta L^2 \rangle(\tau)$  for increasing values of time delay  $\tau$ . We then fitted  $\langle \Delta L^2 \rangle(\tau)$  to an MSD equation containing diffusion with drift:

$$\langle \Delta L^2 \rangle(\tau) = v_g^2 \tau^2 + 2D_p \tau + \sigma_{err}^2$$

where  $\tau$  corresponds to delay,  $v_g$  is the average speed of growth,  $D_p$  is the effective diffusion coefficient for the MT polymerization and  $\sigma_{err}$  is the experimental error.

### SINGLE-MOLECULE FLUORESCENCE INTENSITY ANALYSIS OF CLASP2 $\alpha$

Diluted protein samples of GFP, GFP-MACF43-LZ (Honnappa et al., 2009) and GFP-CLASP2 $\alpha$  were immobilized in adjacent flow chambers of the same plasma cleaned glass coverslip as described previously (Sharma et al., 2016). The flow chambers were washed with MRB80 buffer and sealed with vacuum grease and immediately imaged with a TIRF microscope. 10-20 images of previously unexposed coverslip areas were acquired with 100 ms exposure time and low laser power. GFP, GFP-MACF43LZ and GFP-CLASP2 $\alpha$  were located in different chambers of the same coverslip, so the same

imaging conditions could be preserved. Single molecule fluorescence spots were detected and fitted with 2D Gaussian function using custom written ImageJ plugin DoM-Utrecht ([https://github.com/ekatruxha/DoM\\_Utrecht](https://github.com/ekatruxha/DoM_Utrecht)). The fitted peak intensity values were used to build fluorescence intensity histograms.

### CLASP MOLECULE COUNTING AT MT TIPS AND RESCUE POINTS

To determine the number of molecules of CLASP2 $\alpha$  at a MT tip, we immobilized single molecules of CLASP2 $\alpha$  onto the coverslip of one of the flow chambers and performed the *in vitro* reconstitution assay in the adjacent chamber of the same coverslip as described previously (Sharma et al., 2016). Images of unbleached CLASP2 $\alpha$  single molecules were acquired first and using the same imaging/illumination conditions, time lapse imaging was performed with the *in vitro* assay with CLASP2 $\alpha$  at 3 nM or 30 nM, using 100 ms exposure and 2 s intervals for 5 minutes. The plus end localized CLASP2 $\alpha$  molecules or the molecules present at the rescue site were manually located in each frame and fitted with 2D Gaussian, the amplitude of which was used for the intensity analysis. For CLASP2 $\alpha$  at the rescue site, 2-3 frames after rescue initiation were used to get the intensity values. To build the distributions of CLASP2 $\alpha$  molecule numbers at the MT tip, each CLASP2 $\alpha$  intensity value at the MT plus end or a rescue site was normalized by the average CLASP2 $\alpha$  single molecule intensity from the adjacent chamber.

### QUANTIFICATION AND STATISTICAL ANALYSIS

Kymographs were generated using the ImageJ plugin KymoResliceWide (<http://fiji.sc/KymoResliceWide>). MT dynamics parameters were determined from kymographs using an optimized version of the custom made JAVA plug in for ImageJ as described previously (Montenegro Gouveia et al., 2010; Sharma et al., 2016; Taylor, 1997). ~100-200 MT growth events were analyzed per condition.

The relative standard error for catastrophe frequency was calculated as described previously (Mohan et al., 2013). The relative standard error of mean rescue frequency was calculated in the same way as the standard error of the mean catastrophe frequency, i.e.  $SE_r = \bar{f}_r \frac{SE_{t_{sh}}}{\bar{t}_{sh}}$ , where  $\bar{f}_r, \bar{t}_{sh}$  are average values and  $SE_{f_r}, SE_{t_{sh}}$  are standard errors of rescue frequency and shortening time respectively. When the number of observed rescue events was relatively small (number of rescues  $\leq 10$ ) as compared to the catastrophes, we assumed that they follow a Poisson distribution. The standard deviation of the rescue frequency was calculated as the square root of its mean value and the standard error was calculated according to  $SE_{f_r} = \frac{\sqrt{\bar{f}_r}}{\sqrt{N_r}}$ , where  $\bar{f}_r$  and  $SE_{f_r}$  are the average and the standard error of the rescue frequency and  $N_r$  is the number of rescues.

Statistical comparison between the different conditions was performed with Mann Whitney U test using GraphPad Prism 7.

**SUPPLEMENTARY FIGURES**

All supplementary figures are available online at:

<https://www.cell.com/cms/10.1016/j.devcel.2018.05.032/attachment/ab8680a4-3d84-4554-8664-ced6b2b73055/mmc1.pdf>



# 4

## EB INFORMED DYNAMICS OF THE MICROTUBULE CAP DURING STALLED GROWTH

**Maurits KOK, Florian HUBER, Svenja-Marei KALISCH, and Marileen DOGTEROM**

*There are three kinds of lies:  
lies, damned lies, and statistics.*

Benjamin Disraeli

*The interaction of growing microtubules with steric objects such as the cell cortex is known to promote catastrophes. If microtubules are unable to overcome compressive forces, they remain in a stalled state, leading to accelerated disappearance of a stabilizing GTP/GDP-Pi cap and the subsequent onset of catastrophe. We investigate the dynamics of the cap through in vitro reconstitution of microtubule dynamics in contact with micro-fabricated barriers, using the plus-end binding protein EB3 as a marker for the nucleotide state of the tip. We show that the resulting lifetimes of stalled microtubules, as well as the corresponding life time distributions of freely growing microtubules, can be fully described with a simple phenomenological 1D model based on noisy microtubule growth and a single EB3-dependent hydrolysis rate. This same model is furthermore capable of explaining both the previously reported catastrophe statistics during tubulin washout and the mild catastrophe dependence on microtubule growth rates.*

## 4.1. INTRODUCTION

As a major constituent of the eukaryotic cytoskeleton, microtubules are involved in many essential processes within the cell, including intracellular transport, cell division, and cell morphology (Akhmanova and Steinmetz, 2015; Brangwynne et al., 2006). Throughout these processes, microtubules interact with other cellular components, either through intermediary protein complexes or through direct physical contact (Colin et al., 2018; Dogterom and Koenderink, 2019; Gurel et al., 2014; Howard, 2006; Inoue and Salmon, 1995; Preciado Lopez et al., 2014). These interactions contribute to spindle size regulation (Gregorette et al., 2006; Letort et al., 2016) and to mechanical stability during cell morphogenesis (Bouchet et al., 2016; Brangwynne et al., 2006). During contact, the stability of microtubules is an important factor affecting the function and duration of these interactions (Komarova et al., 2002; Tischer et al., 2009).

Microtubules are hollow cylindrical polymers consisting of  $\alpha\beta$ -tubulin dimers arranged in a head-to-tail fashion to form protofilaments, 13 of which typically constitute the lattice (Tilney et al., 1973; Zhang et al., 2015). The microtubule network fluctuates over time as individual filaments constantly switch between phases of growth and shrinkage, a fundamental process known as dynamic instability (Mitchison and Kirschner, 1984). The biochemical mechanism behind the stochastic transition between growth and shrinkage, known as a catastrophe, is driven by the progressive hydrolysis of the GTP nucleotide bound to  $\beta$ -tubulin (Carlier and Pantaloni, 1982; Nogales, 1999). During polymerization, the microtubule tip is highly dynamic and fluctuates with the continuous addition and removal of tubulin dimers (Gardner et al., 2011; Kerssemakers et al., 2006; Rickman et al., 2017; Schek et al., 2007). As GTP-bound tubulin is incorporated at the microtubule end, hydrolysis of the nucleotide is hypothesized to lead to a destabilization of the lattice by a compaction around the exchangeable nucleotide (Alushin et al., 2014; Zhang et al., 2015). Upon the loss of the resulting stabilizing cap (Carlier and Pantaloni, 1981), a catastrophe follows upon which the strain build-up in the lattice is released during depolymerization.

Direct measurements of the stabilizing cap is possible with the family of end binding proteins (EBs) that can autonomously bind to a specific region at the microtubule tip, resembling the conformational state of GTP $\gamma$ S and GDP-Pi (Maurer et al., 2011). It has been shown that the size of the EB comet at the tip correlates with the size of the stabilizing cap and consequently with microtubule stability (Duellberg et al., 2016; Seetapun et al., 2012; Zhang et al., 2015). Various estimations of the stabilizing cap size have been reported, from short caps of a few terminal tubulin layers (Brun et al., 2009; Caplow and Shanks, 1996; Karr and Purich, 1978; Walker et al., 1991) to longer caps spanning up to dozens of layers (Carlier and Pantaloni, 1981; Seetapun et al., 2012). More recently, tubulin washout experiments showed that not the entire cap is required to prevent a catastrophe, but only a terminal structure of  $\sim 10$  tubulin layers (Duellberg et al., 2016).

Over the years, different types of models had been proposed to gain a better understanding of what triggers a catastrophe. Biochemical models mainly rely on the hydrolysis of tubulin dimers to reduce the size of the stabilizing cap for a catastrophe to occur (Bayley et al., 1989; Chen and Hill, 1985; Gardner et al., 2011; Margolin et al., 2012; Padinhateeri et al., 2012; Piedra et al., 2016; VanBuren et al., 2002). Still, only with

the introduction of lateral interactions between dimers in a 2D model can these models accurately describe the microtubule lifetimes (Gardner et al., 2011). Mechanochemical models on the other hand include the build-up of strain the lattice and protofilament bending at the tip (Coombes et al., 2013; McIntosh et al., 2018; Molodtsov et al., 2005; VanBuren et al., 2005; Zakharov et al., 2015). Both models have their place in explaining experimental observations of dynamic instability, but they can require many fitting parameters, adding to the computational cost. Alternatively, simplified phenomenological models have been useful in characterizing microtubule dynamics and the effect of microtubule associated proteins (MAPs) on it (Brun et al., 2009; Duellberg et al., 2016; Flyvbjerg et al., 1996; Rickman et al., 2017).

Here, we investigate the stability of stalling microtubules through *in vitro* and *in silico* approaches. A stalling microtubule exerts a pushing force smaller than its critical buckling force, resulting in retarded polymerization. The stability of pushing microtubules has previously been studied in the context of buckling and bending microtubules *in vitro* (Janson et al., 2003), *in vivo* (Brangwynne et al., 2007; Odde et al., 1999; Pallavicini et al., 2017), and *in silico* (Das et al., 2014; Valiyakath and Gopalakrishnan, 2018). It has been established that microtubules growing against rigid barriers *in vitro* can generate pushing forces that lead to an increased catastrophe frequency (Janson et al., 2003; Laan et al., 2008). It is believed that this force-induced catastrophe is the result of a reduction in the addition of tubulin dimers as the microtubule growth speed is slowed with increasing force (Janson et al., 2003; Kerssemakers et al., 2006). However, whether the introduced compressive force, the reduction of tubulin addition, or nucleotide hydrolysis governs the lifetime of a stalled microtubule has remained unresolved.

We set out to investigate the contribution of GTP hydrolysis and tip fluctuations to the stability of stalling microtubules using EB3 as a marker for the size of the stabilizing cap. To measure the stability of a stalled microtubule *in vitro*, we studied the dynamics of microtubules growing against micro-fabricated barriers. By introducing a novel barrier design containing an overhang, we ensure that microtubule stalling can be imaged with TIRF microscopy. We observe that microtubule stalling increases the catastrophe frequency in the absence of EB3. In the presence of EB3 the stalling duration is further reduced in a concentration dependent manner. Surprisingly, the full decay of the EB3 comet during microtubule stalling does not necessarily lead to an immediate catastrophe and leaves the microtubule in a metastable state.

To find a minimal model capable of explaining microtubule stalling with the smallest number of fitting parameters, we use coarse-grained Monte Carlo simulations of 1D filaments simulating the key features of microtubule dynamic instability (Flyvbjerg et al., 1996; Margolin et al., 2006; Padinhateeri et al., 2012). We show that both microtubule lifetimes in general and the duration of microtubule stalling specifically can be explained by a combination of random hydrolysis and noisy tip growth. We demonstrate that while the EB binding region is a measure for the size of the stabilizing cap, it is not sufficient to explain the onset of a catastrophe. This apparent discrepancy can be resolved by triggering a catastrophe when a large enough sequence of hydrolysed tubulin dimers becomes exposed at the microtubule tip. Moreover, this 1D biochemical model can also successfully capture microtubule dynamics over a range of tubulin

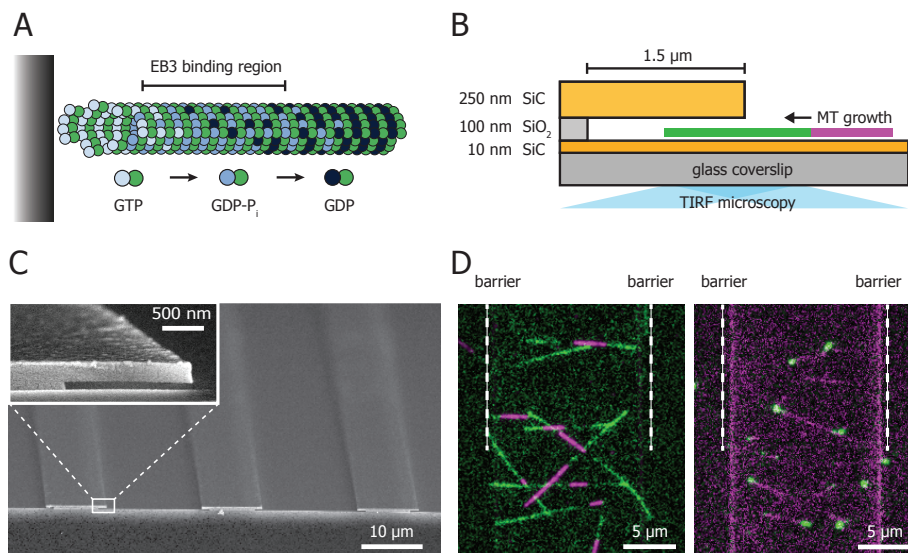


Figure 4.1: *In vitro* reconstitution of microtubule stalling

(A) Schematic depiction of the nucleotide distribution at the microtubule end. Progressive hydrolysis of GTP-tubulin after incorporation leads to a destabilized lattice that is stabilized by a GTP/GDP-Pi cap. EB3 chiefly binds to the GDP-Pi rich region. During microtubule-barrier contact, reduction of microtubule growth and hydrolysis are hypothesized to lead to an accelerated loss of the protective cap.

(B) Schematic of the micro-fabricated barrier with an approximately  $1.5\ \mu\text{m}$  overhang made of SiC. The barrier itself is composed of  $\text{SiO}_2$  and is  $100\ \text{nm}$  high, forcing the growing microtubules into a stalled state within the TIRF illumination field. Microtubules are grown from stabilized GMPCPP seeds towards the barriers.

(C) Scanning Electron Microscope image of two channels with barriers. The insert shows a zoom of the barrier with SiC overhang.

(D) TIRF images of the micro-fabricated channel enclosed by two barriers (white dotted lines). On the left microtubules (green) are nucleated from GMPCPP-stabilized seeds (magenta) towards the barriers and on the right microtubules (magenta) polymerize towards the barriers in the presence of GFP-EB3 (green). See also Fig. S1 and Videos S1 and S2.

concentrations and is in good agreement with previously reported catastrophe delays after tubulin dilution.

## 4.2. RESULTS

### 4.2.1. *In vitro* RECONSTITUTION OF MICROTUBULE STALLING

To investigate the stability of pushing microtubules in the presence of GFP-EB3, we analysed the dynamics of microtubules growing against micro-fabricated barriers using an *in vitro* reconstitution assay (Bieling et al., 2007; Kalisch et al., 2011). We treat a microtubule as a filament comprising three regions: 1) a GTP rich terminal region containing outwardly curved protofilaments (Maurer et al., 2014; McIntosh et al., 2018), 2) a region containing the intermediate GDP-Pi state to which EB3 prefers to bind (Mau-

rer et al., 2011), and 3) the GDP lattice (Fig. 4.1A). The presence of EB3 is known to increase the GTP hydrolysis rate and growth speed by respectively compacting the microtubule lattice and closing the lattice seam (Maurer et al., 2014; Zhang et al., 2015). Microtubules were nucleated from GMPCPP-stabilized seeds towards the barriers and imaged with Total Internal Reflection Fluorescence Microscopy (TIRFM). The barriers are composed of 100 nm SiO<sub>2</sub> and have an amorphous silicon carbide (SiC) overhang, bridging approximately 1.5 μm, to trap the microtubules and force them into a stalled state (Fig. 4.1B,C). SiC is a mechanically stable, optically transparent material with similar passivation and functionalization properties as SiO<sub>2</sub> due to a very thin native oxide layer on the surface (Coletti et al., 2007; Dhar et al., 2009). Although fabrication of the barriers requires a thin 10 nm layer of SiC on the surface (see Methods for details), microtubules can be imaged successfully with TIRFM (Fig. 4.1D and S1). This novel design enables high resolution imaging with TIRF microscopy as the microtubules are forced to remain within 100 nm from the surface during barrier contact, eliminating fluctuations perpendicular to the surface. The width between two barriers is 15 μm, chosen to reduce the probability of observing slipping and buckling events as longer microtubules are less stiff.

#### 4.2.2. COMPLETE EB3 DECAY DOES NOT NEED TO TRIGGER AN IMMEDIATE CATASTROPHE

The microtubule-barrier contact events leading to a stalled microtubule were analysed with kymographs to obtain the contact duration and GFP-EB3 comet intensity prior and during contact (Fig. 4.2A and S1, see Methods for details). Any contact events leading to microtubule buckling or sliding along the barrier were excluded from the analysis. All experiments were performed in the presence of 15 μM tubulin. From the moment of barrier contact, the EB3 intensity at the microtubule tip decreases until the onset of catastrophe (Fig. 4.2B and S1D). We observed that for ~65% of stalling events the EB comet did not fully decay (> 10% of the EB signal remaining) before the onset of catastrophe. The mean comet intensity at the moment of catastrophe was 16% of the pre-contact mean. For the other stalling events we found that a full decay of the EB comet did not immediately lead to a catastrophe. Instead, they remained in contact with the barrier even in the absence of an observable EB3 comet above the intensity on the microtubule lattice (Fig. 4.2C). Fitting the average EB decay from the moment of barrier contact with a mono-exponential function, shows that the decay rate increases with 0.24 s<sup>-1</sup>, 0.29 s<sup>-1</sup>, and 0.40 s<sup>-1</sup> for 20, 50, and 100 nM EB3 respectively (Fig. 4.2D). The presence of EB3 thus increases the decay of the stabilizing cap during stalling as predicted from its effect of increasing the GTP hydrolysis rate.

#### 4.2.3. MONTE CARLO SIMULATION OF MICROTUBULE STALLING

To determine whether microtubule stalling can be understood solely through the loss of tubulin addition during barrier contact and a single stochastic hydrolysis step, we performed Monte Carlo simulations of stalled microtubule growth. Microtubules were treated as 1D filaments with subunits of 8/13 nm comprising two distinct states: GTP/GDP-Pi and GDP (Fig. 4.3A, top). We decided to ignore the initial transition from GTP to GDP-Pi at this point, which was reported to be much faster than the GDP-Pi

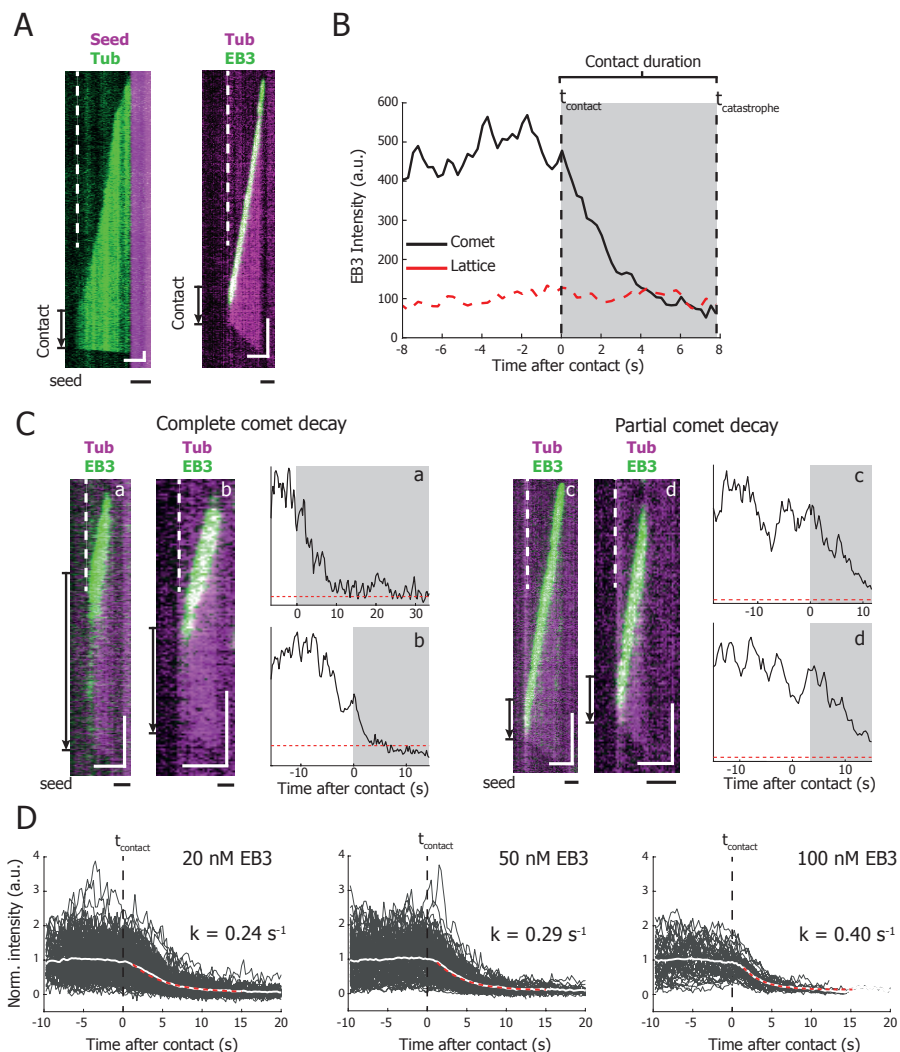


Figure 4.2: **Microtubule stalling events *in vitro***

(A) Representative kymographs of a microtubule-barrier contact event in the presence of  $15 \mu\text{M}$  Hilyte488-labelled tubulin (left) and in the presence of  $15 \mu\text{M}$  rhodamine-labelled tubulin with  $20 \text{ nM}$  GFP-EB3 (right). The dotted line denotes the position of the  $\text{SiO}_2$  barrier. The duration of barrier contact is indicated. Scale bars:  $2 \mu\text{m}$  (horizontal) and  $10 \text{ s}$  (vertical).

(B) Individual mean intensity of the EB3 comet and the EB3 signal on the microtubule lattice of the kymograph on the right in (A). At the moment of microtubule-barrier contact ( $t_{\text{contact}}$ ), the EB3 comet signal decays to the level of the microtubule lattice, ultimately resulting in the onset of a catastrophe ( $t_{\text{catastrophe}}$ ) after  $7.75 \text{ s}$ .

(C) Several examples of stalling microtubules with their respective integrated comet intensity traces. Traces **a-b** show a full comet decay during barrier contact before the onset of a catastrophe, whereas the comet in traces **c-d** only partially decays. All traces were in the presence of  $15 \mu\text{M}$  tubulin. Additionally, trace **a** contained  $20 \text{ nM}$  EB3, trace **b** and **c**  $100 \text{ nM}$  EB3, and trace **d**  $50 \text{ nM}$  EB3. Arrows and shaded regions illustrate the duration of microtubule stalling event. Scale bars:  $2 \mu\text{m}$  (horizontal) and  $10 \text{ s}$  (vertical).

(D) All normalized EB3 comet intensity traces for  $20$ ,  $50$ , and  $100 \text{ nM}$  EB3 aligned on the moment of barrier contact. The mean decays were fitted with a mono-exponential curve and show an increasing decay rate with increasing EB3 concentrations, resulting in decay rates of  $0.24 \text{ s}^{-1}$ ,  $0.29 \text{ s}^{-1}$ , and  $0.40 \text{ s}^{-1}$  for  $20$ ,  $50$ , and  $100 \text{ nM}$  respectively. Number of stalling events analysed:  $20 \text{ nM}$ ,  $n = 230$ ,  $50 \text{ nM}$ ,  $n = 246$ , and  $100 \text{ nM}$ ,  $n = 126$ .

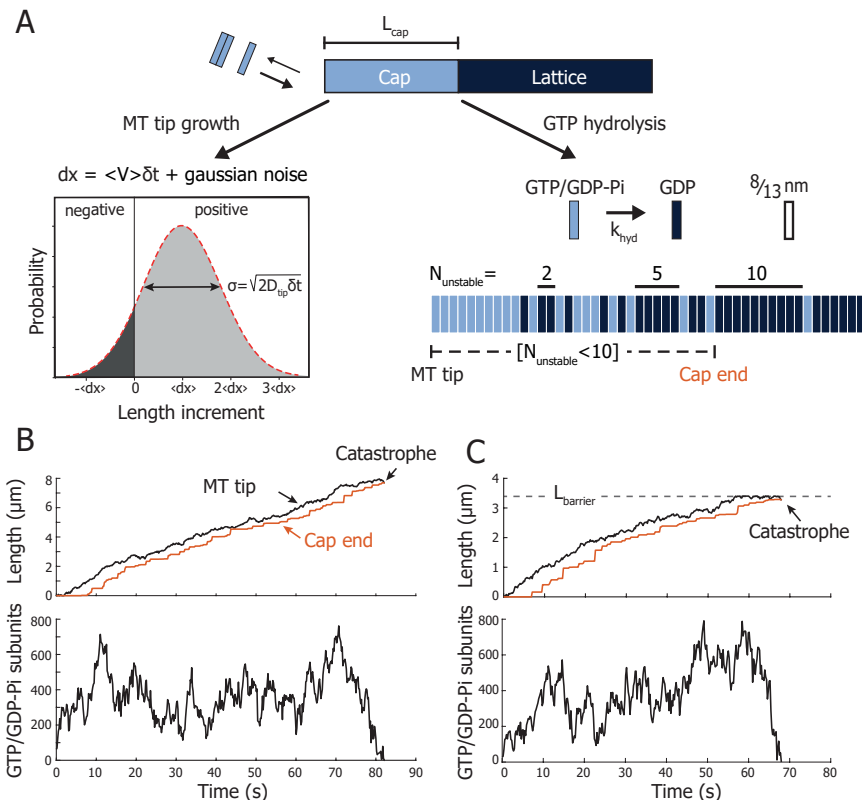


Figure 4.3: **Monte-Carlo simulation of microtubule dynamics**

(A) The microtubule is simulated as a one-dimensional lattice with two states, a GTP/GDP-Pi and a GDP state, constituting a cap and lattice region respectively. Microtubule growth is determined by the mean growth speed with added Gaussian noise, resulting in stochastic tip elongation following a biased random walk. Uncoupled stochastic hydrolysis matures the GTP/GDP-Pi-state into the GDP-state with rate  $k_{hyd}$ . The hydrolysis front, i.e. the border between the lattice and the cap, is set by a minimal number of consecutive GDP-state subunits, defined as  $N_{unstable}$ . The cap is thus the terminal region with fewer than  $N_{unstable}$  GDP subunits.

(B) Simulated microtubule growing event. (top) During the noisy microtubule growth, the hydrolysis front and the microtubule tip fluctuate over time. When the size of the cap is reduced to zero, i.e. when the number of consecutive terminal GDP subunits equals  $N_{unstable}$ , a catastrophe follows, and the simulation is terminated. (bottom) Total number of GTP/GDP-Pi subunits for the simulated microtubule enables a qualitative comparison with experimental data of the EB comet size. Any EB binding kinetics is omitted.

(C) Simulated stalling microtubule length (top) and GTP/GDP-Pi subunit content (bottom). Barrier contact is defined by restricting the maximum length of the microtubule to  $L_{barrier}$ . Upon reaching the barrier, the microtubule can fluctuate before a catastrophe is triggered.

to GDP transition (Kim, 2018; Maurer et al., 2014). We saw this justified by the fact that our key observations changed only very moderately when the first transition was included explicitly, adding to a further reduction of the number of necessary model parameters. Simulated microtubules grow by the addition of GTP/GDP-Pi subunits

which subsequently undergo random hydrolysis to GDP with a rate  $k_{hyd}$  (Fig. 4.3A, right). We treat microtubule growth as a discrete, biased Gaussian random walk (Antal et al., 2007; Flyvbjerg et al., 1996), inspired by experimental observations that revealed a substantial diffusive character of the growing microtubule tip (Gardner et al., 2011; Kersemakers et al., 2006; Rickman et al., 2017; Schek et al., 2007). Following this model, tip growth is fully characterized by the experimentally measured mean growth speed  $\langle V \rangle$  and the diffusion constant  $D_{tip}$  (Fig. 4.3A, left). The length of the cap is determined by the microtubule tip and the transition between the cap and lattice. The latter is positioned at the location defined by the fitting parameter  $N_{unstable}$ , which is the number of uninterrupted GDP subunits required to destabilize the microtubule tip. A catastrophe is triggered when the length of the cap is reduced to zero due to random hydrolysis and noisy growth, i.e. the moment at which the number of uninterrupted GDP subunits at the tip is equal or greater than  $N_{unstable}$  (Fig. 4.3B, top). Depolymerization and rescues are not considered in the model. The simulation thus only requires the three fitting parameters  $k_{hyd}$ ,  $D_{tip}$ , and  $N_{unstable}$ , all of which can be verified with experimental data. The experimental EB3 intensity at the microtubule tip is compared to the total number of GTP-state subunits within the simulated microtubule (Fig. 4.3B, bottom).

Microtubule stalling is simulated by introducing a fixed maximum length  $L_{barrier}$  (Fig. 4.3C). Any growth event that would bring the microtubule length to  $L > L_{barrier}$  is truncated to this maximum length. Since tip fluctuations include a non-zero probability for moderate negative growth (Fig. 4.3A, left), fluctuations of the tip position continue after barrier contact (Fig. 4.3C).

#### 4.2.4. DETERMINING THE CATASTROPHE THRESHOLD

Our 1D model relies on three fitting parameters,  $D_{tip}$ ,  $k_{hyd}$ , and  $N_{unstable}$ . We obtained the values of the mean growth speed  $\langle V \rangle$  for each EB3 concentration and the global median seed-barrier distance  $L_{barrier}$  from the experimental data (Fig. 4.4A,B). Based on existing literature (Maurer et al., 2014), we expected that adding EB3 would affect the transition from GTP/GDP-Pi to GDP state, i.e.  $k_{hyd}$  in our simulations. We hypothesized that growing microtubules can display different diffusive tip growth at different EB concentrations. It hence appeared reasonable to keep  $D_{tip}$  and  $k_{hyd}$  as free fitting parameters, and  $N_{unstable}$  as a global fitting parameter of which we expect it to be largely independent of the presence of EB3.

To find good fitting values, we performed systematic parameter scans across a range of  $D_{tip}$  and  $k_{hyd}$ , simulating 500 microtubule growth events for each parameter combination. We simulated both freely growing microtubules and stalling microtubules, and compared the distributions with the respective experimental distributions. Using a Kolmogorov-Smirnov test as a measure of the similarity between the simulated and experimental distribution, we obtained heatmaps with similarity parameters  $P_1$  and  $P_2$  (Fig. 4.4C). The parameter set best capturing both distributions was then found by calculating  $P_1 \cdot P_2$  (Fig. 4.4A,B and S2).

Our analysis indeed corroborates the independence of  $N_{unstable}$  as we could find simultaneous fits of  $D_{tip}$  and  $k_{hyd}$  that are in excellent agreement with our experimental observations across a wide range of  $N_{unstable}$  values. To determine an ideal

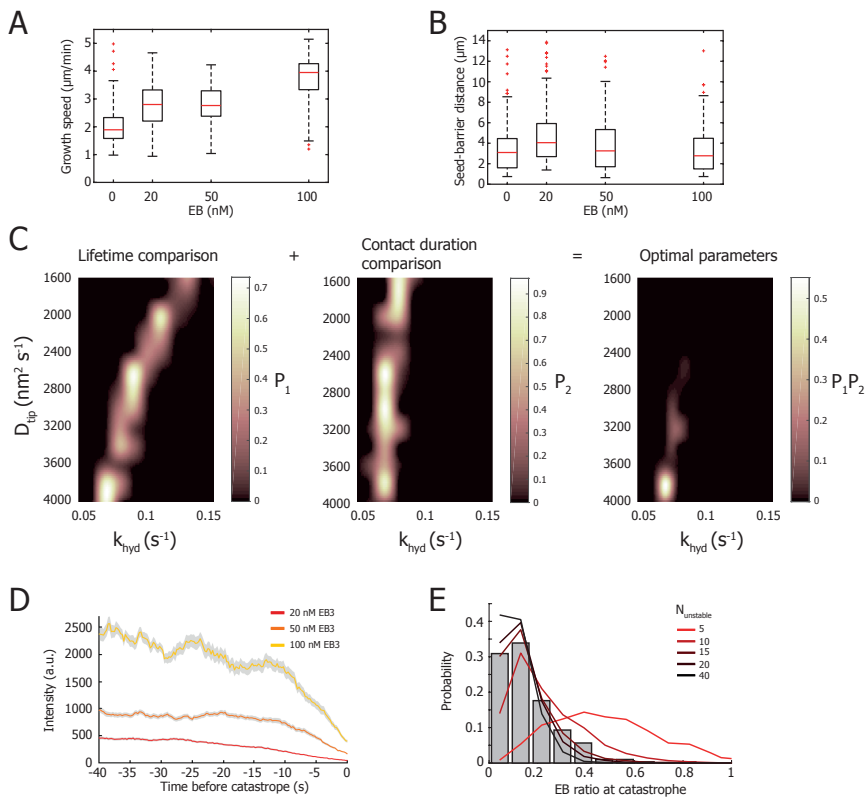


Figure 4.4: **Parameter determination of 1D model.**

(A) The growth speed of freely growing microtubules. For the conditions 0, 20, 50, and 100 nM EB3, growth speeds of 1.68, 2.79, 2.79, and 3.72  $\mu\text{m min}^{-1}$  respectively were obtained and used for the simulation. Red lines indicate the median value and whiskers correspond to a sigma of 2.7.

(B) The distance between the microtubule seed and the barrier. For the simulation a constant distance of 3.4  $\mu\text{m}$  was used for all conditions. Red lines indicate the median value and whiskers correspond to a sigma of 2.7.

(C) The diffusion constant  $D_{tip}$  and hydrolysis rate  $k_{hyd}$  are determined by comparing the simulated microtubule lifetime distributions and contact duration distributions for different parameter combinations with the experimental distributions. From a Kolmogorov-Smirnov test, the statistical similarity values  $P_1$  and  $P_2$  are determined. Evaluating  $P_1 \cdot P_2$  results in a parameter pair best describing both datasets. The shown heatmaps are of experiments with 0 nM EB3. For more details on all fits, see also Fig. S2.

(D) The mean experimental EB3 comet decay during barrier contact, aligned on the moment of catastrophe. The ratio between the steady-state comet intensity prior to contact (from -30 to -15 seconds) and the moment of catastrophe is used to compare to the simulated data. The shaded regions denote the SEM.

(E) Histogram of the combined distributions for 20, 50 and 100 nM of the EB3 ratio between the mean comet intensity during steady-state growth and the comet intensity at the moment of catastrophe. The lines show the simulated EB ratio for  $N_{unstable}$  values of 5, 10, 15, 20, and 40. From this comparison, we obtain a minimum  $N_{unstable}$  of 15 for all simulation conditions.

value for  $N_{unstable}$  to match our data, we focussed on two related experimental observations. Firstly, the EB3 comet decay at the barrier which we expected to be related to  $k_{hyd}$  (Fig. 4.2D). And secondly the ratio between the mean EB3 signal during steady-state growth  $\langle EB \rangle$  and the EB3 signal at the moment of catastrophe  $EB_{cat}$ , as this would also give us a measure of the hydrolysed fraction GTP/GDP-Pi subunits before a catastrophe occurred (Fig. 4.4D and S3). Comparing the combined distributions of the EB3 ratios with simulated ratios for several  $N_{unstable}$  values results in a minimum  $N_{unstable}$  value of  $\sim 15$  subunits (Fig. 4.4E).

#### 4.2.5. BOTH GTP HYDROLYSIS AND TIP FLUCTUATIONS DETERMINE STALLING DURATION

Figures 4.5A and 4.5B show the experimental cumulative fraction of the lifetimes of freely growing microtubules and of the stalling duration respectively (bold lines), in the presence of 15  $\mu\text{M}$  tubulin and 0, 20, 50, and 100 nM GFP-EB3. The distribution of free lifetimes comprises microtubules growing parallel to the barriers. By bootstrapping each simulated distribution obtained with the parameters in Fig. 4.5C, we show 25 simulated traces of equal datapoints as the experimental dataset. The variability in the simulated distributions provides a good visual reference of the similarity between experiment and simulation (Fig. 4.5A,B and S2). The distributions show that an increasing concentration of EB3 decreases the contact duration. In the absence of EB3 the contact duration is  $30.8 \pm 1.3$  seconds (median  $\pm$  SE), whereas in the presence of 20, 50, and 100 nM GFP-EB3 the contact duration is reduced to respectively  $13.8 \pm 0.7$ ,  $9.1 \pm 0.8$ , and  $4.1 \pm 0.3$  seconds (median  $\pm$  SE). The simulated distributions capture the data well and show that both free microtubule lifetimes and microtubule stalling can indeed be captured with a 1D model comprising three parameters (Fig. 4.5A,B and S4A). The decay rate of GTP subunits during stalling matches the experimental dataset (Fig. 4.5D and 4.2D), although the simulated decay is higher for 100 nM EB3. The simulated barrier contact events also show a similar noisy comet intensity (Fig. 4.5D and S3). In addition to an increase in hydrolysis, a decrease in tip fluctuations is required to capture the experimental distributions in the presence of 100 nM EB3 (Fig. 4.5C).

#### 4.2.6. SIMULATING TUBULIN WASHOUT

Recent experiments using microfluidics assisted washout of tubulin *in vitro* have shown that a minimal stable cap has a length of 10 tubulin layers at most, of which 15-30% dimers are still unhydrolysed (Duellberg et al., 2016). The observed delay between tubulin washout and microtubule catastrophe is reported to be  $\sim 7$  seconds and shown to depend on the pre-washout growth speed (Duellberg et al., 2016; Walker et al., 1991). To verify the ability of our model to describe tubulin washout experiments and compare the difference with stalling microtubules, we simulated tubulin washout with our obtained parameter set (Fig. 4.5C). To simulate washout, we prohibit any growth of the microtubule tip, but still allow microtubules to undergo negative growth (Fig. 4.3A). To compare our results to published washout parameters (20  $\mu\text{M}$  tubulin with 0 and 200 nM of Mal3) (Duellberg et al., 2016), we simulate tubulin washout for 15  $\mu\text{M}$  tubulin in the presence of 0 and 20 nM EB3, resulting in a comparable growth speed and hydrolysis rate. The difference between the concentration of Mal3 (fission yeast homologue

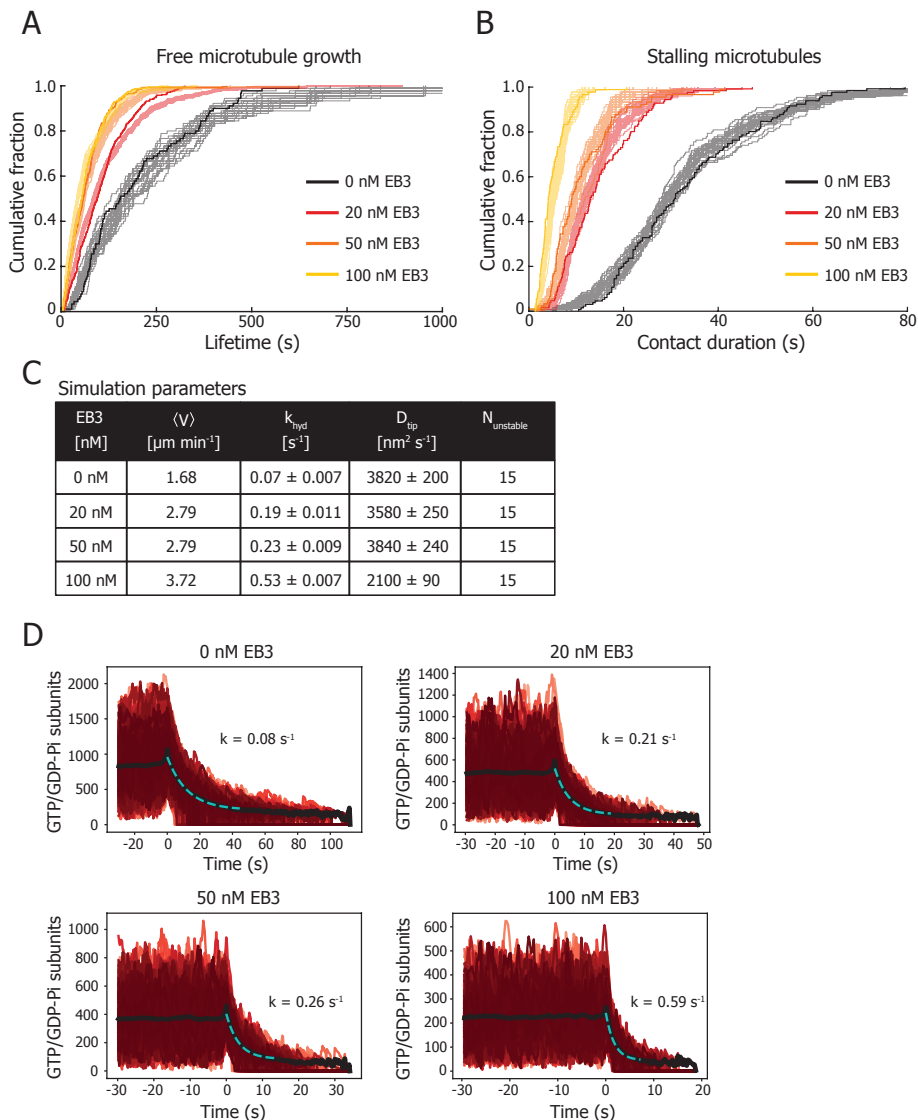


Figure 4.5: **Free microtubule growth and microtubule stalling.**

(A) The cumulative fraction of the lifetimes of freely growing microtubules at increasing concentrations of 0 nM ( $n=90$ ), 20 nM ( $n=384$ ), 50 nM ( $n=262$ ), and 100 nM ( $n=398$ ). All data was obtained with  $15 \mu\text{M}$  tubulin. The bold lines show the experimental data and the thin lines show 25 bootstrapped simulated distribution of equal number of datapoints as the experimental distribution.

(B) The cumulative fraction of the microtubule-barrier contact durations shows that increasing concentrations of 0 nM ( $n=131$ ), 20 nM ( $n=126$ ), 50 nM ( $n=90$ ), and 100 nM ( $n=90$ ) GFP-EB3 decrease the contact duration. All data was obtained with  $15 \mu\text{M}$  tubulin. The bold lines show the experimental data and the thin lines show 25 bootstrapped simulated distribution of equal number of datapoints as the experimental distribution.

(C) Table with the mean growth speed  $\langle V \rangle$ , hydrolysis rate  $k_{hyd}$  (mean  $\pm$  95% CI), diffusion constant  $D_{tip}$  (mean  $\pm$  95% CI), and  $N_{unstable}$  as determined to simulate the lifetimes of freely growing microtubules and the contact duration of stalling microtubules at each EB concentration. The relative goodness of fit can be assessed from the Kolmogorov-Smirnov test score  $P_1 \cdot P_2$ .

(D) Simulated decay of GTP/GDP-Pi subunits during microtubule stalling. Each dataset contains 1500 simulated events.

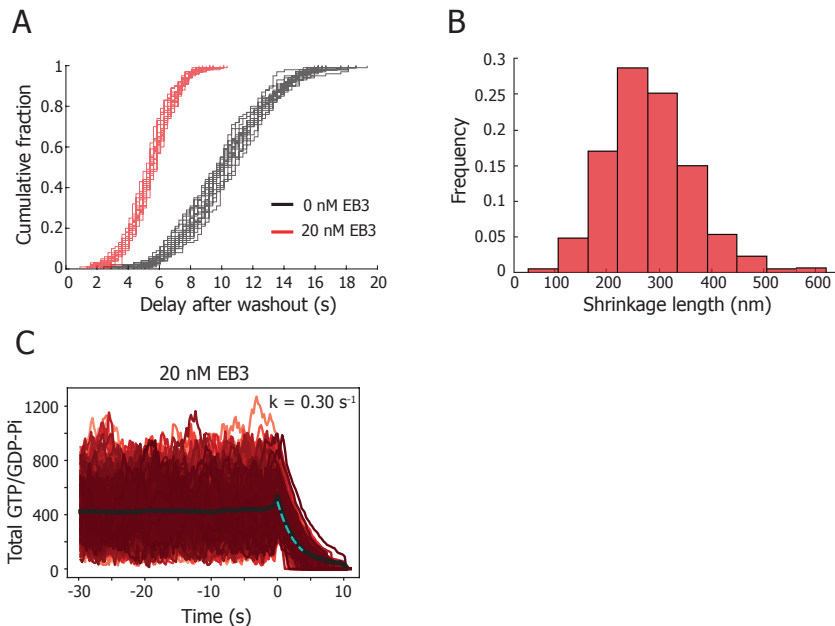


Figure 4.6: **Simulating tubulin washout.**

(A) Simulation of tubulin washout following the parameters in Fig. 4.5C for 0 and 20 nM EB3. For both conditions, 25 bootstrapped distributions of 100 datapoints are shown. The mean delay duration between washout and catastrophe is  $10.3 \pm 3.2$  and  $5.5 \pm 1.8$  seconds for 0 and 20 nM EB3 respectively (mean  $\pm$  std).

(B) Simulation of tubulin washout following the parameters in Fig. 4.5C 20 nM EB3. The mean shrinkage length of the microtubule between washout and catastrophe is  $253 \pm 71$  nm (mean  $\pm$  std).

(C) Simulation of the comet decay during tubulin washout following the parameters in Fig. 4.5C for 20 nM EB3.

of EB1) and EB3 required to obtain a similar hydrolysis rate can be explained by the intrinsic structural differences (Roth et al., 2018; von Loeffelholz et al., 2017). Our simulation of tubulin washout showed a delay between washout and catastrophe of  $10.2 \pm 3.2$  and  $5.5 \pm 1.8$  seconds (mean  $\pm$  std) for 0 and 20 nM EB3 (Fig. 4.6A), similar to the reported values of 7.3 and 3.5 seconds for 0 and 200 nM Mal3 (Duellberg et al., 2016). During the delay, we measured a slow shrinkage of the microtubule tip length during washout and catastrophe of  $253 \pm 71$  nm (mean  $\pm$  std) for 20 nM EB3 (Fig. 4.6B), comparable to the reported  $165 \pm 105$  nm (Duellberg et al., 2016). Furthermore, we find that the simulated decay rate of  $0.30 \text{ s}^{-1}$  (20 nM EB3) of GTP/GDP-Pi subunits from the moment of tubulin washout is in agreement with the reported  $0.33 \text{ s}^{-1}$  (200 nM Mal3) (Fig. 4.6C). We conclude that our model is thus capable of accurately capturing tubulin washout.

### 4.3. DISCUSSION

Microtubules interacting with cellular components such as the cell cortex have an increased probability to undergo a catastrophe during contact, thereby contributing to the regulation of the microtubule network (Gregorette et al., 2006; Letort et al., 2016). To understand microtubule stability and the resulting lifetimes during contact, we investigated the effect of the plus-end tracking protein EB3 on the stability of stalled microtubules both *in vitro* and *in silico*. Using novel micro-fabricated barriers in conjunction with TIRF microscopy, we studied the duration of contact and the size of the stabilizing cap during microtubule stalling. We confirm that stalled microtubules undergo a catastrophe after  $30.8 \pm 1.3$  seconds (median  $\pm$  SE) in the absence of EB3, comparable to previously measured values (Fig 4.6B) (Janson et al., 2003). In addition, the presence of EB3 significantly further reduces the stability in a concentration dependent manner which results in up to seven times shorter residence times at the barriers (Fig 4.5A,B and S4A), in agreement with earlier observations of stalling microtubules in the presence of Mal3 (Fig. S5). This is caused by both an increased cap decay and a smaller mean stabilizing cap during free steady-state growth. Conversely, in the absence of EB3, short contact events are lacking (Fig. 4.5B).

We find that microtubules can remain in a stalled state without the presence of an observable EB comet, suggesting that a stable microtubule does not necessarily require an observable comet. In our experimental setup, this could be a result of steric hindrance from the overhang, prohibiting the microtubule from depolymerising. Also, recent simulations investigating the onset of catastrophes using molecular-dynamics modelling of tubulin-tubulin interactions predict that microtubules without a stabilizing cap are metastable when the tip is blunt (Zakharov et al., 2015). It could well be that stalling microtubules adopt a blunt tip, effectively reducing fluctuating bend protofilaments (McIntosh et al., 2018), and could resemble a microtubule pausing state (Van Buren et al., 2005).

#### A 1D MODEL FULLY CAPTURES MICROTUBULE STALLING

Simulating the microtubule as a two-state system with random hydrolysis and noisy growth successfully describes the dynamic instability of both freely growing microtubules and stalling microtubules. Previously, this type of 1D model was incapable of describing the lifetimes of freely growing microtubules, because tubulin dissociation was hypothesized to be independent from the microtubule growth speed (Bowne-Anderson et al., 2013). This necessitated introducing lateral tubulin-tubulin interactions in a 2D model to accurately capture microtubule lifetimes (Gardner et al., 2011). Here, we showed that introducing a highly dynamic tip in a 1D model is sufficient to capture the microtubule lifetimes. As an additional verification of our model, we simulated microtubule lifetimes and stalling durations based on reported experimental data (Fig. 4.7) (Janson et al., 2003). Our model can simultaneously capture the reported mild catastrophe reduction with increasing growth speed as well as the distribution of stalling durations (Fig. 4.7A,B). Moreover, the required tip noise to do so at a fixed  $k_{hyd}$  of  $0.10 \text{ s}^{-1}$  is in line with the reported dependence of the tip noise on the growth speed (Fig. 4.7C) (Rickman et al., 2017). The absence of any force-coupling in our model suggests that it is not essential for explaining the experimental observa-

tions, although we cannot exclude that compressive forces play a role in the stability of stalling microtubules.

A feature of microtubule stability not present in our model is an age dependent catastrophe frequency. It has been reported that "younger" microtubules are more stable than "older" ones (Gardner et al., 2011). Two proposed processes responsible for inferring this property are based on a multi-step lattice defect model and on taper-

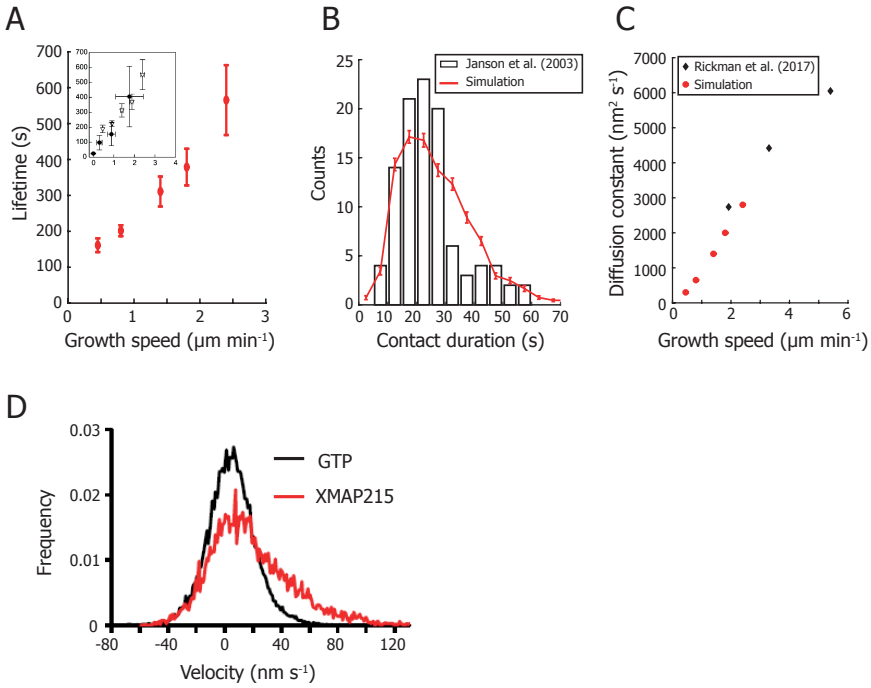


Figure 4.7: **Model evaluation.**

(A) Simulation of microtubule lifetimes for increasing growth speeds. The simulation growth speeds were obtained from (Janson et al., 2003) and combined with a global value for  $k_{hyd}$  of  $0.10 \text{ s}^{-1}$  and our  $N_{unstable}$  of 15. The insert shows the lifetimes for freely growing microtubules (triangles) and for buckling microtubules (dots) (Janson et al., 2003). Our model shows a similarly mild suppression of catastrophes with increasing tubulin concentrations, with the growth speeds of  $0.45, 0.8, 1.4, 1.8,$  and  $2.4 \mu\text{m min}^{-1}$  corresponding to tubulin concentrations of  $7.2$  ( $n=58$ ),  $10$  ( $n=152$ ),  $15.2$  ( $n=49$ ),  $20$  ( $n=51$ ), and  $28 \mu\text{M}$  ( $n=30$ ). Simulated lifetimes are given as mean  $\pm$  SEM with the same number of datapoints as the experimental values.

(B) Histogram of the pooled stalling duration with 103 events measured at  $15.2, 20,$  and  $28 \mu\text{M}$  from (Janson et al., 2003) and the simulated stalling duration. The simulated values represent mean  $\pm$  SD for  $n = 103$  events.

(C) The diffusion constant of the microtubule tip required to simulate the microtubule lifetimes in (A) based on data from (Janson et al., 2003). These values are in line with reported values by (Rickman et al., 2017).

(D) Growth speed fluctuations in the presence (red) and absence (black) of  $150 \text{ nM}$  XMAP215 obtained with optical tweezer experiments ( $20 \mu\text{M}$  tubulin). The addition of XMAP215 stretches the Gaussian noise towards higher growth speeds.

ing of the microtubule tip during growth (Bowne-Anderson et al., 2013; Chretien et al., 1995; Coombes et al., 2013; Duellberg et al., 2016; Mandelkow et al., 1991; VanBuren et al., 2005). We don't observe a clear effect of microtubule ageing in our lifetime or in contact duration distributions (Fig. 4.5A and S4B). Partly, ageing effects could be masked by the strong reduction in microtubule lifetime in the presence of EB3. However, even in the absence of EB3 our model is able to describe the experimental data well without relying on microtubule ageing. The fact that the model even reproduces the non-exponential lifetime distribution (Fig. 4.5A) is here not due to ageing, but simply due to the presence of a stable, non-hydrolysable seed.

In our simulations we observe that catastrophes often occur as a combination of two destabilizing, random events. One is a short period of locally faster hydrolysis (momentarily reducing the size of the stabilizing cap). The second event is a short period of slowed down growth or even shrinkage. For freely growing microtubules both events have a low joint probability of occurring. By stalling microtubules (here at a physical barrier) and hence forcing them into a permanent slow growth regime, the probability of a catastrophe to occur is increased, in our case by a factor of  $\sim 7$ .

### THE THRESHOLD FOR A CATASTROPHE

To determine the required size of the GTP/GDP-Pi cap for stable microtubule growth, we measured the ratio between the EB3 comet intensity at the moment of catastrophe and the mean EB3 comet intensity during steady-state growth. In addition, we evaluated the decay rates of EB3 comets after initial barrier contact. A lower  $N_{unstable}$  resulted in a smaller cap that quickly becomes unstable when GTP/GDP-Pi subunits transition to GDP subunits. To match simulations and experimental data, the hydrolysis rate would need to be comparably slow. At high  $N_{unstable}$  values the end of the stable cap would be positioned far behind the initial GTP/GDP-Pi to GDP transitions, and a faster hydrolysis had to be assumed to explain our data. Both measures converge on a catastrophe threshold  $N_{unstable}$  of  $\sim 15$  uninterrupted hydrolysed terminal subunits, which would approximate a single tubulin layer at the microtubule tip. The notion that the stabilizing cap is large on average, but that only a short stretch of hydrolysed subunits at the microtubule tip is required to trigger a catastrophe, combines short and long cap observations (Brun et al., 2009; Duellberg et al., 2016; Molodtsov et al., 2005; Seetapun et al., 2012; Walker et al., 1991). We thus find that the onset of a catastrophe does not primarily depend on the size of the observed EB comet, but instead on the underlying distribution of hydrolysed subunits at the microtubule tip. In this sense, the EB comet can rather be seen as a signature of the underlying hydrolysis distribution.

### MICROTUBULE GROWTH FLUCTUATIONS

Our model relies on fluctuations of the microtubule tip as a key parameter for describing experimental dynamic instability. It has previously been reported that microtubules undergo substantial fluctuations at the tip with diffusion constants of  $\sim 4400 \text{ nm}^2 \text{ s}^{-1}$  for  $20 \mu\text{M}$  tubulin (Rickman et al., 2017),  $\sim 3000 \text{ nm}^2 \text{ s}^{-1}$  for  $12 \mu\text{M}$  tubulin (Gardner et al., 2011), both in good agreement with our fitted  $D_{tip}$  values (Fig. 4.5C). Additionally, our model requires that the size of the fluctuations decreases in the presence

of 100 nM EB3. This effect would support the hypothesis that the increase in growth speed from the presence of EB3 is the result of a lower tubulin dissociation rate at the microtubule tip. If we assume that the tubulin association rate only depends on the soluble tubulin concentration and is therefore not affected by EB3, we would expect the resulting tip noise  $D_{tip}$  to be smaller. This effect could originate from EB3 binding in between protofilaments and reducing tip fluctuations.

A possible extension of our 1D model to describe the effect of +TIPs could be to characterize them phenomenologically by their effect on GTP hydrolysis and tip fluctuations. As the effect of EB3 can be described this way, we hypothesize that the effect of XMAP215, a microtubule growth promoting +TIP, can be characterized similarly. Earlier observations of microtubule growth obtained with optical tweezers, shows the effect of XMAP215 on microtubule tip fluctuations (Fig 4.7D) (Kersemakers et al., 2006). The biased Gaussian random walk that describes polymerization in the absence of XMAP215 is skewed to higher growth speeds in its presence. To allow future extensions and modifications of our model, we will make our entire source code available under an open source licence and provide extra documentation.

4

### OUR MODEL SUCCESSFULLY DESCRIBES TUBULIN WASHOUT

We showed that tubulin washout can be captured with our model and reproduces a similar catastrophe delay, tip shrinkage, and comet decay as reported (Fig. 4.6)). The reported finding that a microtubule requires a stable cap of  $\sim 10$  tubulin layers at most (Duellberg et al., 2016) is not at odds with our finding that a catastrophe is triggered when the terminal layer of tubulin is hydrolysed. Because the former result is based on the average remaining density of Mal3 at the moment of catastrophe after tubulin washout, it does not inform on a specific catastrophe criterium. We thus conclude that our model can describe tubulin washout and simulate values in good agreement with experiments. The longer catastrophe delay observed with microtubule stalling compared to tubulin washout can be explained by the replenishment of hydrolysed dimers at the microtubule tip due to continuous tip fluctuations. The absence of tubulin after dilution removes this stabilizing effect.

### OUTLOOK

The stability of microtubules interacting with cellular components has been studied in the context of cortical contact (Aher et al., 2018; Bouchet et al., 2016; Chi and Ambrose, 2016; Komarova et al., 2002), spindle positioning (Guild et al., 2017; Laan et al., 2012; Letort et al., 2016; Vleugel et al., 2016), and microtubule organization (Cassimeris et al., 2018; Gregoretto et al., 2006; Zelinski et al., 2012). Here, we extend the knowledge about the stalling process of microtubules by combining experiments and simulations. Our experimental setup will be useful for studying microtubule interactions and the functional effect of stabilizing and destabilizing microtubule associated proteins. Our approach can be used to study the influence of MAPs, tubulin isoforms and PTMs (Sirajuddin et al., 2014) on the stability of pushing microtubules. Furthermore, the SiC overhangs are designed to be compatible with a previously published method to specifically functionalize the barriers with protein complexes (Taberner et al., 2014), enabling the study of end-on interactions.

We developed a coarse-grained model that can capture a very rich set of experimental data on dynamic microtubules. Its sole dependence to tip noise and random hydrolysis makes it possible to build an intuition of key processes in microtubule dynamics. It can capture microtubule lifetimes for a range of tubulin concentrations, cap dynamics during microtubule stalling, and the delay and tip shrinkage after tubulin dilution. The model could be further extended to study the effect of various MAPs and quickly capture their effect on tip noise and GTP hydrolysis.

## 4.4. EXPERIMENTAL METHODS

### PROTEINS

GFP-EB3 was a kind gift from Michel Steinmetz. All tubulin products were acquired from Cytoskeleton Inc, with all unlabelled tubulin specifically from a single lot.

### MICROFACRICATION OF BARRIERS

The fabrication method for the micro-fabricated barriers with an SiC overhang is inspired by (Kalisch et al., 2011; Taberner et al., 2014; Aher et al., 2018). All fabrication steps were performed in a cleanroom environment (van Leeuwenhoek Laboratory, NanoLab NL). The barrier was designed with the following considerations in mind:

- The width of the channels should favour stalling event over buckling events, but remain large enough for GMPCPP-stabilized seeds to easily land.
- A bottom layer of SiC is needed to prevent etching into the coverslip during a Buffered Oxide Etch. This layer needs to be as thin as possible to prevent photon absorption by the semiconductor resulting in a diminished signal-to-noise and surface heating. Using PE-CVD, 10 nm is thinnest layer we could fabricate while still maintaining the layer's integrity to protect the coverslip from the Buffered Oxide Etch.
- The layer of SiO<sub>2</sub> of 100 nm ensures that the microtubule can polymerize underneath the overhang while remaining inside the evanescent wave.
- The top layer of SiC is 250 nm thick to ensure mechanical stability, while still allowing to observe microtubules growing on top of the barrier despite some photon absorption.

To start, glass coverslips (24x24 mm, #1) were cleaned for 10 min with base piranha, a mixture of H<sub>2</sub>O : NH<sub>4</sub>OH : H<sub>2</sub>O<sub>2</sub> in a 5:1:1 ratio heated to 70°C. Then, three sequential layers of SiC (10 nm), SiO<sub>2</sub> (100 nm), and SiC (250 nm) are deposited on the cleaned surface via Plasma-Enhanced Chemical Vapour Deposition (PE-CVD) at 300°C (Oxford Instruments PlasmaPro 80). PE-CVD ensures a surface smooth enough for TIRF microscopy with fast deposition rates (70 nm/min for SiO<sub>2</sub> and 40 nm/min for SiC).

In order to transfer the barrier pattern to the surface, UV lithography is used. First, to aid in the adhesion of the photoresist, a few drops of hexamethyldisilazane (HMDS)

are spin coated on the SiC surface and allowed to dry on a 115°C hotplate for 30 seconds. Then a 1.3 µm layer of the positive photoresist S1813 (MicroChem) is spin coated (5000 rpm) on the surface and pre-baked for 90 seconds on a 115°C hotplate. Exposure of the photoresist through a chromium mask with a near-UV source (320-365 nm, approx. 13 mW/cm<sup>2</sup>) transfers the barrier pattern in 4 seconds (EVgroup EVG 620). Development with MF321 (MicroPosit) for 60 seconds removes the UV-exposed regions of the resist.

Next, Reactive Ion Etching (Leybold Hereaus) with a mixture of CHF<sub>3</sub> : O<sub>2</sub> (50 sccm:2.5 sccm) etches through the exposed regions of the 250 nm SiC layer and into the SiO<sub>2</sub> layer. The etch is performed at 50 µbar and at 50W, resulting in a bias voltage of 400 V. It is important to etch completely through the top SiC layer, but only partly through the SiO<sub>2</sub> layer, to leave the bottom SiC layer intact. Any remaining photoresist after the etch is removed by sonication of the sample in acetone for 10 minutes.

Finally, the sample is submerged in buffered hydrofluoric acid (HF : NH<sub>4</sub>F = 12.5 : 87.5%) to selectively etch the exposed SiO<sub>2</sub> with a rate of approximately 200 nm/min to obtain an overhang of 1.5 µm. The final barriers are 100 nm high with an overhang of 1.5 µm, enclosing channels with a width of 15 µm.

4

### *In vitro* MICROTUBULE DYNAMICS ASSAY

Reconstitution of microtubule dynamics was performed as previously described in (Bieling et al., 2007; Montenegro Gouveia et al., 2010). After cleaning the barrier sample with O<sub>2</sub>-plasma, a flow channel was constructed with a cleaned glass slide and double-sided sticky tape in such a way that the channel direction is perpendicular to the barriers. Then, the surface was consecutively functionalized with 0.5 mg/ml PLL-PEG-biotin(20%) (SuSoS AG, Switzerland), 0.2 mg/ml NeutrAvidin (Invitrogen), and 0.5 mg/ml κ-casein (Sigma). All components were kept in MRB80 buffer, comprised of 80mM piperazine-N,N'-bis(2-ethanesulfonic acid), 4 mM MgCl<sub>2</sub>, and 1 mM EGTA at a pH of 6.8. The reaction mixture contained 15 µM tubulin (7% rhodamine labelled) in the presence of GFP-EB3 or Hilyte488 labelled tubulin in the absence of GFP-EB3, and was supplemented with 0.5 mg/ml κ-casein, 0.15% methylcellulose, 50 mM KCl, 1 mM GTP, oxygen scavenger mix (4 mM DTT, 200 µg/ml catalase, 400 µg/ml glucose oxidase, 50 mM glucose). The reaction mix is then centrifuged in an Airfuge (Beckman Coulter) at 30psi for 8 minutes to remove any aggregated complexes before being introduced to the sample. GMPCPP-stabilized seeds (70% unlabelled tubulin, 18% biotinylated tubulin, 12% rhodamine-labelled tubulin) were introduced to the channel with the flow direction perpendicular to the barriers. Flow cells were sealed with vacuum grease and imaged on a TIRF microscope at between 28 and 30°C.

### TIRF MICROSCOPY

All experiments were imaged using TIRF microscopy, consisting of a Ilas<sup>2</sup> system (Roper Scientific) on a Nikon Ti-E inverted microscope. The Ilas<sup>2</sup> system is a dual illuminator for azimuthal spinning TIRF illumination equipped with a 150 mW 488 nm laser, a 100 mW 561 nm laser, and a ZT405/488/561/640rpc dichroic mirror. Simultaneous dual-acquisition was performed with two Evolve 512 EMCCD camera's (Photometrics) through a 525/50 nm and a 609/54 nm emission filter, using a Nikon CFI Plan Apoc-

hromat 100XH NA1.45 TIRF oil objective. Together with an additional magnifying lens, the final magnification resulted in a pixel size of 107 nm/pixel. The sample was heated with a custom objective heater to 28-30°C and was kept in focus with the Nikon Perfect Focus system. The hardware was controlled with MetaMorph 7.8.8.0 (Molecular Device).

### IMAGE TREATMENT

The image stacks obtained with TIRF microscopy were corrected prior to data analysis. First, simultaneous acquisition of rhodamine-labelled tubulin and GFP-EB3 on two cameras introduced a non-linear spatial offset between the two image stacks due to imperfections in the dichroic mirror and in the alignment of the two cameras. By scanning multiple FOVs of a calibration slide containing 100 nm TetraSpeck beads (ThermoFisher) and automatically locating the centroids through a custom written MATLAB script, a non-linear registration profile accounting for the spatial offset was obtained. The misaligned image stack was corrected by applying this registration profile based on the position of ~500 bead positions. Additionally, any sample drift was corrected by subpixel image registration through cross-correlation (Guizar-Sicairos et al., 2008).

Secondly, some scattering of excitation light at the edge of the SiC overhang made proper determination of the EB3-GFP signal near the barrier difficult. Although this effect was mostly mediated by creating a wide undercut that physically separated the overhang from the barrier, a correction was nonetheless applied. To remove the signal, the minimum intensity value of each pixel in the image stack was subtracted from that pixel in each image. This correction enabled tracking of the EB3 comet near the barrier and accurate measurement of the EB3 comet intensity.

Thirdly, a general background subtraction was performed in Fiji (Schindelin et al., 2012) to correct for inhomogeneous illumination.

### IMAGE ANALYSIS

Analysis of the images was partly performed with Fiji and partly in MATLAB. After image treatment, kymographs were created by drawing straight lines of 9 pixel width (0.95  $\mu\text{m}$ ) along growing MTs using KymoResliceWide plugin with maximum transverse intensity (<http://fiji.sc/KymoResliceWide>). Each growth event in the kymographs was manually traced to determine the position of the MT end. This position was then used to fit the EB3 comet to obtain the precise position and intensity, using the profile:

$$I(x) = I_A \cdot \exp\left(-\frac{(x - x_c)^2}{\sigma^2}\right) + I_{BKG}$$

where  $I(x)$  is the fluorescence intensity,  $I_{BKG}$  is the background intensity,  $I_A$  is the intensity amplitude,  $x_c$  is the position of the peak of the EB3 comet, and  $\sigma$  is the width of the EB3 comet. As the EB3 comet decays at the barrier and fitting is not possible, the intensity during contact was determined by calculating the average intensity value in a region around the comet position and around the barrier (Fig. S1). Subsequently, the barrier contact duration and the comet decay duration were determined manually.

## MONTE CARLO SIMULATION

Simulations of growing microtubules were run as a series of discrete, fixed time-steps. The length of the time steps  $\delta t$  was chosen small enough to properly account for the random hydrolysis of the subunits ( $P_{hyd}$ , the probability for a dimer to undergo hydrolysis within one time step was kept at  $<0.05$ ). Further restrictions were to not exceed the desired frame rate, in our case the lowest used experimental frame rate of 250 ms. Due to the discrete nature microtubule growth in subunits, it was then chosen for the next-lowest time-step for which  $\langle V \rangle \frac{\delta t}{L_0}$  became an integer, with  $L_0 = \frac{8}{13} nm$  the length increment per subunit and  $\langle V \rangle$  the microtubule mean growth speed.

Each microtubule simulation started from a few initial subunits (a 'seed') that were excluded from hydrolysis, and that were not allowed to be removed during microtubule tip fluctuations. Microtubule growth was simulated as a discrete, biased, Gaussian random walk. This means that for each time-step  $\delta t$ , the microtubule length was changed by a discretized random number of subunits that were drawn from a Gaussian distribution with standard deviation  $\sigma = \sqrt{2D_{tip}\delta t}$  and centred at  $\langle dx \rangle / L_0$ .

During each time step, subunits transition from the GTP/GDP-Pi to the GDP state by random hydrolysis with a rate  $k_{hyd}$ . Whenever the foremost uninterrupted strand of GDP state subunits ( $\geq N_{unstable}$  subunits in a row) is changed, the position of the end of the stable cap will jump to the front element of this strand, which we interpret as the new position of the end of the stable cap  $L_{end-of-cap}$ .

A simulation run ends when a catastrophe occurs. This happens when the stable cap shrinks to zero, i.e. if  $L_{tip} - L_{end-of-cap} = 0$ , where  $L_{tip}$  is defined as the position of the foremost subunit of the microtubule. The growth duration was defined as the time from initial growth until catastrophe.

The presence of a physical barrier is modelled by introducing a fixed barrier position  $L_{barrier}$ . Tip dynamics and random hydrolysis remained unchanged, only the microtubule length was truncated whenever it would penetrate the barrier. This means the length of the microtubule was set back to  $L_{barrier}$  if  $L_{tip} > L_{barrier}$ . The barrier contact time was then defined as the time from the microtubules first contact with the barrier until its catastrophe.

The simulation written in Python 3.6 and was run on standard PCs. The code to run the simulation will be made available under an open-license on GitHub after publication.

## AUTHOR CONTRIBUTIONS

M.K. designed the micro-fabricated barriers. M.K. fabricated the barriers, performed experiments with EB and analysed the data. SM.K. performed and analysed the experiments with Mal3. EH. wrote the code and ran the simulations. M.K, EH., and M.D. wrote the paper. M.D. coordinated the project.

## ACKNOWLEDGEMENTS

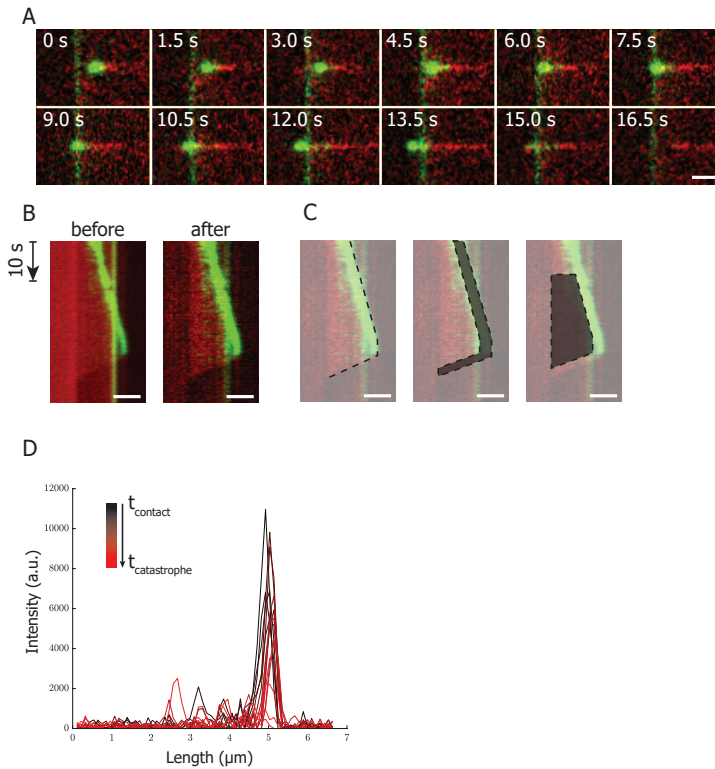
We thank M.O. Steinmetz for the gift of GFP-EB3 and the technicians of the van Leeuwenhoek Laboratory for their technical assistance in the fabrication of the barriers. We thank Vladimir Volkov and Louis Reese for critical reading of the manuscript. This

work was supported by the European Research Council Synergy grant 6098822 to Marileen Dogterom.

### **COMPETING FINANCIAL INTERESTS**

The authors declare no competing financial interests.

## Supplementary figure 1



4

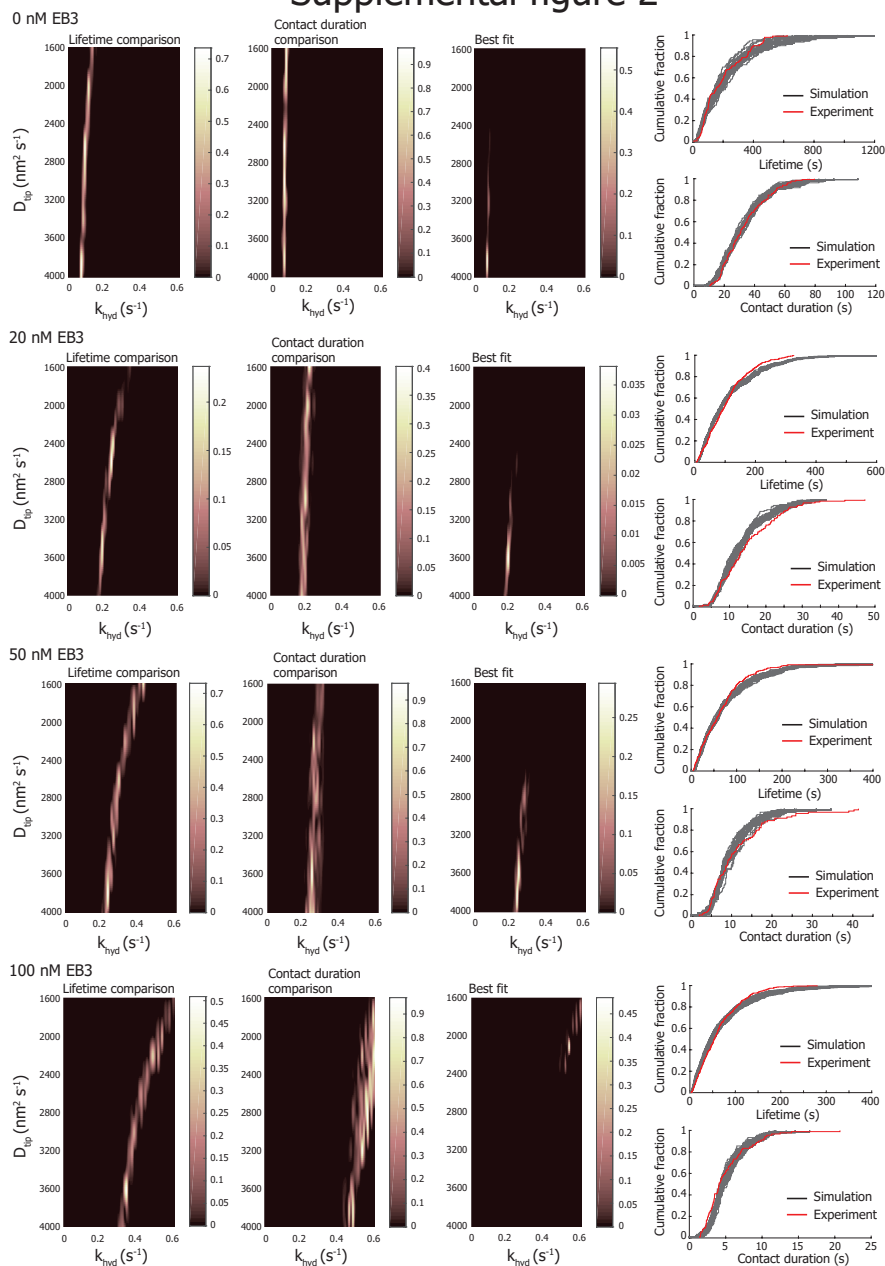
**(A)** Montage of a microtubule-barrier stalling event in the presence of 20nM EB3. During barrier contact microtubule polymerization halts, the EB3 signal at the plus end diminishes as GTP hydrolysis progresses, and a catastrophe event ensues. Scale bar denotes 5  $\mu\text{m}$ .

**(B)** In order to increase the signal to noise and remove the scattering at the edge of the overhang, a minimum projection of the stack is subtracted from each pixel. The kymographs show the data before and after correction of the event in **(A)**.

**(C)** Determination of the position of the microtubule tip is obtained by manual tracking (left). Due to the loss of the EB signal during stalling and insufficient signal-to-noise of the microtubule signal, automatic tracking is not possible. The intensity of the EB3 comet is obtained from a region surrounding the manual trace with a width of 10 pixels or 1,1  $\mu\text{m}$  (middle). The mean EB3 signal at the microtubule tip is corrected by the mean lattice intensity (right).

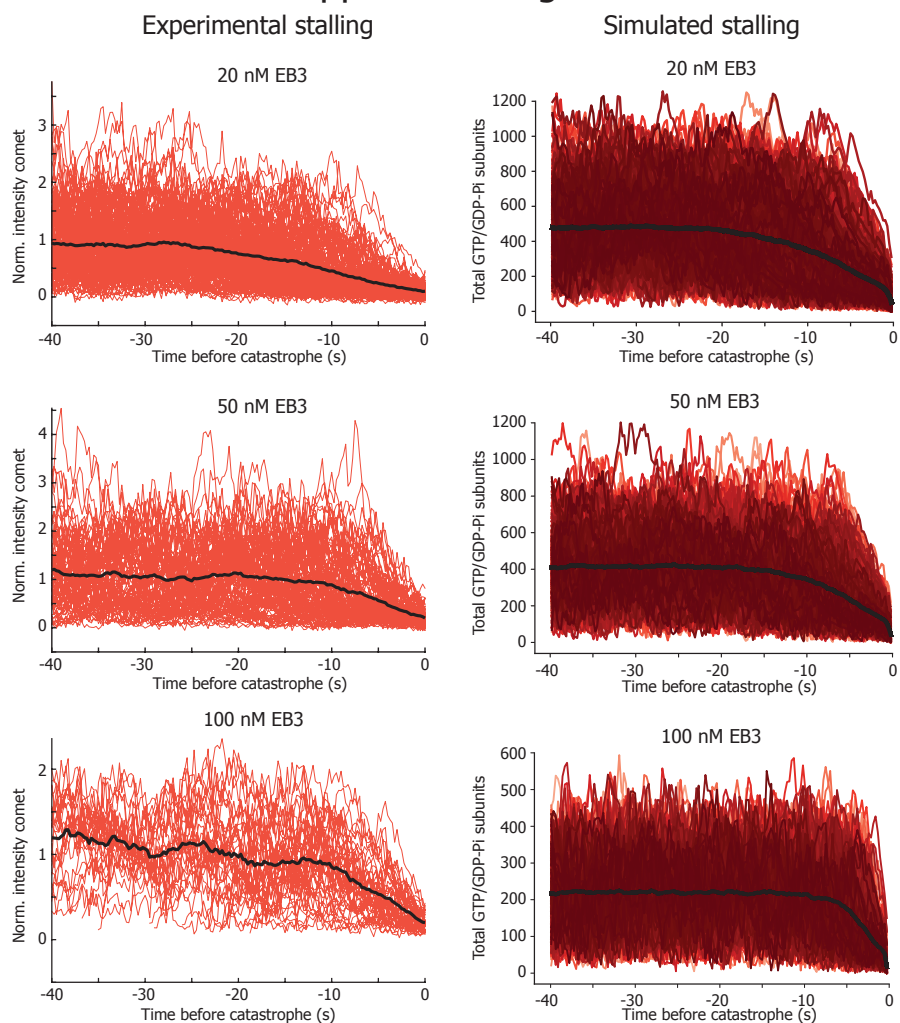
**(D)** EB3 comet decay during microtubule-barrier contact of the event in **(A)**. The total contact duration is 3.75 seconds.

## Supplemental figure 2



In order to compare the distributions of the experimental and simulated microtubule lifetimes and stalling durations, we perform a Kolmogorov-Smirnov test. By simulating 500 events of  $D_{tip}$  and  $k_{hyd}$  combinations for 0, 20, 50, and 100 nM EB3, we obtain heatmaps of similarity for microtubule lifetime distributions ( $P_1$ ) and stalling duration distributions ( $P_2$ ). To determine the parameter set best capturing both distributions, we calculate  $(P_1 \cdot P_2)$  and plot the experimental and 25 bootstrapped simulated distributions accordingly.

## Supplemental figure 3



(A) Individual and mean EB3 comet intensity traces of stalling microtubules aligned to the moment of catastrophe. The intensity is normalized with the mean of the steady-state EB3 comet intensity prior to barrier contact.

(B) Simulated traces of the number of GTP/GDP-Pi subunits aligned to the moment of catastrophe.

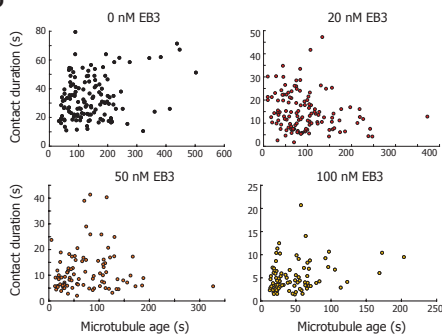
## Supplemental figure 4

A

[EB3]	Experiment		Simulation	
	Free	Stalling	Free	Stalling
0 nM	155 ± 15 s	30.8 ± 1.3 s	168 ± 9.2 s	29.5 ± 0.9 s
20 nM	94 ± 3.7 s	13.0 ± 0.7 s	84.5 ± 4.6 s	11.7 ± 0.4 s
50 nM	57 ± 3.5 s	9.1 ± 0.8 s	57.6 ± 3.1 s	8.7 ± 0.3 s
100 nM	54 ± 2.4 s	4.1 ± 0.3 s	47.6 ± 1.8 s	4.7 ± 0.2 s

4

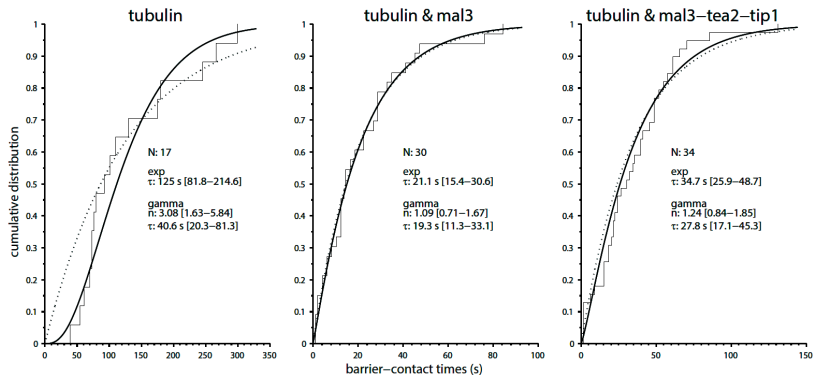
B



(A) Table with overview of experimental and simulated microtubule lifetimes and stalling durations. Values are in seconds and denote median and standard error.

(B) Contact duration as a function of the microtubule age at the moment of contact for 0, 20, 50, and 100 nM EB3.

## Supplementary Figure 5



Previously unpublished data of the barrier contact duration using the barrier design published in (Kalisch et al., 2011). The barriers were composed of SiO with a height of approximately 1.5  $\mu\text{m}$ . Microtubules were nucleated from GMPCPP-seeds towards the barriers in the presence of 15  $\mu\text{M}$  tubulin alone, and with addition of 200 nM Mal3-Alexa488, and with the combined addition of 200 nM Mal3-Alexa488, 8 nM Tea2, and 50 nM Tip1. The cumulative density distributions are fitted to a mono-exponential distribution and a Gamma distribution.

# 5

## GUIDED BY LIGHT: OPTICAL CONTROL OF MICROTUBULE GLIDING ASSAYS

*Force generation by molecular motors drives biological processes such as asymmetric cell division and cell migration. Microtubule gliding assays, in which surface-immobilized motor proteins drive microtubule propulsion, are widely used to study basic motor properties as well as the collective behaviour of active self-organized systems. While such assays allow tight control over the experimental conditions, spatiotemporal control of force generation has remained underdeveloped. Here we use light-inducible protein-protein interactions to recruit molecular motors to the surface to control microtubule gliding activity in vitro. We show that the motor proteins dynein and Ncd can be recruited to the surface in patterns. We further demonstrate that light-controlled recruitment of these motor proteins result in activation of microtubule gliding along the surface, enabling control over local microtubule motility. Our approach to locally control force generation offers a way to study the effects of non-uniform pulling forces on microtubule arrays in synthetic environments.*

---

This chapter is partly based on the publication *Guided by light: Optical control of microtubule gliding assays*, Roderick P. Tas, Chiung-Yi Chen, Eugene A. Katrukha, Mathijs Vleugel, Maurits Kok, Marileen Dogterom, Anna Akhmanova, and Lukas C. Kapitein, *Nano Lett.* **2018**, *18:12*, 7524-7528. <https://doi.org/10.1021/acs.nanolett.8b03011>. Here, we present additional unpublished results.

## 5.1. INTRODUCTION

Force generation by molecular motors on the microtubule cytoskeleton drives biological processes such as asymmetric cell division and cell migration. To better understand these processes, *in vitro* reconstitution assays are often used to decipher the underlying interactions and principles (Nedelec et al., 1997; Akhmanova and Steinmetz, 2015; Kerssemakers et al., 2006). Microtubule gliding assays, in which motor proteins are immobilized on the surface to propel microtubules, are a widely used example of such experiments. Applications of these assays range from studying basic properties of motor proteins to exploring collective and swarming behaviour of self-organized systems (Alper et al., 2013; Howard et al., 1989; Sumino et al., 2012; Lam et al., 2018; Nitzsche et al., 2010; Keya et al., 2018; Yanagida et al., 1984).

Controlling these assays with both spatial and temporal precision has however remained a longstanding challenge. Previous studies used micro-fabricated or pre-patterned surfaces to spatially confine, guide, and steer microtubules (van den Heuvel et al., 2005; Reuther et al., 2017; Bhagawati et al., 2009). Furthermore, temporal control to activate microtubule gliding on pre-defined structures has been achieved through electric field manipulation (van den Heuvel et al., 2006) and heat responsive polymer tracks (Ramsey et al., 2014; Schroeder et al., 2013), while slow light-controlled gliding (10-20 nm/s) of actin filaments has been achieved using engineered myosin motors (Nakamura et al., 2014). Additionally, control of microtubule gliding has been achieved using a light-to-heat converting layer in combination with heat-responsive polymers that compact upon heating and allow access of microtubules to surface-attached motors (Reuther et al., 2014). Furthermore, azobenzene switches fused to inhibitory peptides have been used to control kinesin-dependent motility with light (Rahim et al., 2011; Kumar et al., 2014). However, the majority of these approaches requires extensive surface modifications or complicated molecular engineering, leaving simultaneous spatial and temporal control of force generation on non-predefined patterns underdeveloped.

Additionally, a main research effort in realising a synthetic cell is the implementation of spatiotemporal control over protein activity. The ability to activate and localize proteins on cue would enable the control over processes such as artificial chromosome segregation and asymmetric cell division *in vitro*. Establishing spatiotemporal control over a gliding assay would be a first proof-of-principle for future implementation of force producing modules in artificial cellular environments.

Here, we report the activation of microtubule gliding by direct light-inducible recruitment of two minus-end directed motor protein to the surface: cytoplasmic dynein from *S. cerevisiae* (Reck-Peterson et al.; 2006) and the non-processive kinesin Ncd from *D. melanogaster*. Dynein is an essential component in mitotic spindle positioning *in vivo* (Schmidt et al., 2017) and has been used to position microtubule asters in micro-fabricated chambers *in vitro* (Laan et al.; 2012; Laan et al.; 2012), whereas Ncd is known to be involved in meiotic and mitotic spindle formation (Fink et al., 2009; McDonald et al., 1990; Walker et al., 1990). It has been shown that tunable, light-controlled interacting protein tags (TULIPs) can be efficiently used to control intracellular protein recruitment and intracellular transport (Strickland et al., 2012; van Bergeijk et al., 2015). The system is based on the engineered second light-oxygen-voltage (LOV) domain of

*A. sativa* phototropin 1. Upon blue light exposure, the J $\alpha$ -helix undocks from the core and can bind to an engineered PDZ (ePDZ) domain (Harper et al., 2003; Strickland et al., 2012). We argued that light-inducible interactions based on TULIPs can be used to reversibly control local protein recruitment *in vitro* (Fig. 5.1A). Therefore, we generated recombinant proteins fused to TULIPs to induce local heterodimerization under the control of blue light. By coupling the motor protein to ePDZ, we would be able to recruit it to the surface and reversibly activate microtubule gliding. To create a flexible platform for rapid testing of the recruitment of various motor proteins, we engineered an ePDZ fused to a GFP-nanobody (V<sub>H</sub>H) (Kubala et al., 2010), which associates with GFP-fused proteins with high affinity ( $K_d \approx 1$  nM). This should enable quick screening of any GFP-tagged protein, without the need to create and purify separate recombinant proteins. We demonstrate that both dynein and Ncd can be successfully recruited to a coverslip and initiate microtubule gliding. This approach allows for spatiotemporal control of microtubule gliding on homogeneously coated surfaces providing an adaptive platform to manipulate microtubule motility and force generation.

## 5.2. RESULTS

## 5

### 5.2.1. LIGHT-INDUCED SURFACE RECRUITMENT OF EPDZ

First, to test whether the TULIP based interactions are sufficient for spatiotemporal control of protein recruitment *in vitro*, we designed an optical readout of ePDZ recruitment to the surface. We purified the LOVpep fused to biotin, which was immobilized on a microscopy coverslip functionalized with PLL-PEG-biotin and NeutrAvidin (Fig. 5.1A). Upon illumination of the sample with blue light, ePDZ-V<sub>H</sub>H::GFP-Atto647 is recruited from solution. In order to decouple the activation and imaging spectra during testing, we labelled GFP with an Atto-647 dye.

Upon global exposure of blue light, ePDZ is recruited to surface together with GFP-Atto647 during illumination with a 488 nm evanescent field (Fig. 5.1B). After 120 seconds of continuous activation, the density of ePDZ reaches steady state. Upon the arrest of activation, complete dissociation of ePDZ was observed with a half time of ~25 seconds (Fig. 5.1B). Spatiotemporal control over the activation can be achieved with blue light from a scanning confocal module. Thus, protein recruitment was not limited to a single shape but could be structured into a variety of patterns. Depending on the power and duration of the activation pulse, both reversible as well as irreversible activation was achieved (Fig. 5.1C,D). Here, we obtain an irreversible ~2-fold change. In contrast to protein recruitment in predefined patterns, these light-induced interactions allow for sequential, reversible, and irreversible custom patterning *in situ* with high contrast and precision.

### 5.2.2. LIGHT-INDUCED MICROTUBULE GLIDING ASSAY

Having successfully recruited GFP-Atto647 to the surface, we proceeded with the light-induced recruitment of dynein-GFP-Atto660 and Ncd-GFP. Global illumination of the surface with blue light should initiate microtubule gliding by recruiting the motor proteins through ePDZ-V<sub>H</sub>H to the surface (Fig. 5.2A). In the case of the non-processive motor Ncd, we additionally functionalized the surface with Ase1 to prevent micro-

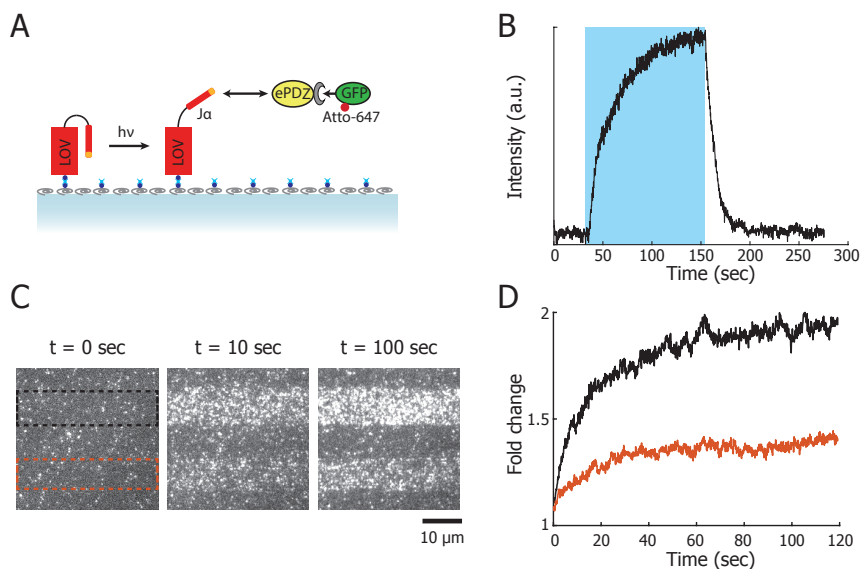


Figure 5.1: **Light-induced local recruitment of GFP-Atto647 through ePDZ-V<sub>H</sub>H.**

(A) Schematic of the light-inducible hetero-dimerization *in vitro*. Biotinylated LOV is tethered to the glass surface via PLL-PEG-biotin and NeutrAvidin. Upon illumination of the sample with blue light (488 nm), ePDZ-V<sub>H</sub>H can bind to the exposed J $\alpha$ -helix. To separate the activation and imaging wavelengths, we recruit GFP-Atto647 via the GFP-nanobody to the surface, allowing activation with the 488 nm laser and imaging with the 642 nm laser with TIRF.

(B) Intensity trace of reversible light-induced recruitment of GFP-Atto647 during global exposure of blue light with an evanescent wave.

(C) Montage of local surface activation with blue light through confocal scanning and the subsequent irreversible recruitment of GFP-Atto647. The top region was illuminated with double the laser power compared to the bottom region. Illumination duration for both exposures was the same. The scale bar denotes 10  $\mu$ m.

(D) Intensity trace of recruited ePDZ to the activated regions in (C) shows a factor of two difference in the steady-state recruitment between the two regions.

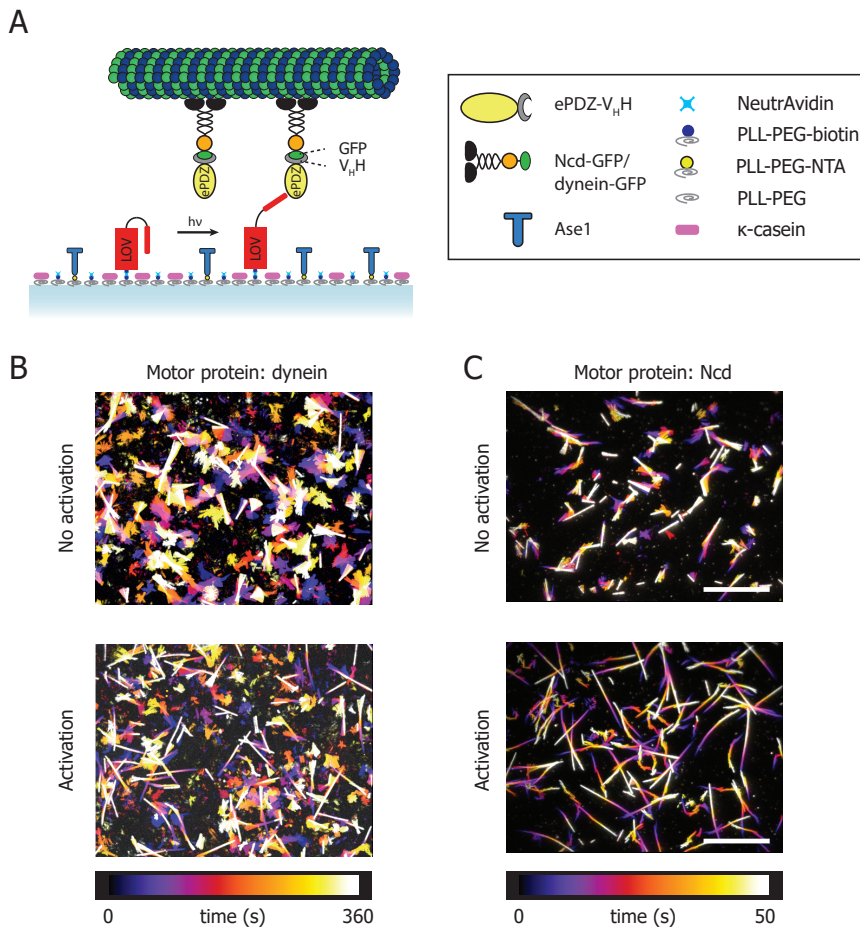


Figure 5.2: **Global activation of microtubule gliding assay.**

(A) Schematic of the light-induced microtubule gliding assay. Upon activation of the surface-tethered LOV with blue light, the undocked J $\alpha$ -helix can bind to the GFP-labelled motor protein. Recruitment of the Ncd motor will be performed in the presence of Ase1 to provide an additional microtubule surface interaction and prevent microtubules from extensive diffusive motion.

(B) Temporal colour-coded maximum projection of microtubule displacement during inactivation (**top**) and activation (**bottom**) in the presence of 2 nM dynein.

(C) Temporal colour-coded maximum projection of microtubule displacement during inactivation (**top**) and activation (**bottom**) in the presence of 50 nM Ncd and surface-immobilized Ase1.

tubules from undergoing extensive diffusion. Ase1 is an anti-parallel microtubule bundler from fission yeast that acts as a microtubule length-dependent brake preventing overlapping microtubules from sliding (Braun et al., 2011). Ase1 was tethered through its His-tag to surface-bound PLL-PEG-NTA chelated to nickel ions.

In the absence of blue light, rhodamine-labelled GMPCPP-stabilized microtubules displayed a mostly non-directional, diffusive motion on the surface. The strong microtubule enrichment near the coverslip was due to the presence of methylcellulose (Uyeda et al., 1990), while the occasional directional events were presumably due to dark-state activation or non-specific adsorption of the motors to the surface (Fig. 5.2B,C top). In contrast, upon global recruitment of dynein or Ncd motors to the surface with blue light, microtubules moved directionally along the coverslip (Fig. 5.2B,C bottom). As the observed speed of Ncd is higher than dynein, the light-induced directional gliding motion is more prominent. Also, a higher affinity of dynein for the microtubule can result in traffic jam formation (Ciandrini et al., 2014; Leduc et al., 2012). For dynein concentrations above  $\sim 5$  nM, accumulation at the minus-end could prevent microtubules from gliding altogether.

## 5

### 5.2.3. CHARACTERIZATION OF MICROTUBULE GLIDING

To better understand and quantify the effect Ncd recruitment on the directional motion of the microtubules, we tracked the position and orientation of each microtubule (see Methods for details). Our analysis is based on determining the mean squared displacement (MSD), which reports the squared displacement as a function of time interval  $\Delta t$ . The global MSD is calculated by computing the weighted ensemble mean of individual time-averaged MSD curves during the time interval  $\Delta t$  (Fig. 5.3A). The ensemble mean can subsequently be fitted with a model incorporating the contribution of random diffusion and directed motion (Imafuku et al., 2008; Palacci et al., 2016; Saxton, 2007):

$$\langle r^2 \rangle = 2D\Delta t + v^2\Delta t^2 \quad (5.1)$$

Here,  $2D\Delta t$  is the contribution of random diffusion and  $v$  the velocity of the directed motion. Fitting the calculated MSD with equation 5.1 shows the increase in directional motion upon global activation with blue light from on average  $\sim 50$  to  $\sim 225$  nm/s (Fig. 5.3B). The increase in directional velocity correlates with the recruitment of Ncd-GFP to the surface (Fig. 5.3C).

## 5.3. DISCUSSION

Here we have extended the classical microtubule gliding assays by implementing light-inducible protein patterning on a homogeneous surface. This approach allows for both spatial and temporal control of microtubule gliding activity within minutes on micrometer length scales with high efficiency. First, we showed that proteins fused to an ePDZ domain can be reliably coupled to surface immobilized LOVpep. Using an ePDZ-V<sub>HH</sub> fusion, both dynein-GFP and Ncd-GFP motors could be recruited to the surface upon activation with light to propel microtubules along the surface. Recruitment of the non-processive motor protein Ncd in the presence of the microtubule

bundler Ase1 results in concentration-dependent microtubule gliding. The recruitment of dynein however does not induce microtubule gliding to the same degree due to its higher processivity. While previous studies mostly focused on either spatial or temporal control (van den Heuvel et al., 2005; Reuther et al., 2017; van den Heuvel et al., 2006; Ramsey et al., 2014; Schroeder et al., 2013), our adaptive platform now offers simultaneous optical control of both, opening up new possibilities for microtubule gliding assays.

Our approach is complementary to a previously developed approach in which a light-to-heat converting layer was used in combination with heat-responsive polymers that compact upon heating and allow access of microtubules to surface-attached motors (Reuther et al., 2014). However, the current approach requires fewer surface modifications and does not induce local temperature changes. Compared to previous developments that have used custom-engineered myosin motors to achieve slow (10-20 nm/s) light-controlled gliding of actin filaments (Nakamura et al., 2014), the use of a generic heterodimerization strategy combined with a GFP-nanobody makes our approach readily applicable to a variety of different motor proteins.

Additionally, our approach can be used to reconstitute and understand biologi-

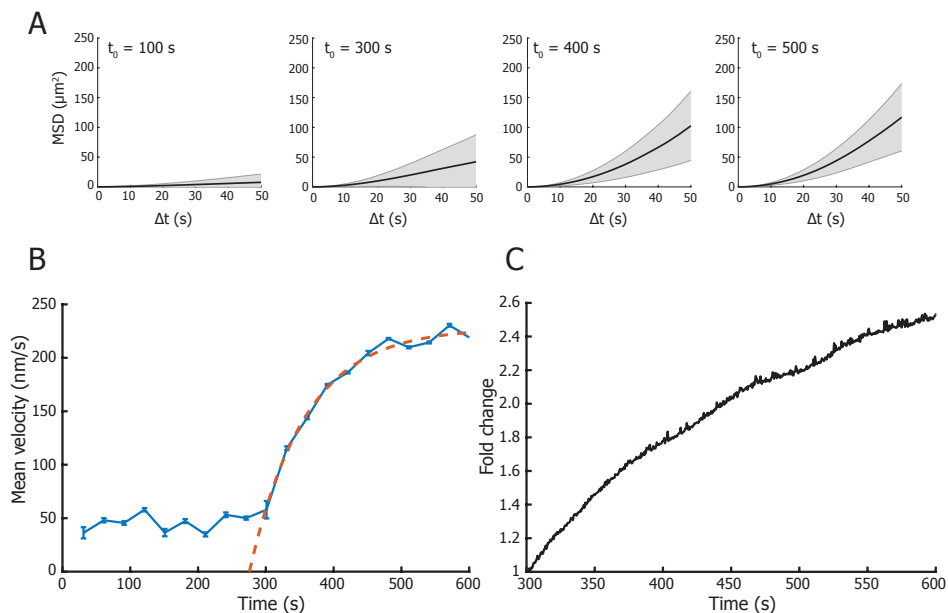


Figure 5.3: **Directional velocity of gliding microtubules increases with Ncd motor density**

(A) Calculation of the MSD from the weighted ensemble mean of the traces from the individual microtubules. The shaded area represents the standard deviation.

(B) The mean directional velocity  $v$  of microtubule motion before and during activation at  $t=300$  sec. Error bars represent the SEM.

(C) Surface intensity Ncd-GFP upon global activation with blue light. The intensity is normalized to the intensity at  $t=300$  sec when activation was initiated.

cal processes that rely on asymmetric forces produced by complex microtubule arrays. For example, light-inducible control of motor proteins can be used to locally impose forces on reconstituted spindle-like structures or on confined microtubule networks. This could guide the formation of complex microtubule arrays and enable control of cortical pulling forces (Heald et al., 1996; Laan et al., 2012). The asymmetric, local, force generation on cytoskeletal arrays by anchoring of molecular motors has been extended to the cellular environments with molecular genetic LOVpep anchors (Fielmich et al., 2018). However, when recruitment takes place in a closed environment containing a centrosome-nucleated microtubule network *in vitro*, such as in water-in-oil droplets (Roth et al., 2014; Vleugel et al., 2016), the high affinity of dynein for the microtubules could hinder cortical recruitment. As the minus-end directed dynein accumulates at the centrosome, depletion of dynein pool prevents significant cortical recruitment. Instead, a strategy based on the light-inducible homo-oligomerization of CRY2 could be explored (Duan et al., 2017). A fusion protein of CRY2 and dynein permanently anchored to the cortex would not be depleted through microtubule binding and could still be locally concentrated on the cortex to induce a high local pulling force on the microtubule network.

Furthermore, the ability to pattern ePDZ-tagged fusion proteins could have additional applications for *in vitro* studies. Direct optical protein recruitment results in the local enrichment of an effector protein, thereby increasing the local density and inducing concentration dependent activity. Future work could be aimed at introducing additional light sensitive modules to expand the level of control. Inclusion of the recently described LOVTRAP (van Haren et al., 2018; Wang et al., 2016) would for example enable a reversible blue light sensitive switch that recruits different motor proteins in the presence or absence of blue light. Furthermore, phytochrome based protein interactions could introduce red-light sensitivity (Levskaya et al., 2009) and bidirectional control (Adrian et al., 2017). The use of light inducible interactions to control microtubule gliding assays therefore provides exciting new possibilities to help reconstituting and understanding complex biophysical and biological processes.

## 5.4. METHODS

### PLASMIDS

GST-ePDZ-V<sub>H</sub>H and GST-aviTag-LOVpep were cloned into a pGEX-6p-1 vector linearized with BamHI and XhoI restriction enzymes for GST-PreScission purification. Both were cloned by PCR amplification of the individual domains, restriction digestion and ligation into the vector. A HindIII restriction site was amplified between inserts. Ligation was performed via Gibson assembly.

### PROTEIN PURIFICATION OF LOV FROM *E. coli*

Protein purification was performed in ER2566/Rosetta cells containing the plasmid with Amp/Cam. An overnight grown culture was diluted 1:1000 in LB and grown during the day at 37°C to an OD<sub>600</sub> of 0.5. The bacteria were induced with 0.15 mM IPTG and grown overnight at 30°C. After cell harvest, the cells were washed with PBS before resuspension in lysis buffer (PBS supplemented with 10 mM EDTA, 0.1% Tween,

250 mM NaCl, 1 tablet Protease Inhibitor) and lysed by sonication (amplitude 25%, 10 seconds on, 30 seconds off, 10 repetitions). The lysate was then centrifuged (16k rpm at 4°C for 15 min) and the supernatant was incubated for 1 hour with Glutathione Sepharose 4B GST-tagged beads (GE healthcare) that had been washed 3x in lysis buffer. Next, the beads were washed 2x with 50mM TrisHCl pH8.0, 150mM K-glutamate and resuspended in 318µl TrisHCl pH8.0, 150mM K-glutamate, add 40µl BiomixB (from biotinylation kit), 40µl BIO200 (from biotinylation kit), 2µl BirA (stock concentration 5mg/ml) for an overnight incubation at 4°C. Then, the beads were washed 2x with PreScission Cleavage buffer (50 mM Tris-HCl, 150 mM NaCl, 10 mM EDTA, 1 mM DTT, pH 8.0). The washed beads were incubated for 2 hours at 4°C with PreScission Protease to allow full cleavage of the PreScission sequence. Finally, the beads were spun down and the supernatant was snap-frozen with 10% glycerol. The concentration was determined with the NanoDrop.

### PROTEIN PURIFICATION FROM *S. cerevisiae*

Purification and labelling of yeast cytoplasmic dynein was performed following the protocol outlined in (Reck-Peterson et al., 2006).

### LIGHT-INDUCIBLE PATTERNING AND GLIDING ASSAYS

After cleaning the glass coverslip sample with O<sub>2</sub>-plasma, a flow chamber with a volume of ~6µl was constructed with a cleaned glass slide and double-sided sticky tape. For the surface recruitment of ePDZ-V<sub>H</sub>H::GFP-Atto647 and dynein-induced microtubule gliding, the surface was consecutively functionalized with 0.5 mg/ml PLL-PEG-biotin(50%) (SuSoS AG, Switzerland), 0.2 mg/ml NeutrAvidin (Invitrogen), and 0.5 mg/ml κ-casein (Sigma). For the Ncd-mediated gliding, the surface was consecutively functionalized with a mixture of 0.02 mg/ml PLL-PEG-[Tris-Ni(II)-NTA] (Bhagawati et al., 2013) and 0.2 mg/ml PLL-PEG-biotin(50%), 10 mM NiSiO<sub>4</sub>, 0.5 mg/ml NeutrAvidin (Invitrogen). All samples were then incubated with ~3µM of LOV-biotin for 10 minutes. The sample containing the PLL-PEG-[Tris-Ni(II)-NTA] were further incubated with ~8µM of His-Ase1 for an additional 20 minutes. All components were kept in MRB80 buffer, comprised of 80mM piperazine-N,N'-bis(2-ethanesulfonic acid), 4 mM MgCl<sub>2</sub>, and 1 mM EGTA at a pH of 6.8.

The reaction mixture for surface patterning contained MRB80 buffer supplemented with 50 nM ePDZ-V<sub>H</sub>H, 50 nM GFP-Atto647, 0.5 mg/ml κ-casein, 0.1% methyl-cellulose, 50 mM KCL, oxygen scavenger mix (4 mM DTT, 200 µg/ml catalase, 400 µg/ml glucose oxidase, 50 mM glucose). The reaction mixture containing dynein-GFP-Atto660 contained MRB80 buffer supplemented with 10 nM ePDZ-V<sub>H</sub>H, 2 nM dynein-GFP-Atto660, 0.5 mg/ml κ-casein, 0.1% methyl-cellulose, 50 mM KCL, 1 mM ATP, oxygen scavenger mix (4 mM DTT, 200 µg/ml catalase, 400 µg/ml glucose oxidase, 50 mM glucose). The reaction mixture containing Ncd-GFP contained MRB80 buffer supplemented with 50 nM ePDZ-V<sub>H</sub>H, 50 nM GFP-Atto647, 0.5 mg/ml 0.1% methyl-cellulose, 50 mM KCL, 2 mM ATP, oxygen scavenger mix (4 mM DTT, 200 µg/ml catalase, 400 µg/ml glucose oxidase, 50 mM glucose).

All reaction mixes were kept on ice during preparation and are then centrifuged in an Airfuge (Beckman Coulter) at 30 psi for 8 minutes to remove any aggregated com-

plexes before being introduced to the sample. Microtubule seeds were polymerized using 20  $\mu\text{M}$  unlabelled tubulin, 12% rhodamine-tubulin (Cytoskeleton) and 1 mM GMPCPP (Jena Bioscience). The seeds were included after centrifugation of the reaction mix. Flow cells were sealed with vacuum grease and imaged on a TIRF microscope at room temperature.

## IMAGING AND ACTIVATION

All experiments were imaged using TIRF microscopy, consisting of a Ilas<sup>2</sup> system (Roper Scientific) on a Nikon Ti-E inverted microscope. The Ilas<sup>2</sup> system is a dual illuminator for azimuthal spinning TIRF illumination equipped with a 150 mW 488 nm laser, a 100 mW 561 nm laser, a 110 mW 642 nm laser, and a ZT405/488/561/640rpc dichroic. Simultaneous dual-acquisition was performed with two Evolve 512 EMCCD camera's (Photometrics) through a 525/50 nm and a 609/54 nm or a 700/75 nm emission filter, using a Nikon CFI Plan Apochromat 100XH NA1.45 TIRF oil objective (160 nm/pixel). All experiments were performed at room temperature and the sample was kept in focus with the Nikon Perfect Focus system. The hardware was controlled with MetaMorph 7.8.8.0 (Molecular Device). Activation of surface-tethered LOV was performed either globally (TIRF) or locally (FRAP module).

## DATA ANALYSIS

To track the microtubules that were imaged with TIRF for global activation, the Fiji plugin *Ridge Detection*<sup>1</sup> was used (Steger, 1998; Wagner et al., 2017). Parameters were set such that microtubules shorter than 2.5  $\mu\text{m}$  were excluded. The coordinates of the centre line of each microtubule in each frame were saved for further processing in Matlab.

To identify and link each microtubule through the frames, a modified version of the *Simple Tracker*<sup>2</sup> package was used to build the microtubule trajectories throughout the measured frames using a multiple particle tracking routine with gap closing (Cao and Tinevez, 2018). Additionally, we removed all tracks shorter than 10 frames. The output was then restructured for further analysis with the 'msdanalyzer' Matlab class (Tarantino et al., 2014).

Temporal-colour coded projections to visualize microtubule trajectories were made with the ImageJ plugin [https://imagej.net/Temporal-Color\\_Code](https://imagej.net/Temporal-Color_Code).

## ACKNOWLEDGEMENTS

This work is supported by the Netherlands Organization for Scientific Research (NWO) (NWO-ALW-VIDI to Lukas C. Kapitein) and the European Research Council (ERC Starting Grant to Lukas C. Kapitein, ERC Synergy Grant to Anna Akhmanova and Marileen Dogterom).

<sup>1</sup>This analysis routine is advised for microtubule data obtained with a high signal-to-noise microscopy technique such as TIRF. For lower signal-to-noise data, we direct the reader to an image correlation approach based on the method found at <https://github.com/ekatrunkha/rods-detection-in-noisy-images>.

<sup>2</sup><https://nl.mathworks.com/matlabcentral/fileexchange/34040-simple-tracker>

# 6

## CHARACTERIZATION OF LIGHT-INDUCED HETERODIMERIZATION *in vitro*

**Maurits KOK, Kim VENDEL, Anne DOERR, Mathijs VLEUGEL, Roderick P. TAS, Lukas C. KAPITEIN, and Marileen DOGTEROM**

*The truth is rarely pure and never simple.*

Richard Feynman

*Regulating the temporal activation and spatial localization of cellular components is an essential feature of cell dynamics. However, probing the regulatory network can be difficult in cells due to the large number of involved proteins. Reconstitution assays can reduce the complexity by investigating the functional interaction of only a few purified components, but realizing spatiotemporal control is currently underdeveloped. Implementing such control would enable the study of simple cellular processes out of equilibrium by reversibly perturbing the system in situ. Here, we characterize the use of a light-inducible protein-dimerization strategy in two and three-dimensional in vitro assays and study the achievable level of spatiotemporal control. We show that activation and deactivation can be regulated through the activation energy, the activation duration, and through biochemical effectors. The effect of these parameters on the kinetics have been mapped and combined into a single model that describes the activation and binding process.*

## 6.1. INTRODUCTION

Cellular processes are beautiful orchestrations of protein activity and localization in a timely and reversible fashion. Elucidating the intricate dynamics of these processes has been a primary focus of cell biologists for the past decades. Yet, the complexity of a cellular environment can make detailed measurements of individual processes difficult. Leaving the constraints of a cell to gain a more engineering perspective of the system has resulted in the development of *in vitro* reconstitution assays. These assays, in which the interaction and function of a few purified cellular components is examined, have been a highly successful tool to dissect protein interactions in a controlled environment (Akhmanova and Steinmetz, 2015; Laan et al., 2012; Nedelec et al., 1997). Starting with a simple two-component system and gradually adding complexity has allowed researchers to study the system by gradual reassembly (Vleugel et al., 2016). Given that reconstitution assays are relatively simple representations of complex systems, not all functional regulatory properties, such as localization and activation, can be easily included and controlled. A necessary next step in designing reconstituting cellular systems *in vitro* is therefore to implement spatiotemporal control.

Previous strategies to control and perturb reconstitution assays include chemical dimerization through the rapalog system (Clackson et al.; 1998; Banaszynski et al., 2005; Voss et al., 2015), by irreversible component uncaging (Caldwell et al., 2018; Kaplan and Somlyo, 1989) or by changing buffer conditions with a quick solution exchange (Duellberg et al., 2016). Disadvantages of these techniques include limited spatiotemporal control, irreversibility, and/or the need for an open system to exchange components. To overcome these drawbacks, we explore the use of a light-inducible hetero-dimerization strategy to enable spatiotemporal control over protein activity *in vitro* (Hallett et al., 2016). The emergence of light-inducible interactions in studying cellular processes, known as optogenetics (Deisseroth et al., 2006), has provided a versatile layer of control on cellular dynamics. The technique, whereby light-inducible proteins are genetically encoded, enables external control over specific cellular processes and has been used to regulate organelle position (van Bergeijk et al., 2015), cell growth (Miliás-Argeitis et al., 2016), GTPase signalling (Guntas et al., 2015), gene transcription (Shimizu-Sato et al., 2002), and recently microtubule interactions (Adikes et al., 2018; van Haren et al., 2018). Functional application of light-inducible proteins *in vitro* has yet to take off, although initial experiments with cortical recruitment on GUVs have been established (Bartelt et al., 2018).

One key envisioned application of light-induced control over the localization of proteins is in reconstituting asymmetric spindle positioning (Grill and Hyman, 2005; Minc et al., 2011; Schmidt et al., 2017; Tanenbaum and Medema, 2010). Recently, the role of dynein-mediated pulling forces on mitotic spindle positioning has been probed with light-inducible membrane anchors (Fielmich et al., 2018). Previous *in vitro* efforts have been successful in establishing a stable configuration of two centrosomes encapsulated in water-in-oil droplets in the presence of cortical dynein (Roth et al., 2014; Vleugel et al., 2016). Dynein generates a pulling force from the cortex onto the astral microtubules, resulting in a net centering effect of the centrosome. If the localization of dynein on the cortex could be controlled in space and time, we would be able to reconstitute asymmetric centrosome positioning by locally varying the density of pulling

motors.

In this chapter, we investigate the application of a light-inducible heterodimerization approach based on the second light-oxygen-voltage domain (LOV) of *Avena sativa* (asLOV2) to control protein localization *in vitro* (Crosson and Moffat, 2001; Harper et al., 2003; Kennis et al., 2003). We use an improved light-inducible dimerization (iLID) based on a fusion of LOV with the bacterial SsrA peptide and its natural binding partner SspB (Guntas et al., 2015). Here, we only use the SspB construct known as Nano (and hereafter named as such), the  $K_d$  of which was determined to be 132 nM and 4.7  $\mu$ M for the active and inactive state of iLID respectively (Guntas et al., 2015). We show that Nano can be recruited to an iLID functionalized glass coverslip through global and local activation. Reversibility of the iLID activation depends on the applied laser power as high laser powers can induce permanent iLID activation. We further demonstrate successful cortical recruitment of Nano in water-in-oil droplets. We thus provide a proof-of-principle for introducing regulatory control on *in vitro* reconstitution assays through a light-inducible protein-protein dimerization strategy.

## 6.2. RESULTS

Quantitative characterization of the kinetics of LOV-based heterodimerization is a necessary step for successful *in vitro* application. Previous measurements were performed mostly *in vivo* (Benedetti et al., 2018; Zimmerman et al., 2016) or with *in vitro* bulk fluorescence polarization assays *in vitro* (Hallett et al., 2016; Guntas et al., 2015; Lungu et al., 2012) and focussed on (de)activation half times and dissociation constants. However, to have a full understanding of the kinetics, we need to characterize all involved reaction rates *in situ*.

Here, we developed a fluorescence-based assay to measure the recruitment of a

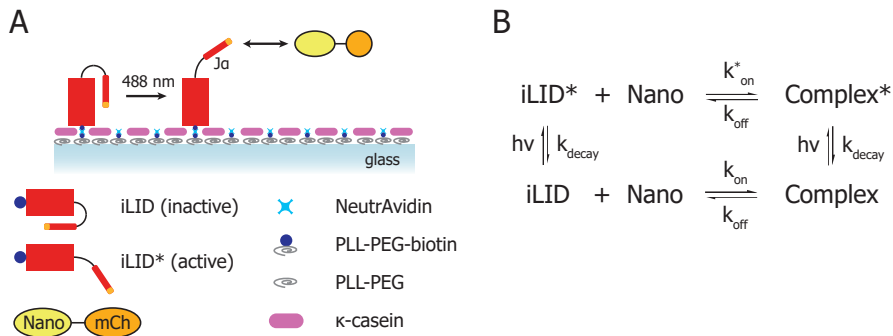


Figure 6.1: **Light-inducible heterodimerization *in vitro*.**

(A) Schematic of the light-inducible heterodimerization *in vitro*. Biotinylated iLID is tethered to the glass surface via PLL-PEG-biotin and NeutrAvidin. Upon illumination of the sample with blue light (488 nm), the soluble binding partner Nano can associate reversibly with the undocked J $\alpha$ -helix.

(B) The reaction scheme describing the activation ( $h\nu$ ), deactivation ( $k_{\text{decay}}$ ), association ( $k_{\text{on}}$  and  $k_{\text{on}}^*$ ), and dissociation ( $k_{\text{off}}$ ) steps. Upon activation of iLID with blue light, it can associate with Nano to form a Complex. The \* denotes the active state of iLID.

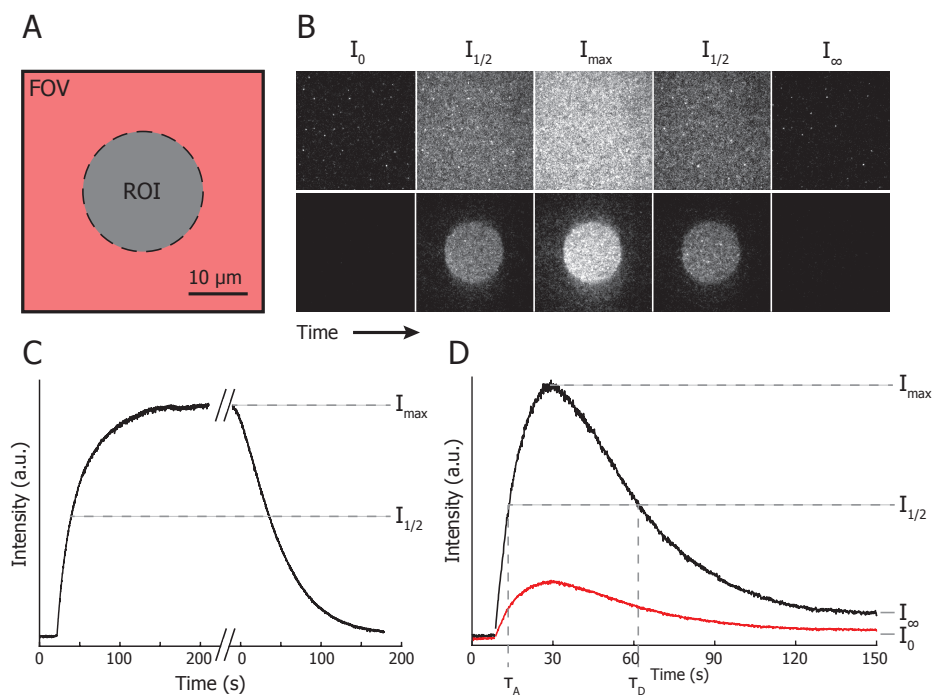


Figure 6.2: **Recruitment of SspB-mCherry to a planar surface.**

(A) Schematic view of the field of view (FOV) of the activated region of interest (ROI).

(B) Activation and deactivation of surface-tethered iLID can be achieved with an evanescent field on the full FOV (**top row**) or a local well-defined ROI with a scanning confocal laser (**bottom row**). The images denote a montage of the timepoints at which the intensity increases from the pre-activated value  $I_0$  (equal to the dark-state recruitment at steady-state), via the half-maximum intensity  $I_{1/2}$ , to the maximum intensity  $I_{max}$ . Deactivation is then followed through the half-maximum intensity to the steady-state  $I_{\infty}$ . The sample contains 50 nM Nano in solution.

(C) Intensity trace of Nano at the surface (**B top row**) during activation and dark state recovery in the absence of blue light.

(D) Intensity trace of Nano after pulsed activation of an ROI (**B bottom row**). The red trace shows the recruitment of Nano outside of the ROI within the FOV.

Nano-mCherry fusion after activation of surface-bound iLID (Fig. 6.1A). From the subsequent fluorescence intensity change on the surface measured with TIRF microscopy, we can study the involved reaction rates and their dependence on laser power, illumination duration, and influencing biochemical moieties. To study the recruitment of Nano, we tethered purified biotinylated iLID to a PLL-PEG-biotin and NeutrAvidin functionalized glass surface (Fig. 6.1A). After illumination of the surface with blue light (488 nm), the J $\alpha$ -helix undocks and is available for binding to its protein partner in solution. To ensure future compatibility with microtubule reconstitution assays, buffer conditions are chosen accordingly (Bieling et al., 2007).

The surface can be activated either globally with an evanescent field or locally with a pulsed confocal scanning laser (Fig. 6.2A). The total area illuminated by the evanes-

cent wave is significantly larger than our FOV, ensuring homogeneous illumination and recruitment. During illumination of the surface with a blue (488 nm) evanescent field, an intensity increase following the recruitment of Nano-mCh was observed (Fig. 6.2B,C). After ceasing blue light exposure, full dark state recovery followed through the release of Nano and docking of the J $\alpha$ -helix (Fig. 6.2B,C). Similarly for the pulsed activation, Nano is recruited to the illuminated ROI on the surface and subsequently released (Fig. 6.2B,D). Note that Nano is not only recruited inside the ROI, but also in the surrounding area.

### 6.2.1. DETERMINING REACTION RATES

We evaluate our measurements according to a reaction scheme that includes dimerization in both the active and the dark state (Fig. 6.1B). To interpret the data and determine the underlying rate constants, our model is based on the following assumptions:

1. It is assumed that the photophysical activation of iLID to iLID\* is instantaneous, as the activation duration is in the order of microseconds (Iuliano et al., 2018). The photon density and exposure duration with blue light could however affect the fraction of activated iLID molecules on the surface, resulting in a slower activation of iLID.
2. Depletion of soluble Nano is deemed negligible during activation as only a relatively small surface area is activated compared to the total volume of the sample.
3. Diffusion is considered to be very fast compared to the imaging frame rate and rate constants, resulting in reaction-limited kinetics.
4. Continuous activation of the sample with blue light prevents the dark-state recovery of iLID, resulting in  $k_{decay} = 0$ .
5. The dark state binding kinetics are ensured to be at steady-state before activation by keeping the sample in the dark for 3-5 min. Any signal contribution from dark-state dimerization can thus be considered constant.
6. Any activation of iLID with wavelengths longer than 488 nm is considered negligible (Fig. S1).

From the reaction scheme and the assumption above, we can formulate a set of differential equations describing the activation, deactivation and binding kinetics of each species (for details see Methods). The solutions of these equations are provided for each separate type of experiment.

The experimental readout is the fluorescence intensity  $I(t)$  at the glass surface, represented in the reaction scheme as  $I(t) = [\text{Complex}] + [\text{Complex}^*]$ . To determine the different rate constants, we need to address each individually and consecutively *in situ*. First, we determine the dissociation rate  $k_{off}$  by performing Fluorescence Recovery After Photobleaching (FRAP) of a continuously activated sample. The resulting normalized recovery curve following (Sprague et al., 2004) is described by:

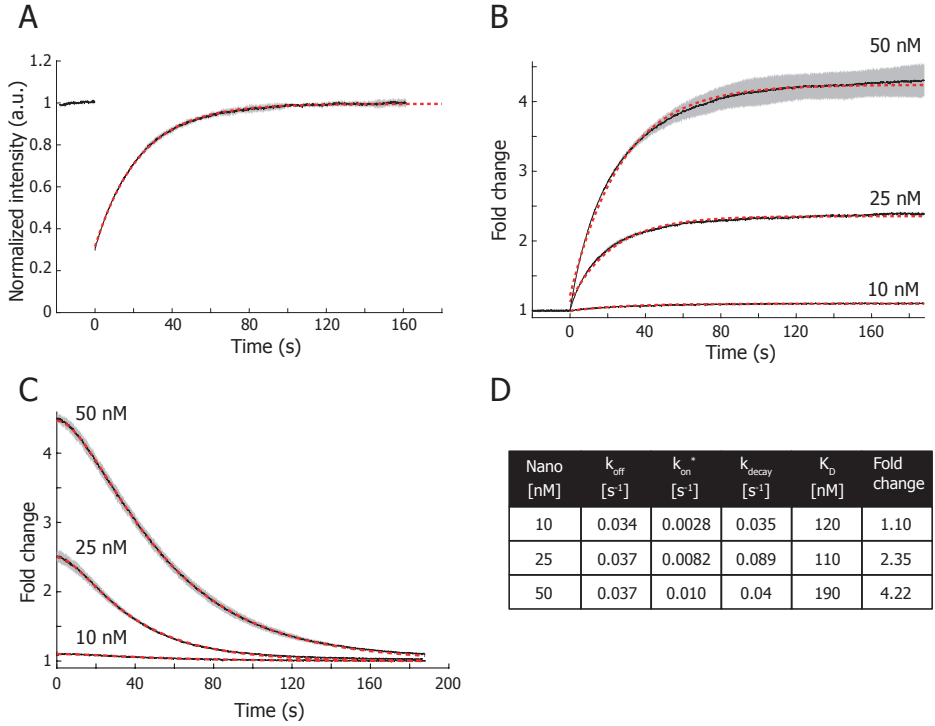


Figure 6.3: **Determination of the rate parameters.**

(A) Mean normalized trace of the intensity recovery after photobleaching. The trace is normalized to the steady-state intensity during continuous activation and fitted with equation (6.1).

(B) Fold change recruitment of Nano to the surface during continuous activation of iLID with an evanescent field. The data is fitted with equation (6.2).

(C) Fold change during dark-state recovery of iLID as Nano is released from the surface. Data is fitted with equation (6.3).

(D) Table with the reaction rates obtained with a non-linear least squares fitting routine in MATLAB.

Red dashed lines show the fit to the respective equations. All shaded regions denote the standard deviation.

$$I(t) = 1 - \frac{k_{on}^*}{k_{on}^* + k_{off}} e^{-k_{off}t} \quad (6.1)$$

Thus, the rate of FRAP recovery depends solely on  $k_{off}$  and is determined to be  $0.036 \pm 0.001 \text{ s}^{-1}$  (Fig. 6.3A,D). Next, we determined the association rate  $k_{on}$  by continuously activating the sample with an evanescent field, ensuring  $k_{decay} = 0$ . The rate of recruitment will depend on both the association and dissociation rates, and can be obtained through the fold change in surface intensity:

$$I(t) = I_0 \cdot \left[ 1 - e^{-t(k_{on}^* + k_{off})} \right] + 1 \quad (6.2)$$

with  $I(0) = \frac{k_{on}^*}{k_{on}^* + k_{off}} \cdot I_f$ . Here,  $I_f$  is a Nano dependent bulk property for the mea-

sured fold change. The measured intensity is normalized to 1 as the pre-activation value. Using the measured mean  $k_{off}$  from the FRAP measurements, we obtain good fits to the above equation and obtain  $k_{on}^* = 2.7 \cdot 10^{-4} \pm 6 \cdot 10^{-5} \text{ nM}^{-1}\text{s}^{-1}$ , resulting in a mean dissociation constant of  $K_D = 139 \pm 43 \text{ nM}$  (Fig. 6.3B,D).

Finally, we probe the dark state recovery of iLID governed by the rate  $k_{decay}$ . After global continuous activation reaches steady-state, we cease activation and measure the dark state recovery through the intensity decay. The recovery kinetics are governed by the following expressions:

$$I(t) = I_0 \frac{1}{\gamma_2 - \gamma_1} [\gamma_2 e^{-\gamma_1 t} - \gamma_1 e^{-\gamma_2 t}] \quad (6.3)$$

$$\gamma_1 \cdot \gamma_2 = k_{decay} \cdot k_{off}$$

$$\gamma_1 + \gamma_2 = k_{decay} + k_{on}^* + k_{off}$$

Using the obtained mean values for  $k_{off}$  and  $k_{on}^*$  values as fixed fitting parameters, we obtain a  $k_{decay}$  of  $0.054 \pm 0.024 \text{ s}^{-1}$ .

During development of the assay, we identified two important experimental properties that significantly affect the measured recruitment and subsequent fitted reaction rates. First, fluorophore bleaching can reduce the measured intensity, especially during continuous global activation with blue light. Preferably, bleaching is prevented by optimizing imaging conditions, but it could be accounted for in our model by introducing a bleaching step. To find the bleaching rate, adsorbed mCherry to a coverslip and measured the intensity decrease upon global illumination with increasing laser powers (Fig. S2). Introducing this irreversible bleach step with rate  $k_{bleach}$  to the model results in the following relation for continuous activation:

$$I(t) = C_1 - C_2 e^{-t(k_{on}^* + k_{off})} + C_3 e^{-t(k_{off} + k_{bleach})} \quad (6.4)$$

$$C_1 = I(0) \frac{k_{on}^* \cdot k_{off}}{(k_{on}^* + k_{off})(k_{off} + k_{bleach})}$$

$$C_2 = I(0) \frac{k_{on}^{*2}}{(k_{on}^* + k_{off})(k_{off} - k_{bleach})}$$

$$C_3 = I(0) \frac{k_{on}^* \cdot k_{bleach}}{(k_{off} + k_{bleach})(k_{on}^* - k_{bleach})}$$

Secondly, insufficient surface passivation can interfere with the release of Nano from activated iLID, resulting in a continued recruitment of Nano to the surface. We found that dissociation of Nano is decreased by  $\sim 75\%$  in the absence of surface passivation with  $\kappa$ -casein (data not shown). Introducing  $\kappa$ -casein as a passivation layer and in solution prevents the build-up of Nano on the surface.

### 6.2.2. LOCAL ACTIVATION

To gain spatial control over the activation of iLID, we used a confocal laser to illuminate specific regions for a set duration. By scanning a region of interest, the area can be

activated on the surface *in situ*. If we assume that the photo-physical activation of iLID is instantaneous upon excitation with a 488 nm photon, we reason that the fraction of activated iLID molecules on the surface can be controlled with the photon density of each pulse and the number of excitation repetitions. The dynamics of such a pulsed activation is described by:

$$I(t) = \alpha \cdot I_0 \cdot k_{on}^* \frac{1}{\gamma_2 - \gamma_1} [e^{-\gamma_1 t} - e^{-\gamma_2 t}] + I_{Inf} \quad (6.5)$$

$$\gamma_1 \cdot \gamma_2 = k_{decay} \cdot k_{off}$$

$$\gamma_1 + \gamma_2 = k_{decay} + k_{on}^* + k_{off}$$

Here,  $\alpha$  is the fraction of activated iLID molecules on the surface and  $I_{Inf}$  the intensity after complete dark-state recovery in the case of irreversible activation of iLID (Fig.

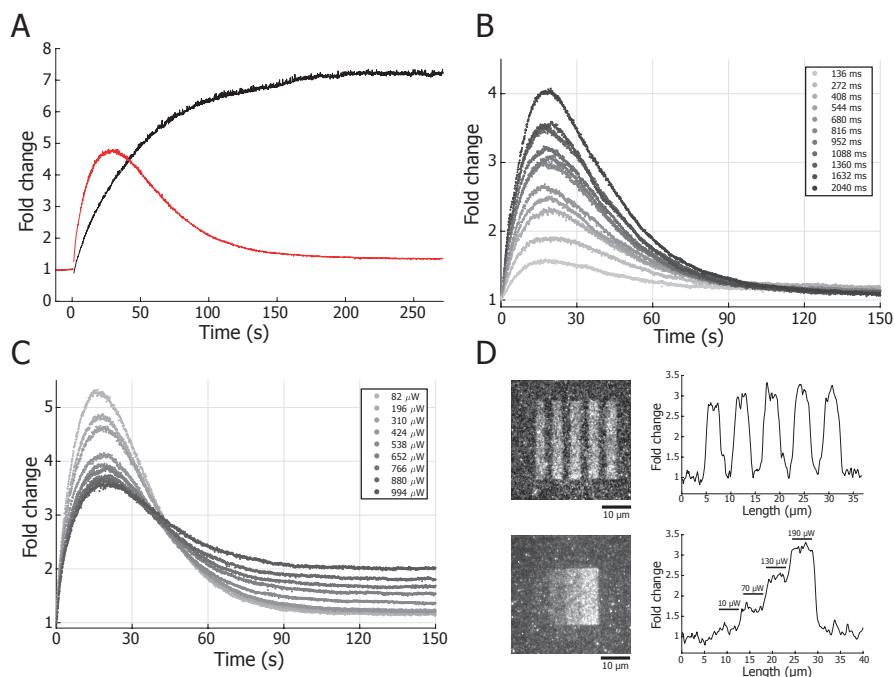


**Figure 6.4: Local recruitment of Nano with a pulsed confocal laser.**

(A) Exposure of a ROI with a pulsed laser of 3.5 mW results in the presence of 50 nM Nano results in irreversible activation in the ROI (black curve) and reversible activation outside the ROI (red curve).

(B) Intensity traces of 50 nM Nano in the activated ROI at various excitation durations. All traces were activated with a laser power of 0.16 μW.

(C) Intensity traces of Nano in the activated ROI at various laser powers. The activation duration for all traces was 136 ms.

(D) Pattern formation on a surface after irreversible iLID activation. The images are taken at the peak of Nano recruitment. A spatial resolution of ~5 μm and a recruitment 4-step gradient between a 1.5- and 3-fold change was achieved.

6.4A). We show that the fraction of activated molecules can be regulated by changing both the laser power and pulse duration (Fig. 6.4B,C). Keeping the laser power constant at  $0.16 \mu\text{W}$  and varying the number of excitation repetitions shows that the activated fraction of iLID can be controlled (Fig. 6.4B). The fraction of activated iLID  $\alpha$  in fact scales linearly with the excitation durations between 100 and 2000 ms.

Interestingly, increasing the laser power and keeping the illumination duration constant (136 ms) shows that above a threshold of  $\sim 100 \mu\text{W}$  the recruitment of Nano is reduced (Fig. 6.4C). Moreover, a fraction of the excited iLID remains in an activated state and does not revert back to its dark-state as is evident from the remaining fluorescence  $I_{Inf}$ . Thus, higher photon densities can give rise to the permanent activation of iLID above the threshold of  $\sim 400 \mu\text{W}$ . Clearly this property needs to be taken into account when a system is designed for the most optimal recruitment and needs to be considered together with the probability of activation outside the illuminated ROI (Fig. 6.2D). We reasoned however that permanent activation can also be used to pattern the surface with various densities *in situ*. Indeed, by varying the laser power, we can create well-defined patterns of Nano with distinct local densities (Fig. 6.4D).

### 6.2.3. IMIDAZOLE SPEEDS UP THE DARK STATE RECOVERY

An important property of the applicability of spatiotemporal control with iLID is the flexibility of the system. We have shown that recruitment of Nano can be controlled through the activation energy and duration, but the system does not offer a way to specifically change deactivation kinetics. It has been previously established that imidazole can increase the dark-state recovery of LOV through a base-catalyzed reaction (Alexandre et al., 2007; Strickland et al., 2012). In our model, this would result in an increase in  $k_{decay}$  for increasing concentrations of imidazole.

To investigate the effect of imidazole, we performed local reversible activation in

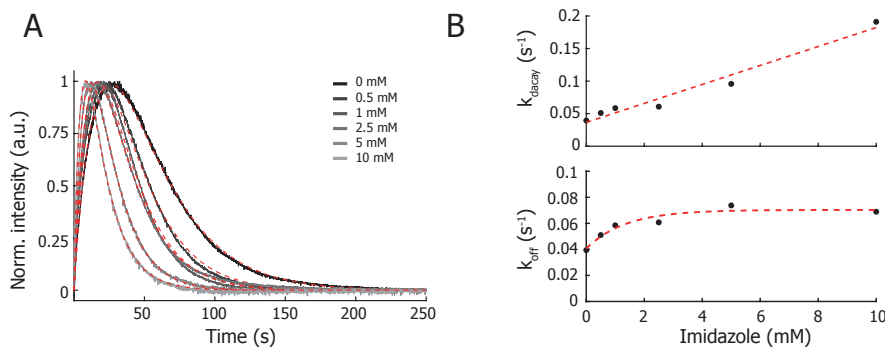


Figure 6.5: **Imidazole increases dark-state recovery.**

(A) Normalized pulsed activation traces of 50 nM Nano in the presence of 0, 0.5, 1, 2.5, 5, and 10 mM imidazole. The fits were obtained with equation (6.5) using the fixed value  $k_{on}^* = 0.01 \text{ s}^{-1}$ , while keeping  $k_{decay}$  and  $k_{off}$  as free fitting parameters (Fig. 6.3D).

(B) Fitted  $k_{decay}$  values show a linear dependence on the imidazole concentrations, whereas  $k_{off}$  values increase only mildly.

the presence of increasing imidazole concentrations. We find that imidazole increases the dark-state recovery of iLID (Fig. 6.5A). We fit the obtained intensity traces with a fixed  $k_{on}^* = 0.01 \text{ s}^{-1}$  (Fig. 6.3D), while keeping  $k_{off}$  and  $k_{decay}$  as free fitting parameters. We find that  $k_{decay}$  increases linearly with the imidazole concentration, while  $k_{decay}$  increases only mildly (Fig. 6.5B). We can thus exert control over the dark-state recovery of iLID, although one must be aware that the achievable fold change is lower during pulsed activation.

#### 6.2.4. BARRIER FUNCTIONALIZATION

In Chapter 2, we developed micro-fabricated barriers with a SiC overhang to study the stability of stalling microtubules. We have shown that these barriers can be selectively functionalized with specific proteins following previously developed protocols (Fig. 6.6A) (Taberner et al., 2014). As a proof-of-principle, we extend these protocols to functionalize the barriers with iLID in order to make protein recruitment light-inducible. In short, the sample is coated with PLL-PEG-biotin and subsequently irradiated with deep UV. The PLL-PEG-biotin will be cleaved from the surface at the exposed regions, but will remain intact underneath the SiC overhang (Fig. 6.6A) (Azioune et al., 2009). iLID can then be specifically attached underneath the SiC overhang through the linkage with NeutrAvidin. During global continuous illumination with a 488 nm evanescent wave, Nano is recruited to the barrier and subsequently released after activation (Fig. 6.6B,C).

6

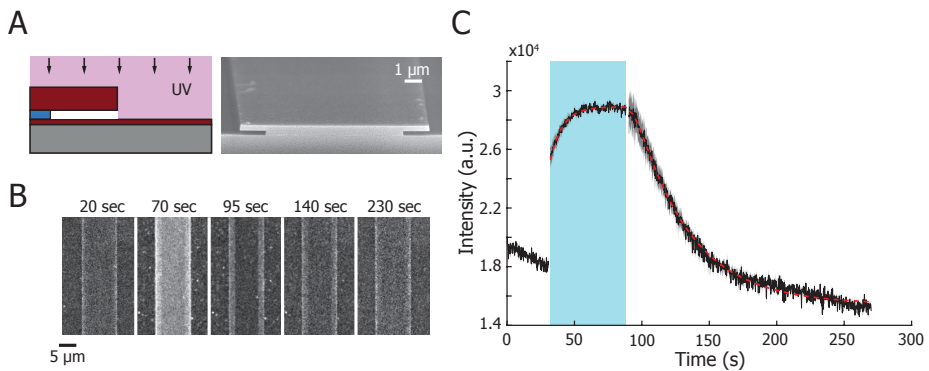


Figure 6.6: **Barrier functionalization with iLID.**

(A) Schematic of barrier functionalization and SEM image of the barriers. After functionalizing the surface with PLL-PEG-biotin, the sample is exposed to UV which removes the PLL-PEG-biotin from all exposed surfaces. Subsequent passivation with PLL-PEG (without biotin) leaves only the barriers biotinylated. Subsequent incubation with NeutrAvidin and biotinylated iLID results in iLID-coated barriers.

(B) Montage of fluorescent images of iLID activation localized underneath the barriers. Activation during 50 seconds recruits Nano to the barriers and is subsequently released during dark-state recovery.

(C) Intensity trace of Nano recruitment underneath the barriers.

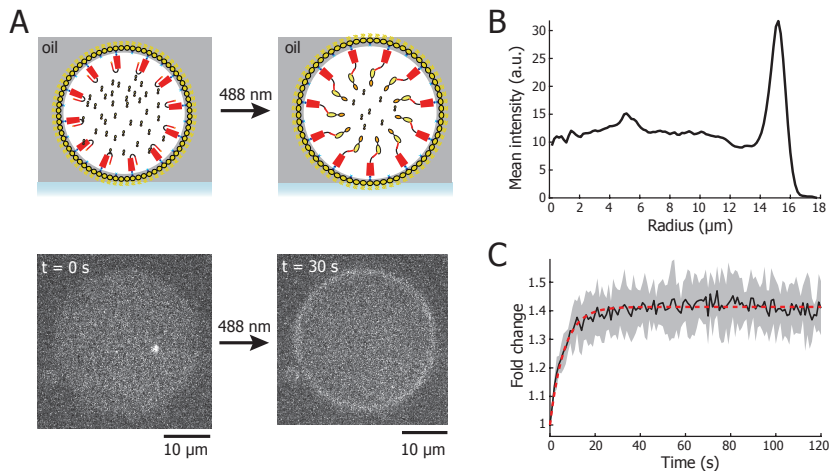


Figure 6.7: **Recruitment of Nano to the cortex of water-in-oil droplets.**

(A) Cartoon of Nano recruitment from the cytoplasm to iLID immobilized at the cortex after illumination with blue light (488 nm) (**top**). A droplet with a radius of  $15 \mu\text{m}$  containing  $500 \text{ nM}$  Nano is continuously illuminated with blue light during which Nano is recruited to the cortex (**below**).

(B) Mean radial intensity of the droplet after 30 seconds of excitation with blue light.

(C) Cortical intensity of Nano during iLID activation. Intensity is given as the mean  $\pm$  std of 7 droplets.

### 6.2.5. LIGHT-INDUCED CORTICAL RECRUITMENT IN WATER-IN-OIL DROPLETS

Light-activated dimerization has already been successfully applied in cells to recruit proteins to the cell cortex or to the membranes of organelles (Fielmich et al., 2018; van Bergeijk et al., 2015). The establishment of a localized signal in the cortex of artificial cell-like compartments is an essential step towards creating a user-controlled polarized system *in vitro*. Having successfully established iLID activation and Nano recruitment on a planar surface, we moved to its establishment in a 3D environment. To do so, we used water-in-oil droplets containing a lipid monolayer as our closed container (Roth et al., 2014; Vleugel et al., 2016). Biotinylated iLID was immobilized on a streptavidin functionalized lipid cortex with  $500 \text{ nM}$  Nano present in solution inside the droplet (Fig. 6.7A). The droplets were measured in a Spinning Disk confocal microscope focussed slightly below the equator of the droplets. The intensity change at the cortex in response to Nano recruitment was followed during global wide-field activation with blue light (Fig. 6.7A,B). Upon illumination, Nano recruitment to the cortex reached steady-state after 20 seconds (Fig. 6.7C). Fitting the intensity traces of recruitment to equation (6.2), we obtain  $k_{on}^* = 0.12 \pm 0.004 \text{ s}^{-1}$  (mean  $\pm$  std) with a 1.4 fold change of the cortical intensity. The association rate agrees with our previously determined values as it would correspond to a Nano concentration of  $\sim 450 \text{ nM}$ . However, our model relies on the assumption that depletion of Nano from solution is negligible and that iLID does not diffuse. Our obtained estimate of  $k_{on}^*$  could thus be considered a lower bound. We also find that the fold change is lower compared to recruitment on

a surface. This could be caused by the lower signal to noise resulting from Spinning Disk microscopy combined with a high background signal of Nano. Additionally, the iLID density on the cortex could be considerably lower compared to a surface.

### 6.3. DISCUSSION

In this chapter, we developed and characterized the *in vitro* application of light-inducible hetero-dimerization based on iLID (Guntas et al., 2015). We showed that Nano-mCherry can be reversibly recruited to a planar surface upon global and local activation of surface-tethered iLID. We were able to determine the involved reaction rates to fully describe the kinetics of iLID activation and Nano binding *in situ*. The measured dissociation constant  $K_D$  is in agreement with previously published values, although none have determined all underlying rates *in situ* (Hallett et al., 2016; Zimmerman et al., 2016). We found that activation can be made irreversible, depending on the photon density used for activation. This property can be very useful in creating protein patterns of controlled density with high resolution *in situ*, enabling on the spot perturbations. Until now, most strategies use predefined surface patterning through contact printing (Ricoult et al., 2014) or require specialized equipment (Strale et al., 2016), reducing applicability and flexibility.

We also explored the use of iLID as a light-inducible cortical recruiter inside spherical water-in-oil droplets. We showed that Nano can be recruited from the water phase to the iLID immobilized on the lipid cortex with a  $\sim 1.4$  fold change. Only global recruitment has so far been successful due to the chosen method of widefield illumination. Extending iLID-Nano recruitment to asymmetric rod-shaped water-in-oil droplets would provide the flexibility to create a polarized cortical pattern (Taberner et al., 2015). An important aspect to take into account however is diffusion of iLID in the cortex. Local recruitment of Nano is only possible if diffusion of iLID is slow compared to the dark-state recovery of iLID. Changing the diffusive nature of the lipid monolayer through the addition of cholesterol could be sufficient. An additional strategy to avoid this would be to make use of light-inducible homo-oligomerization of CRY2 in the cortex (Duan et al., 2017). The induced aggregation of cortex-tethered CRY2 could produce the required stable localization to establish a polarized cell *in vitro*. Future application of this technique could thus be very valuable in reconstituting asymmetric spindle position (Vleugel et al., 2016).

### 6.4. EXPERIMENTAL METHODS

#### PROTEIN PURIFICATION

Protein purification was performed in ER2566/Rosetta cells containing the plasmid with Amp/Cam. An overnight grown culture was diluted 1:1000 in LB and grown during the day at 37°C to an  $OD_{600}$  of 0.5. The bacteria were induced with 0.15 mM IPTG and grown overnight at 30°C. After cell harvest, the cells were washed with PBS before resuspension in lysis buffer (PBS supplemented with 10 mM EDTA, 0.1% Tween, 250 mM NaCl, 1 tablet Protease Inhibitor) and lysed by sonication (amplitude 25%, 10 seconds on, 30 seconds off, 10 repetitions). The lysate was then centrifuged (16k rpm at 4°C for 15 min) and the supernatant was incubated for 1 hour with Glutathione

Sepharose 4B GST-tagged beads (GE healthcare) that had been washed 3x in lysis buffer.

Next, the beads were washed 2x with 50 mM TrisHCl pH 8.0, 150 mM K-glutamate and resuspended in 318  $\mu$ l TrisHCl pH 8.0, 150mM K-glutamate, add 40  $\mu$ l BiomixB (from biotinylation kit), 40  $\mu$ l BIO200 (from biotinylation kit), 2  $\mu$ l BirA (stock concentration 5 mg/ml) for an overnight incubation at 4°C. Then, the beads were washed 2x with PreScission Cleavage buffer (50 mM Tris-HCl, 150 mM NaCl, 10 mM EDTA, 1 mM DTT, pH 8.0). The washed beads were incubated for 2 hours at 4°C with PreScission Protease to allow full cleavage of the PreScission sequence. Finally, the beads were spun down and the supernatant was snap-frozen with 10% glycerol.

### SAMPLE PREPARATION

Flow chambers were constructed from glass coverslips and glass slides separated by lanes of sticky tape to create channels with a volume of approximately 6  $\mu$ l. The glass coverslips were cleaned with base piranha (1:1:5 of H<sub>2</sub>O<sub>2</sub>:NH<sub>4</sub>OH:H<sub>2</sub>O at 70°C) for 10 min. The chambers were passivated with 0.2 mg/ml PLL-PEG-biotin (50%) (Susos AG, Switzerland) and 0.5 mg/ml  $\kappa$ -casein, and functionalized with 0.1 mg/ml NeutrAvidin (Invitrogen) in MRB80 buffer (80 mM PIPES, 4 mM MgCl<sub>2</sub>, and 1 mM EGTA at pH 6.8). Biotinylated iLID (10  $\mu$ l solution of 2  $\mu$ M) was incubated in the chambers for 10 min. A solution containing SspB-Nano-mCh supplemented with 50 mM KCl and oxygen scavenger mix (4 mM DTT, 200  $\mu$ g/ml catalase, 400  $\mu$ g/ml glucose oxidase, 50 mM glucose) was supplied to the chamber, which is thereafter sealed with silicon grease.

### FLUORESCENCE MICROSCOPY

All experiments were imaged using TIRF microscopy, consisting of a Ilas<sup>2</sup> system (Roper Scientific) on a Nikon Ti-E inverted microscope. The Ilas<sup>2</sup> system is a dual illuminator for azimuthal spinning TIRF illumination equipped with a 150 mW 488 nm laser, a 100 mW 561 nm laser, and a ZT405/488/561/640rpc dichroic. Simultaneous dual-acquisition was performed with two Evolve 512 EMCCD camera's (Photometrics) through a 525/50 nm and a 609/54 emission filter, using a Nikon CFI Plan Apochromat 100XH NA1.45 TIRF oil objective. Together with an additional magnifying lens, the final magnification resulted in a pixel size of 107 nm/pixel. All experiments were performed at room temperature and the sample was kept in focus with the Nikon Perfect Focus system. The hardware was controlled with MetaMorph 7.8.8.0 (Molecular Device).

Continuous activation of the LID system was performed by illuminating surface-bound iLID with a 488nm evanescent wave extending roughly 100 nm into the solution (Fig. 6.1A). During activation the recruitment of SspB-mCh was recorded with a frame rate of 10 Hz.

Imaging of the water-in-oil droplets was performed with a Yokogawa CSU-W1-T2 Spinning Disk Confocal Scanning module containing the emission filters mentioned above. Due to the negative effect of the refractive properties of water-in-oil droplets, no images above the equator can be successfully taken. Therefore, all droplets were imaged slightly below the equator at a frame rate of 1 Hz. All measurements were performed at room temperature.

### WATER-IN-OIL DROPLET PREPARATION

Mix DOPS (56  $\mu$ l of 10 mg/ml) and Biotinyl-cap-PE (8  $\mu$ l of 10 mg/ml) lipids (dissolved in chloroform; Avanti 840035C) in a glass vial and dry with nitrogen flow into a lipid film on the wall of the vial, followed by 2 hrs in vacuum dessicator to evaporate all remaining chloroform. Add 973  $\mu$ l mineral oil and 27  $\mu$ l Span80 to the mix and sonicate for 30 min at room temperature to dissolve the lipids. The lipid mix can be stored at 4°C up to one month.

A 15  $\mu$ l reaction mix containing 2  $\mu$ M streptavidin, 2 mg/ml BSA, 0.5 mg/ml  $\kappa$ -casein, 1  $\mu$ M biotinylated iLID, 500 nM SspB-Nano-mCherry supplemented with 50 mM KCl and oxygen scavenger mix (4 mM DTT, 200  $\mu$ g/ml catalase, 400  $\mu$ g/ml glucose oxidase, 50 mM glucose) was prepared on ice. Emulsify 0.5  $\mu$ l of reaction mix in 40  $\mu$ l lipid mix by pipetting vigorously up and down approximately 50 times. Transfer 10  $\mu$ l of the emulsion droplets into a PDMS well (2 cm x 2 cm PDMS square with a 5 mm diameter hole to hold the droplets, on top of a glass coverslip). Imaging is performed with a confocal spinning disc fluorescence microscope.

### DROPLET ANALYSIS

The droplet images are analyzed with a custom ImageJ macro that measures the intensity of a 100 equally distributed lines from the centre of the droplet to the cortex. All 100 lines per frame are then averaged to calculate the mean intensity per radial position. To localize the cortex, we fit the mean profile of each line over all frames with a Gaussian distribution. We can then calculate the mean intensity around the acquired cortical position and track the intensity.

### BARRIER FUNCTIONALIZATION WITH iLID

The barriers were functionalized as outlined in the protocol in Chapter 2.

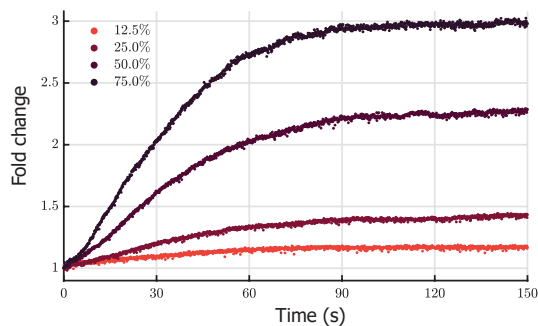
### AUTHOR CONTRIBUTIONS

M.K. has written the chapter. M.K., K.V. and A.D. designed and performed the experiments, M.K. and K.V. analysed the data, M.K. developed the model, A.D. and M.V. purified the iLID and SspB proteins, R.T. designed the constructs. L.K. and M.D. supervised the project.

### ACKNOWLEDGEMENTS

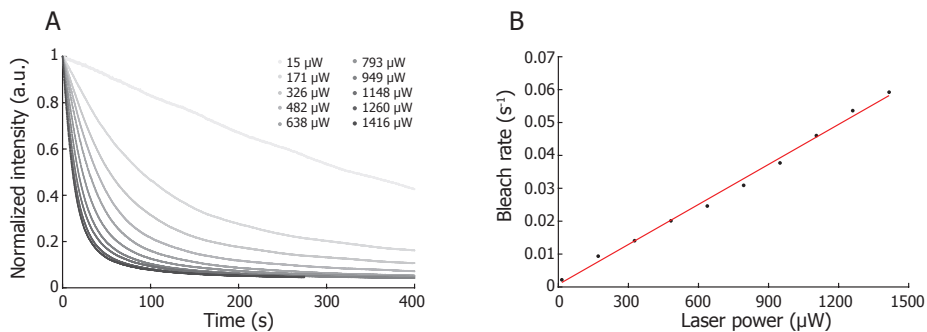
We would like to thank Teodora Trandafir, Arent Kievits, and Nemo Andrea for their exploratory experiments as part of their Bachelor internship.

Supplemental Figure 1

**Activation of iLID with 561 nm laser light.**

iLID can be activated with 561 nm TIRE. Without compromising the signal to noise, we settled on a laser setting of 12.5%. Higher laser powers resulted in a considerable activation of iLID and recruitment of Nano (50 nM).

Supplemental Figure 2

**Photobleaching of mCherry during light-induced recruitment.**

(A) Surface adsorbed mCherry bleaching at increasing laser power.

(B) Bleach rate determined by fitting the bleach profiles in (A) with a mono-exponential model. The measured bleach rate is linearly dependent on the laser power.



# 7

## DISCUSSION AND OUTLOOK

*That which can be asserted without evidence,  
can be dismissed without evidence.*

Christopher Hitchens

For decades, the phenomenal molecular complexity and self-organizational properties of living cells have been a fascination for biologists and physicists alike. A principle exponent of supramolecular organisation is the cytoskeleton. Cytoskeletal networks are the driving force behind cell structure and polarity, playing major roles in cell division, cell morphology, cell motility, and intracellular transport. Microtubules are a key constituent of the cytoskeleton and are rigid, dynamic filaments, able to quickly respond to the organisational needs of a cell. Both the molecular basis for and the emergent properties of their dynamic behaviour has been studied both in cells and in reconstitution assays, the latter of which involves the investigation of purified components in a controlled environment. At the interface between biology and physics, we are now able to engineer synthetic systems that can reconstitute key cellular processes. By rebuilding cellular systems from the bottom up we can arrive at a minimal set of functional components. The latest approaches are aimed at capturing the complex function of microtubules in cell-like compartments. Designing closed systems demands a solid understanding of the individual components and an ability to regulate them. Spatiotemporal control of microtubule stability enables a living cell to impart different functions to the microtubule network. Of these, interactions with the cell cortex play a significant role. Reconstituting these regulatory mechanisms will provide new fundamental insights into their function and lead to their application in novel synthetic biology.

Previous *in vitro* efforts established that pushing microtubules are less stable (Janson et al., 2003), but can be regulated through end-on interactions with motor proteins

(Laan et al., 2012). The effect of ubiquitous microtubule associated proteins on microtubule assembly under force remained unresolved.

In this thesis we investigate two aspects of microtubule dynamics in confinement. First, we set out to measure the stability of microtubules that encounter novel rigid barriers (Chapter 2) in the presence of +TIPs. We demonstrate that the duration of contact is dominated by GTP hydrolysis in the presence of EB3 and that the dynamics can be captured with a 1D biochemical model (Chapter 4). We also characterized the catastrophe suppressing function of CLASP2 $\alpha$  on the stability of pushing microtubules (Chapter 3). Secondly, we explored the application of light-inducible protein-protein interactions as a potential regulator in *in vitro* reconstitutions. We characterized the function of iLID *in vitro* (Chapter 6) and engineered a light-induced microtubule gliding assay (Chapter 5). Our established experimental designs and the results we obtained will open up new research directions to investigate and engineer synthetic microtubule systems.

## MICRO-FABRICATED BARRIERS

We developed and optimized the fabrication of micron-sized barriers designed to study the interaction of microtubules with a rigid object *in vitro*. With the introduction of a stable silicon carbide overhang at the barrier, we managed to stall growing microtubules and image them with TIRF microscopy. We have shown that the application of SiC as a substrate for TIRF microscopy has little impact on the image quality when compared to glass, although proper data treatment is essential. As an inert and non-toxic compound it has been used for medical implants, but has received very little attention as a material in cell biological (Iliescu et al., 2008; Oliveros et al., 2013). To our knowledge, this is the first implementation of SiC as a substrate in fluorescence microscopy.

Previous micro-fabricated barriers and chambers were incompatible with high resolution TIRF microscopy and required complex functionalization strategies (Romet-Lemonne et al., 2005) or suffered from interfering optical properties (Taberner et al., 2014). With SiC, we can avoid the use of metals, which in general have unfavourable reflective properties and are difficult to passivate. Moreover, the barriers are compatible with developed techniques for selective functionalization (Taberner et al., 2014). This opens up the study of end-on interactions of microtubules with microtubule associated proteins or motor proteins at high resolution (Laan et al., 2012). Combining such assays with the end binding protein EB3 as a marker the microtubule cap could provide insight into the specific effect of end-on interactions on microtubule cap dynamics.

Moreover, integrating multiple cytoskeletal systems containing both a microtubule and an actin network could be investigated. Reconstituting an actin cortex underneath the SiC overhangs by selective nucleation would enable reconstituting microtubule-actin interactions in a 2D confinement (Adikes et al., 2018; Colin et al., 2018; Dogterom and Koenderink, 2019; Preciado Lopez et al., 2014; Preciado Lopez et al., 2014). This will more closely mimic the cortical interactions *in vivo*.

## THE STABILITY OF STALLING MICROTUBULES

We established that the plus-end tracking CLASP2 $\alpha$  is a potent catastrophe suppressor and can rescue microtubule depolymerization by stabilizing individual protofilaments. In cells, CLASPs are essential for proper spindle assembly and poleward flux during interphase (Logarinho et al., 2012; Maiato et al., 2005). Their presence at the leading edge of cells promotes rescues during migration and can suppress catastrophes at the tips of cell protrusions (Bouchet et al., 2016; Mimori-Kiyosue et al., 2005). We found that CLASP can suppress force-induced catastrophes and stabilize pushing microtubules in the presence of EB3, mimicking microtubules navigating the sharp angles in plant cell (Ambrose et al., 2011).

A possible extension of these observations would be to investigate whether CLASP can stabilize microtubules through an end-on interaction. By functionalizing microfabricated barriers or the cortex inside water-in-oil droplets with CLASP, the stability of pushing microtubule and its effect on microtubule organization could be examined. Preliminary experiments suggest that CLASP is indeed capable of suppressing catastrophes through end-on interactions (Taberner, 2016).

To gain more detailed insights into the stability of stalling microtubules, we reconstituted force-induced catastrophes in a simplified system *in vitro* and studied them with Monte Carlo simulations *in silico*. We developed a coarse-grained 1D biochemical model that can capture a rich set of experimental data of dynamic microtubules. Its reduction to fluctuations of the tip combined with GTP hydrolysis provides a simple model that is useful to characterize the effect of a range of microtubule associated proteins. As such a question we have yet to address, is how the function of CLASP fits within our observation that only a short terminal layer of hydrolysed subunits is required to trigger a catastrophe. Can its function solely be understood as a modulator of tip fluctuations for our 1D biochemical model? First, CLASPs prevent catastrophe onset but do not slow down MT shortening (Lawrence et al., 2018). This finding combined with the experiments showing TOG2-S enrichment behind the outmost tip at the MT plus end suggests that CLASPs, through their TOG2 domain, promote the stability of the microtubule region corresponding to the GTP (or GDP-Pi) cap so long as it is present. Given that only a few CLASP molecules are required to suppress a catastrophe and that an EB binding region is still present on average when a catastrophe is triggered, CLASP could prevent further destabilization by mechanically suppressing a catastrophe when the terminal region of the microtubule tip is hydrolysed. We furthermore observed that diffusive noise of the microtubule tip is reduced in the presence of both EB3 and CLASP2 as well as the mean growth speed. Considering our 1D model, this could in turn result in fewer negative growth excursions, thereby lowering the probability of triggering a catastrophe. During this stabilizing episode, sufficient addition of GTP-tubulin at the tip would reinitiate microtubule polymerization and prevent a catastrophe.

## LIGHT-INDUCIBLE REGULATION *in vitro*

Spatiotemporal control of protein activity and location is an essential feature of cells and warrants an equally robust reconstituted molecular system. Our developed method based on the light-induced activation of LOV/iLID can be used to reconstitute and un-

derstand biological processes that rely on asymmetric force production by complex microtubule arrays. For example, light-inducible control of motor proteins can be used to locally impose forces on reconstituted spindle-like structures or confined microtubule networks to guide the formation of complex microtubule arrays or to study cortical pulling forces (Heald et al., 1996; Laan et al., 2012). However, careful design is required when recruitment takes place in a closed environment containing a microtubule network, such as in water-in-oil droplets (Roth et al., 2014; Vleugel et al., 2016). Depletion effects and aspecific clustering of proteins will need to be carefully managed. Perhaps a strategy based on the light-inducible homo-oligomerization of CRY2 could be further explored as an alternative to generate local enrichment on the cortex (Duan et al., 2017). In conjunction, recently developed strategies using the light-inducible tip tracking in cells are currently being explored *in vitro* (Adikes et al., 2018; van Haren et al., 2018).

## OUTLOOK

Although many essential steps still have to be taken, the development of an entirely synthetic cell containing a regulated multi-component cytoskeletal system is looming on the technological horizon. Successful incorporation of a functional cytoskeleton will contribute to the establishment a polarized cell and to cell division. Our insights into microtubule dynamics in closed environments coupled with regulatory control will be a key part. And until this cell is able to exert spatiotemporal control on its components and processes through integrated feedback loops, the use of light as a local on/off switch will be very valuable.

# BIBLIOGRAPHY

- Adams, P. D., Afonine, P. V., Bunkoczi, G., Chen, V. B., Davis, I. W., Echols, N., Headd, J. J., Hung, L. W., Kapral, G. J., Grosse-Kunstleve, R. W., McCoy, A. J., Moriarty, N. W., Oeffner, R., Read, R. J., Richardson, D. C., Richardson, J. S., Terwilliger, T. C., and Zwart, P. H. PHENIX: a comprehensive Python-based system for macromolecular structure solution. *Acta Crystallogr D Biol Crystallogr*, 66(Pt 2):213–21, 2010. <https://doi.org/10.1107/S09074444909052925>.
- Adikes, R. C., Hallett, R. A., Saway, B. F., Kuhlman, B., and Slep, K. C. Control of microtubule dynamics using an optogenetic microtubule plus end-F-actin cross-linker. *J Cell Biol*, 217(2):779–793, 2018. <https://doi.org/10.1083/jcb.201705190>.
- Adrian, M., Nijenhuis, W., Hoogstraaten, R. I., Willems, J., and Kapitein, L. C. A phytochrome-derived photoswitch for intracellular transport. *ACS Synth Biol*, 6(7):1248–1256, 2017. <https://doi.org/10.1021/acssynbio.6b00333>.
- Aher, A., Kok, M., Sharma, A., Rai, A., Olieric, N., Rodriguez-Garcia, R., Katrukha, E. A., Weinert, T., Olieric, V., Kapitein, L. C., Steinmetz, M. O., Dogterom, M., and Akhmanova, A. CLASP suppresses microtubule catastrophes through a single TOG domain. *Dev Cell*, 46(1):40–58.e8, 2018. <https://doi.org/10.1016/j.devcel.2018.05.032>.
- Akhmanova, A. and Steinmetz, M. O. Tracking the ends: a dynamic protein network controls the fate of microtubule tips. *Nat Rev Mol Cell Biol*, 9(4):309–22, 2008. <https://doi.org/10.1038/nrm2369>.
- Akhmanova, A. and Steinmetz, M. O. Control of microtubule organization and dynamics: two ends in the limelight. *Nat Rev Mol Cell Biol*, 16(12):711–26, 2015. <https://doi.org/10.1038/nrm4084>.
- Akhmanova, A., Hoogenraad, C. C., Drabek, K., Stepanova, T., Dortland, B., Verkerk, T., Vermeulen, W., Burgering, B. M., De Zeeuw, C. I., Grosveld, F., and Galjart, N. CLASPs are CLIP-115 and -170 associating proteins involved in the regional regulation of microtubule dynamics in motile fibroblasts. *Cell*, 104(6):923–35, 2001. [https://doi.org/10.1016/S0092-8674\(01\)00288-4](https://doi.org/10.1016/S0092-8674(01)00288-4).
- Akiyoshi, B., Sarangapani, K. K., Powers, A. F., Nelson, C. R., Reichow, S. L., Arellano-Santoyo, H., Gonen, T., Ranish, J. A., Asbury, C. L., and Biggins, S. Tension directly stabilizes reconstituted kinetochore-microtubule attachments. *Nature*, 468(7323):576–9, 2010. <https://doi.org/10.1038/nature09594>.
- Al-Bassam, J. and Chang, F. Regulation of microtubule dynamics by TOG-domain proteins XMAP215/Dis1 and CLASP. *Trends Cell Biol*, 21(10):604–14, 2011. <https://doi.org/10.1016/j.tcb.2011.06.007>.

- Al-Bassam, J., Kim, H., Brouhard, G., van Oijen, A., Harrison, S. C., and Chang, F. CLASP promotes microtubule rescue by recruiting tubulin dimers to the microtubule. *Dev Cell*, 19(2):245–58, 2010. <https://doi.org/10.1016/j.devcel.2010.07.016>.
- Alexandre, M. T., Arents, J. C., van Grondelle, R., Hellingwerf, K. J., and Kennis, J. T. A base-catalyzed mechanism for dark state recovery in the *Avena sativa* phototropin-1 LOV2 domain. *Biochemistry*, 46(11):3129–37, 2007. <https://doi.org/10.1021/bi062074e>.
- Alper, J. D., Tovar, M., and Howard, J. Displacement-weighted velocity analysis of gliding assays reveals that *Chlamydomonas* axonemal dynein preferentially moves conspecific microtubules. *Biophys J*, 104(9):1989–98, 2013. <https://doi.org/10.1016/j.bpj.2013.03.041>.
- Alushin, G. M., Lander, G. C., Kellogg, E. H., Zhang, R., Baker, D., and Nogales, E. High-resolution microtubule structures reveal the structural transitions in  $\alpha\beta$ -tubulin upon GTP hydrolysis. *Cell*, 157(5):1117–29, 2014. <https://doi.org/10.1016/j.cell.2014.03.053>.
- Ambrose, C., Allard, J. F., Cytrynbaum, E. N., and Wasteneys, G. O. A CLASP-modulated cell edge barrier mechanism drives cell-wide cortical microtubule organization in *Arabidopsis*. *Nat Commun*, 2:430, 2011. <https://doi.org/10.1038/ncomms1444>.
- Antal, T., Krapivsky, P. L., Redner, S., Mailman, M., and Chakraborty, B. Dynamics of an idealized model of microtubule growth and catastrophe. *Phys Rev E Stat Nonlin Soft Matter Phys*, 76(4 Pt 1):041907, 2007. <https://doi.org/10.1103/PhysRevE.76.041907>.
- Aumeier, C., Schaedel, L., Gaillard, J., John, K., Blanchoin, L., and Thery, M. Self-repair promotes microtubule rescue. *Nat Cell Biol*, 2016. <https://doi.org/10.1038/ncb3406>.
- Ayaz, P., Ye, X., Huddleston, P., Brautigam, C. A., and Rice, L. M. A TOG: $\alpha\beta$ -tubulin complex structure reveals conformation-based mechanisms for a microtubule polymerase. *Science*, 337(6096):857–60, 2012. <https://doi.org/10.1126/science.1221698>.
- Azioune, A., Storch, M., Bornens, M., Thery, M., and Piel, M. Simple and rapid process for single cell micro-patterning. *Lab Chip*, 9(11):1640–2, 2009. <https://doi.org/10.1039/b821581m>.
- Banaszynski, L. A., Liu, C. W., and Wandless, T. J. Characterization of the FKBP-rapamycin-FRB ternary complex. *J Am Chem Soc*, 127(13):4715–21, 2005. <https://doi.org/10.1021/ja043277y>.
- Barisic, M., Silva e Sousa, R., Tripathy, S. K., Magiera, M. M., Zaytsev, A. V., Pereira, A. L., Janke, C., Grishchuk, E. L., and Maiato, H. Microtubule detirosination guides

- chromosomes during mitosis. *Science*, 348(6236):799–803, 2015. <https://doi.org/10.1126/science.aaa5175>.
- Bartelt, S. M., Chervyachkova, E., Steinkuhler, J., Ricken, J., Wieneke, R., Tampe, R., Dimova, R., and Wegner, S. V. Dynamic blue light-switchable protein patterns on giant unilamellar vesicles. *Chem Commun (Camb)*, 54(8):948–951, 2018. <https://doi.org/10.1039/c7cc08758f>.
- Bayley, P., Schilstra, M., and Martin, S. A lateral cap model of microtubule dynamic instability. *FEBS Lett*, 259(1):181–4, 1989. [https://doi.org/10.1016/0014-5793\(89\)81523-6](https://doi.org/10.1016/0014-5793(89)81523-6).
- Beinhauer, J. D., Hagan, I. M., Hegemann, J. H., and Fleig, U. Mal3, the fission yeast homologue of the human APC-interacting protein EB-1 is required for microtubule integrity and the maintenance of cell form. *J Cell Biol*, 139(3):717–28, 1997. <https://doi.org/10.1083/jcb.139.3.717>.
- Benedetti, L., Barentine, A. E. S., Messa, M., Wheeler, H., Bewersdorf, J., and De Camilli, P. Light-activated protein interaction with high spatial subcellular confinement. *Proc Natl Acad Sci U S A*, 2018. <https://doi.org/10.1073/pnas.1713845115>.
- Bhagawati, M., Ghosh, S., Reichel, A., Froehner, K., Surrey, T., and Piehler, J. Organization of motor proteins into functional micropatterns fabricated by a photoinduced fenton reaction. *Angew Chem Int Ed Engl*, 48(48):9188–91, 2009. <https://doi.org/10.1002/anie.200904576>.
- Bhagawati, M., You, C., and Piehler, J. Quantitative real-time imaging of protein-protein interactions by LSPR detection with micropatterned gold nanoparticles. *Anal Chem*, 85(20):9564–71, 2013. <https://doi.org/10.1021/ac401673e>.
- Bieling, P., Laan, L., Schek, H., Munteanu, E. L., Sandblad, L., Dogterom, M., Brunner, D., and Surrey, T. Reconstitution of a microtubule plus-end tracking system in vitro. *Nature*, 450(7172):1100–5, 2007. <https://doi.org/10.1038/nature06386>.
- Bouchard, P., Penningroth, S. M., Cheung, A., Gagnon, C., and Bardin, C. W. erythro-9-[3-(2-hydroxynonyl)]adenine is an inhibitor of sperm motility that blocks dynein ATPase and protein carboxylmethylase activities. *Proc Natl Acad Sci U S A*, 78(2):1033–6, 1981.
- Bouchet, B. P., Noordstra, I., van Amersfoort, M., Katrukha, E. A., Ammon, Y. C., Ter Hoeve, N. D., Hodgson, L., Dogterom, M., Derksen, P. W., and Akhmanova, A. Mesenchymal cell invasion requires cooperative regulation of persistent microtubule growth by SLAIN2 and CLASP1. *Dev Cell*, 39(6):708–723, 2016. <https://doi.org/10.1016/j.devcel.2016.11.009>.
- Bowne-Anderson, H., Zanic, M., Kauer, M., and Howard, J. Microtubule dynamic instability: a new model with coupled GTP hydrolysis and multistep catastrophe. *Bioessays*, 35(5):452–61, 2013. <https://doi.org/10.1002/bies.201200131>.

- Bowne-Anderson, H., Hibbel, A., and Howard, J. Regulation of microtubule growth and catastrophe: Unifying theory and experiment. *Trends Cell Biol*, 25(12):769–79, 2015. <https://doi.org/10.1016/j.tcb.2015.08.009>.
- Brangwynne, C. P., MacKintosh, F. C., Kumar, S., Geisse, N. A., Talbot, J., Mahadevan, L., Parker, K. K., Ingber, D. E., and Weitz, D. A. Microtubules can bear enhanced compressive loads in living cells because of lateral reinforcement. *J Cell Biol*, 173(5):733–41, 2006. <https://doi.org/10.1083/jcb.200601060>.
- Brangwynne, C. P., MacKintosh, F. C., and Weitz, D. A. Force fluctuations and polymerization dynamics of intracellular microtubules. *Proc Natl Acad Sci U S A*, 104(41):16128–33, 2007. <https://doi.org/10.1073/pnas.0703094104>.
- Bratman, S. V. and Chang, F. Stabilization of overlapping microtubules by fission yeast CLASP. *Dev Cell*, 13(6):812–27, 2007. <https://doi.org/10.1016/j.devcel.2007.10.015>.
- Braun, M., Lansky, Z., Fink, G., Ruhnnow, F., Diez, S., and Janson, M. E. Adaptive braking by Ase1 prevents overlapping microtubules from sliding completely apart. *Nat Cell Biol*, 13(10):1259–64, 2011. <https://doi.org/10.1038/ncb2323>.
- Brouhard, G. J. Dynamic instability 30 years later: complexities in microtubule growth and catastrophe. *Mol Biol Cell*, 26(7):1207–10, 2015. <https://doi.org/10.1091/mbc.E13-10-0594>.
- Brouhard, G. J. and Rice, L. M. The contribution of  $\alpha\beta$ -tubulin curvature to microtubule dynamics. *J Cell Biol*, 207(3):323–34, 2014. <https://doi.org/10.1083/jcb.201407095>.
- Brouhard, G. J. and Rice, L. M. Microtubule dynamics: an interplay of biochemistry and mechanics. *Nat Rev Mol Cell Biol*, 19(7):451–463, 2018. <https://doi.org/10.1038/s41580-018-0009-y>.
- Brouhard, G. J., Stear, J. H., Noetzel, T. L., Al-Bassam, J., Kinoshita, K., Harrison, S. C., Howard, J., and Hyman, A. A. XMAP215 is a processive microtubule polymerase. *Cell*, 132(1):79–88, 2008. <https://doi.org/10.1016/j.cell.2007.11.043>.
- Brun, L., Rupp, B., Ward, J. J., and Nedelec, F. A theory of microtubule catastrophes and their regulation. *Proc Natl Acad Sci U S A*, 106(50):21173–8, 2009. <https://doi.org/10.1073/pnas.0910774106>.
- Brunner, D. and Nurse, P. CLIP170-like tip1p spatially organizes microtubular dynamics in fission yeast. *Cell*, 102(5):695–704, 2000. [https://doi.org/10.1016/S0092-8674\(00\)00091-X](https://doi.org/10.1016/S0092-8674(00)00091-X).
- Buey, R. M., Mohan, R., Leslie, K., Walzthoeni, T., Missimer, J. H., Menzel, A., Bjelic, S., Bargsten, K., Grigoriev, I., Smal, I., Meijering, E., Aebbersold, R., Akhmanova, A., and Steinmetz, M. O. Insights into EB1 structure and the role of its C-terminal domain for discriminating microtubule tips from the lattice. *Mol Biol Cell*, 22(16):2912–23, 2011. <https://doi.org/10.1091/mbc.E11-01-0017>.

- Burakov, A., Nadezhdina, E., Slepchenko, B., and Rodionov, V. Centrosome positioning in interphase cells. *J Cell Biol*, 162(6):963–9, 2003. <https://doi.org/10.1083/jcb.200305082>.
- Caldwell, R. M., Bermudez, J. G., Thai, D., Aonbangkhen, C., Schuster, B. S., Courtney, T., Deiters, A., Hammer, D. A., Chenoweth, D. M., and Good, M. C. Optochemical control of protein localization and activity within cell-like compartments. *Biochemistry*, 57(18):2590–2596, 2018. <https://doi.org/10.1021/acs.biochem.8b00131>.
- Campbell, J. N. and Slep, K. C.  $\alpha\beta$ -Tubulin and microtubule-binding assays. *Methods Mol Biol*, 777:87–97, 2011. [https://doi.org/10.1007/978-1-61779-252-6\\_6](https://doi.org/10.1007/978-1-61779-252-6_6).
- Cande, W. Z. Inhibition of spindle elongation in permeabilized mitotic cells by erythro-9-[3-(2-hydroxyonyl)] adenine. *Nature*, 295(5851):700–1, 1982. <https://doi.org/10.1038/295700a0>.
- Cao, Y. and Tinevez, J. Y. Simple tracker. 2018.
- Caplow, M. and Shanks, J. Evidence that a single monolayer tubulin-GTP cap is both necessary and sufficient to stabilize microtubules. *Mol Biol Cell*, 7(4):663–75, 1996. <https://doi.org/10.1091/mbc.7.4.663>.
- Caplow, M., Shanks, J., and Ruhlen, R. L. Temperature-jump studies of microtubule dynamic instability. *J Biol Chem*, 263(21):10344–52, 1988.
- Carrier, M. F. and Pantaloni, D. Kinetic analysis of guanosine 5'-triphosphate hydrolysis associated with tubulin polymerization. *Biochemistry*, 20(7):1918–24, 1981.
- Carrier, M. F. and Pantaloni, D. Assembly of microtubule protein: role of guanosine di- and triphosphate nucleotides. *Biochemistry*, 21(6):1215–24, 1982.
- Carrier, M. F., Didry, D., and Pantaloni, D. Microtubule elongation and guanosine 5'-triphosphate hydrolysis. Role of guanine nucleotides in microtubule dynamics. *Biochemistry*, 26(14):4428–37, 1987.
- Carminati, J. L. and Stearns, T. Microtubules orient the mitotic spindle in yeast through dynein-dependent interactions with the cell cortex. *J Cell Biol*, 138(3):629–41, 1997.
- Cassimeris, L., Leung, J. C., and Odde, D. J. Monte Carlo simulations of microtubule arrays: The critical roles of rescue transitions, the cell boundary, and tubulin concentration in shaping microtubule distributions. *PLoS One*, 13(5):e0197538, 2018. <https://doi.org/10.1371/journal.pone.0197538>.
- Chang, F. and Nurse, P. How fission yeast fission in the middle. *Cell*, 84(2):191–4, 1996.

- Chazeau, A., Katrukha, E. A., Hoogenraad, C. C., and Kapitein, L. C. Studying neuronal microtubule organization and microtubule-associated proteins using single molecule localization microscopy. *Methods Cell Biol*, 131:127–49, 2016. <https://doi.org/10.1016/bs.mcb.2015.06.017>.
- Chen, V. B., Arendall, W. B., r., Headd, J. J., Keedy, D. A., Immormino, R. M., Kapral, G. J., Murray, L. W., Richardson, J. S., and Richardson, D. C. Molprobit: all-atom structure validation for macromolecular crystallography. *Acta Crystallogr D Biol Crystallogr*, 66(Pt 1):12–21, 2010. <https://doi.org/10.1107/S09074444909042073>.
- Chen, Y. and Hill, T. L. Use of Monte Carlo calculations in the study of microtubule subunit kinetics. *Proc Natl Acad Sci U S A*, 80(24):7520–3, 1983.
- Chen, Y. D. and Hill, T. L. Monte Carlo study of the GTP cap in a five-start helix model of a microtubule. *Proc Natl Acad Sci U S A*, 82(4):1131–5, 1985.
- Chi, Z. and Ambrose, C. Microtubule encounter-based catastrophe in Arabidopsis cortical microtubule arrays. *BMC Plant Biol*, 16:18, 2016. <https://doi.org/10.1186/s12870-016-0703-x>.
- Chretien, D., Fuller, S. D., and Karsenti, E. Structure of growing microtubule ends: two-dimensional sheets close into tubes at variable rates. *J Cell Biol*, 129(5):1311–28, 1995. <https://doi.org/10.1083/jcb.129.5.1311>.
- Ciandrini, L., Neri, I., Walter, J. C., Dauloudet, O., and Parmeggiani, A. Motor protein traffic regulation by supply-demand balance of resources. *Phys Biol*, 11(5):056006, 2014. <https://doi.org/10.1088/1478-3975/11/5/056006>.
- Clackson, T., Yang, W., Rozamus, L. W., Hatada, M., Amara, J. F., Rollins, C. T., Stevenson, L. F., Magari, S. R., Wood, S. A., Courage, N. L., Lu, X., Cerasoli, F. J., Gilman, M., and Holt, D. A. Redesigning an FKBP-ligand interface to generate chemical dimerizers with novel specificity. *Proc Natl Acad Sci U S A*, 95(18):10437–42, 1998.
- Coletti, C., Jaroszeski, M. J., Pallaoro, A., Hoff, A. M., Iannotta, S., and Sadow, S. E. Biocompatibility and wettability of crystalline SiC and Si surfaces. *Conf Proc IEEE Eng Med Biol Soc*, 2007:5850–3, 2007. <https://doi.org/10.1109/IEMBS.2007.4353678>.
- Colin, A., Singaravelu, P., They, M., Blanchoin, L., and Gueroui, Z. Actin-network architecture regulates microtubule dynamics. *Curr Biol*, 2018. <https://doi.org/10.1016/j.cub.2018.06.028>.
- Coombes, C. E., Yamamoto, A., Kenzie, M. R., Odde, D. J., and Gardner, M. K. Evolving tip structures can explain age-dependent microtubule catastrophe. *Curr Biol*, 23(14):1342–8, 2013. <https://doi.org/10.1016/j.cub.2013.05.059>.

- Cosentino Lagomarsino, M., Tanase, C., Vos, J. W., Emons, A. M., Mulder, B. M., and Dogterom, M. Microtubule organization in three-dimensional confined geometries: evaluating the role of elasticity through a combined in vitro and modeling approach. *Biophys J*, 92(3):1046–57, 2007. <https://doi.org/10.1529/biophysj.105.076893>.
- Cowtan, K. The Buccaneer software for automated model building. 1. tracing protein chains. *Acta Crystallogr D Biol Crystallogr*, 62(Pt 9):1002–11, 2006. <https://doi.org/10.1107/S0907444906022116>.
- Crosson, S. and Moffat, K. Structure of a flavin-binding plant photoreceptor domain: insights into light-mediated signal transduction. *Proc Natl Acad Sci U S A*, 98(6): 2995–3000, 2001. <https://doi.org/10.1073/pnas.051520298>.
- Cytrynbaum, E. N., Scholey, J. M., and Mogilner, A. A force balance model of early spindle pole separation in *Drosophila* embryos. *Biophys J*, 84(2 Pt 1):757–69, 2003. [https://doi.org/10.1016/S0006-3495\(03\)74895-4](https://doi.org/10.1016/S0006-3495(03)74895-4).
- Daga, R. R., Yonetani, A., and Chang, F. Asymmetric microtubule pushing forces in nuclear centering. *Curr Biol*, 16(15):1544–50, 2006. <https://doi.org/10.1016/j.cub.2006.06.026>.
- Das, D., Das, D., and Padinhateeri, R. Force-induced dynamical properties of multiple cytoskeletal filaments are distinct from that of single filaments. *PLoS One*, 9(12): e114014, 2014. <https://doi.org/10.1371/journal.pone.0114014>.
- Deisseroth, K., Feng, G., Majewska, A. K., Miesenbock, G., Ting, A., and Schnitzer, M. J. Next-generation optical technologies for illuminating genetically targeted brain circuits. *J Neurosci*, 26(41):10380–6, 2006. <https://doi.org/10.1523/JNEUROSCI.3863-06.2006>.
- Desai, A. and Mitchison, T. J. Microtubule polymerization dynamics. *Annu Rev Cell Dev Biol*, 13:83–117, 1997. <https://doi.org/10.1146/annurev.cellbio.13.1.83>.
- Desai, A., Verma, S., Mitchison, T. J., and Walczak, C. E. Kin I kinesins are microtubule-destabilizing enzymes. *Cell*, 96(1):69–78, 1999.
- Dhar, S., Seitz, O., Halls, M. D., Choi, S., Chabal, Y. J., and Feldman, L. C. Chemical properties of oxidized silicon carbide surfaces upon etching in hydrofluoric acid. *J Am Chem Soc*, 131(46):16808–13, 2009. <https://doi.org/10.1021/ja9053465>.
- di Pietro, F., Echard, A., and Morin, X. Regulation of mitotic spindle orientation: an integrated view. *EMBO Rep*, 17(8):1106–30, 2016. <https://doi.org/10.15252/embr.201642292>.
- Dimitrov, A., Quesnoit, M., Moutel, S., Cantaloube, I., Pous, C., and Perez, F. Detection of GTP-tubulin conformation in vivo reveals a role for GTP remnants in microtubule rescues. *Science*, 322(5906):1353–6, 2008. <https://doi.org/10.1126/science.1165401>.

- Dogterom, M. and Koenderink, G. H. Actin-microtubule crosstalk in cell biology. *Nat Rev Mol Cell Biol*, 20(1):38–54, 2019. <https://doi.org/10.1038/s41580-018-0067-1>.
- Dogterom, M. and Yurke, B. Measurement of the force-velocity relation for growing microtubules. *Science*, 278(5339):856–60, 1997.
- Dogterom, M., Kerssemakers, J. W., Romet-Lemonne, G., and Janson, M. E. Force generation by dynamic microtubules. *Curr Opin Cell Biol*, 17(1):67–74, 2005. <https://doi.org/10.1016/j.ceb.2004.12.011>.
- Doodhi, H., Prota, A. E., Rodriguez-Garcia, R., Xiao, H., Custar, D. W., Bargsten, K., Katrukha, E. A., Hilbert, M., Hua, S., Jiang, K., Grigoriev, I., Yang, C. P., Cox, D., Horwitz, S. B., Kapitein, L. C., Akhmanova, A., and Steinmetz, M. O. Termination of protofilament elongation by eribulin induces lattice defects that promote microtubule catastrophes. *Curr Biol*, 26(13):1713–21, 2016. <https://doi.org/10.1016/j.cub.2016.04.053>.
- Drabek, K., van Ham, M., Stepanova, T., Draegestein, K., van Horssen, R., Sayas, C. L., Akhmanova, A., Ten Hagen, T., Smits, R., Fodde, R., Grosveld, F., and Galjart, N. Role of CLASP2 in microtubule stabilization and the regulation of persistent motility. *Curr Biol*, 16(22):2259–64, 2006. <https://doi.org/10.1016/j.cub.2006.09.065>.
- Dragestein, K. A., van Cappellen, W. A., van Haren, J., Tsibidis, G. D., Akhmanova, A., Knoch, T. A., Grosveld, F., and Galjart, N. Dynamic behavior of GFP-CLIP-170 reveals fast protein turnover on microtubule plus ends. *J Cell Biol*, 180(4):729–37, 2008. <https://doi.org/10.1083/jcb.200707203>.
- Duan, L., Hope, J., Ong, Q., Lou, H. Y., Kim, N., McCarthy, C., Acero, V., Lin, M. Z., and Cui, B. Understanding CRY2 interactions for optical control of intracellular signaling. *Nat Commun*, 8(1):547, 2017. <https://doi.org/10.1038/s41467-017-00648-8>.
- Duellberg, C., Trokter, M., Jha, R., Sen, I., Steinmetz, M. O., and Surrey, T. Reconstitution of a hierarchical +TIP interaction network controlling microtubule end tracking of dynein. *Nat Cell Biol*, 16(8):804–11, 2014. <https://doi.org/10.1038/ncb2999>.
- Duellberg, C., Cade, N. I., Holmes, D., and Surrey, T. The size of the EB cap determines instantaneous microtubule stability. *Elife*, 5, 2016. <https://doi.org/10.7554/eLife.13470>.
- Duellberg, C., Cade, N. I., and Surrey, T. Microtubule aging probed by microfluidics-assisted tubulin washout. *Mol Biol Cell*, 27(22):3563–3573, 2016. <https://doi.org/10.1091/mbc.E16-07-0548>.
- Dujardin, D. L., Barnhart, L. E., Stehman, S. A., Gomes, E. R., Gundersen, G. G., and Vallee, R. B. A role for cytoplasmic dynein and LIS1 in directed cell movement. *J Cell Biol*, 163(6):1205–11, 2003. <https://doi.org/10.1083/jcb.200310097>.

- Efimov, A., Kharitonov, A., Efimova, N., Loncarek, J., Miller, P. M., Andreyeva, N., Gleeson, P., Galjart, N., Maia, A. R., McLeod, I. X., Yates, J. R., r., Maiato, H., Khodjakov, A., Akhmanova, A., and Kaverina, I. Asymmetric CLASP-dependent nucleation of noncentrosomal microtubules at the trans-Golgi network. *Dev Cell*, 12(6):917–30, 2007. <https://doi.org/10.1016/j.devcel.2007.04.002>.
- Emsley, P. and Cowtan, K. Coot: model-building tools for molecular graphics. *Acta Crystallogr D Biol Crystallogr*, 60(Pt 12 Pt 1):2126–32, 2004. <https://doi.org/10.1107/S09074444904019158>.
- Etienne-Manneville, S. Microtubules in cell migration. *Annu Rev Cell Dev Biol*, 29:471–99, 2013. <https://doi.org/10.1146/annurev-cellbio-101011-155711>.
- Faivre-Moskalenko, C. and Dogterom, M. Dynamics of microtubule asters in micro-fabricated chambers: the role of catastrophes. *Proc Natl Acad Sci U S A*, 99(26):16788–93, 2002. <https://doi.org/10.1073/pnas.252407099>.
- Fielmich, L. E., Schmidt, R., Dickinson, D. J., Goldstein, B., Akhmanova, A., and Van den Heuvel, S. Optogenetic dissection of mitotic spindle positioning in vivo. *Elife*, 7, 2018. <https://doi.org/10.7554/eLife.38198>.
- Fink, G., Schuchardt, I., Colombelli, J., Stelzer, E., and Steinberg, G. Dynein-mediated pulling forces drive rapid mitotic spindle elongation in *Ustilago maydis*. *EMBO J*, 25(20):4897–908, 2006. <https://doi.org/10.1038/sj.emboj.7601354>.
- Fink, G., Hajdo, L., Skowronek, K. J., Reuther, C., Kasprzak, A. A., and Diez, S. The mitotic kinesin-14 Ncd drives directional microtubule-microtubule sliding. *Nat Cell Biol*, 11(6):717–23, 2009. <https://doi.org/10.1038/ncb1877>.
- Flyvbjerg, H., Holy, T. E., and Leibler, S. Microtubule dynamics: Caps, catastrophes, and coupled hydrolysis. *Phys Rev E Stat Phys Plasmas Fluids Relat Interdiscip Topics*, 54(5):5538–5560, 1996.
- Fourest-Lieuvin, A., Peris, L., Gache, V., Garcia-Saez, I., Juillan-Binard, C., Lantez, V., and Job, D. Microtubule regulation in mitosis: tubulin phosphorylation by the cyclin-dependent kinase Cdk1. *Mol Biol Cell*, 17(3):1041–50, 2006. <https://doi.org/10.1091/mbc.E05-07-0621>.
- Franck, A. D., Powers, A. F., Gestaut, D. R., Gonen, T., Davis, T. N., and Asbury, C. L. Tension applied through the Dam1 complex promotes microtubule elongation providing a direct mechanism for length control in mitosis. *Nat Cell Biol*, 9(7):832–7, 2007. <https://doi.org/10.1038/ncb1609>.
- Galjart, N. CLIPs and CLASPs and cellular dynamics. *Nat Rev Mol Cell Biol*, 6(6):487–98, 2005. <https://doi.org/10.1038/nrm1664>.
- Galjart, N. Plus-end-tracking proteins and their interactions at microtubule ends. *Curr Biol*, 20(12):R528–37, 2010. <https://doi.org/10.1016/j.cub.2010.05.022>.

- Ganguly, A., Yang, H., Zhang, H., Cabral, F., and Patel, K. D. Microtubule dynamics control tail retraction in migrating vascular endothelial cells. *Mol Cancer Ther*, 12(12):2837–46, 2013. <https://doi.org/10.1158/1535-7163.MCT-13-0401>.
- Gardner, M. K., Charlebois, B. D., Janosi, I. M., Howard, J., Hunt, A. J., and Odde, D. J. Rapid microtubule self-assembly kinetics. *Cell*, 146(4):582–92, 2011. <https://doi.org/10.1016/j.cell.2011.06.053>.
- Gardner, M. K., Zanic, M., Gell, C., Bormuth, V., and Howard, J. Depolymerizing kinesins Kip3 and MCAK shape cellular microtubule architecture by differential control of catastrophe. *Cell*, 147(5):1092–103, 2011. <https://doi.org/10.1016/j.cell.2011.10.037>.
- Gardner, M. K., Zanic, M., and Howard, J. Microtubule catastrophe and rescue. *Curr Opin Cell Biol*, 25(1):14–22, 2013. <https://doi.org/10.1016/j.ceb.2012.09.006>.
- Gell, C., Bormuth, V., Brouhard, G. J., Cohen, D. N., Diez, S., Friel, C. T., Helenius, J., Nitzsche, B., Petzold, H., Ribbe, J., Schaffer, E., Stear, J. H., Trushko, A., Varga, V., Widlund, P. O., Zanic, M., and Howard, J. Microtubule dynamics reconstituted in vitro and imaged by single-molecule fluorescence microscopy. *Methods Cell Biol*, 95:221–45, 2010. [https://doi.org/10.1016/S0091-679X\(10\)95013-9](https://doi.org/10.1016/S0091-679X(10)95013-9).
- Gregoretto, I. V., Margolin, G., Alber, M. S., and Goodson, H. V. Insights into cytoskeletal behavior from computational modeling of dynamic microtubules in a cell-like environment. *J Cell Sci*, 119(Pt 22):4781–8, 2006. <https://doi.org/10.1242/jcs.03240>.
- Grigoriev, I., Gouveia, S. M., van der Vaart, B., Demmers, J., Smyth, J. T., Honnappa, S., Splinter, D., Steinmetz, M. O., Putney, J. W., J., Hoogenraad, C. C., and Akhmanova, A. STIM1 is a MT-plus-end-tracking protein involved in remodeling of the ER. *Curr Biol*, 18(3):177–82, 2008. <https://doi.org/10.1016/j.cub.2007.12.050>.
- Grill, S. W. and Hyman, A. A. Spindle positioning by cortical pulling forces. *Dev Cell*, 8(4):461–5, 2005. <https://doi.org/10.1016/j.devcel.2005.03.014>.
- Grill, S. W., Howard, J., Schaffer, E., Stelzer, E. H., and Hyman, A. A. The distribution of active force generators controls mitotic spindle position. *Science*, 301(5632):518–21, 2003. <https://doi.org/10.1126/science.1086560>.
- Grimaldi, A. D., Maki, T., Fitton, B. P., Roth, D., Yampolsky, D., Davidson, M. W., Svitkina, T., Straube, A., Hayashi, I., and Kaverina, I. CLASPs are required for proper microtubule localization of end-binding proteins. *Dev Cell*, 30(3):343–52, 2014. <https://doi.org/10.1016/j.devcel.2014.06.026>.
- Grishchuk, E. L., Molodtsov, M. I., Ataullakhanov, F. I., and McIntosh, J. R. Force production by disassembling microtubules. *Nature*, 438(7066):384–8, 2005. <https://doi.org/10.1038/nature04132>.

- Guild, J., Ginzberg, M. B., Hueschen, C. L., Mitchison, T. J., and Dumont, S. Increased lateral microtubule contact at the cell cortex is sufficient to drive mammalian spindle elongation. *Mol Biol Cell*, 28(14):1975–1983, 2017. <https://doi.org/10.1091/mbc.E17-03-0171>.
- Guizar-Sicairos, M., Thurman, S. T., and Fienup, J. R. Efficient subpixel image registration algorithms. *Opt Lett*, 33(2):156–8, 2008.
- Guntas, G., Hallett, R. A., Zimmerman, S. P., Williams, T., Yumerefendi, H., Bear, J. E., and Kuhlman, B. Engineering an improved light-induced dimer (iLID) for controlling the localization and activity of signaling proteins. *Proc Natl Acad Sci U S A*, 112(1):112–7, 2015. <https://doi.org/10.1073/pnas.1417910112>.
- Gurel, P. S., Hatch, A. L., and Higgs, H. N. Connecting the cytoskeleton to the endoplasmic reticulum and Golgi. *Curr Biol*, 24(14):R660–R672, 2014. <https://doi.org/10.1016/j.cub.2014.05.033>.
- Hallak, M. E., Rodriguez, J. A., Barra, H. S., and Caputto, R. Release of tyrosine from tyrosinated tubulin. some common factors that affect this process and the assembly of tubulin. *FEBS Lett*, 73(2):147–50, 1977.
- Hallett, R. A., Zimmerman, S. P., Yumerefendi, H., Bear, J. E., and Kuhlman, B. Correlating in vitro and in vivo activities of light-inducible dimers: A cellular optogenetics guide. *ACS Synth Biol*, 5(1):53–64, 2016. <https://doi.org/10.1021/acssynbio.5b00119>.
- Hammond, J. W., Cai, D., and Verhey, K. J. Tubulin modifications and their cellular functions. *Curr Opin Cell Biol*, 20(1):71–6, 2008. <https://doi.org/10.1016/j.cub.2007.11.010>.
- Hannak, E. and Heald, R. Xorbit/CLASP links dynamic microtubules to chromosomes in the *Xenopus* meiotic spindle. *J Cell Biol*, 172(1):19–25, 2006. <https://doi.org/10.1083/jcb.200508180>.
- Harper, S. M., Neil, L. C., and Gardner, K. H. Structural basis of a phototropin light switch. *Science*, 301(5639):1541–4, 2003. <https://doi.org/10.1126/science.1086810>.
- Heald, R., Tournebize, R., Blank, T., Sandaltzopoulos, R., Becker, P., Hyman, A., and Karsenti, E. Self-organization of microtubules into bipolar spindles around artificial chromosomes in *Xenopus* egg extracts. *Nature*, 382(6590):420–5, 1996. <https://doi.org/10.1038/382420a0>.
- Hendricks, A. G., Lazarus, J. E., Persson, E., Gardner, M. K., Odde, D. J., Goldman, Y. E., and Holzbaur, E. L. Dynein tethers and stabilizes dynamic microtubule plus ends. *Curr Biol*, 22(7):632–7, 2012. <https://doi.org/10.1016/j.cub.2012.02.023>.

- Hernandez-Vega, A., Braun, M., Scharrel, L., Jahnelt, M., Wegmann, S., Hyman, B. T., Alberti, S., Diez, S., and Hyman, A. A. Local nucleation of microtubule bundles through tubulin concentration into a condensed tau phase. *Cell Rep*, 20(10):2304–2312, 2017. <https://doi.org/10.1016/j.celrep.2017.08.042>.
- Holy, T. E., Dogterom, M., Yurke, B., and Leibler, S. Assembly and positioning of microtubule asters in microfabricated chambers. *Proc Natl Acad Sci U S A*, 94(12): 6228–31, 1997. <https://doi.org/10.1073/pnas.94.12.6228>.
- Honnappa, S., Gouveia, S. M., Weisbrich, A., Damberger, F. F., Bhavesh, N. S., Jawhari, H., Grigoriev, I., van Rijssel, F. J., Buey, R. M., Lawera, A., Jelesarov, I., Winkler, F. K., Wuthrich, K., Akhmanova, A., and Steinmetz, M. O. An EB1-binding motif acts as a microtubule tip localization signal. *Cell*, 138(2):366–76, 2009. <https://doi.org/10.1016/j.cell.2009.04.065>.
- Hoog, J. L., Schwartz, C., Noon, A. T., O'Toole, E. T., Mastronarde, D. N., McIntosh, J. R., and Antony, C. Organization of interphase microtubules in fission yeast analyzed by electron tomography. *Dev Cell*, 12(3):349–61, 2007. <https://doi.org/10.1016/j.devcel.2007.01.020>.
- Howard, J. Elastic and damping forces generated by confined arrays of dynamic microtubules. *Phys Biol*, 3(1):54–66, 2006. <https://doi.org/10.1088/1478-3975/3/1/006>.
- Howard, J. and Hyman, A. A. Growth, fluctuation and switching at microtubule plus ends. *Nat Rev Mol Cell Biol*, 10(8):569–74, 2009. <https://doi.org/10.1038/nrm2713>.
- Howard, J., Hudspeth, A. J., and Vale, R. D. Movement of microtubules by single kinesin molecules. *Nature*, 342(6246):154–8, 1989. <https://doi.org/10.1038/342154a0>.
- Hyman, A. A., Salser, S., Drechsel, D. N., Unwin, N., and Mitchison, T. J. Role of GTP hydrolysis in microtubule dynamics: information from a slowly hydrolyzable analogue, GMPCPP. *Mol Biol Cell*, 3(10):1155–67, 1992.
- Iliescu, C., Chen, B. T., Poenar, D. P., and Lee, Y. Y. PECVD amorphous silicon carbide membranes for cell culturing. *Sensors and Actuators B-Chemical*, 129(1):404–411, 2008. <https://doi.org/10.1016/j.snb.2007.08.043>.
- Iliescu, C., Chen, B. T., Wei, J. S., and Pang, A. J. Characterisation of silicon carbide films deposited by plasma-enhanced chemical vapour deposition. *Thin Solid Films*, 516(16):5189–5193, 2008. <https://doi.org/10.1016/j.tsf.2007.07.013>.
- Imafuku, Y., Mitarai, N., Tawada, K., and Nakanishi, H. Anomalous fluctuations in sliding motion of cytoskeletal filaments driven by molecular motors: model simulations. *J Phys Chem B*, 112(5):1487–93, 2008. <https://doi.org/10.1021/jp0748381>.

- Inoue, S. and Salmon, E. D. Force generation by microtubule assembly/disassembly in mitosis and related movements. *Mol Biol Cell*, 6(12):1619–40, 1995.
- Iuliano, J. N., Gil, A. A., Laptенок, S. P., Hall, C. R., Tolentino Collado, J., Lukacs, A., Hag Ahmed, S. A., Abyad, J., Daryaei, T., Greetham, G. M., Sazanovich, I. V., Illarionov, B., Bacher, A., Fischer, M., Towrie, M., French, J. B., Meech, S. R., and Tonge, P. J. Variation in LOV photoreceptor activation dynamics probed by time-resolved infrared spectroscopy. *Biochemistry*, 57(5):620–630, 2018. <https://doi.org/10.1021/acs.biochem.7b01040>.
- Janke, C. The tubulin code: molecular components, readout mechanisms, and functions. *J Cell Biol*, 206(4):461–72, 2014. <https://doi.org/10.1083/jcb.201406055>.
- Janson, M. E., de Dood, M. E., and Dogterom, M. Dynamic instability of microtubules is regulated by force. *J Cell Biol*, 161(6):1029–34, 2003. <https://doi.org/10.1083/jcb.200301147>.
- Janson, M. E., Loughlin, R., Loiodice, I., Fu, C., Brunner, D., Nedelec, F. J., and Tran, P. T. Crosslinkers and motors organize dynamic microtubules to form stable bipolar arrays in fission yeast. *Cell*, 128(2):357–68, 2007. <https://doi.org/10.1016/j.cell.2006.12.030>.
- Joshi, H. C. and Cleveland, D. W. Differential utilization of  $\beta$ -tubulin isoforms in differentiating neurites. *J Cell Biol*, 109(2):663–73, 1989.
- Juniper, M. P. N., Weiss, M., Platzman, I., Spatz, J. P., and Surrey, T. Spherical network contraction forms microtubule asters in confinement. *Soft Matter*, 14(6):901–909, 2018. <https://doi.org/10.1039/c7sm01718a>.
- Kabsch, W. Integration, scaling, space-group assignment and post-refinement. *Acta Crystallogr D Biol Crystallogr*, 66(Pt 2):133–44, 2010. <https://doi.org/10.1107/S0907444909047374>.
- Kabsch, W. Xds. *Acta Crystallogr D Biol Crystallogr*, 66(Pt 2):125–32, 2010. <https://doi.org/10.1107/S0907444909047337>.
- Kalisch, S. M., Laan, L., and Dogterom, M. Force generation by dynamic microtubules in vitro. *Methods Mol Biol*, 777:147–65, 2011. [https://doi.org/10.1007/978-1-61779-252-6\\_11](https://doi.org/10.1007/978-1-61779-252-6_11).
- Kaplan, J. H. and Somlyo, A. P. Flash photolysis of caged compounds: new tools for cellular physiology. *Trends Neurosci*, 12(2):54–9, 1989.
- Karr, T. L. and Purich, D. L. Examination of tubulin-nucleotide interactions by protein fluorescence quenching measurements. *Biochem Biophys Res Commun*, 84(4):957–61, 1978.

- Kennis, J. T., Crosson, S., Gauden, M., van Stokkum, I. H., Moffat, K., and van Grondelle, R. Primary reactions of the LOV2 domain of phototropin, a plant blue-light photoreceptor. *Biochemistry*, 42(12):3385–92, 2003. <https://doi.org/10.1021/bi034022k>.
- Kerssemakers, J. W., Janson, M. E., Van der Horst, A., and Dogterom, M. Optical trap setup for measuring microtubule pushing forces. *Applied Physics Letters*, 83(21): 4441–4443, 2003. <https://doi.org/10.1063/1.1629796>.
- Kerssemakers, J. W., Munteanu, E. L., Laan, L., Noetzel, T. L., Janson, M. E., and Dogterom, M. Assembly dynamics of microtubules at molecular resolution. *Nature*, 442(7103):709–12, 2006. <https://doi.org/10.1038/nature04928>.
- Keya, J. J., Suzuki, R., Kabir, A. M. R., Inoue, D., Asanuma, H., Sada, K., Hess, H., Kuzuya, A., and Kakugo, A. DNA-assisted swarm control in a biomolecular motor system. *Nat Commun*, 9(1):453, 2018. <https://doi.org/10.1038/s41467-017-02778-5>.
- Kikumoto, M., Kurachi, M., Tosa, V., and Tashiro, H. Flexural rigidity of individual microtubules measured by a buckling force with optical traps. *Biophys J*, 90(5): 1687–96, 2006. <https://doi.org/10.1529/biophysj.104.055483>.
- Kim, T.; Rice, L. A role for long-range, through-lattice coupling in microtubule catastrophe. *bioRxiv*, 2018. <https://doi.org/10.1101/443283>.
- Kiyomitsu, T. and Cheeseman, I. M. Cortical dynein and asymmetric membrane elongation coordinately position the spindle in anaphase. *Cell*, 154(2):391–402, 2013. <https://doi.org/10.1016/j.cell.2013.06.010>.
- Kollman, J. M., Merdes, A., Mourey, L., and Agard, D. A. Microtubule nucleation by  $\gamma$ -tubulin complexes. *Nat Rev Mol Cell Biol*, 12(11):709–21, 2011. <https://doi.org/10.1038/nrm3209>.
- Kolomeisky, A. B. and Fisher, M. E. Force-velocity relation for growing microtubules. *Biophys J*, 80(1):149–54, 2001. [https://doi.org/10.1016/S0006-3495\(01\)76002-X](https://doi.org/10.1016/S0006-3495(01)76002-X).
- Komarova, Y., Lansbergen, G., Galjart, N., Grosveld, F., Borisov, G. G., and Akhmanova, A. EB1 and EB3 control CLIP dissociation from the ends of growing microtubules. *Mol Biol Cell*, 16(11):5334–45, 2005. <https://doi.org/10.1091/mbc.E05-07-0614>.
- Komarova, Y., De Groot, C. O., Grigoriev, I., Gouveia, S. M., Munteanu, E. L., Schober, J. M., Honnappa, S., Buey, R. M., Hoogenraad, C. C., Dogterom, M., Borisov, G. G., Steinmetz, M. O., and Akhmanova, A. Mammalian end binding proteins control persistent microtubule growth. *J Cell Biol*, 184(5):691–706, 2009. <https://doi.org/10.1083/jcb.200807179>.

- Komarova, Y. A., Vorobjev, I. A., and Borisy, G. G. Life cycle of MTs: persistent growth in the cell interior, asymmetric transition frequencies and effects of the cell boundary. *J Cell Sci*, 115(Pt 17):3527–39, 2002.
- Kotak, S. and Gonczy, P. Mechanisms of spindle positioning: cortical force generators in the limelight. *Curr Opin Cell Biol*, 25(6):741–8, 2013. <https://doi.org/10.1016/j.ceb.2013.07.008>.
- Kubala, M. H., Kovtun, O., Alexandrov, K., and Collins, B. M. Structural and thermodynamic analysis of the GFP:GFP-nanobody complex. *Protein Sci*, 19(12):2389–401, 2010. <https://doi.org/10.1002/pro.519>.
- Kumar, K. R., Kamei, T., Fukaminato, T., and Tamaoki, N. Complete ON/OFF photo-switching of the motility of a nanobiomolecular machine. *ACS Nano*, 8(5):4157–65, 2014. <https://doi.org/10.1021/nn5010342>.
- Kurachi, M., Hoshi, M., and Tashiro, H. Buckling of a single microtubule by optical trapping forces: direct measurement of microtubule rigidity. *Cell Motil Cytoskeleton*, 30(3):221–8, 1995. <https://doi.org/10.1002/cm.970300306>.
- Laan, L., Husson, J., Munteanu, E. L., Kerssemakers, J. W., and Dogterom, M. Force-generation and dynamic instability of microtubule bundles. *Proc Natl Acad Sci U S A*, 105(26):8920–5, 2008. <https://doi.org/10.1073/pnas.0710311105>.
- Laan, L., Pavin, N., Husson, J., Romet-Lemonne, G., van Duijn, M., Lopez, M. P., Vale, R. D., Julicher, F., Reck-Peterson, S. L., and Dogterom, M. Cortical dynein controls microtubule dynamics to generate pulling forces that position microtubule asters. *Cell*, 148(3):502–14, 2012. <https://doi.org/10.1016/j.cell.2012.01.007>.
- Laan, L., Roth, S., and Dogterom, M. End-on microtubule-dynein interactions and pulling-based positioning of microtubule organizing centers. *Cell Cycle*, 11(20):3750–7, 2012. <https://doi.org/10.4161/cc.21753>.
- Lachaine, R., Boutopoulos, C., Lajoie, P. Y., Boulais, E., and Meunier, M. Rational design of plasmonic nanoparticles for enhanced cavitation and cell perforation. *Nano Lett*, 16(5):3187–94, 2016. <https://doi.org/10.1021/acs.nanolett.6b00562>.
- Lacroix, B., Bourdages, K. G., Dorn, J. F., Ihara, S., Sherwood, D. R., Maddox, P. S., and Maddox, A. S. In situ imaging in *C. elegans* reveals developmental regulation of microtubule dynamics. *Dev Cell*, 29(2):203–16, 2014. <https://doi.org/10.1016/j.devcel.2014.03.007>.
- Lam, A. T., Tsitkov, S., Zhang, Y., and Hess, H. Reversibly bound Kinesin-1 motor proteins propelling microtubules demonstrate dynamic recruitment of active building blocks. *Nano Lett*, 18(2):1530–1534, 2018. <https://doi.org/10.1021/acs.nanolett.7b05361>.

- Lansbergen, G., Grigoriev, I., Mimori-Kiyosue, Y., Ohtsuka, T., Higa, S., Kitajima, I., Demmers, J., Galjart, N., Houtsmuller, A. B., Grosveld, F., and Akhmanova, A. CLASPs attach microtubule plus ends to the cell cortex through a complex with LL5 $\beta$ . *Dev Cell*, 11(1):21–32, 2006. <https://doi.org/10.1016/j.devcel.2006.05.012>.
- Lansky, Z., Braun, M., Ludecke, A., Schlierf, M., ten Wolde, P. R., Janson, M. E., and Diez, S. Diffusible crosslinkers generate directed forces in microtubule networks. *Cell*, 160(6):1159–68, 2015. <https://doi.org/10.1016/j.cell.2015.01.051>.
- Lawrence, E. J., Arpag, G., Norris, S. R., and Zanic, M. Human CLASP2 specifically regulates microtubule catastrophe and rescue. *Mol Biol Cell*, 29(10):1168–1177, 2018. <https://doi.org/10.1091/mbc.E18-01-0016>.
- Leano, J. B., Rogers, S. L., and Slep, K. C. A cryptic TOG domain with a distinct architecture underlies CLASP-dependent bipolar spindle formation. *Structure*, 21(6): 939–50, 2013. <https://doi.org/10.1016/j.str.2013.04.018>.
- Leduc, C., Padberg-Gehle, K., Varga, V., Helbing, D., Diez, S., and Howard, J. Molecular crowding creates traffic jams of kinesin motors on microtubules. *Proc Natl Acad Sci U S A*, 109(16):6100–5, 2012. <https://doi.org/10.1073/pnas.1107281109>.
- Leterrier, C., Dubey, P., and Roy, S. The nano-architecture of the axonal cytoskeleton. *Nat Rev Neurosci*, 18(12):713–726, 2017. <https://doi.org/10.1038/nrn.2017.129>.
- Letort, G., Nedelec, F., Blanchoin, L., and Thery, M. Centrosome centering and de-centering by microtubule network rearrangement. *Mol Biol Cell*, 27(18):2833–43, 2016. <https://doi.org/10.1091/mbc.E16-06-0395>.
- Leung, C. L., Sun, D., Zheng, M., Knowles, D. R., and Liem, R. K. Microtubule actin cross-linking factor (MACF): a hybrid of dystonin and dystrophin that can interact with the actin and microtubule cytoskeletons. *J Cell Biol*, 147(6):1275–86, 1999.
- Levskaya, A., Weiner, O. D., Lim, W. A., and Voigt, C. A. Spatiotemporal control of cell signalling using a light-switchable protein interaction. *Nature*, 461(7266):997–1001, 2009. <https://doi.org/10.1038/nature08446>.
- Li, P., Banjade, S., Cheng, H. C., Kim, S., Chen, B., Guo, L., Llaguno, M., Hollingsworth, J. V., King, D. S., Banani, S. F., Russo, P. S., Jiang, Q. X., Nixon, B. T., and Rosen, M. K. Phase transitions in the assembly of multivalent signalling proteins. *Nature*, 483(7389):336–40, 2012. <https://doi.org/10.1038/nature10879>.
- Li, T., Zheng, F., Cheung, M., Wang, F., and Fu, C. Fission yeast mitochondria are distributed by dynamic microtubules in a motor-independent manner. *Sci Rep*, 5: 11023, 2015. <https://doi.org/10.1038/srep11023>.

- Logarinho, E., Maffini, S., Barisic, M., Marques, A., Toso, A., Meraldi, P., and Maiato, H. CLASPs prevent irreversible multipolarity by ensuring spindle-pole resistance to traction forces during chromosome alignment. *Nat Cell Biol*, 14(3):295–303, 2012. <https://doi.org/10.1038/ncb2423>.
- Loiodice, I., Staub, J., Setty, T. G., Nguyen, N. P., Paoletti, A., and Tran, P. T. Ase1p organizes antiparallel microtubule arrays during interphase and mitosis in fission yeast. *Mol Biol Cell*, 16(4):1756–68, 2005. <https://doi.org/10.1091/mbc.E04-10-0899>.
- Losi, A., Gardner, K. H., and Moglich, A. Blue-light receptors for optogenetics. *Chem Rev*, 118(21):10659–10709, 2018. <https://doi.org/10.1021/acs.chemrev.8b00163>.
- Lungu, O. I., Hallett, R. A., Choi, E. J., Aiken, M. J., Hahn, K. M., and Kuhlman, B. Designing photoswitchable peptides using the AsLOV2 domain. *Chem Biol*, 19(4):507–17, 2012. <https://doi.org/10.1016/j.chembiol.2012.02.006>.
- Maiato, H., Fairley, E. A., Rieder, C. L., Swedlow, J. R., Sunkel, C. E., and Earnshaw, W. C. Human CLASP1 is an outer kinetochore component that regulates spindle microtubule dynamics. *Cell*, 113(7):891–904, 2003.
- Maiato, H., Khodjakov, A., and Rieder, C. L. Drosophila CLASP is required for the incorporation of microtubule subunits into fluxing kinetochore fibres. *Nat Cell Biol*, 7(1):42–7, 2005. <https://doi.org/10.1038/ncb1207>.
- Maki, T., Grimaldi, A. D., Fuchigami, S., Kaverina, I., and Hayashi, I. CLASP2 has two distinct TOG domains that contribute differently to microtubule dynamics. *J Mol Biol*, 427(14):2379–95, 2015. <https://doi.org/10.1016/j.jmb.2015.05.012>.
- Maly, V. I. and Maly, I. V. Symmetry, stability, and reversibility properties of idealized confined microtubule cytoskeletons. *Biophys J*, 99(9):2831–40, 2010. <https://doi.org/10.1016/j.bpj.2010.09.017>.
- Mandelkow, E. M., Schultheiss, R., Rapp, R., Muller, M., and Mandelkow, E. On the surface lattice of microtubules: helix starts, protofilament number, seam, and handedness. *J Cell Biol*, 102(3):1067–73, 1986.
- Mandelkow, E. M., Mandelkow, E., and Milligan, R. A. Microtubule dynamics and microtubule caps: a time-resolved cryo-electron microscopy study. *J Cell Biol*, 114(5):977–91, 1991.
- Margolin, G., Gregoret, I. V., Goodson, H. V., and Alber, M. S. Analysis of a mesoscopic stochastic model of microtubule dynamic instability. *Phys Rev E Stat Nonlin Soft Matter Phys*, 74(4 Pt 1):041920, 2006. <https://doi.org/10.1103/PhysRevE.74.041920>.
- Margolin, G., Gregoret, I. V., Cickovski, T. M., Li, C., Shi, W., Alber, M. S., and Goodson, H. V. The mechanisms of microtubule catastrophe and rescue: implications from

- analysis of a dimer-scale computational model. *Mol Biol Cell*, 23(4):642–56, 2012. <https://doi.org/10.1091/mbc.E11-08-0688>.
- Martin, S. R., Schilstra, M. J., and Bayley, P. M. Dynamic instability of microtubules: Monte Carlo simulation and application to different types of microtubule lattice. *Biophys J*, 65(2):578–96, 1993. [https://doi.org/10.1016/S0006-3495\(93\)81091-9](https://doi.org/10.1016/S0006-3495(93)81091-9).
- Martin-Cofreces, N. B., Robles-Valero, J., Cabrero, J. R., Mittelbrunn, M., Gordon-Alonso, M., Sung, C. H., Alarcon, B., Vazquez, J., and Sanchez-Madrid, F. MTOC translocation modulates IS formation and controls sustained T cell signaling. *J Cell Biol*, 182(5):951–62, 2008. <https://doi.org/10.1083/jcb.200801014>.
- Marx, A., Jagla, A., and Mandelkow, E. Microtubule assembly and oscillations induced by flash photolysis of caged-GTP. *Eur Biophys J*, 19(1):1–9, 1990.
- Maton, G., Edwards, F., Lacroix, B., Stefanutti, M., Laband, K., Lieury, T., Kim, T., Espeut, J., Canman, J. C., and Dumont, J. Kinetochore components are required for central spindle assembly. *Nat Cell Biol*, 17(7):953, 2015. <https://doi.org/10.1038/ncb3199>.
- Maurer, S. P., Bieling, P., Cope, J., Hoenger, A., and Surrey, T. GTP $\gamma$ S microtubules mimic the growing microtubule end structure recognized by end-binding proteins (EBs). *Proc Natl Acad Sci U S A*, 108(10):3988–93, 2011. <https://doi.org/10.1073/pnas.1014758108>.
- Maurer, S. P., Fourniol, F. J., Bohner, G., Moores, C. A., and Surrey, T. EBs recognize a nucleotide-dependent structural cap at growing microtubule ends. *Cell*, 149(2):371–82, 2012. <https://doi.org/10.1016/j.cell.2012.02.049>.
- Maurer, S. P., Cade, N. I., Bohner, G., Gustafsson, N., Boutant, E., and Surrey, T. EB1 accelerates two conformational transitions important for microtubule maturation and dynamics. *Curr Biol*, 24(4):372–84, 2014. <https://doi.org/10.1016/j.cub.2013.12.042>.
- Maurer, S. P., Fourniol, F. J., Hoenger, A., and Surrey, T. Seeded microtubule growth for cryoelectron microscopy of end-binding proteins. *Methods Mol Biol*, 1136:247–60, 2014. [https://doi.org/10.1007/978-1-4939-0329-0\\_11](https://doi.org/10.1007/978-1-4939-0329-0_11).
- McDonald, H. B., Stewart, R. J., and Goldstein, L. S. The kinesin-like Ncd protein of *Drosophila* is a minus end-directed microtubule motor. *Cell*, 63(6):1159–65, 1990.
- McIntosh, J. R., O’Toole, E., Morgan, G., Austin, J., Ulyanov, E., Ataullakhanov, F., and Gudimchuk, N. Microtubules grow by the addition of bent guanosine triphosphate tubulin to the tips of curved protofilaments. *J Cell Biol*, 2018. <https://doi.org/10.1083/jcb.201802138>.
- Milias-Argeitis, A., Rullan, M., Aoki, S. K., Buchmann, P., and Khammash, M. Automated optogenetic feedback control for precise and robust regulation of gene expression and cell growth. *Nat Commun*, 7:12546, 2016. <https://doi.org/10.1038/ncomms12546>.

- Mimori-Kiyosue, Y. Shaping microtubules into diverse patterns: molecular connections for setting up both ends. *Cytoskeleton (Hoboken)*, 68(11):603–18, 2011. <https://doi.org/10.1002/cm.20540>.
- Mimori-Kiyosue, Y., Grigoriev, I., Lansbergen, G., Sasaki, H., Matsui, C., Severin, E., Galjart, N., Grosveld, E., Vorobjev, I., Tsukita, S., and Akhmanova, A. CLASP1 and CLASP2 bind to EB1 and regulate microtubule plus-end dynamics at the cell cortex. *J Cell Biol*, 168(1):141–53, 2005. <https://doi.org/10.1083/jcb.200405094>.
- Minc, N., Burgess, D., and Chang, F. Influence of cell geometry on division-plane positioning. *Cell*, 144(3):414–26, 2011. <https://doi.org/10.1016/j.cell.2011.01.016>.
- Mishima, M., Maesaki, R., Kasa, M., Watanabe, T., Fukata, M., Kaibuchi, K., and Hakoshima, T. Structural basis for tubulin recognition by cytoplasmic linker protein 170 and its autoinhibition. *Proc Natl Acad Sci U S A*, 104(25):10346–51, 2007. <https://doi.org/10.1073/pnas.0703876104>.
- Mitchison, T. and Kirschner, M. Dynamic instability of microtubule growth. *Nature*, 312(5991):237–42, 1984.
- Mitchison, T. and Kirschner, M. Microtubule assembly nucleated by isolated centrosomes. *Nature*, 312(5991):232–7, 1984.
- Mitchison, T., Wuhr, M., Nguyen, P., Ishihara, K., Groen, A., and Field, C. M. Growth, interaction, and positioning of microtubule asters in extremely large vertebrate embryo cells. *Cytoskeleton (Hoboken)*, 69(10):738–50, 2012. <https://doi.org/10.1002/cm.21050>.
- Mohan, R., Katrukha, E. A., Doodhi, H., Smal, I., Meijering, E., Kapitein, L. C., Steinmetz, M. O., and Akhmanova, A. End-binding proteins sensitize microtubules to the action of microtubule-targeting agents. *Proc Natl Acad Sci U S A*, 110(22):8900–5, 2013. <https://doi.org/10.1073/pnas.1300395110>.
- Molodtsov, M. I., Ermakova, E. A., Shnol, E. E., Grishchuk, E. L., McIntosh, J. R., and Ataullakhanov, F. I. A molecular-mechanical model of the microtubule. *Biophys J*, 88(5):3167–79, 2005. <https://doi.org/10.1529/biophysj.104.051789>.
- Montenegro Gouveia, S., Leslie, K., Kapitein, L. C., Buey, R. M., Grigoriev, I., Wagenbach, M., Smal, I., Meijering, E., Hoogenraad, C. C., Wordeman, L., Steinmetz, M. O., and Akhmanova, A. In vitro reconstitution of the functional interplay between MCAK and EB3 at microtubule plus ends. *Curr Biol*, 20(19):1717–22, 2010. <https://doi.org/10.1016/j.cub.2010.08.020>.
- Moore, J. K. and Cooper, J. A. Coordinating mitosis with cell polarity: Molecular motors at the cell cortex. *Semin Cell Dev Biol*, 21(3):283–9, 2010. <https://doi.org/10.1016/j.semcdb.2010.01.020>.

- Moriwaki, T. and Goshima, G. Five factors can reconstitute all three phases of microtubule polymerization dynamics. *J Cell Biol*, 215(3):357–368, 2016. <https://doi.org/10.1083/jcb.201604118>.
- Muller-Reichert, T., Chretien, D., Severin, E., and Hyman, A. A. Structural changes at microtubule ends accompanying GTP hydrolysis: information from a slowly hydrolyzable analogue of GTP, guanylyl (alpha,beta)methylenediphosphate. *Proc Natl Acad Sci U S A*, 95(7):3661–6, 1998.
- Nakamura, M., Chen, L., Howes, S. C., Schindler, T. D., Nogales, E., and Bryant, Z. Remote control of myosin and kinesin motors using light-activated gearshifting. *Nat Nanotechnol*, 9(9):693–7, 2014. <https://doi.org/10.1038/nnano.2014.147>.
- Nawrotek, A., Knossow, M., and Gigant, B. The determinants that govern microtubule assembly from the atomic structure of GTP-tubulin. *J Mol Biol*, 412(1):35–42, 2011. <https://doi.org/10.1016/j.jmb.2011.07.029>.
- Nedelec, F. J., Surrey, T., Maggs, A. C., and Leibler, S. Self-organization of microtubules and motors. *Nature*, 389(6648):305–8, 1997. <https://doi.org/10.1038/38532>.
- Nguyen-Ngoc, T., Afshar, K., and Gonczy, P. Coupling of cortical dynein and G $\alpha$  proteins mediates spindle positioning in *Caenorhabditis elegans*. *Nat Cell Biol*, 9(11):1294–302, 2007. <https://doi.org/10.1038/ncb1649>.
- Nitzsche, B., Bormuth, V., Brauer, C., Howard, J., Ionov, L., Kerssemakers, J., Korten, T., Leduc, C., Ruhnnow, F., and Diez, S. Studying kinesin motors by optical 3D-nanometry in gliding motility assays. *Methods Cell Biol*, 95:247–71, 2010. [https://doi.org/10.1016/S0091-679X\(10\)95014-0](https://doi.org/10.1016/S0091-679X(10)95014-0).
- Niu, J., Ben Johny, M., Dick, I. E., and Inoue, T. Following optogenetic dimerizers and quantitative prospects. *Biophys J*, 111(6):1132–1140, 2016. <https://doi.org/10.1016/j.bpj.2016.07.040>.
- Nogales, E. A structural view of microtubule dynamics. *Cell Mol Life Sci*, 56(1-2):133–42, 1999.
- Nogales, E. Structural insights into microtubule function. *Annu Rev Biochem*, 69:277–302, 2000. <https://doi.org/10.1146/annurev.biochem.69.1.277>.
- Nogales, E., Whittaker, M., Milligan, R. A., and Downing, K. H. High-resolution model of the microtubule. *Cell*, 96(1):79–88, 1999.
- Oakley, B. R. An abundance of tubulins. *Trends Cell Biol*, 10(12):537–42, 2000. [https://doi.org/10.1016/S0962-8924\(00\)01857-2](https://doi.org/10.1016/S0962-8924(00)01857-2).
- Odde, D. J., Cassimeris, L., and Buettner, H. M. Kinetics of microtubule catastrophe assessed by probabilistic analysis. *Biophys J*, 69(3):796–802, 1995. [https://doi.org/10.1016/S0006-3495\(95\)79953-2](https://doi.org/10.1016/S0006-3495(95)79953-2).

- Odde, D. J., Ma, L., Briggs, A. H., DeMarco, A., and Kirschner, M. W. Microtubule bending and breaking in living fibroblast cells. *J Cell Sci*, 112 ( Pt 19):3283–8, 1999.
- Olieric, N., Kuchen, M., Wagen, S., Sauter, M., Crone, S., Edmondson, S., Frey, D., Ostermeier, C., Steinmetz, M. O., and Jaussi, R. Automated seamless DNA co-transformation cloning with direct expression vectors applying positive or negative insert selection. *BMC Biotechnol*, 10:56, 2010. <https://doi.org/10.1186/1472-6750-10-56>.
- Oliferenko, S. and Balasubramanian, M. K. Astral microtubules monitor metaphase spindle alignment in fission yeast. *Nat Cell Biol*, 4(10):816–20, 2002. <https://doi.org/10.1038/ncb861>.
- Oliveros, A., Guiseppi-Elie, A., and Sadow, S. E. Silicon carbide: a versatile material for biosensor applications. *Biomed Microdevices*, 15(2):353–68, 2013. <https://doi.org/10.1007/s10544-013-9742-3>.
- Padinhateeri, R., Kolomeisky, A. B., and Lacoste, D. Random hydrolysis controls the dynamic instability of microtubules. *Biophys J*, 102(6):1274–83, 2012. <https://doi.org/10.1016/j.bpj.2011.12.059>.
- Palacci, H., Idan, O., Armstrong, M. J., Agarwal, A., Nitta, T., and Hess, H. Velocity fluctuations in Kinesin-1 gliding motility assays originate in motor attachment geometry variations. *Langmuir*, 32(31):7943–50, 2016. <https://doi.org/10.1021/acs.langmuir.6b02369>.
- Palazzo, A. F., Joseph, H. L., Chen, Y. J., Dujardin, D. L., Alberts, A. S., Pfister, K. K., Vallee, R. B., and Gundersen, G. G. Cdc42, dynein, and dynactin regulate MTOC reorientation independent of Rho-regulated microtubule stabilization. *Curr Biol*, 11(19):1536–41, 2001. [https://doi.org/10.1016/S0960-9822\(01\)00475-4](https://doi.org/10.1016/S0960-9822(01)00475-4).
- Pallavicini, C., Monastra, A., Bardeci, N. G., Wetzler, D., Levi, V., and Bruno, L. Characterization of microtubule buckling in living cells. *Eur Biophys J*, 2017. <https://doi.org/10.1007/s00249-017-1207-9>.
- Pathak, G. P., Vrana, J. D., and Tucker, C. L. Optogenetic control of cell function using engineered photoreceptors. *Biol Cell*, 105(2):59–72, 2013. <https://doi.org/10.1111/boc.201200056>.
- Pavin, N., Laan, L., Ma, R., Dogterom, M., and Julicher, F. Positioning of microtubule organizing centers by cortical pushing and pulling forces. *New Journal of Physics*, 14, 2012. <https://doi.org/10.1088/1367-2630/14/10/105025>.
- Perez, F., Diamantopoulos, G. S., Stalder, R., and Kreis, T. E. CLIP-170 highlights growing microtubule ends in vivo. *Cell*, 96(4):517–527, 1999. [https://doi.org/http://dx.doi.org/10.1016/S0092-8674\(00\)80656-X](https://doi.org/http://dx.doi.org/10.1016/S0092-8674(00)80656-X).
- Peris, L., Thery, M., Faure, J., Saoudi, Y., Lafanechere, L., Chilton, J. K., Gordon-Weeks, P., Galjart, N., Bornens, M., Wordeman, L., Wehland, J., Andrieux, A., and Job,

- D. Tubulin tyrosination is a major factor affecting the recruitment of CAP-Gly proteins at microtubule plus ends. *J Cell Biol*, 174(6):839–49, 2006. <https://doi.org/10.1083/jcb.200512058>.
- Peris, L., Wagenbach, M., Lafanechere, L., Brocard, J., Moore, A. T., Kozielski, F., Job, D., Wordeman, L., and Andrieux, A. Motor-dependent microtubule disassembly driven by tubulin tyrosination. *J Cell Biol*, 185(7):1159–66, 2009. <https://doi.org/10.1083/jcb.200902142>.
- Pham, H. PE-CVD Silicon Carbide - a structured material for surface micro-machined devices. *Doctoral Thesis*, 2004. <https://doi.org/uuid:91e396a8-5857-4e93-ba27-8a82d0d9f2b7>.
- Piedra, F. A., Kim, T., Garza, E. S., Geyer, E. A., Burns, A., Ye, X., and Rice, L. M. GDP-to-GTP exchange on the microtubule end can contribute to the frequency of catastrophe. *Mol Biol Cell*, 27(22):3515–3525, 2016. <https://doi.org/10.1091/mbc.E16-03-0199>.
- Preciado Lopez, M., Huber, F., Grigoriev, I., Steinmetz, M. O., Akhmanova, A., Dogterom, M., and Koenderink, G. H. In vitro reconstitution of dynamic microtubules interacting with actin filament networks. *Methods Enzymol*, 540:301–20, 2014. <https://doi.org/10.1016/B978-0-12-397924-7.00017-0>.
- Preciado Lopez, M., Huber, F., Grigoriev, I., Steinmetz, M. O., Akhmanova, A., Koenderink, G. H., and Dogterom, M. Actin-microtubule coordination at growing microtubule ends. *Nat Commun*, 5:4778, 2014. <https://doi.org/10.1038/ncomms5778>.
- Pudasaini, A., El-Arab, K. K., and Zoltowski, B. D. LOV-based optogenetic devices: light-driven modules to impart photoregulated control of cellular signaling. *Front Mol Biosci*, 2:18, 2015. <https://doi.org/10.3389/fmolb.2015.00018>.
- Rahim, M. K., Fukaminato, T., Kamei, T., and Tamaoki, N. Dynamic photocontrol of the gliding motility of a microtubule driven by kinesin on a photoisomerizable monolayer surface. *Langmuir*, 27(17):10347–50, 2011. <https://doi.org/10.1021/la2024499>.
- Ramsey, L., Schroeder, V., van Zalinge, H., Berndt, M., Korten, T., Diez, S., and Nicolau, D. V. Control and gating of kinesin-microtubule motility on electrically heated thermo-chips. *Biomed Microdevices*, 16(3):459–63, 2014. <https://doi.org/10.1007/s10544-014-9848-2>.
- Reck-Peterson, S. L., Yildiz, A., Carter, A. P., Gennerich, A., Zhang, N., and Vale, R. D. Single-molecule analysis of dynein processivity and stepping behavior. *Cell*, 126(2):335–48, 2006. <https://doi.org/10.1016/j.cell.2006.05.046>.
- Redeker, V., Levilliers, N., Vinolo, E., Rossier, J., Jaillard, D., Burnette, D., Gaertig, J., and Bre, M. H. Mutations of tubulin glycylation sites reveal cross-talk between the C termini of  $\alpha$ - and  $\beta$ -tubulin and affect the ciliary matrix in *Tetrahymena*. *J Biol Chem*, 280(1):596–606, 2005. <https://doi.org/10.1074/jbc.M408324200>.

- 
- Renthal, R., Schneider, B. G., Miller, M. M., and Luduena, R. F. Beta IV is the major beta-tubulin isotype in bovine cilia. *Cell Motil Cytoskeleton*, 25(1):19–29, 1993. <https://doi.org/10.1002/cm.970250104>.
- Reuther, C., Tucker, R., Ionov, L., and Diez, S. Programmable patterning of protein bioactivity by visible light. *Nano Lett*, 14(7):4050–7, 2014. <https://doi.org/10.1021/nl501521q>.
- Reuther, C., Mittasch, M., Naganathan, S. R., Grill, S. W., and Diez, S. Highly-efficient guiding of motile microtubules on non-topographical motor patterns. *Nano Lett*, 17(9):5699–5705, 2017. <https://doi.org/10.1021/acs.nanolett.7b02606>.
- Rickman, J., Duellberg, C., Cade, N. I., Griffin, L. D., and Surrey, T. Steady-state EB cap size fluctuations are determined by stochastic microtubule growth and maturation. *Proc Natl Acad Sci U S A*, 114(13):3427–3432, 2017. <https://doi.org/10.1073/pnas.1620274114>.
- Ricoult, S. G., Nezhad, A. S., Knapp-Mohammady, M., Kennedy, T. E., and Juncker, D. Humidified microcontact printing of proteins: universal patterning of proteins on both low and high energy surfaces. *Langmuir*, 30(40):12002–10, 2014. <https://doi.org/10.1021/la502742r>.
- Robison, P., Caporizzo, M. A., Ahmadzadeh, H., Bogush, A. I., Chen, C. Y., Margulies, K. B., Shenoy, V. B., and Prosser, B. L. Detyrosinated microtubules buckle and bear load in contracting cardiomyocytes. *Science*, 352(6284):aaf0659, 2016. <https://doi.org/10.1126/science.aaf0659>.
- Romet-Lemonne, G., VanDuijn, M., and Dogterom, M. Three-dimensional control of protein patterning in microfabricated devices. *Nano Lett*, 5(12):2350–4, 2005. <https://doi.org/10.1021/nl0507111>.
- Rosenberg, M. and Petrie, T. A. Theoretical study on the possible use of SiC microparticles as photothermal agents for the heating of bacteria. *Nanotechnology*, 23(5):055103, 2012. <https://doi.org/10.1088/0957-4484/23/5/055103>.
- Roth, D., Fitton, B. P., Chmel, N. P., Wasiluk, N., and Straube, A. Spatial positioning of EB family proteins at microtubule tips involves distinct nucleotide-dependent binding properties. *J Cell Sci*, 132(4), 2018. <https://doi.org/10.1242/jcs.219550>.
- Roth, S., Laan, L., and Dogterom, M. Reconstitution of cortical dynein function. *Methods Enzymol*, 540:205–30, 2014. <https://doi.org/10.1016/B978-0-12-397924-7.00012-1>.
- Ruan, Y. and Wasteneys, G. O. CLASP: a microtubule-based integrator of the hormone-mediated transitions from cell division to elongation. *Curr Opin Plant Biol*, 22:149–58, 2014. <https://doi.org/10.1016/j.pbi.2014.11.003>.

- Ruhnow, F., Zwicker, D., and Diez, S. Tracking single particles and elongated filaments with nanometer precision. *Biophys J*, 100(11):2820–8, 2011. <https://doi.org/10.1016/j.bpj.2011.04.023>.
- Sanders, A. A. and Kaverina, I. Nucleation and dynamics of Golgi-derived microtubules. *Front Neurosci*, 9:431, 2015. <https://doi.org/10.3389/fnins.2015.00431>.
- Saxton, M. J. Modeling 2D and 3D diffusion. *Methods Mol Biol*, 400:295–321, 2007. [https://doi.org/10.1007/978-1-59745-519-0\\_20](https://doi.org/10.1007/978-1-59745-519-0_20).
- Schaedel, L., John, K., Gaillard, J., Nachury, M. V., Blanchoin, L., and Thery, M. Microtubules self-repair in response to mechanical stress. *Nat Mater*, 14(11):1156–63, 2015. <https://doi.org/10.1038/nmat4396>.
- Schek, H. T., Gardner, M. K., Cheng, J., Odde, D. J., and Hunt, A. J. Microtubule assembly dynamics at the nanoscale. *Curr Biol*, 17(17):1445–55, 2007. <https://doi.org/10.1016/j.cub.2007.07.011>.
- Schiff, P. B., Fant, J., and Horwitz, S. B. Promotion of microtubule assembly in vitro by taxol. *Nature*, 277(5698):665–7, 1979. <https://doi.org/10.1038/277665a0>.
- Schindelin, J., Arganda-Carreras, I., Frise, E., Kaynig, V., Longair, M., Pietzsch, T., Preibisch, S., Rueden, C., Saalfeld, S., Schmid, B., Tinevez, J. Y., White, D. J., Hartenstein, V., Eliceiri, K., Tomancak, P., and Cardona, A. Fiji: an open-source platform for biological-image analysis. *Nat Methods*, 9(7):676–82, 2012. <https://doi.org/10.1038/nmeth.2019>.
- Schmidt, J. C., Arthanari, H., Boeszoermentyi, A., Dashkevich, N. M., Wilson-Kubalek, E. M., Monnier, N., Markus, M., Oberer, M., Milligan, R. A., Bathe, M., Wagner, G., Grishchuk, E. L., and Cheeseman, I. M. The kinetochore-bound Ska1 complex tracks depolymerizing microtubules and binds to curved protofilaments. *Dev Cell*, 23(5):968–80, 2012. <https://doi.org/10.1016/j.devcel.2012.09.012>.
- Schmidt, R., Fielmich, L. E., Grigoriev, I., Katrukha, E. A., Akhmanova, A., and van den Heuvel, S. Two populations of cytoplasmic dynein contribute to spindle positioning in *C. elegans* embryos. *J Cell Biol*, 216(9):2777–2793, 2017. <https://doi.org/10.1083/jcb.201607038>.
- Schroeder, V., Korten, T., Linke, H., Diez, S., and Maximov, I. Dynamic guiding of motor-driven microtubules on electrically heated, smart polymer tracks. *Nano Lett*, 13(7):3434–8, 2013. <https://doi.org/10.1021/nl402004s>.
- Schroer, T. A. Dynactin. *Annu Rev Cell Dev Biol*, 20:759–79, 2004. <https://doi.org/10.1146/annurev.cellbio.20.012103.094623>.
- Schuyler, S. C. and Pellman, D. Microtubule "plus-end-tracking proteins": The end is just the beginning. *Cell*, 105(4):421–4, 2001. [https://doi.org/10.1016/S0092-8674\(01\)00364-6](https://doi.org/10.1016/S0092-8674(01)00364-6).

- 
- Seetapun, D., Castle, B. T., McIntyre, A. J., Tran, P. T., and Odde, D. J. Estimating the microtubule GTP cap size in vivo. *Curr Biol*, 22(18):1681–7, 2012. <https://doi.org/10.1016/j.cub.2012.06.068>.
- Sen, I., Veprintsev, D., Akhmanova, A., and Steinmetz, M. O. End binding proteins are obligatory dimers. *PLoS One*, 8(9):e74448, 2013. <https://doi.org/10.1371/journal.pone.0074448>.
- Sharma, A., Aher, A., Dynes, N. J., Frey, D., Katrukha, E. A., Jaussi, R., Grigoriev, I., Croisier, M., Kammerer, R. A., Akhmanova, A., Gonczy, P., and Steinmetz, M. O. Centriolar CPAP/SAS-4 imparts slow processive microtubule growth. *Dev Cell*, 37(4):362–76, 2016. <https://doi.org/10.1016/j.devcel.2016.04.024>.
- Shelden, E. A., Colburn, Z. T., and Jones, J. C. Focusing super resolution on the cytoskeleton. *F1000Res*, 5, 2016. <https://doi.org/10.12688/f1000research.8233.1>.
- Sheldrick, G. M. Experimental phasing with SHELXC/D/E: combining chain tracing with density modification. *Acta Crystallogr D Biol Crystallogr*, 66(Pt 4):479–85, 2010. <https://doi.org/10.1107/S0907444909038360>.
- Shimizu-Sato, S., Huq, E., Tepperman, J. M., and Quail, P. H. A light-switchable gene promoter system. *Nat Biotechnol*, 20(10):1041–4, 2002. <https://doi.org/10.1038/nbt734>.
- Sirajuddin, M., Rice, L. M., and Vale, R. D. Regulation of microtubule motors by tubulin isoforms and post-translational modifications. *Nat Cell Biol*, 16(4):335–44, 2014. <https://doi.org/10.1038/ncb2920>.
- Slep, K. C. Structural and mechanistic insights into microtubule end-binding proteins. *Curr Opin Cell Biol*, 22(1):88–95, 2010. <https://doi.org/10.1016/j.ceb.2009.10.009>.
- Sousa, A., Reis, R., Sampaio, P., and Sunkel, C. E. The drosophila CLASP homologue, Mast/Orbit regulates the dynamic behaviour of interphase microtubules by promoting the pause state. *Cell Motil Cytoskeleton*, 64(8):605–20, 2007. <https://doi.org/10.1002/cm.20208>.
- Sprague, B. L., Pego, R. L., Stavreva, D. A., and McNally, J. G. Analysis of binding reactions by fluorescence recovery after photobleaching. *Biophys J*, 86(6):3473–95, 2004. <https://doi.org/10.1529/biophysj.103.026765>.
- Steger, C. An unbiased detector of curvilinear structures. *IEEE Trans Pattern Analysis and Machine Intelligence*, 20(2):113–125, 1998.
- Strale, P. O., Azoune, A., Bugnicourt, G., Lecomte, Y., Chahid, M., and Studer, V. Multi-protein printing by light-induced molecular adsorption. *Adv Mater*, 28(10):2024–9, 2016. <https://doi.org/10.1002/adma.201504154>.

- Strickland, D., Lin, Y., Wagner, E., Hope, C. M., Zayner, J., Antoniou, C., Sosnick, T. R., Weiss, E. L., and Glotzer, M. TULIPs: tunable, light-controlled interacting protein tags for cell biology. *Nat Methods*, 9(4):379–84, 2012. <https://doi.org/10.1038/nmeth.1904>.
- Sumino, Y., Nagai, K. H., Shitaka, Y., Tanaka, D., Yoshikawa, K., Chate, H., and Oiwa, K. Large-scale vortex lattice emerging from collectively moving microtubules. *Nature*, 483(7390):448–52, 2012. <https://doi.org/10.1038/nature10874>.
- Taberner, N. A minimal system to establish microtubule-based polarity in vitro. *Dissertation*, 2016. <https://doi.org/10.4233/uuid:c87db99c-45f8-4ee9-bcf6-c0667c2be618>.
- Taberner, N., Weber, G., You, C., Dries, R., Piehler, J., and Dogterom, M. Reconstituting functional microtubule-barrier interactions. *Methods Cell Biol*, 120:69–90, 2014. <https://doi.org/10.1016/B978-0-12-417136-7.00005-7>.
- Taberner, N., Lof, A., Roth, S., Lamers, D., Zeijlemaker, H., and Dogterom, M. In vitro systems for the study of microtubule-based cell polarity in fission yeast. *Methods Cell Biol*, 128:1–22, 2015. <https://doi.org/10.1016/bs.mcb.2015.02.008>.
- Tanenbaum, M. E. and Medema, R. H. Mechanisms of centrosome separation and bipolar spindle assembly. *Dev Cell*, 19(6):797–806, 2010. <https://doi.org/10.1016/j.devcel.2010.11.011>.
- Tarantino, N., Tinevez, J. Y., Crowell, E. F., Boisson, B., Henriques, R., Mhlanga, M., Agou, F., Israel, A., and Laplantine, E. TNF and IL-1 exhibit distinct ubiquitin requirements for inducing NEMO-IKK supramolecular structures. *J Cell Biol*, 204(2):231–45, 2014. <https://doi.org/10.1083/jcb.201307172>.
- Taylor, J. An introduction to error analysis. *Sausalito, University Science Books*, 1997.
- Tilney, L. G., Bryan, J., Bush, D. J., Fujiwara, K., Mooseker, M. S., Murphy, D. B., and Snyder, D. H. Microtubules: evidence for 13 protofilaments. *J Cell Biol*, 59(2 Pt 1): 267–75, 1973. <https://doi.org/10.1083/jcb.59.2.267>.
- Tischer, C., Brunner, D., and Dogterom, M. Force- and kinesin-8-dependent effects in the spatial regulation of fission yeast microtubule dynamics. *Mol Syst Biol*, 5:250, 2009. <https://doi.org/10.1038/msb.2009.5>.
- Toettcher, J. E., Gong, D., Lim, W. A., and Weiner, O. D. Light-based feedback for controlling intracellular signaling dynamics. *Nat Methods*, 8(10):837–9, 2011. <https://doi.org/10.1038/nmeth.1700>.
- Tolic-Norrelykke, I. M., Sacconi, L., Thon, G., and Pavone, F. S. Positioning and elongation of the fission yeast spindle by microtubule-based pushing. *Curr Biol*, 14(13): 1181–6, 2004. <https://doi.org/10.1016/j.cub.2004.06.029>.

- Tolic-Norrellykke, I. M., Sacconi, L., Stringari, C., Raabe, I., and Pavone, F. S. Nuclear and division-plane positioning revealed by optical micromanipulation. *Curr Biol*, 15(13):1212–6, 2005. <https://doi.org/10.1016/j.cub.2005.05.052>.
- Tran, P. T., Doye, V., Chang, F., and Inoue, S. Microtubule-dependent nuclear positioning and nuclear-dependent septum positioning in the fission yeast *Schizosaccharomyces pombe* [correction of *Saccharomyces pombe*]. *Biol Bull*, 199(2):205–6, 2000. <https://doi.org/10.2307/1542900>.
- Tran, P. T., Marsh, L., Doye, V., Inoue, S., and Chang, F. A mechanism for nuclear positioning in fission yeast based on microtubule pushing. *J Cell Biol*, 153(2):397–411, 2001. <https://doi.org/10.1083/jcb.153.2.397>.
- Umbreit, N. T., Gestaut, D. R., Tien, J. F., Vollmar, B. S., Gonen, T., Asbury, C. L., and Davis, T. N. The Ndc80 kinetochore complex directly modulates microtubule dynamics. *Proc Natl Acad Sci U S A*, 109(40):16113–8, 2012. <https://doi.org/10.1073/pnas.1209615109>.
- Uyeda, T. Q., Kron, S. J., and Spudich, J. A. Myosin step size. estimation from slow sliding movement of actin over low densities of heavy meromyosin. *J Mol Biol*, 214(3):699–710, 1990. [https://doi.org/10.1016/0022-2836\(90\)90287-V](https://doi.org/10.1016/0022-2836(90)90287-V).
- Valiyakath, J. and Gopalakrishnan, M. Polymerisation force of a rigid filament bundle: diffusive interaction leads to sublinear force-number scaling. *Sci Rep*, 8(1):2526, 2018. <https://doi.org/10.1038/s41598-018-20259-7>.
- van Bergeijk, P., Adrian, M., Hoogenraad, C. C., and Kapitein, L. C. Optogenetic control of organelle transport and positioning. *Nature*, 518(7537):111–114, 2015. <https://doi.org/10.1038/nature14128>.
- van den Heuvel, M. G., Butcher, C. T., Smeets, R. M., Diez, S., and Dekker, C. High rectifying efficiencies of microtubule motility on kinesin-coated gold nanostructures. *Nano Lett*, 5(6):1117–22, 2005. <https://doi.org/10.1021/nl0506554>.
- van den Heuvel, M. G., de Graaff, M. P., and Dekker, C. Molecular sorting by electrical steering of microtubules in kinesin-coated channels. *Science*, 312(5775):910–4, 2006. <https://doi.org/10.1126/science.1124258>.
- van der Vaart, B., Manatschal, C., Grigoriev, I., Olieric, V., Gouveia, S. M., Bjelic, S., Demmers, J., Vorobjev, I., Hoogenraad, C. C., Steinmetz, M. O., and Akhmanova, A. SLAIN2 links microtubule plus end-tracking proteins and controls microtubule growth in interphase. *J Cell Biol*, 193(6):1083–99, 2011. <https://doi.org/10.1083/jcb.201012179>.
- van Dijk, J., Miro, J., Strub, J. M., Lacroix, B., van Dorselaer, A., Edde, B., and Janke, C. Polyglutamylation is a post-translational modification with a broad range of substrates. *J Biol Chem*, 283(7):3915–22, 2008. <https://doi.org/10.1074/jbc.M705813200>.

- van Doorn, G. S., Tanase, C., Mulder, B. M., and Dogterom, M. On the stall force for growing microtubules. *Eur Biophys J*, 29(1):2–6, 2000. <https://doi.org/10.1007/s002490050245>.
- van Haren, J., Charafeddine, R. A., Ettinger, A., Wang, H., Hahn, K. M., and Wittmann, T. Local control of intracellular microtubule dynamics by EB1 photodissociation. *Nat Cell Biol*, 20(3):252–261, 2018. <https://doi.org/10.1038/s41556-017-0028-5>.
- van Riel, W. E., Rai, A., Bianchi, S., Katrukha, E. A., Liu, Q., Heck, A. J., Hoogenraad, C. C., Steinmetz, M. O., Kapitein, L. C., and Akhmanova, A. Kinesin-4 KIF21B is a potent microtubule pausing factor. *Elife*, 6, 2017. <https://doi.org/10.7554/eLife.24746>.
- VanBuren, V., Odde, D. J., and Cassimeris, L. Estimates of lateral and longitudinal bond energies within the microtubule lattice. *Proc Natl Acad Sci U S A*, 99(9):6035–40, 2002. <https://doi.org/10.1073/pnas.092504999>.
- VanBuren, V., Cassimeris, L., and Odde, D. J. Mechanochemical model of microtubule structure and self-assembly kinetics. *Biophys J*, 89(5):2911–26, 2005. <https://doi.org/10.1529/biophysj.105.060913>.
- Verde, F., Dogterom, M., Stelzer, E., Karsenti, E., and Leibler, S. Control of microtubule dynamics and length by cyclin A- and cyclin B-dependent kinases in *Xenopus* egg extracts. *J Cell Biol*, 118(5):1097–108, 1992. <https://doi.org/10.1083/jcb.118.5.1097>.
- Verhey, K. J. and Gaertig, J. The tubulin code. *Cell Cycle*, 6(17):2152–60, 2007. <https://doi.org/10.4161/cc.6.17.4633>.
- Vleugel, M., Kok, M., and Dogterom, M. Understanding force-generating microtubule systems through in vitro reconstitution. *Cell Adh Migr*, pages 475–494, 2016. <https://doi.org/10.1080/19336918.2016.1241923>.
- Vleugel, M., Roth, S., Groenendijk, C. F., and Dogterom, M. Reconstitution of basic mitotic spindles in spherical emulsion droplets. *J Vis Exp*, -(114), 2016. <https://doi.org/10.3791/54278>.
- von Loeffelholz, O., Venables, N. A., Drummond, D. R., Katsuki, M., Cross, R., and Moores, C. A. Nucleotide- and Mal3-dependent changes in fission yeast microtubules suggest a structural plasticity view of dynamics. *Nat Commun*, 8(1):2110, 2017. <https://doi.org/10.1038/s41467-017-02241-5>.
- Voss, S., Klewer, L., and Wu, Y. W. Chemically induced dimerization: reversible and spatiotemporal control of protein function in cells. *Curr Opin Chem Biol*, 28:194–201, 2015. <https://doi.org/10.1016/j.cbpa.2015.09.003>.
- Wagner, T., Hiner, M., and xraynaud. thorstenwagner/ij-ridgedetection: Ridge Detection 1.4.0. *Zenodo*, 2017. <https://doi.org/10.5281/zenodo.845874>.

- Walker, R. A., O'Brien, E. T., Pryer, N. K., Soboeiro, M. F., Voter, W. A., Erickson, H. P., and Salmon, E. D. Dynamic instability of individual microtubules analyzed by video light microscopy: rate constants and transition frequencies. *J Cell Biol*, 107(4):1437–48, 1988. <https://doi.org/10.1083/jcb.107.4.1437>.
- Walker, R. A., Salmon, E. D., and Endow, S. A. The drosophila claret segregation protein is a minus-end directed motor molecule. *Nature*, 347(6295):780–2, 1990. <https://doi.org/10.1038/347780a0>.
- Walker, R. A., Pryer, N. K., and Salmon, E. D. Dilution of individual microtubules observed in real time in vitro: evidence that cap size is small and independent of elongation rate. *J Cell Biol*, 114(1):73–81, 1991. <https://doi.org/10.1083/jcb.114.1.73>.
- Wang, H., Vilela, M., Winkler, A., Tarnawski, M., Schlichting, I., Yumerefendi, H., Kuhlman, B., Liu, R., Danuser, G., and Hahn, K. M. LOVTRAP: an optogenetic system for photoinduced protein dissociation. *Nat Methods*, 13(9):755–8, 2016. <https://doi.org/10.1038/nmeth.3926>.
- Wang, H. W. and Nogales, E. Nucleotide-dependent bending flexibility of tubulin regulates microtubule assembly. *Nature*, 435(7044):911–5, 2005. <https://doi.org/10.1038/nature03606>.
- Watanabe, T., Noritake, J., and Kaibuchi, K. Regulation of microtubules in cell migration. *Trends Cell Biol*, 15(2):76–83, 2005. <https://doi.org/10.1016/j.tcb.2004.12.006>.
- Waterman-Storer, C. M. and Salmon, E. D. Endoplasmic reticulum membrane tubules are distributed by microtubules in living cells using three distinct mechanisms. *Curr Biol*, 8(14):798–806, 1998. [https://doi.org/10.1016/S0960-9822\(98\)70321-5](https://doi.org/10.1016/S0960-9822(98)70321-5).
- Waterman-Storer, C. M., Gregory, J., Parsons, S. F., and Salmon, E. D. Membrane/microtubule tip attachment complexes (TACs) allow the assembly dynamics of plus ends to push and pull membranes into tubulovesicular networks in interphase *Xenopus* egg extracts. *J Cell Biol*, 130(5):1161–9, 1995. <https://doi.org/10.1083/jcb.130.5.1161>.
- Waterman-Storer, C. M., Desai, A., Bulinski, J. C., and Salmon, E. D. Fluorescent speckle microscopy, a method to visualize the dynamics of protein assemblies in living cells. *Curr Biol*, 8(22):1227–30, 1998. [https://doi.org/10.1016/S0960-9822\(07\)00515-5](https://doi.org/10.1016/S0960-9822(07)00515-5).
- Wieczorek, M., Bechstedt, S., Chaaban, S., and Brouhard, G. J. Microtubule-associated proteins control the kinetics of microtubule nucleation. *Nat Cell Biol*, 17(7):907–16, 2015. <https://doi.org/10.1038/ncb3188>.
- Xiong, R., Drullion, C., Verstraelen, P., Demeester, J., Skirtach, A. G., Abbadie, C., De Vos, W. H., De Smedt, S. C., and Braeckmans, K. Fast spatial-selective delivery

- into live cells. *J Control Release*, 2017. <https://doi.org/10.1016/j.jconrel.2017.09.033>.
- Xu, Z., Schaedel, L., Portran, D., Aguilar, A., Gaillard, J., Marinkovich, M. P., They, M., and Nachury, M. V. Microtubules acquire resistance from mechanical breakage through intralumenal acetylation. *Science*, 356(6335):328–332, 2017. <https://doi.org/10.1126/science.aai8764>.
- Yaffe, M. P., Stuurman, N., and Vale, R. D. Mitochondrial positioning in fission yeast is driven by association with dynamic microtubules and mitotic spindle poles. *Proc Natl Acad Sci U S A*, 100(20):11424–8, 2003. <https://doi.org/10.1073/pnas.1534703100>.
- Yamamoto, A., Tsutsumi, C., Kojima, H., Oiwa, K., and Hiraoka, Y. Dynamic behavior of microtubules during dynein-dependent nuclear migrations of meiotic prophase in fission yeast. *Mol Biol Cell*, 12(12):3933–46, 2001. <https://doi.org/10.1091/mbc.12.12.3933>.
- Yanagida, T., Nakase, M., Nishiyama, K., and Oosawa, F. Direct observation of motion of single F-actin filaments in the presence of myosin. *Nature*, 307(5946):58–60, 1984. <https://doi.org/10.1038/307058a0>.
- Yi, J., Wu, X., Chung, A. H., Chen, J. K., Kapoor, T. M., and Hammer, J. A. Centrosome repositioning in T cells is biphasic and driven by microtubule end-on capture-shrinkage. *J Cell Biol*, 202(5):779–92, 2013. <https://doi.org/10.1083/jcb.201301004>.
- Yu, N., Signorile, L., Basu, S., Ottema, S., Lebbink, J. H., Leslie, K., Smal, I., Dekkers, D., Demmers, J., and Galjart, N. Isolation of functional tubulin dimers and of tubulin-associated proteins from mammalian cells. *Curr Biol*, 26(13):1728–36, 2016. <https://doi.org/10.1016/j.cub.2016.04.069>.
- Zakharov, P., Gudimchuk, N., Voevodin, V., Tikhonravov, A., Ataullakhanov, F. I., and Grishchuk, E. L. Molecular and mechanical causes of microtubule catastrophe and aging. *Biophys J*, 109(12):2574–91, 2015. <https://doi.org/10.1016/j.bpj.2015.10.048>.
- Zaliapin, I., Semenova, I., Kashina, A., and Rodionov, V. Multiscale trend analysis of microtubule transport in melanophores. *Biophys J*, 88(6):4008–16, 2005. <https://doi.org/10.1529/biophysj.104.057083>.
- Zanic, M., Widlund, P. O., Hyman, A. A., and Howard, J. Synergy between XMAP215 and EB1 increases microtubule growth rates to physiological levels. *Nat Cell Biol*, 15(6):688–93, 2013. <https://doi.org/10.1038/ncb2744>.
- Zelinski, B., Muller, N., and Kierfeld, J. Dynamics and length distribution of microtubules under force and confinement. *Phys Rev E Stat Nonlin Soft Matter Phys*, 86(4 Pt 1):041918, 2012. <https://doi.org/10.1103/PhysRevE.86.041918>.

- 
- Zhai, Y., Kronebusch, P. J., Simon, P. M., and Borisy, G. G. Microtubule dynamics at the G2/M transition: abrupt breakdown of cytoplasmic microtubules at nuclear envelope breakdown and implications for spindle morphogenesis. *J Cell Biol*, 135(1):201–14, 1996. <https://doi.org/10.1083/jcb.135.1.201>.
- Zhang, D., Grode, K. D., Stewman, S. F., Diaz-Valencia, J. D., Liebling, E., Rath, U., Riera, T., Currie, J. D., Buster, D. W., Asenjo, A. B., Sosa, H. J., Ross, J. L., Ma, A., Rogers, S. L., and Sharp, D. J. *Drosophila* katanin is a microtubule depolymerase that regulates cortical-microtubule plus-end interactions and cell migration. *Nat Cell Biol*, 13(4):361–70, 2011. <https://doi.org/10.1038/ncb2206>.
- Zhang, R., Alushin, G. M., Brown, A., and Nogales, E. Mechanistic origin of microtubule dynamic instability and its modulation by EB proteins. *Cell*, 162(4):849–59, 2015. <https://doi.org/10.1016/j.cell.2015.07.012>.
- Zhao, T., Graham, O. S., Raposo, A., and St Johnston, D. Growing microtubules push the oocyte nucleus to polarize the *Drosophila* dorsal-ventral axis. *Science*, 336(6084):999–1003, 2012. <https://doi.org/10.1126/science.1219147>.
- Zheng, Z., Wan, Q., Meixiong, G., and Du, Q. Cell cycle-regulated membrane binding of NuMA contributes to efficient anaphase chromosome separation. *Mol Biol Cell*, 25(5):606–19, 2014. <https://doi.org/10.1091/mbc.E13-08-0474>.
- Zimmerman, S. P., Hallett, R. A., Bourke, A. M., Bear, J. E., Kennedy, M. J., and Kuhlman, B. Tuning the binding affinities and reversion kinetics of a light inducible dimer allows control of transmembrane protein localization. *Biochemistry*, 55(37):5264–71, 2016. <https://doi.org/10.1021/acs.biochem.6b00529>.



# ACKNOWLEDGEMENTS

A scientific journey that spans over five years cannot be undertaken without the help and support of family, friends and colleagues. The BN department is an incredibly friendly and open environment to pursue a PhD. I would like to thank everyone who had a part in the realization of my thesis and has helped me to manoeuvre the bumpy road. In particular, I would like to thank the following people:

Marileen, I would like to thank you for giving me the freedom to explore my project and regions beyond. You allowed me to get stuck on my projects and unstuck on my own. Thank you for your patience and guidance.

To all the former and current lab members, thank you for making the lab a fun place to work and a supporting environment to share the failures and successes. Sophie, Magdalena, Stef, Gesa, Georges, Marian, thank you for introducing me to the world of reconstitution biology and showing me the ropes in the lab. Celine, Marco, Harmen, thanks for all discussions on actin and illuminating the theory behind our experiments. Jolijn, thank you for all your help and expertise. Reza and Ajay, thanks for continuing my research, I hope I left fertile soil. Kim, your bright enthusiasm is contagious and showed me that even experimental setbacks should be greeted with a smile. Renu, thanks for indulging me in my attempts to troubleshoot your uncooperative droplets, it was fun to brainstorm for solutions. Vladimir, your unwavering and just critique has often make me rethink and improve my assumptions and conclusions. Louis, thanks for your keen theoretical insights and for spiking my interest in Monte Carlo simulations. Mathijs, your easygoing nature was of great help in meeting our deadlines. N ria, your persistence and dedication to your work were an inspiration for me. Florian, special thanks to you for rejoining the lab at a crucial time in my PhD project. Your input was a great motivator and it was a pleasure to discuss the details of my experiments with you. Also a big thanks to all the students I had the pleasure to supervise. Your engagement was most rewarding and your questions made me aware of all the blind spots in my understanding.

The unsung hero's of any and all experimental endeavours are the technicians. Anne, Eseng l, Eli, Roland, Dani l, Jeremie, Sacha, Andrea, thank you for your assistance and perseverance with badly behaving proteins. Marc, thank you for teaching me the ins and outs of the cleanroom.

I would like to thank all collaborators in the groups of Anna Akhmanova and Lukas Kapitein in Utrecht. Amol, I really enjoyed our synergistic collaboration and our discussions on CLASP and science in general.

Bart, I always enjoy our discussions about science and music, usually over a cup of coffee or a glass of good whisky. It was great to share our PhD experiences and reflect on the meaning of it all.

And lastly, I would like to thank my parents and brother for their supporting perspectives from the world outside of science.



# CURRICULUM VITÆ

## Maurits William Adriaan KOK

28-04-1987      Born in Utrecht, the Netherlands.

## EDUCATION

1998–2004      Grammar School  
Utrechts Stedelijk Gymnasium, Utrecht

2004–2005      Music studies - Jazz  
Chichester College, Chichester, UK

2005–2008      Bachelor of Science in Life Science & Technology  
Technische Universiteit Delft  
Universiteit Leiden

2008–2009      Bachelor of Music, 1st year  
Codarts - Hogeschool voor de kunsten, Rotterdam

2009–2013      Master of Science in Applied Physics  
Technische Universiteit Delft

2014–2019      Ph.D. Biophysics  
Technische Universiteit Delft  
*Thesis:*      The dynamics of microtubule stability - A reconstituted of regulated microtubule assembly under force  
*Promotor:*   Prof. dr. M. Dogterom



# LIST OF PUBLICATIONS

6. **M. Kok**, R. Amini Hounejani, M. Dogterom, *Microtubule assembly under force at micron-sized barriers with a silicon carbide overhang*, [in preparation].
5. **M. Kok**, F. Huber, S. Kalisch, M. Dogterom, *EB informed dynamics of the microtubule cap during stalled growth*, [in preparation].
4. R. Tas, C. Chen, E.A. Katrukha, M. Vleugel, **M. Kok**, M. Dogterom, A. Akhmanova, L.C. Kapitein, *Guided by Light: Optical Control of Microtubule Gliding Assays*, Nano Letters, 18 (12), 7524-7528 (2018)
3. A. Aher, **M. Kok**, A. Sharma, A. Rai, N. Olieric, R. Rodriguez-Garcia, E.A. Katrukha, T. Weinert, V. Olieric, L.C. Kapitein, M.O. Steinmetz, M. Dogterom, A. Akhmanova, *CLASP Suppresses Microtubule Catastrophes through a Single TOG Domain*, Developmental Cell **46**, 1-19 (2018).
2. M. Vleugel, **M. Kok**, M. Dogterom, *Understanding Force-Generating Microtubule Systems through in vitro Reconstitution*, Cell Adhesion & Migration **10**:5, 475-494 (2016).
1. P. van Nies, Z. Nourian, **M. Kok**, R. van Wijk, J. Moeskops, I. Westerlaken, J.M. Poolman, R. Eelkema, J.H. van Esch, Y. Kuruma, T. Ueda, C. Danelon, *Unbiased Tracking of the Progression of mRNA and Protein Synthesis in Bulk and in Liposome-Confined Reactions*, ChemBioChem **14**:15, 1963-1966 (2013)